

WISSENSCHAFTLICH-TECHNISCHE BERICHTE

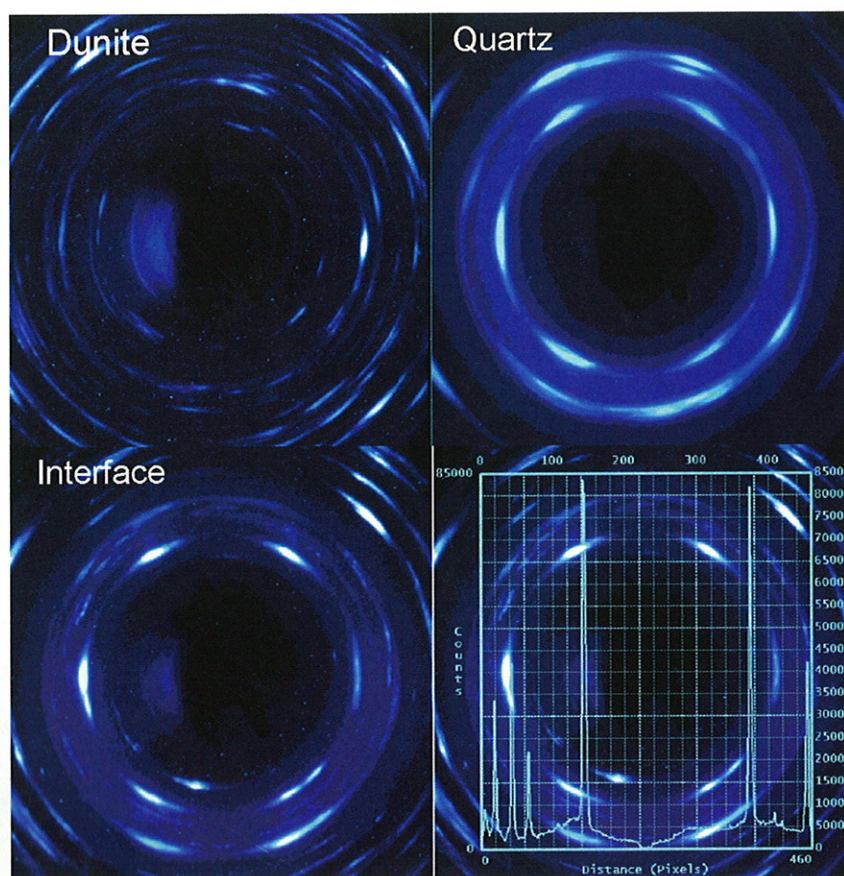
FZR-364

Januar 2003

ISSN 1437-322X



Project-Group ESRF-Beamline (ROBL-CRG)



Bi-Annual Report 2001/2002

Cover picture:

Debye-Scherrer cones for texture analysis of a shock wave deformed quartz dunite sample in transmission at 17.749 keV. The pictures are taken with a CCD camera by Dr. K. Walther in a collaboration of the FZR with the GeoForschungsZentrum Potsdam. The use of the two-dimensional detector allows rapid data collection. Immediately one can see the strong texture of quartz (bright spots on the rings) while the dunite is more homogenously crystallized. In the interface region the minerals have mixed (see Experimental Report 20_02_IH7 and also Experimental Report 20_02_048 for texture investigations on different minerals).

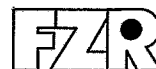
Forschungszentrum Rossendorf e. V.

Postfach 51 01 19
D-01314 Dresden
Bundesrepublik Deutschland

Telefon +33 (0) 4.76.88.23.67
Telefax +33 (0) 4.76.88.25.05
E-Mail schell@esf.fr
Internet <http://www.fz-rossendorf.de/FWE/>

FORSCHUNGSZENTRUM ROSSENDORF

Mitglied der Wissenschaftsgemeinschaft Gottfried Wilhelm Leibniz



WISSENSCHAFTLICH-TECHNISCHE BERICHTE

FZR-364

Januar 2003

Bi-Annual Report 2001/2002

**Project-Group ESRF-Beamline
(ROBL-CRG)**

Editor: N. Schell

Preface

The third report from the Project-Group ESRF-Beamline of the Forschungszentrum Rossendorf covers the period from January 2001 until December 2002. The ROssendorf BeamLine (ROBL) at the European Synchrotron Radiation Facility (ESRF) in Grenoble performed again well during this time – although we had major staff fluctuations, including two times a change in the project-management: Dr. W. Matz became head of the Technical Infrastructure at FZR, and Dr. T. Reich had been offered a professorship at the University of Mainz. We congratulate both of them. In the beamtime used by the FZR and collaborating institutes 77 different experiments were scheduled, while in the ESRF scheduled beamtime 21 experiments were performed by external groups. Additionally, a distinct amount of beamtime was devoted to commissioning of new equipment.

The main effort from the technical point of view during the reporting period was made in the improvement of equipment. At the radiochemistry end-station an electrochemical cell for *in-situ* chemical manipulation of the sample environment was tested, and a software upgrade for control and data acquisition in the EXAFS/XANES experiments was installed. At the materials research end-station a Ge channel-cut analyser system in front of the detector for high-resolution experiments and a one-dimensional linear position sensitive detector with a drastically improved time resolution were commissioned during the period. Additionally, a small chamber for annealing studies with a hemispherical Be-dome, i.e. a 2π -scattering access, was designed and commissioned. In the general beamline optics a sagittally bent second crystal in the double crystal monochromator was used for the first time.

Since February 2000 ROBL has been part of the EU programme "Access to Research Infrastructures" (HPRI-CT-1999-00077) which supports user groups from member and associated states during experiments at ROBL. In the year 2001 ROBL hosted 10 groups for experiments, in 2002 even 12 groups. In the corresponding Contract Review Hearing in June 2002 before an independent panel ROBL got high marks for its scientific and administrative performance. In August 2002 a project for the "structure design of TiAlN layers by real-time *in-situ* x-ray diffraction" for materials research was granted by the DFG (SCHE 682). Finally, in September 2002 a WTZ-cooperation with ITME, Warsaw, was started (POL 01/105) which includes increased access to ROBL for our Polish colleagues. A first group has already been welcome in Grenoble.

The ROBL-CRG would like to thank all partners, research groups, review panel members and organisations who supported its progress during the last 24 months. Special thanks are due to the FZR management, the CRG office – also with a change in the liason engineer – and the safety group of the ESRF.

In spring 2003 ROBL will be evaluated by the ESRF before signing the contract prolongation for hopefully another five years exciting work with interesting scientific results in an international environment.

The report is organised in three main parts. The first part contains extended contributions on results obtained at ROBL. The second part gives an overview about the general experimental possibilities, scheduled experiments, publications, guests having visited ROBL with support of the EC, and staff information. Finally, the third part collects the experimental reports of the user groups received.

Dr. Norbert Schell

Contents

	Page
Contributions	
The nanostructure evolution during and after magnetron deposition of Au films	5
An <i>in-situ</i> grazing incidence x-ray diffraction study of the crystallisation of Ni-Ti thin films	11
Determination of the chemical composition profile and the relaxation process for thin semiconducting heterostructures	17
EXAFS investigations of uranium complexes formed by different bacteria isolated from uranium mining wastes	26
EXAFS study of pH dependence of uranium(VI) complexation with protocatechuic acid – application of iterative transformation factor analysis to EXAFS and UV-vis spectroscopy	31
EXAFS studies of reactions of neptunyl(V) with mackinawite	40
Overview of the technical characteristics of ROBL	47
Overview of the beamtime distribution at ROBL	50
Support of user groups by the European Commission	52
List of EC supported users of ROBL	52
Scheduled experiments at the radiochemistry end-station	55
Scheduled experiments at the materials research end-station	59
List of publications	63
Personnel of the Project-Group ESRF-Beamline	68
Experimental reports	
Experimental reports from the radiochemistry end-station (No. 20_01_xxx)	71
Experimental reports from the materials research end-station (No. 20_02_xxx)	112
Experimental reports from experiments scheduled by the ESRF	143

The nanostructure evolution during and after magnetron deposition of Au films

N. Schell^{1,2}

¹Project-Group ESRF-Beamline, ²Institute of Ion Beam Physics and Materials Research
Forschungszentrum Rossendorf, P.O. Box 51 01 19, 01314 Dresden, Germany

T. Jensen, J.H. Petersen, K.P. Andreasen, M. Skov Jensen, J. Bøttiger, J. Chevallier
Department of Physics and Astronomy, University of Aarhus, 8000 Aarhus C, Denmark

1. Introduction

Nanocrystalline materials are a new class of materials with grain sizes between a few nanometers and 100 nm [1]. Due to the extremely small grain sizes, a large volume fraction of the atoms is located at the grain boundaries. This gives to the materials unique properties and offers a great potential for industrial applications [2]. Due to the enhanced diffusivity and the smaller grains, grain growth, which may deteriorate the material, occurs in single-phase nanocrystalline material at significantly lower temperatures than in coarser-grained materials. Two-phase nanocomposites are introduced to thermally stabilize nanocrystalline materials and at the same time to build in additional beneficial properties [3-10].

Nanocrystalline materials, including nanocomposites, are produced by many different techniques [2], including quenching from the liquid phase (melt spinning) and from the vapour phase (sputtering). Magnetron sputtering has turned out to be a versatile technique for deposition of thin-film nanocrystalline materials.

The nanostructure determines the physical and chemical properties of the materials, so for optimum performance of a nanocrystalline thin film, the nanostructure has to be tailored for the specific application. This requires a knowledge of the dependence of the nanostructure on the deposition parameters and an understanding of the mechanisms that control the formation and evolution of the nanostructure.

Gold was chosen as a nanocrystalline model material (no oxidation), and we used it for the experimental study of the evolution of the nanostructure *during growth* and after subsequent *annealing*. Specifically, by *in-situ* synchrotron x-ray diffraction and reflection measurements, the development of the preferred orientation of the grains, the lattice constant (stress), the grain size, and the microstrain (reflecting lattice defects) were studied during and after growth. The parts of the studies which include the development of the peak area of the Au(111) diffraction peak, the grain size, the microstrain and the lattice constant have been submitted for publication [11], while a manuscript dealing with the studies of the development of the texture is in preparation.

2. Experimental

The deposition chamber [12] is mounted on the six-circle goniometer at the ROBL beamline. It is equipped with Kapton windows for letting x-rays in and out of the chamber. Two magnetrons are placed at a distance of 100 mm from the substrate and tilted 30° away from the substrate normal.

For the *in-situ* experimental studies, two different x-ray diffraction geometries were used: (1) Bragg-Brentano large-angle scattering. Such measurements give information on texture (the preferred orientation of the various grains). In addition, the exact positions of the Bragg peaks yield the out-of-plane lattice strain, and from the widths and shapes of the peaks, out-of-plane grain sizes and microstrain (lattice defects) are obtained. (2) Grazing incidence and grazing exit in-plane large angle scattering (GIXS). In contrast to the Bragg-Brentano geometry, where crystallographic planes parallel to the film surface are probed, GIXS identifies planes perpendicular to the surface.

3. Experimental results and discussion

In Fig. 1 a typical Bragg-Brentano x-ray diffractogram is shown for a 750 Å Au film deposited at room temperature with a (substrate) bias voltage of -30 V and annealed at 95°C . In all the recorded Bragg-Brentano diffractograms, including Fig. 1, only the Au(111) diffraction peak was observed, arising from grains with a (111) plane parallel to the film surface. Grains with a (111) plane oriented so it forms a small or zero angle to the film surface are denoted (111) grains. A pseudo Voigt profile, a sum of a Gaussian and a Lorentzian peak, was fitted to the diffraction profile, see Fig. 1. From the widths of this Gaussian and Lorentzian peaks, the microstrain and the grain size were calculated [13].

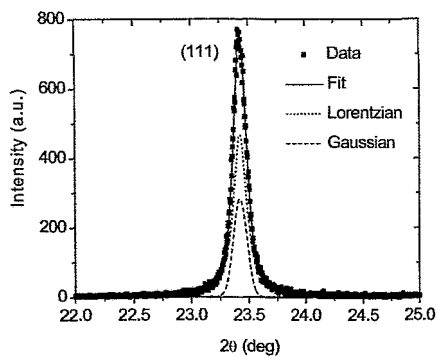


Fig. 1: Bragg-Brentano x-ray diffractogram from a 750 Å Au film deposited at room temperature with a bias voltage of -30 V.

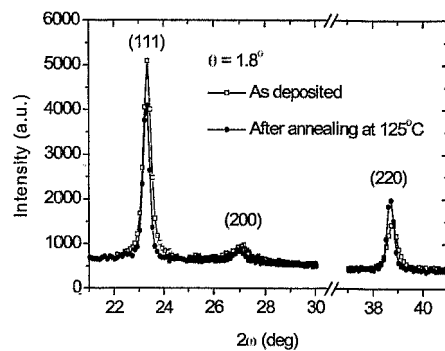


Fig. 2: GIXS diffractograms from a 750 Å Au film deposited at room temperature with -30 V bias. Open squares: as deposited; filled circles: after annealing at 125°C .

With GIXS diffraction geometry, grains with (111), (200) or (220) planes perpendicular to the film surface were observed (Fig. 2). The grains, which gave rise to the GIXS (220) diffraction signal, were the (111) grains detected with Bragg-Brentano diffraction geometry, while the grains yielding (111) and (220) GIXS signals could not be observed with Bragg-Brentano geometry.

Using Bragg-Brentano geometry, we measured the Au(111) peak *during the growth* of an Au film, which was deposited at room temperature with a bias voltage of -30 V. The film thickness increased linearly with deposition time, and a deposition time of 10 min. corresponded to a film thickness of 750 Å. The results are displayed in Fig. 3.

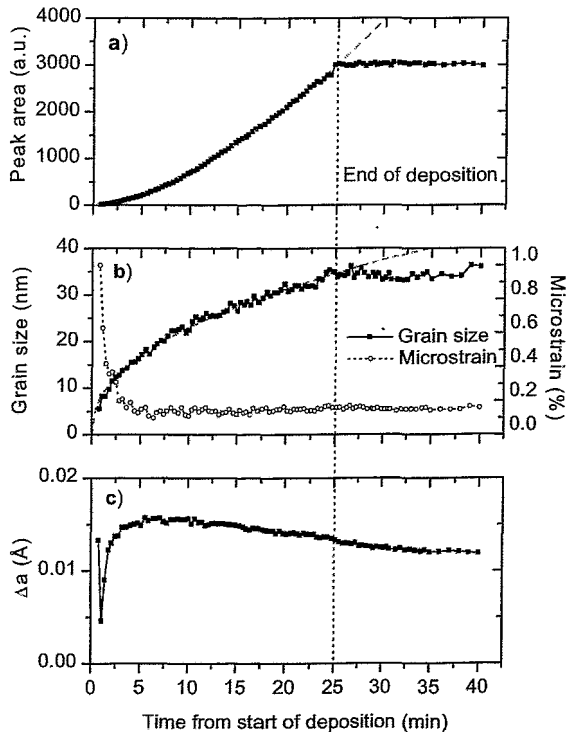


Fig. 3: The Bragg-Brentano Au(111) peak was measured as a function of thickness *during* growth of an Au film deposited at room temperature with a bias voltage of -30 V. (a) The peak area *versus* deposition time; (b) the microstrain and the grain size, respectively, *versus* deposition time; (c) the deviation of the lattice constant from the tabulated Au lattice constant [14] *versus* deposition time.

In Fig. 3a, the Au(111) peak area is shown as a function of deposition time. From the figure it is seen that, initially, the area increased more than linearly with deposition time (film thickness), and the peak area kept constant after stop of the growth. This more than linear increase in peak area with film thickness may be explained by a change of texture with time of growth (see later) and by an increase during growth in (111) grains relative to grains, which were observed as a GIXS Au(111) signal.

In Fig. 3b, the average grain size and the microstrain, respectively, are shown as a function of the deposition time. The grain size increased with film thickness, with the rate of increase levelling off at larger film thicknesses. No grain growth was observed when the growth stopped. In the first few minutes of growth, the grain size equalled the film thickness. The microstrain decreased drastically during the first few minutes of growth while, concurrently, the grain size more than doubled. During subsequent growth the microstrain became constant. As seen in Fig. 3b, normal thermal grain growth was absent when the deposition stopped. Therefore, the increase in the average grain size with the time of growth was connected to the dynamic growth process and was not of purely thermal origin. The initial large microstrain was connected to the initial small grain size, since the *intrinsic* microstrain is approximately proportional to the reciprocal of the grain diameter [13].

Fig. 3c displays the lattice constant shown as the deviation from the tabulated Au lattice constant, 4.078 Å [14]. Assuming the normal Poisson effect, i.e. an increase in the in-plane lattice constant results in a decrease in the out-of-plane lattice constant and *vice versa*, a decrease (increase) in the out-of-plane lattice constant corresponds to the stress changing in the tensile (compressive) direction. Fig. 3c shows that in the first minute of

growth, the film stress decreased sharply due to a tensile contribution. This was due to island coalescence. During subsequent growth, the compressive stress increased, reached a maximum, after which it decreased again. This decrease continued after the growth was stopped.

After growth, 750 Å thin Au films deposited at room temperature with a bias voltage of -30 V were annealed for one hour at various temperatures. During this annealing, the Au(111) Bragg-Brentano peak was monitored. Concurrently with the decrease of the microstrain and relaxation of the stress, grain growth was observed. From an Arrhenius plot, an activation energy for grain growth, $Q = 0.25 \pm 0.02$ eV, was obtained. This value is surprisingly small, and we cannot explain this. Typically, most grain boundary migration processes have activation energies close to the ones of grain boundary self-diffusion, and the activation energy for grain boundary self-diffusion in Au is 0.88 eV [15]. We speculate that the grain boundaries, just after deposition and before relaxation has taken place, may be very special with more open structure than the ones after relaxation, resulting in small activation energies. In contrast to most grain-growth studies, the present studies' lack of impurities in the grain boundaries may also result in a smaller activation energy than normally found.

To get the *orientation distribution* of the (111) grains (with (111) planes forming a small angle to the film surface), χ scans were carried out. With θ and 2θ fixed corresponding to standard Bragg-Brentano diffraction geometry, the Au(111) diffraction intensity was measured as a function of the sample tilt χ , the tilt axis lying both in the film surface and in the scattering plane. As a quantitative measure of the orientation distribution (the texture), we used the widths (FWHM) of the χ scans.

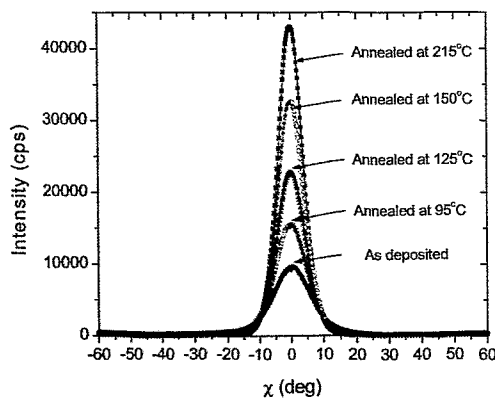


Fig. 4: Au(111) χ scans from 750 Å Au films deposited at room temperature with a bias voltage of -30 V. The five scans correspond to measurements of a film as deposited and four films annealed for one hour at various temperatures.

Fig. 4 shows the results of such χ scans, carried out with 750 Å films deposited at room temperature with -30 V bias voltage, one film as deposited and four films annealed for one hour at 95°C , 125°C , 150°C , and 215°C , respectively. The orientation distributions narrowed with increasing annealing temperature, i.e. the angles between the (111) planes and the film surface became smaller. This is probably the result of small rotations of the individual (111) grains, but recrystallization may also play a role.

The development of the orientation distribution of the (111) grains during growth at room temperature with -30 V bias voltage is displayed in Fig. 5. The FWHM of χ scans is shown as a function of the deposition time (filled squares). Also shown is the FWHM versus deposition time, where the growth was interrupted at regular intervals to allow for texture changes of only thermal origin (open triangles).

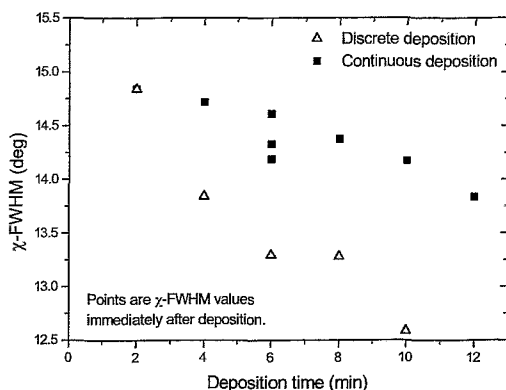


Fig. 5: The development of the FWHM of χ scans during growth (filled squares), and as a function of film thickness (i.e. deposition time), where the growth was interrupted at regular intervals to allow for texture changes of only thermal origin (open triangles).

From Fig. 5 it is seen that both during growth and during the interruption of the growth for an hours time, the orientation distributions narrowed significantly. The times of growth were short compared to the periods of time required, when the growth was interrupted, for observing texture changes. Therefore, the mechanisms for texture changes during growth were different from the mechanisms of purely thermal origin, which were in play when the growth was interrupted.

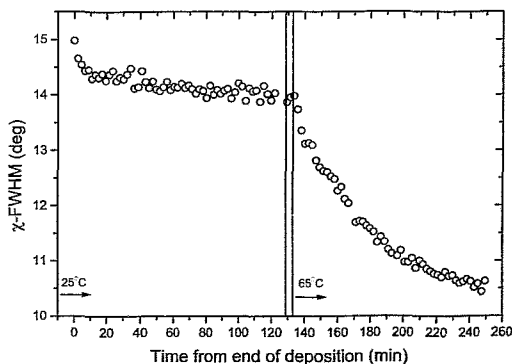


Fig. 6: The FWHM of χ scans versus time after growth, for details see text.

Fig. 6 illustrates the narrowing of the orientation distribution of the (111) grains with time after deposition at room temperature with -30 V bias of an Au film. The FWHM is shown as a function of time. The first two hours after growth, the film was kept at room temperature, after which the temperature was raised to 65°C . A higher temperature clearly increased the rate of change of the width. Similar data was obtained with the 65°C replaced with various other temperatures. From an Arrhenius plot $-\log(\text{Initial rate of change of the FWHM})$ versus the reciprocal of the temperature – an activation energy was obtained for the change in texture, $Q = 0.68 \pm 0.08$ eV.

4. Summary

During growth and subsequent annealing, the evolution of the nanostructure of magnetron sputtered Au films has been experimentally studied. With Bragg-Brentano and GIXS diffraction geometries, grains with (111) planes parallel with the film surface and grains with (111) or (200) planes perpendicular to film surface have been identified. The microstrain decreased strongly during the initial growth and at the beginning of the annealing period, while continued grain growth was observed both during film deposition and during annealing. A surprisingly small activation energy of grain growth of 0.25 ± 0.02 eV was found. During the first few minutes of growth, the compressive film stress was strongly reduced due to a tensile contribution arising from the coalescence of the initially formed islands. During annealing, stress relaxation was also observed. The orientation distribution of grains with a (111) plane forming a small angle with the film surface narrowed both during the short times of growth and during subsequent annealing. The activation energy for texture changes was found to be 0.68 ± 0.08 eV.

Acknowledgements

The authors wish to thank U. Strauch for his technical support and assistance during the measurements in Grenoble.

References

- [1] A.S. Edelstein, R.C. Cammarata (eds), *Nanomaterials: Synthesis, Properties and Applications*, Institute of Physics Publishing, Bristol, 1998
- [2] C. Suryanarayana, *Inter. Mater. Rev.* **40** (1995) 41
- [3] G. Liang, J. Huot, S. Boily, A. van Neste, R. Schulz, *J. Alloys Comp.* **291** (1999) 295
- [4] A. Niederhofer, P. Nesládek, H.-D. Männling, K. Moto, S. Veprek, M. Jílek, *Surf. Coat. Technol.* **120-121** (1999) 173
- [5] P. Zeman, R. Cerstvy, P.H. Mayrhofer, C. Mitterer, J. Musil, *Mat. Sci. Eng.* **A289** (2000) 189
- [6] J. Musil, *Surf. Coat. Technol.* **125** (2000) 322
- [7] P.H. Mayrhofer, C. Mitterer, *Surf. Coat. Technol.* **133-134** (2000) 131
- [8] S. Veprek, A. Niederhofer, K. Moto, T. Bolom, H.-D. Männling, P. Nesládek, G. Dollinger, A. Bergmaier, *Surf. Coat. Technol.* **133-134** (2000) 152
- [9] A.A. Voevodin, J.S. Zabinski, *Thin Solid Films* **370** (2000) 223
- [10] J. Musil, P. Karvánková, J. Kasl, *Surf. Coat. Technol.* **139** (2001) 101
- [11] N. Schell, T. Jensen, J.H. Petersen, K.P. Andreasen, J. Bøttiger, J. Chevallier, *submitted to Thin Solid Films*
- [12] W. Matz, N. Schell, W. Neumann, J. Bøttiger, J. Chevallier, *Rev. Sci. Instrum.* **72** (2001) 3344
- [13] Th.de Keijsers, J.I. Langford, E.J. Mittemeijer, A.B.P. Vogels, *J. Appl. Cryst.* **15** (1982) 308
- [14] PDF-2 Database, Datasets 1-48, release 1998, ICDD, Newton Square, PA, pp. 38-1420
- [15] D. Gupta, *J. Appl. Phys.* **44** (1973) 4455

An *in-situ* grazing incidence x-ray diffraction study of the crystallisation of Ni-Ti thin films

F.M. Braz Fernandes, R.M.S. Martins, R.J.C. Silva, A. Marques, R. Martins
CENIMAT – Centro de Investigação de Materiais
Campus da FCT/UNL, 2829-516 Monte de Caparica, Portugal

N. Schell^{1,2}

¹Project-Group ESRF-Beamline, ²Institute of Ion Beam Physics and Materials Research
Forschungszentrum Rossendorf, P.O. Box 51 01 19, 01314 Dresden, Germany

1. Introduction

The shape memory effect (SMA) relies on martensitic transformations which are macroscopically due to a pseudo-shearing deformation, resulting from a deformation mode similar to slip or twinning in ordinary metals and alloys under stress. However, since martensitic thermoelastic transformations are reversible, the deformation behaviour of alloys that undergo this type of transformations is remarkably different from that of ordinary metals and alloys in which the deformation, by slip or by twinning, is not recoverable [1]. The martensitic transformation starts (in cooling) at a certain temperature M_s , and is completed when a lower temperature M_f is reached. When this martensite is deformed (below M_f) it undergoes a strain, which, within certain values, is completely recoverable upon heating. The shape recovery begins at a temperature A_s (where the martensite \rightarrow austenite transformation starts), and is completed at a higher temperature A_f (where the transformation martensite \rightarrow austenite is finished). The M_s , M_f , A_s and A_f temperatures are characteristic of the alloy system, and recoverable strains typically range from 2% to 10%. The martensite in shape memory alloys (SMA's) may also be isothermally induced above the M_s temperature by the application of a stress [2]. The NiTi system is the most popular of the SMA's because of the considerable work per unit mass it can produce during recovery (work output ~ 1 Joule/g), because of the value of the transformation temperature (near room temperature, i.e. from -100°C to $+100^\circ\text{C}$) and because of its good oxidation resistance.

The thin films of SMA's can be electrically driven using joule heating, and they demonstrate fast cooling rates because of their large surface-to-volume ratio. The control of film composition and properties has proven difficult in sputter-deposited films, and further study of deposition techniques is needed [3].

It is known that NiTi alloys need to be composed of around 50 at% Ni - 50 at% Ti to have shape memory, with any slight change in alloy composition causing a significant deterioration in this property. Although a number of techniques have been tried for depositing NiTi SMA thin films, from the practical point of view, only the sputter deposition has succeeded so far. Historically, the first attempt at the formation of NiTi SMA thin films was vacuum evaporation. However, this method has failed to form NiTi alloy thin films with good shape memory properties. This is because conventional vacuum evaporation of NiTi binary alloy entails the potential problem of the evaporation rates of each component not being the same due to differences in vapour pressure. A flash evaporation method has been proposed to solve this problem providing an alternative to sputtering deposition [4], and the thermo-mechanical properties have been studied [5–8] in order to optimise their application as microactuators [8–10] and microsensors [11].

At CENIMAT, work has been performed on the optimisation of the flash evaporation and sputter deposition techniques, aiming to obtain improved thin films with higher performances [12].

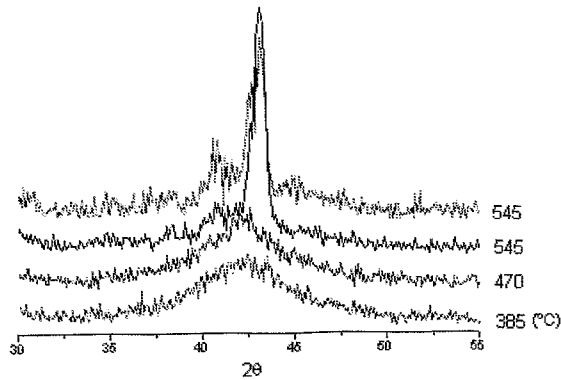


Fig. 1: High temperature *in-situ* XRD of a sputtered Ni-Ti film.

The as deposited films are amorphous; a crystallisation process is necessary in order to induce the shape memory effect, see Fig. 1. A deeper understanding of this crystallisation is needed in order to obtain materials presenting different transformation temperature ranges, for different applications. It is also aimed at obtaining the lowest crystallisation temperature, because this will allow the use of flexible (polymeric) substrates. Thus, before starting to test the feasibility of microsystems construction based on these thin films, it is intended to optimise the crystallisation conditions by studying at a finer dimensional scale the structural changes that are induced and their correlation with the localized chemical composition changes associated with the precipitation of different intermetallic phases of the Ni-Ti system, e.g. Ni_3Ti and NiTi_2 (Fig. 2). The strong dependency of the temperature T_0 for the austenite–martensite thermodynamic equilibrium (and, as a consequence, M_s/M_f and A_s/A_f) on composition (Fig. 3), gives a high sensitivity of SMA properties to a variation in composition, especially in Ni rich alloys.

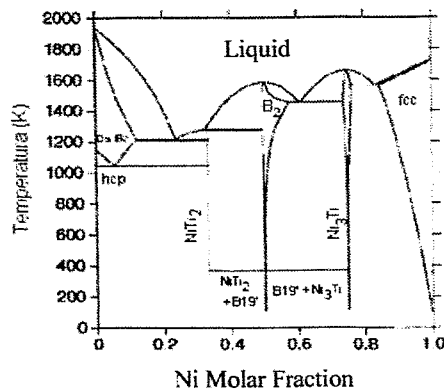


Fig. 2: Ni-Ti phase diagram [13].

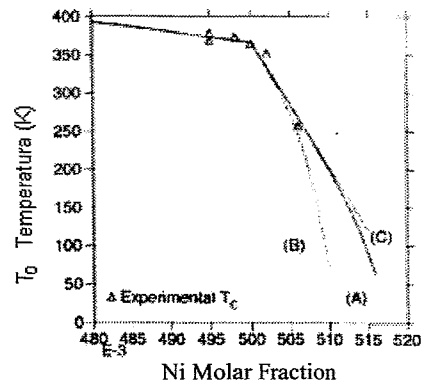


Fig. 3: T_0 versus Ni content (T_0 can be expressed as $(M_s+A_s)/2$) [13].

In this article we present the results of the optimisation of the sputter deposition technique, as well as the heat treating procedure leading to the crystallisation of the thin

films. The crystallisation sequence was studied by using grazing incidence x-ray diffraction (GIXRD) at the materials research station of ROBL at ESRF [14].

2. Experimental method

2.1 Thin films production

The NiTi thin films were deposited on Si(100) wafers using sputtering rf technique with the parameters given in Table 1. The chemical composition of the target material was 44 wt% Ni – 56 wt% Ti, i.e. 49 at% Ni – 51 at%Ti.

Table 1: Parameters used for sputtering deposition.

	S 8	S 11	S 12
Distance target-substrate (mm)	70	90	186
Initial pressure (mbar)	4.4×10^{-6}	8.5×10^{-6}	4.8×10^{-5}
Argon pressure ($\times 10^{-3}$ mbar)	1.1	1.1	1.1
Deposition pressure ($\times 10^{-2}$ mbar)	1.0	1.0	1.0
Argon flow rate (sccm)	10	14	14
R.f. power (W)	150	200	200
Thickness (μm)	1	1	0.3

2.2 GIXRD *in-situ* annealing

Samples of $10 \times 10 \text{ mm}^2$ were cut to be analysed. The annealing of the films took place under vacuum (pressures ranging from 5.7×10^{-6} mbar to 1.4×10^{-5} mbar). A half-spherical Be-dome furnace was used to study the kinetics of the crystallisation of the thin films using GIXRD under grazing incidence of 1° and with a wavelength of 1.54 Å. The six-circle goniometer itself allows equally well full horizontal as well as vertical scattering geometries. A closed Eulerian cradle (χ circle with beam direction as rotation axis) is fitted to the θ circle (incidence angle on sample), and with an identical rotation axis the 2θ circle (vertical scattering angle) is independently mounted. A fourth ϕ rotation allows an azimuthal sample orientation (surface normal as rotation axis). All four circles described rest on two other horizontal circles, ω and 2ω , with the same vertical rotation axis. The inner circles ϕ and χ are used for the orientation of the furnace, i.e. the sample orientation (as the sample is fixed inside the furnace). The two scattering planes are realized with the $\theta/2\theta$ circles for the vertical as well as the $\omega/2\omega$ circles for the horizontal plane. The half-spherical Be-dome furnace was installed on the ϕ circle inside the Eulerian cradle, thus allowing full 2π access in the horizontal, as well as in the vertical planes. These two geometries are accessible without change of the experimental configuration.

Samples of 0.3–1 μm thick NiTi thin films deposited on Si(100) wafers with different sputtering conditions were studied. The temperature range covered for the crystallisation studies was from room temperature (RT) to 525°C.

3. Results

The samples S8 (Fig. 4) and S11 (Fig. 5) – distance target-substrate during sputtering 70 and 90 mm, respectively – showed, *after annealing*, the presence of the austenite phase (B2) of the Ni-Ti system and the intermetallic Ni_3Ti , as well as the presence of silicides. The sample S12 (Fig. 6) – distance target-substrate 186 mm – only shows the presence of the Ni-rich solid solution of Ti and TiO_2 . Both S8 and S11 are not crystallised at 325°C, but they show a significant degree of crystallisation at 365°C. Increasing the temperature up to 445°C or 525°C, improves the degree of crystallisation.

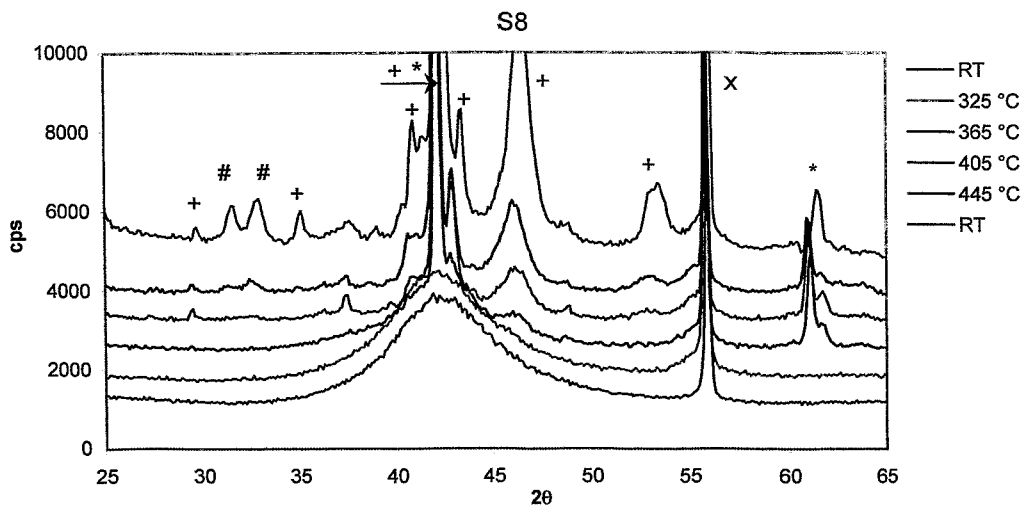


Fig. 4: GIXRD spectra of sample S8 at room temperature and different annealing temperatures (* B2, + Ni_3Ti , # Ni_2Si , x Si).

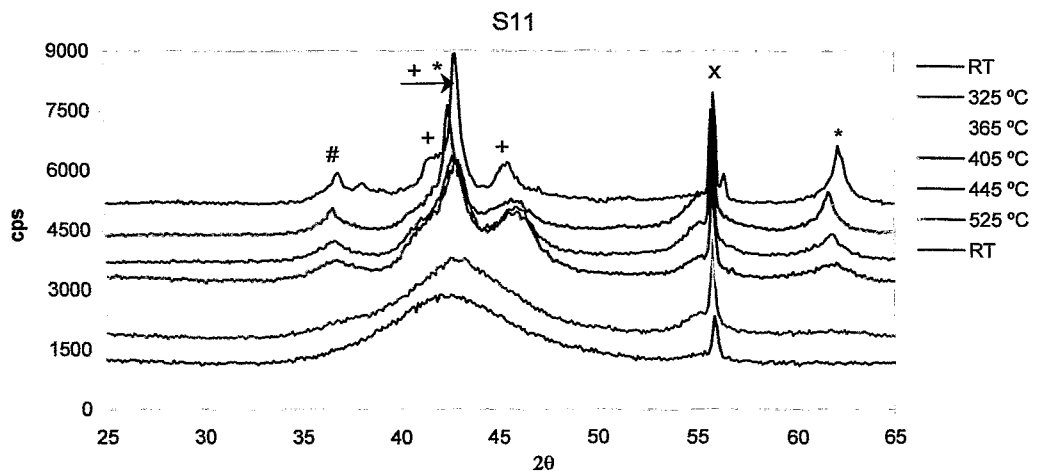


Fig. 5: GIXRD spectra of sample S11 at room temperature and different annealing temperatures (* B2, + Ni_3Ti , # Ti_5Si_3 , x Si).

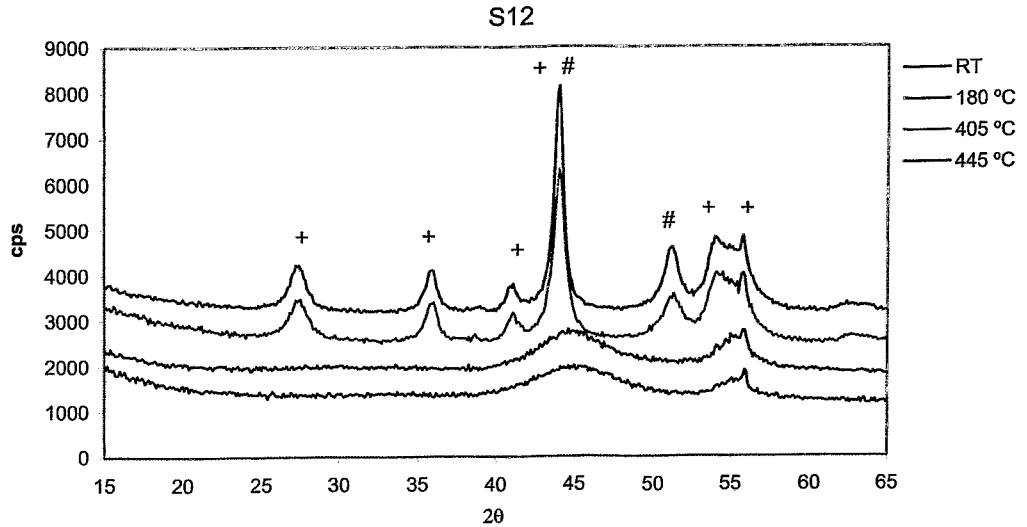


Fig. 6: GIXRD spectra of sample S12 at room temperature and different annealing temperatures (+ TiO₂, # Ni).

A stress state determination by GIXRD was performed on sample S8 at room temperature, after annealing at 445°C. The results in Fig. 7 show that the *residual stress state is very low*.

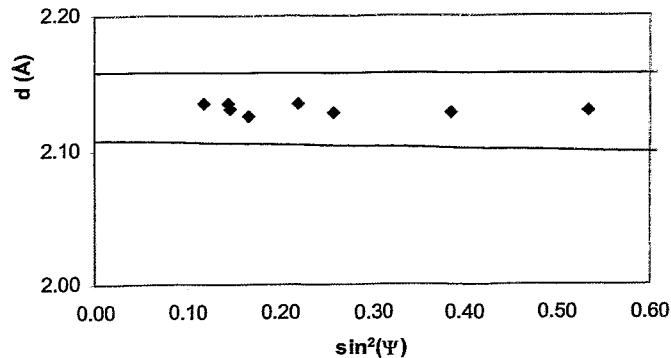


Fig. 7: GIXRD stress state determination on sample S8 at room temperature, after annealing at 445°C (the two lines show the limits of the 95% confidence interval).

4. Discussion

The experiments performed at ROBL allowed us to obtain a very clear definition of the peaks associated with the intermetallics, i.e. Ni₃Ti, that are present in minor quantities in our samples. The experimental results show that:

- The greater distance target-substrate (186 mm) used for sample S12 led to a significant Ti depletion on the sputtered thin film. During annealing, a further depletion of Ti by oxide formation led to the appearance of the Ni solid solution (Ti solute). This type of result is consistent with oxidation studies previously reported [15].

- The films S8 and S11 with the smaller target-substrate distances showed the formation of the B2 phase, the crystallisation temperature being comprised between 325°C and 365°C. The presence of Ni₃Ti intermetallic shows that the sputtered thin film is slightly enriched in Ni.
- The residual stress state of the S8 film after annealing appears to be very low.

Acknowledgements

The authors would like to express their thanks to the "Fundação para a Ciência e Tecnologia" for the pluriannual financial support of CENIMAT and the European Commission for the financial support of the experiments at ROBL under the contract HPRI-CT-1999-00077 within the Human Potential Programme – Access to Research Infrastructures.

References

- [1] K. Shimizu, T. Tadaki, *Shape Memory Effect*, Chapter 1 in "Shape Memory Alloys", **Vol. I** of "Precision Machinery and Robotics", Edited by H. Funakubo, Gordon & Breach Science Publishers, Glasgow, 1984
- [2] C.M. Wayman, *Shape Memory and Related Phenomena*, *Progress in Materials Science* **36** (1992) 203-224
- [3] Committee on Advanced Materials and Fabrication Methods for Microelectromechanical Systems, *Microelectromechanical systems, advanced materials and fabrication methods*, National Materials Advisory Board, National Academy Press, Washington, D.C. 1997
- [4] E. Makino, M. Uenoyama, T. Shibata, *Flash evaporation of TiNi shape memory thin film for microactuators*, *Sensors and Actuators* **71A** (1998) 187-192
- [5] A. Ishida, K. Ogawa, M. Sato, S. Miyazaki, *Microstructure of Ti-48.2 at. pct Ni shape memory thin films*, *Metall. Mater. Trans.* **28A** (1997) 1985-1991
- [6] E. Makino, K. Kato, T. Shibata, *Thermo-mechanical properties of TiNi shape memory thin film formed by flash evaporation*, *Sensors and Actuators* **75A** (1999) 156-161
- [7] E. Makino, T. Shibata, K. Kato, *Dynamic thermo-mechanical properties of evaporated TiNi shape memory thin film*, *Sensors and Actuators* **78A** (1999) 163-167
- [8] J.-L. Seguin, M. Bendahan, A. Isalgue, V. Esteve-Cano, H. Carchano, V. Torra, *Low temperature crystallised Ti-rich NiTi shape memory alloy films for microactuators*, *Sensors and Actuators* **74A** (1999) 65-69
- [9] C.M. Pemble, B.C. Towe, *A miniature shape memory alloy pinch valve*, *Sensors and Actuators* **77A** (1999) 145-148
- [10] M. Kohl, K.D. Skrobaneck, S. Miyazaki, *Development of stress-optimised shape memory microvalves*, *Sensors and Actuators* **72A** (1999) 243-250
- [11] M. Bendahan, K. Aguir, J.-L. Seguin, H. Carchano, *NiTi thin films as a gate of M.O.S. capacity sensors*, *Sensors and Actuators* **74A** (1998) 242-245
- [12] F.M. Braz Fernandes, R. Martins, M.^a T. Nogueira, R.J.C. Silva, P. Nunes, D. Costa, I. Ferreira, R. Martins, *Structural characterisation of NiTi thin film shape memory alloys*, *Sensors and Actuators* **99/1-2** (2002) 53-56
- [13] W. Tang, B. Sundman, R. Sandström, C. Qiu, *New modelling of the B2 phase and its associated martensitic transformation in the Ti-Ni system*, *Acta mater.* **47** (1999) 3457-3468
- [14] N. Schell, W. Matz, F. Prokert, F. Eichhorn, F. Berberich, *Synchrotron radiation studies of thin films and implanted layers with the materials research endstation of ROBL*, *Journal of Alloys and Compounds* **328** (2001) 105-111
- [15] S.K. Wu, C.L. Chu, Y.C. Yen, *Oxidation behavior of equiatomic TiNi alloy in high temperature air environment*, *Materials Science and Engineering A* **216** (1996) 193-200

Determination of the chemical composition profile and the relaxation process for thin semiconducting heterostructures

J. Gaca, A. Gładki, A. Jasik, K. Mazur, J. Sass, W. Strupinski, A. Turos, M. Wojcik
Institute of Electronic Materials Technology
01 919 Warsaw Wolczynska 133, Poland

A. Bauer¹, F. Eichhorn², F. Prokert², N. Schell^{1,2}
¹ Project-Group ESRF-Beamline, ² Institute of Ion Beam Physics and Materials Research
Forschungszentrum Rossendorf, P.O. Box 51 01 19, 01314 Dresden, Germany

1. Introduction

Low-dimensional heterostructures of semiconducting compounds have become the core of modern electronic devices. Constant optimization of the growth technology stimulates the creation process of new device ideas in micro- and optoelectronics. The high technical level of the equipment and the very high purity of starting materials nowadays enabled metal-organic chemical vapor deposition (MOCVD) to be commonly applied in the realization of extremely sophisticated configurations of heterostructures, including nanometric multi quantum wells (MQW).

The know-how of the smooth, abrupt interfaces, apart from the ideal structure and the low background impurities level, is the basic feature of modern epitaxial growth technology. The character of the interface plays the main role in the functioning and reliability of device parameters [1], and what is more, it delivers an important information about the growth process [2]. All individual layers should grow pseudomorphically (strained) with a smooth surface for a good continuous growth of succeeding layers. However, the material may grow partially relaxed with misfit dislocations and a wavy surface if the thickness of an individual layer exceeds a critical value (*critical thickness*). This is especially important for the MOCVD method which opens up the possibility of various compounds deposition – binary, ternary and quaternary (In, Ga, Al, As).

Epitaxial growth is more complicated when it is aimed at getting the ideal interfaces between succeeding layers. The growth rate should be optimized to protect 2D nucleation on the one hand and to avoid interdiffusion effects on the other hand. Growth interruption plays also an important role, especially when InGaAs/GaAs heterostructures are demanded. The presence of indium gives rise to a large lattice mismatch between InGaAs and GaAs and makes the epitaxial process difficult. The influence of all these conditions on the resulting crystalline structure is much easier to be observed in the case of thin strained heterostructures because they allow to follow up all instabilities related to the early stages of deposition which otherwise would be very difficult to detect.

2. Experimental and results

The purpose of a series of experiments done at the materials research station of ROBL was on the one hand to determine the chemical composition profiles of layers of InGaAs/GaAs heterostructures, and on the other hand to investigate the relaxation processes, especially of the first few growth layers. The samples were grown by low pressure metal-organic vapor phase epitaxy (LP MOVPE) in the Institute of Electronic Materials Technology (ITME), Warsaw.

2.1 Chemical composition profiles of InGaAs/GaAs MQW heterostructures

High resolution x-ray diffraction (HRXRD) is a very convenient method for determining the chemical composition as well as scattering factor and interplanar spacing profiles in the growth direction. Structural details of the heterostructure – such as thickness and composition of succeeding layers and the shape of interface regions – can be inferred from diffraction patterns. The method applied for the identification of the chemical composition profile in the case of heterostructures is based on computer simulations employing Darwin dynamical diffraction theory [3]. Algorithms based on this theory [4] allow to regard the crystal investigated as a series of succeeding (004) atomic planes. The chemical composition of any plane is an independent parameter for simulation. Given the chemical composition of each atomic plane, the interplanar spacing and scattering power profiles in the [001] growth direction for the whole crystalline structure are calculated by means of Vegard's law (and in this way, they are not independent parameters for the calculation).

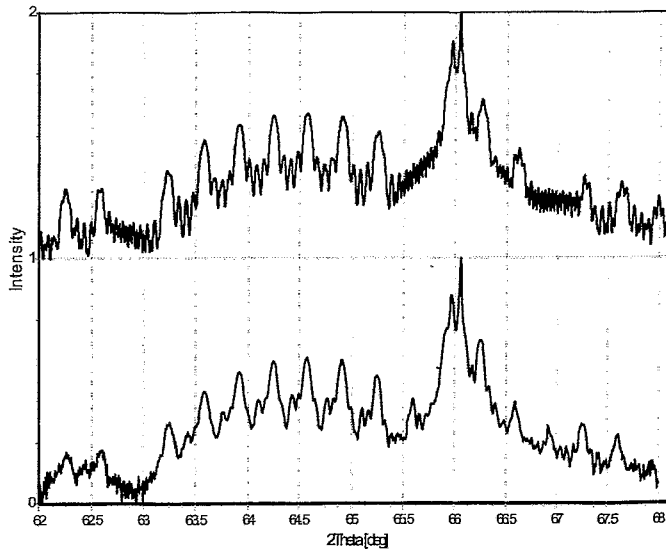
As a crucial feedback for technical deposition parameters, the chemical composition profile of InGaAs/GaAs MQW grown on laterally homogeneous (001) GaAs substrate has been investigated as a function of the growth rate and the interruption time. Since the thickness of the investigated MQW is very small, x-ray synchrotron radiation with the wavelength $\lambda = 1.54 \text{ \AA}$ was used at ROBL.

Four samples of the same heterostructure have been measured for which the growth rate ranged from 2.0 to 3.0 monolayers per second [ml/s] with and without interruption time. The assumed chemical composition of this heterostructure, presented in Table 1 below, will be referred to later on as the reference one.

Table 1: Assumed chemical layer composition.

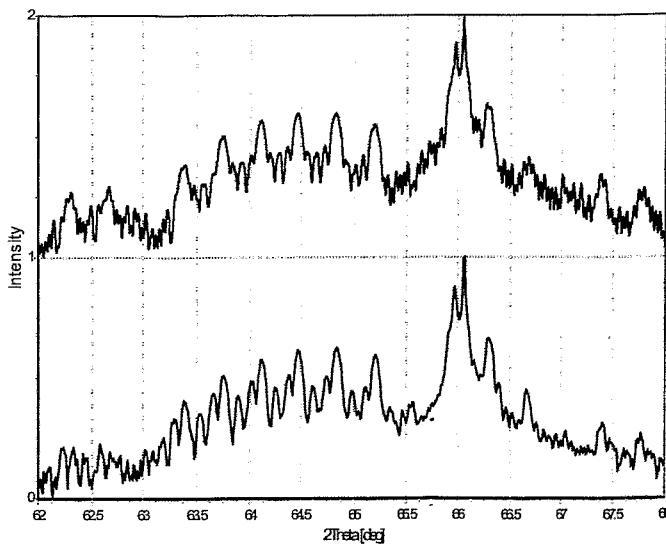
Layer	Composition	Thickness [nm]
1	GaAs	140.0
2	Ga _{0.6} Al _{0.4} As	15.0
3	GaAs	15.0
4	In_{0.2}Ga_{0.8}As	8.0
5	GaAs	20.0
6	In _{0.2} Ga _{0.8} As	8.0
7	GaAs	15.0
8	Ga _{0.6} Al _{0.4} As	670
9	GaAs	substrate

Data for the experimental diffraction profiles have been collected as $\theta/2\theta$ symmetrical scans performed in the vicinity of the substrate GaAs(004) reflection. For each measured diffraction profile the best calculated fit has been found. The experimental and simulated diffraction profiles for the heterostructures investigated are presented in Figs 1 and 2, with the tables on the right side of each figure containing the chemical composition profile derived from the simulation. The heterostructures investigated consist of two GaAlAs barriers, and located between them InGaAs/GaAs MQW. From our detailed analysis results we are not able to find any differences between the composition and thickness of barriers in succeeding samples, but the diffraction profile is very sensitive to any change of the chemical composition profile of MQW. The results of the analysis of the QW composition and thickness are presented in Table 2 below.



Growth rate: **2.0 ml/s**
 Interruption time: **0 s**

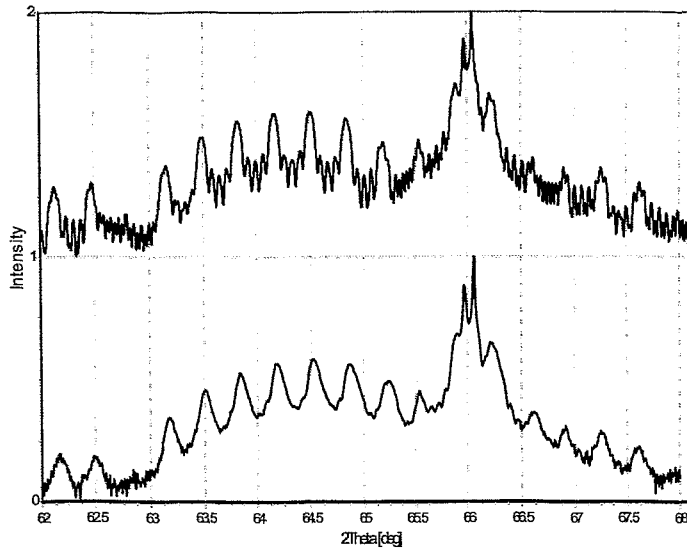
No	Composition	Thickness [nm]
1	GaAs	140.0
2	Ga _{0.75} Al _{0.25} As	15.0
3	GaAs	15.0
4	In_{0.18}Ga_{0.82}As	6.79
5	In_{0.17}Ga_{0.83}As	0.85
6	GaAs	23.22
7	In _{0.18} Ga _{0.82} As	8.21
8	In _{0.17} Ga _{0.83} As	0.85
9	GaAs	15.86
10	Ga _{0.6} Al _{0.4} As	657.0
	GaAs	Semi-infinite



Growth rate: **2.5 ml/s**
 Interruption time: **0 s**

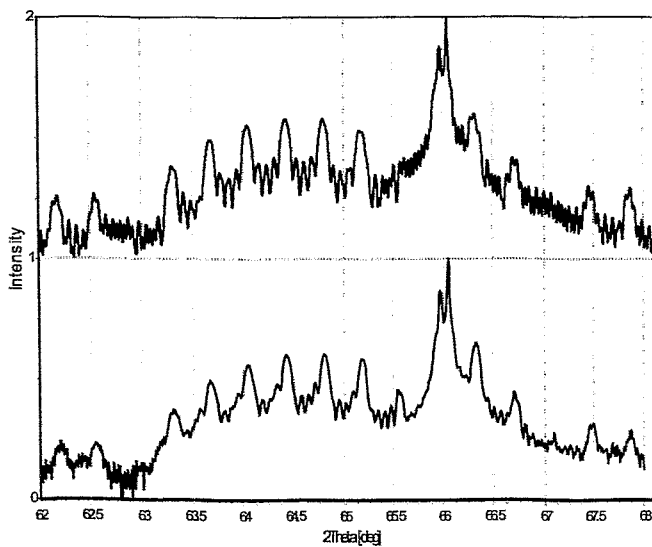
No	Composition	Thickness [nm]
1	GaAs	140.0
2	Ga _{0.75} Al _{0.25} As	15.0
3	GaAs	25.0
4	In_{0.174}Ga_{0.826}As	7.08
5	In_{0.16}Ga_{0.84}As	0.85
6	GaAs	20.67
7	In _{0.174} Ga _{0.826} As	8.49
8	In _{0.16} Ga _{0.84} As	0.85
9	GaAs	15.57
10	Ga _{0.6} Al _{0.4} As	657.0
	GaAs	Semi-infinite

Fig. 1: HRXRD diffraction profiles for heterostructures with the chemical composition each given in the table on the right (bottom – experimental, top – simulated). The samples were grown both without interruption, in the upper part with a growth rate of 2.0 ml/s, in the lower part with a growth rate of 2.5 ml/s.



Growth rate: **2.5 ml/s**
Interruption time: **7 s**

No	Composition	Thickness [nm]
1	GaAs	140.0
2	Ga _{0.75} Al _{0.25} As	15.0
3	GaAs	15.0
4	In_{0.193}Ga_{0.807}As	7.08
5	In_{0.16}Ga_{0.84}As	0.85
6	GaAs	22.34
7	In _{0.193} Ga _{0.807} As	8.50
8	In _{0.16} Ga _{0.84} As	0.85
9	GaAs	15.57
10	Ga _{0.6} Al _{0.4} As	657.0
	GaAs	Semi-infinite



Growth rate: **3.0 ml/s**
Interruption time: **0 s**

No	Composition	Thickness [nm]
1	GaAs	140.0
2	Ga _{0.75} Al _{0.25} As	15.0
3	GaAs	15.0
4	In_{0.18}Ga_{0.82}As	6.51
5	In_{0.16}Ga_{0.84}As	0.85
6	GaAs	20.10
7	In _{0.18} Ga _{0.82} As	8.5
8	In _{0.16} Ga _{0.84} As	0.85
9	GaAs	15.57
10	Ga _{0.6} Al _{0.4} As	657.0
	GaAs	Semi-infinite

Fig. 2: HRXRD diffraction profiles for heterostructures with the chemical composition each given in the table on the right (bottom – experimental, top – simulated). The samples were grown with a growth rate of 2.5 ml/s and 7 s interruption (upper part) and with a growth rate of 3.0 ml/s and 0 s interruption, i.e. no interruption (lower part).

Table 2: Deviations of the simulated data from the *reference* in QW composition and thickness.

Growth rate [ml/s]	Interruption time [s]	Relative deviation from <i>reference</i> Indium composition in QW	Relative deviation from <i>reference</i> QW thickness
2.0	0	-10%	+10%
2.5	0	-13%	+2%
3.0	0	-10%	+8%
2.5	7	-3.5%	-2%

The comparison between chemical composition and thickness of the QW in the different samples shows that the least deviation between *reference* and actual chemical composition has been observed for the sample grown with non-zero interruption time. On the other hand, the least deviation between *reference* and actual QW thickness has been observed for samples grown with the growth rate 2.5 ml/s. At the same time we were able to observe some instabilities related to the early stages of epitaxial deposition. They resulted in the loss of MQW periodicity, which amounted in the extreme case of the sample with the growth rate 2.5 ml/s and zero interruption time to ± 4 atomic planes per QW period. Another problem closely related to the deposition instability is the problem of the shape of the interfaces between succeeding layers. At this stage of our investigations we are not yet able to determine if the deviation from the assumed QW composition is uniformly distributed throughout the whole volume of the layer or clusters round the interface region. The simulations carried out for these samples are not conclusive in this respect. This will be the subject of future investigations.

2.2 Relaxation processes for $\text{In}_{0.13}\text{Ga}_{0.87}\text{As}/\text{GaAs}$ heterostructures

The lattice misfit of $\text{In}_{0.13}\text{Ga}_{0.87}\text{As}/\text{GaAs}$ is equal to 9.3×10^{-3} and the *critical thickness* $t_c = 200 \text{ \AA}$. It has been shown that non-equilibrium growth conditions in various epitaxial techniques generally lead to a critical thickness depending on the growth temperature. Consequently, metastable pseudomorphic layers much thicker than the equilibrium critical thickness can be achieved, and it is necessary to *determine experimentally* the layer thickness at which the strain begins to relax and also to show how this happens.

For the identification of relaxation processes, $\text{In}_{0.13}\text{Ga}_{0.87}\text{As}/\text{GaAs}$ layers on GaAs(001) with a thicknesses range of 300-1000 \AA were investigated by HRXRD and x-ray reflectometry (XRR) both with synchrotron radiation at ROBL and also at a laboratory source in Warsaw, again with a wavelength $\lambda = 1.54 \text{ \AA}$. Additionally, microscopy techniques with Nomarski phase contrast were applied for further characterizing the surface morphology.

In longitudinal scans (coupled $\theta/2\theta$ scans) of the $\text{In}_{0.13}\text{Ga}_{0.87}\text{As}$ epitaxial layers, the angular distance $\Delta\theta$ between the layer and substrate reflections starts to decrease with an epi-layer thickness $\geq 800 \text{ \AA}$. This can be caused by variations of composition or strain. With transverse scans (ω scans) in connection with a low-aperture detector it was first proved that all epitaxial layers investigated were flat – i.e. the radius of curvature was $> 50 \text{ m}$.

Chemical composition and strain can both be evaluated from asymmetrical reflections. Fig. 3 shows a reciprocal space map around the (224) reciprocal lattice point of the $\text{In}_{0.13}\text{Ga}_{0.87}\text{As}/\text{GaAs}$ heterostructure with an epi-layer of 580 \AA thickness. From the mutual positions of the substrate and layer peaks one finds:

1. coherence between the substrate and the epi-layer
2. tetragonal symmetry for the strained epi-layer lattice
3. an indium concentration $x = 0.13$

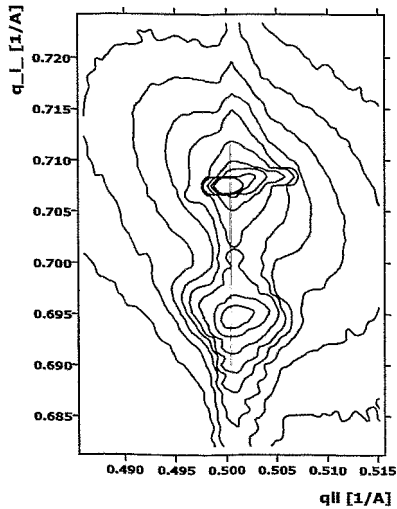


Fig. 3: Reciprocal space map around the (224) reciprocal lattice point of the $\text{In}_{0.13}\text{Ga}_{0.87}\text{As}/\text{GaAs}$ heterostructure with epi-layer 580 Å (azimuth is [110]).

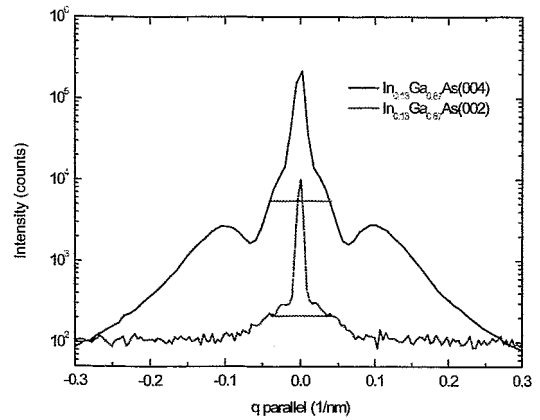


Fig. 4: (002) and (004) transverse scans of the $\text{In}_{0.13}\text{Ga}_{0.87}\text{As}/\text{GaAs}$ heterostructure with epi-layer thickness 580 Å (azimuth is [110]).

Fig. 4 shows two scans perpendicular to the diffraction vector (angular scans) for the symmetrical (004) and (002) Bragg reflections. A two-component (bimodal) line shape is observed: there is a sharp coherent component as well as diffuse scattering, which has a peak intensity an order of magnitude weaker. The diffuse component is due to scattering from misfit dislocations existing in the interface, whereas the coherent component comes from the area between the misfit dislocations. The two satellites in the diffuse intensity confirm the existence of 60° dislocations in the interface [5]. These satellites would be absent in the case of pure edge dislocations.

If the angular width $\Delta\theta$ of the diffuse scattering in a transverse scan is independent of Q_z (Q_z – the perpendicular component of the scattering vector), as is the case in Fig. 4, the FWHM of the diffuse scattering directly reflects the correlation length in the layer [6]. Under such conditions it is possible to evaluate the density of misfit dislocations in the interface. The calculated mean distance between the dislocations for the 580 Å epi-layer was thus found to be 1200 Å. When the average distance between the misfit dislocations exceeds the layer thickness, the strain relaxation process cannot be observed [5].

Fig. 5 shows a reciprocal space map around the (224) reciprocal lattice point of the $\text{In}_{0.13}\text{Ga}_{0.87}\text{As}/\text{GaAs}$ heterostructure with 800 Å epi-layer thickness. In the epi-layer reflection there is only the diffuse component related to the misfit dislocations (with Gaussian distribution of intensity in [224] and perpendicular direction). The coherent component is strongly damped because of overlapping of the deformation fields from neighboring dislocations.

The mechanism of the epi-layer strain relaxation is also presented in Fig. 5: the construction of the relaxation triangle was based on the angle φ between the 001 and 224 directions (in cubic symmetry $\varphi = 35.26^\circ$) and the angle α calculated from the relation $\text{tg}(\alpha) = \text{tg}(\varphi) c_{11}/2c_{12}$ where c_{ij} are the epi-layer stiffness coefficients. Most of the semiconductor materials with 001 substrate orientation have α values close to the value of φ . For the $\text{In}_{0.13}\text{Ga}_{0.87}\text{As}/\text{GaAs}$ heterostructure considered, the value of α is 35.53° . The epi-layer reflection point lies on the relaxation line RL , which is characteristic for *tetragonal*

deformation of the epi-layer. The relaxation coefficient is approximately 40 %. The average distance between the misfit dislocations is 376 Å as calculated from the components of the momentum transfer q and is, therefore, smaller than the epi-layer thickness [5]. The principal relaxation process thus is the slip of 60° misfit dislocations on (111) planes. Such lattice relaxation generally degrades the structural, electrical and optical quality of epitaxial layers. The indium concentration in the epi-layer can be calculated from the vertical side of the relaxation triangle and was found to be $x = 0.13$.

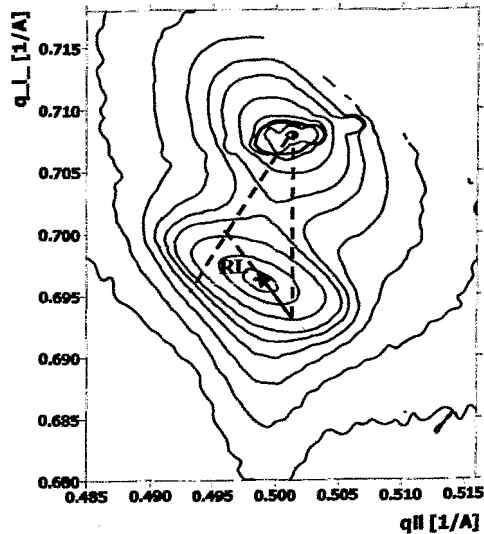
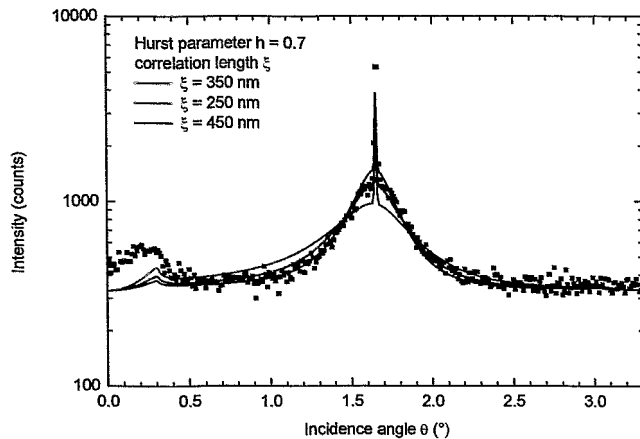


Fig. 5: Reciprocal space map around the (224) reciprocal lattice point of the $\text{In}_{0.13}\text{Ga}_{0.87}\text{As}/\text{GaAs}$ heterostructure with an epi-layer of 800 Å thickness, the azimuth is [110].

2.3 Surface morphology investigations for $\text{In}_{0.13}\text{Ga}_{0.87}\text{As}/\text{GaAs}$ heterostructures

From literature it is known, that in heterostructure systems with lattice misfit $< 1\%$, the principal relaxation process is due to slipping of 60° misfit dislocations on (111) planes. Such dislocations have the Burgers vector component perpendicular to the interface. Due to this vertical component of the Burgers vector, a step formation on the epi-layer surface will be observed (*cross-hatch*). The surface with cross-hatches is, however, not suitable for the production of device elements with sub-micron properties.

The morphological properties of our samples were investigated by means of specular and non-specular XRR [7] and also by Nomarski phase contrast microscopy. Though the Kiessig fringes in specular XRR have only a small amplitude (because of the small difference between the electron densities in the substrate and the epi-layer), thickness and roughness values can accurately be determined by a comparison with simulations [2]. In order to characterize the statistical properties of the epi-layer surface, the non-specular reflectivity was measured for fixed detector position ($2\theta = 4.6^\circ$) with a penetration depth (evaluated from kinematical theory as to be 4000 Å) which exceeds the layer thickness and, therefore, gives information coming from the interface. The non-specular measurements allow to determine two parameters: the *correlation length* ξ and the *Hurst parameter* h [7] which describe the correlation of roughness between layers and the ruggedness of the interface or surface, respectively. Fig. 6 gives an example for the non-specular intensity profile of the sample with epi-layer thickness 800 Å showing a two-component (bimodal) line shape: the coherent (specular) component with a narrow FWHM and the broad diffuse component with a lower intensity.



← Fig. 6: Non-specular diffuse scattering (transversal scans) of the $\text{In}_{0.13}\text{Ga}_{0.87}\text{As}/\text{GaAs}$ heterostructure with epi-layer 800 Å (dots – measured; lines – simulated [2]).

In reflectometry such bimodal intensity distributions indicate that the scale factor $\sigma q \ll 1$ (σ – mean square of step height; q – momentum transfer) [8]. Under such circumstances it is possible to evaluate the correlation length directly from the FWHM of the non-specular diffuse component. Similar results were found for the sample with epi-layer thickness 580 Å. However, the $\text{In}_{0.13}\text{Ga}_{0.87}\text{As}/\text{GaAs}$ heterostructure with lowest epi-layer thickness of 300 Å shows only the coherent component of reflection due to the flat surface of the heterostructure: thus it has no steps on the surface. For this latter sample we also found a very low diffuse scattering intensity for the (004) high-angle transverse scan. This means, that its interface is free of misfit dislocations. By Nomarski phase contrast microscopy one can directly see steps on a surface (Fig. 7). The data confirm what has been found by x-ray techniques and give values for step distances. Table 3 compiles the data found for our samples.

Fig. 7: Images from Nomarski microscopy of $\text{In}_{0.13}\text{Ga}_{0.87}\text{As}/\text{GaAs}$ heterostructures with various epi-layer thickness: top 300 Å, middle 580 Å and bottom 800 Å. No steps are discernible in the top image, while steps in the middle image have a distance of 0.89 μm and in the bottom one only 0.31 μm. →

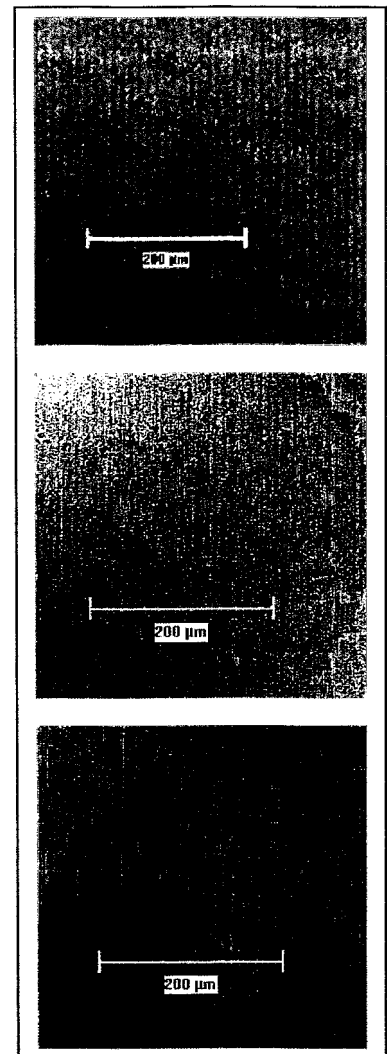


Table 3: XRR and microscopy results for the $\text{In}_{0.13}\text{Ga}_{0.87}\text{As}/\text{GaAs}$ heterostructures.

Heterostructure with epilayer [Å]	Thickness [Å]	Roughness σ [Å]	Correlation length [Å]	Hurst Parameter	Step distance [Å]
580	576	9.45	2000	0.38	8900
800	820	8.31	3500	0.70	3100

3. Conclusions

With HRXRD we studied low-dimensional semiconducting InGaAs/GaAs compound heterostructures consisting of two GaAlAs barriers, and InGaAs/GaAs nanometric multi quantum wells located between them. We do not find any differences between the composition and thickness of barriers in succeeding samples, but the diffraction profile is very sensitive to any change of the chemical composition profile of the MQW. We furthermore observe some instabilities related to the early stages of epitaxial deposition which resulted in the loss of MQW periodicity.

For the $\text{In}_{0.13}\text{Ga}_{0.87}\text{As}/\text{GaAs}$ heterostructures with lattice misfit 1 % and critical thickness $t_c = 200 \text{ \AA}$, we found – by combining HRXRD, XRR and Nomarski phase contrast microscopy:

- the heterostructure to be practically flat (radius of curvature $> 50 \text{ m}$)
- coherence between the substrate and the epi-layer up to a layer thickness of $2t_c$
- the principal relaxation process to be a slip of 60° misfit dislocations
- for layers exceeding $4t_c$ thickness the relaxation process to be advanced (with a relaxation coefficient of approximately 40 %)
- heterostructures with epi-layer thickness $< 300 \text{ \AA}$ not to be stepped
- density steps (*cross-hatches*) to arise with increasing misfit dislocation

Those results are a valuable confirmation of the deposition parameters which allow the epitaxial growth of state of the art functional heterostructure devices.

Acknowledgements

The authors would like to thank the European Commission for the financial support of part of the experiments at ROBL under the contract HPRI-CT-1999-00077 within the Human Potential Programme – Access to Research Infrastructures.

References

- [1] M.S. Goorsky, K.M. Matney, M. Meshkinpour, D.C. Streit, T.R. Block, *Il Nuovo Cimento D* **19** (1997) 257-266
- [2] D. Mogilyanski, E. Gartstein, M. Blumin, D. Fekete, R. Köhler, *J. Phys. D: Appl. Phys.* **34** (2001) A19-24
- [3] S.M. Durbin, G.C. Follis, *Phys. Rev. B* **51** (15) (1995) 10-127
- [4] Bede RADS Mercury, Bede plc, Belmont Business Park, Durham, DH1 1TW, UK
- [5] V.M. Kaganer, *et al.*, *Phys. Rev. B* **55** (1997) 1793-1810
- [6] P.F. Miceli, C.J. Palmstrom, *Phys. Rev. B* **51** (1995) 5506-5509
- [7] S.K. Sinha, *et al.*, *Phys. Rev. B* **38** (1988) 2297
- [8] S.R. Andrews, R.A. Cowley, *J. Phys. C: Solid State Phys.* **18** (1985) 6427-6439

EXAFS investigations of uranium complexes formed by different bacteria isolated from uranium mining wastes

M. Merroun, C. Hennig, A. Rossberg, H. Funke, S. Selenska-Pobell, T. Reich*

Institute of Radiochemistry

Forschungszentrum Rossendorf, P.O. Box 51 01 19, 01314 Dresden, Germany

* present address: Institut für Kernchemie

Johannes Gutenberg-Universität Mainz, Fritz-Straßmann-Weg 2, 55128 Mainz

1. Introduction

Contamination of the environment with radionuclides, toxic metals, metalloids and organo-metals is of considerable economic and environmental significance. There is considerable interest in the microbiological processes which affect the behaviour of contaminants in natural and engineered environments and also in their potential to bioremediate the contaminants. The extent to which these processes can affect the behaviour of contaminants is dependent on the identity and chemical form of the radionuclide released and the physical and chemical nature of the contaminated site or substance. Microbial processes which solubilise radionuclides increase their bioavailability and potential toxicity, whereas those that immobilise them, reduce their bioavailability. Microorganisms can mobilise radionuclides/metals through autotrophic and heterotrophic leaching, chelation by microbial metabolites and siderophores, and methylation which can result in volatilisation. Conversely, immobilisation can result from sorption to cell components or exopolymers, transport into cells and intracellular sequestration or precipitation as insoluble organic and inorganic compounds [1].

Biosorption processes essentially are chemical ones whereby the biomass acts as a surface upon which metals bind by ligand interactions or by ion exchange. Living and dead microorganisms possess abundant functional groups, such as carboxyl, hydroxyl and phosphate on their surface that bind metal ions [2]. In this paper, we present results of U L_{III}-edge Extended X-ray Absorption Fine Structure (EXAFS) spectroscopy of the uranium complexes formed by different bacteria strains of *Acidithiobacillus ferrooxidans*, *Stenotrophomonas maltophilia* and *Bacillus sphaericus* which were isolated from uranium mining wastes. Also some reference strains, namely *Pseudomonas stutzeri* ATCC 17588 and *Pseudomonas migulae* CIP 105470 were involved in the study because they represent predominant indigenous bacterial populations of the uranium wastes.

2. Material and methods

2.1 Bacterial strains used

The bacterial strains used in this work are: *P. stutzeri* ATCC 17588, *P. migulae* CIP 105470, *A. ferrooxidans* D2, *B. sphaericus* JG-A12, *S. maltophilia* JG-2. *A. ferrooxidans* D2 was recovered from the depths of a Canadian uranium mine; *S. maltophilia* JG-2 and *B. sphaericus* JG-A12 were isolated from a uranium mining waste pile near the town of Johanngeorgenstadt in Germany. The two *Pseudomonas* strains, *S. maltophilia* JG-2 and *B. sphaericus* JG-A12 were cultured in nutrient medium containing 5 g of peptone and 3 g of meat extract per liter. The *A. ferrooxidans* strain was cultured in 9K liquid medium containing 3 g of (NH₄)₂SO₄, 0.5 g of K₂HPO₄, 44.2 g of FeSO₄·7H₂O, 0.5 g of MgSO₄·7H₂O and 0.1 g of KCl and 0.014 g of Ca(NO₃)₂·4H₂O per liter.

2.2 Experimental procedure for the EXAFS sample preparation

Bacterial cells grown to the mid-exponential were harvested by centrifugation (12500 rpm for 30 min at 4 °C) and washed three times with 0.1 M NaClO₄ to remove the disturbing ingredients of the growth medium. The washed cells were resuspended and shaken for 48 h in 10 mL 0.5 mM solution of uranyl (VI) resolved in 0.1 M NaClO₄, pH 4.5. After the uranyl contact, the cells were harvested and washed with 0.1 M NaClO₄. The pellet samples was dried at 30 °C for 24 h and ground.

2.3 EXAFS measurements

Uranium L_{III}-edge x-ray absorption spectra were collected at room temperature in fluorescence mode at the Rossendorf Beamline (ROBL) using the Si(111) double-crystal monochromator. The energy was calibrated by measuring the Y K-edge transmission spectrum of a yttrium foil and defining the first inflection point as 17038 eV. Bacterial/uranyl samples were measured as dry samples. Eight scans for each sample were recorded. The EXAFS oscillations were isolated from the raw, averaged data by removal of the pre-edge background, approximated by a first-order polynomial, followed by E₀-removal via spline fitting techniques and normalized using a Victoreen function. Dead-time correction was applied. The ionization energy for the U L_{III} edge, E₀, was arbitrarily defined as 17185 eV for all averaged spectra. The EXAFS spectra were analyzed according to the standard procedures using the program EXAFSPAK [3]. The theoretical scattering phase and amplitude functions used in data analysis were calculated using FEFF8 [4].

3. Results and discussion

The k^3 -weighted χ spectra determined from extended x-ray absorption spectroscopy (EXAFS) analyses of the uranium species formed at pH 4.5 by *P. stutzeri* ATCC 17588, *P. migulae* CIP 105470, *S. maltophilia* JG-2, *B. sphaericus* JG-A12 and *A. ferrooxidans* D2 are presented in Fig. 1 along with the best fits obtained from the fitting procedure.

3.1 Oxygen and carbon neighbors

Quantitative fit results, given in Table 1, indicate that the adsorbed U(VI) has the common linear trans-dioxo structure: two axial oxygens at about 1.78 Å, and an equatorial shell of 4 to 5 oxygens at 2.26-2.41 Å.

The U-O_{eq1} bond distances of the *A. ferrooxidans* D2 uranium complexes (2.36 ± 0.02 Å); *P. stutzeri* ATCC 17588 (2.29 ± 0.02 Å); *P. migulae* CIP 105470, *S. maltophilia* JG-2, and *B. sphaericus* JG-A12 (2.27 ± 0.02 Å) are within the range of previously reported values for the oxygen atom of the phosphate bound to uranyl [5, 6].

The FT spectra of the uranium complexes formed by *B. sphaericus* JG-A12 required other oxygen shell to obtain reasonable fits (U-O_{eq2}) (Table 1). This longer equatorial oxygen bond length (2.42 ± 0.02 Å) is similar to previously reported values for the oxygen atom of the carboxyl or water bound to uranyl (2.41 to 2.51 Å) [7, 8].

For the same sample of *B. sphaericus* JG-A12, the 4th FT peak was modelled to the contribution of carbon atom. The best-fit value for the U-C Path length ($r = 2.89 \pm 0.02$ Å) is consistent with the aqueous uranyl acetate standard [5] and similar to previously reported values for acetate bound to uranyl. On the basis of previous studies, a uranyl to carbon distance of approximately 2.90 Å indicates a bidentate carboxyl bond [8]. In this study,

bidentate refers to an inner-sphere complex where two oxygen atoms of a single carboxyl functional groups are shared with uranyl ion.

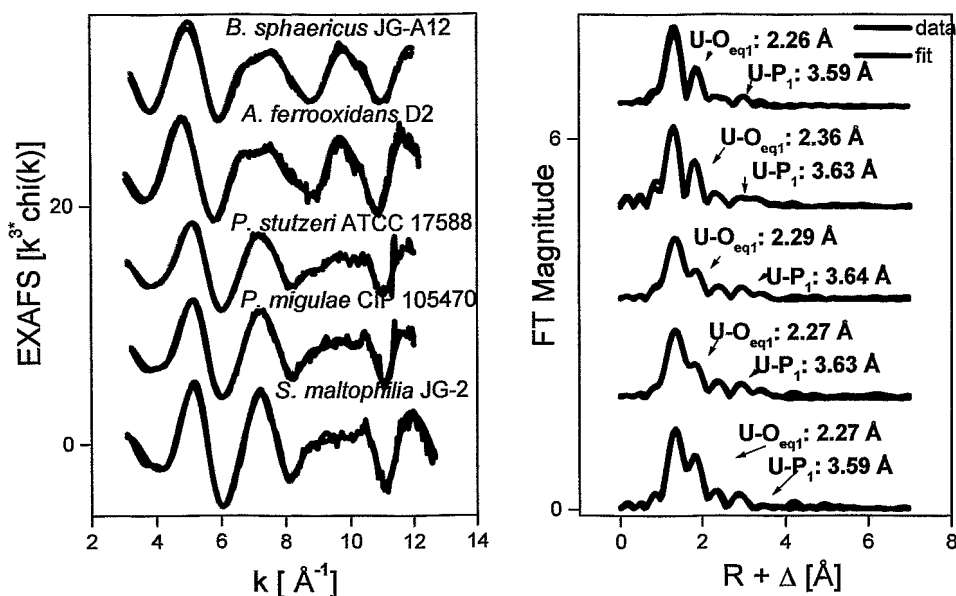


Fig. 1: Uranium L_{III}-edge k³-weighted EXAFS spectra (left) and corresponding FT (right) of the bacterial uranium complexes.

The FT spectra of the uranium complexes formed by the other bacteria studied in this work (*P. stutzeri*, *P. migulae*, *S. maltophilia*, *A. ferrooxidans*) contain the same FT peak as found in *B. sphaericus* (interpreted as a contribution of carbon atom) at about 2.3 Å. After correcting for the scattering phase shift, this distance is typical for carbonate groups coordinated to U(VI) in a bidentate fashion [9]. Indeed, carbon atoms at 2.86 to 2.91 Å provide a good fit to the 2.3 Å FT peak. However, infrared spectroscopy of the same samples indicated that the carboxyl groups are not implicated in the interaction of these bacteria with uranium [10, 11]. Moreover, if this FT peak originates from bidentate carboxyl ligands, the U-O_{eq1} bond distance should be approximately 2.46-2.49 Å [12], which is not the case in this work (2.27 to 2.36 ± 0.02 Å). For these two reasons, we exclude the possibility of interpreting this shell as a contribution of carbon atoms. Moreover, this shell is too short to be attributed to MS pathways. Oxygen neighbours (O_{eq2}) provide a good fit to the residual EXAFS spectrum corresponding to this shell. Thus, we interpret this peak in the FT as oxygen neighbors.

3.2. Phosphorous neighbors

For all samples, the distance between uranium and phosphorus (U-P) is within the range of previously reported values for phosphate bound to uranyl in microorganisms [6, 13].

The broad FT peak between 2.7 and 3.9 Å could according to Kelly *et al.* [5] arise from:

- a phosphorus and the twofold degenerated 3-legged MS path U-O_{eq1}-P₁
- or from a phosphorus and an additional SS path U-P₂ instead of the MS path U-O_{eq1}-P₁

Table1: Structural parameters of the uranium bacterial complexes.

Sample	Shell	N ^a	R[Å] ^b	σ^2 [Å ²] ^c
<i>B. sphaericus</i>	U-O _{ax}	2 ^d	1.76	0.0017
	U-O _{eq1}	2.2(1)	2.26	0.0040
	U-O _{eq2}	2.8(3)	2.41	0.0024
	U-C	1.4	2.91	0.0038
	U-P	1	3.59	0.0050
<i>A. ferrooxidans</i>	U-O _{ax}	2 ^d	1.77	0.0016
	U-O _{eq1}	4.4(4)	2.36	0.0071
	U-O _{eq2}	1 ^d	2.88	0.0026
	U-P ₁	1.5(8)	3.63	0.0042
	U-P ₂	2.9(8)	3.86	0.0076
<i>P. stutzeri</i>	U-O _{ax}	2 ^d	1.78	0.0040
	U-O _{eq1}	2.5(2)	2.29	0.0050
	U-O _{eq2}	1 ^d	2.87	0.0044
	U-P ₁	1.6(5)	3.64	0.004 ^d
	U-P ₂	1.7(6)	3.85	0.004 ^d
<i>P. migulae</i>	U-O _{ax}	2 ^d	1.78	0.036
	U-O _{eq1}	3.3(2)	2.27	0.0060
	U-O _{eq2}	1 ^d	2.87	0.0032
	U-P ₁	2.3(3)	3.63	0.004 ^d
	U-P ₂	2.4(3)	3.84	0.004 ^d
<i>S. maltophilia</i>	U-O _{ax}	2 ^d	1.78	0.0024
	U-O _{eq1}	4.3(4)	2.27	0.0043
	U-O _{eq2}	1	2.86	0.0043
	U-P ₁	2.0(4)	3.63	0.004 ^d
	U-P ₂	1.8(4)	3.81	0.004 ^d

a: Errors in coordination numbers are $\pm 25\%$ and standard deviations as estimated by EXAFSPAK are given in brackets

b: errors in distance are ± 0.02 Å

c: Debye-Waller factor

d: value fixed for calculation

4. Conclusions

Extended x-ray absorption fine structure (EXAFS) measurements were used at the U L3-edge to directly determine the functional groups responsible for the absorption of aqueous UO_2^{2+} by *B. sphaericus* JG-A12, *P. stutzeri* ATCC 17588, *P. migulae* CIP 105470, *A. ferrooxidans* D2 and *S. maltophilia* JG-2 at pH 4.5. Fits to EXAFS spectra indicate that in the case of *B. sphaericus* JG-A12, the U(VI) is coordinated to carboxyl groups in a bidentate fashion with an average distance between the U atom and the C atom of 2.91 ± 0.02 Å and to phosphate groups in a monodentate fashion with an average distance between the U atom and the P atom of 3.59 ± 0.02 Å. This U-P distance indicates inner-sphere complexes with an oxygen atom shared between uranyl ion and phosphoryl ligand. However, in the case of the other bacteria, phosphate are the main functional groups implicated in the complexation of uranium in a monodentate mode, with an average distance between the U atom and the P atom of 3.63 ± 0.02 Å.

References

- [1] G.M. Gadd, in: *Interactions of microorganisms with radionuclides*, Eds. M.J. Keith-Roach, F.R. Livens (Elsevier, Oxford, 2002) pp.179-203
- [2] A.J. Francis, *Biotransformation of uranium and other actinides in radioactive wastes*, J. Alloys Compounds **271-273** (1998) 78-84
- [3] G.N. George, I.J. Pickering, *EXAFSPAK: A suite of computer programs for analysis of x-ray absorption spectra*, Stanford Synchrotron Radiation Laboratory, Stanford, CA, USA 1995
- [4] A.L. Ankudinov, B. Ravel, J.J. Rehr, S.D. Conradson, *Multiple-scattering calculations of x-ray-absorption spectra*, Phys. Rev. B **52(4)** (1998) 7565
- [5] S.D. Kelly, K.M. Kemmer, J.B. Fein, D.A. Fowle, M.I. Boyanov, B.A. Bunker, N. Yee, *X-ray absorption fine structure determination of pH-dependent U-bacterial cell wall interactions*, Geochim. Cosmochim. Acta **65** (2002) 3855-3871
- [6] C. Hennig, P.J. Panak, T. Reich, A. Roßberg, J. Raff, S. Selenska-Pobell, W. Matz, J.J. Bucher, G. Bernhard, H. Nitsche, *EXAFS investigation of uranium (VI) complexes formed at bacillus cereus and bacillus sphaericus surfaces*, Radiochim. Acta **89** (2001) 625-631
- [7] J.R. Bargar, R. Reitmeyer, J.J. Lenhart, J.A. Davis, *Characterization of U(VI)-carbonato ternary complexes on hematite: EXAFS and electrophoretic mobility measurements*, Geochim. Cosmochim. Acta **64** (2000) 2737-2749
- [8] J. Howatson, D.M. Grev, B. Morosin, *Crystal and molecular structure of uranyl acetate dihydrate*, J. Inorg. Nucl. Chem. **37** (1975) 1933-1935
- [9] A. Coda, A.D. Giusta, V. Tazzoli, *The structure of synthetic andersonite, Na₂Ca[UO₂(CO₃)₃] · H₂O*, Acta Cryst. **B37** (1981) 1496
- [10] M.L. Merroun, C. Hennig, A. Roßberg, T. Reich, R. Nicolai, K.-H. Heise, S. Selenska-Pobell, *Characterization of uranium (VI) complexes formed by different bacteria relevant to uranium mining waste piles, in: Uranium in the aquatic environment*, Eds. B. Merkel, Planer-Friedrich, C. Wolkersdorfer (Springer, 2002) p. 505-511
- [11] M.L. Merroun, G. Geipel, R. Nicolai, K.-H. Heise, S. Selenska-Pobell, *Complexation of uranium (VI) by three eco-types of Acidithiobacillus ferrooxidans studied using time-resolved laser-induced fluorescence spectroscopy and infrared spectroscopy*, Biometals **16** (2003) 331-339
- [12] M.A. Denecke, T. Reich, S. Pompe, M. Bubner, K.-H. Heise, H. Nitsche, P.G. Allen, J.J. Bucher, N.M. Edelstein, D.K. Shuh, *Differentiating between monodentate and bidentate carboxylate ligands coordinated to uranyl ions using EXAFS*, J. Phys. IV France **7 C2** (1997) 637
- [13] S.D. Kelly, M.I. Boyanov, B.A. Bunker, J.B. Fein, D.A. Fowle, N. Yee, K.M. Kemmer, *XAFS determination of the bacterial cell wall functional groups responsible for complexation of Cd and U as a function of pH*, J. Synchrotron Rad. **8** (2001) 946-948

EXAFS study of pH dependence of uranium(VI) complexation with protocatechuic acid – application of iterative transformation factor analysis to EXAFS and UV-vis spectroscopy

A. Roßberg, M. Acker, G. Bernhard, T. Reich*

Institute of Radiochemistry

Forschungszentrum Rossendorf, P.O. Box 51 01 19, 01314 Dresden, Germany

* present address: Institut für Kernchemie

Johannes Gutenberg-Universität Mainz, Fritz-Straßmann-Weg 2, 55128 Mainz

1. Introduction

3,4-Di-hydroxybenzoic acid, protocatechuic acid (PCA), is one of the natural decay products of lignin [1-5]. PCA forms stable complexes with uranium in aqueous solution [6]. We wanted to determine the speciation of the uranium(VI)/PCA complexes as a function of pH directly using the structure-dependent Extended X-ray Absorption Fine Structure (EXAFS) signal. Since all uranium species present in a solution contribute to the measured EXAFS signal, it is necessary that the samples contain the desired species nearly to 100%. However, the speciation calculations for the system uranium(VI)/PCA showed that several uranium species coexist over a wide pH range. Therefore, we developed a new approach to the EXAFS analysis aiming at the quantitative decomposition of the EXAFS spectra of mixtures into the different spectral components/constituents. Our approach is based on iterative transformation factor analysis. As a result, we determined the structure and the speciation of uranium(VI) complexes with PCA in the pH range 4.0–6.8. Furthermore, the factor analysis was applied to a series of ultraviolet-visible (UV-vis) spectra measured at pH 11.0 of aqueous PCA solutions as a function of uranium(VI) concentration. From the combined results of the EXAFS and UV-vis measurements, we deduced the pH-dependent speciation of the system uranium(VI)/PCA in the pH range 4.0–11.0.

2. Experimental

2.1 EXAFS – sample preparation and measurement

Seven samples were prepared between pH 4.0 and 6.8 with an ionic strength of 0.1 mol/L NaClO₄. For all samples the total uranium concentration was 1.0·10⁻³ mol/L and the concentration of PCA was 5.0·10⁻² mol/L. The pH was measured with a glass electrode (Ingold Inc.) and pH-meter (Wiss. Technische Werkstätten GmbH) with a precision of ±0.05 pH units. All samples were prepared from carbonate-free substances under high-purity nitrogen. The U L_{III}-edge x-ray absorption spectra of the aqueous uranium(VI)/PCA mixtures were measured using the Si(111) double-crystal monochromator in channel cut mode [7]. Due to the low concentration of uranium, we used a 4-pixel germanium solid-state detector to record the fluorescent signal. The energy scale was calibrated using the maximum of the first derivative of the U L_{III}-edge x-ray absorption spectrum of the samples. The ionization potential of the U L_{III}-edge was defined as 17185 eV. The EXAFSPAK software package [8] was used for EXAFS-analysis. The theoretical scattering phases and amplitudes were calculated with the scattering code FEFF6 [9] using the crystal structure of sodium uranyl(VI)-triacetate [10].

2.2 UV-vis – sample preparation and measurement

Fourteen aqueous solutions with a constant PCA concentration of $1.0 \cdot 10^{-4}$ mol/L and variable uranium(VI) concentration ranging from 0 to $2.1 \cdot 10^{-4}$ mol/L were prepared at pH 11.0. The ionic strength was adjusted with NaClO_4 to 0.01 mol/L in all samples. For the preparation of the samples, the same chemicals were used as mentioned in section 2.1. The UV-vis measurements were done with a CARY5G (Varian Inc.) device in the spectral range from 220 nm to 350 nm using quartz cuvettes with a path length of $d = 1$ cm. According to the deprotonation constants of PCA [6, 11], at pH 11.0 $1.0 \cdot 10^{-4}$ mol/L PCA is twofold deprotonated as HL^{2-} . In a $2.1 \cdot 10^{-4}$ mol/L U(VI) solution at pH 11.0, nearly 100% of the uranium forms the species $\text{UO}_2(\text{OH})_3^-$ [11-13].

3. Iterative transformation factor analysis (ITFA)

In case of a sample containing d different complexes of the corresponding metal ion, the experimental EXAFS signal $\chi_{\text{total}}(\mathbf{k})$ can be written as:

$$\chi_{\text{total}}(\mathbf{k}) = \sum_{i=1}^d \chi_i(\mathbf{k})c_i \quad (1)$$

\mathbf{k} – wavevector in \AA^{-1} ; c_i – relative concentration of metal complex i

The EXAFS spectra $\chi_i(\mathbf{k})$ are the signals of the individual metal complexes i with their corresponding near-neighbor surroundings. c_i is the relative concentration of the complex i in the sample. If only the EXAFS spectra $\chi_{\text{total}}(\mathbf{k})$ in a series of measurements are known, the goal of our ITFA algorithm is the determination of $\chi_i(\mathbf{k})$ of the pure metal complexes and their concentrations c_i for each spectrum. In the first step of the ITFA algorithm, the measured EXAFS spectra (number of measuring points in \mathbf{k} space is n , number of spectra is m) are accumulated as rows in a data matrix $\mathbf{D}_{(n,m)}$. The eigenanalysis of \mathbf{D} yields a m -dimensional abstract factor solution with $\mathbf{D} = \mathbf{R}_{\text{abs.}(n,m)} \mathbf{C}_{\text{abs.}(m,m)}$ (abs. stands for abstract). The eigenvectors in $\mathbf{R}_{\text{abs.}}$ and $\mathbf{C}_{\text{abs.}}$ contain no physical interpretable information. Only the spectra of d primary factors (i.e. spectra of the metal complexes) are necessary for the reproduction of \mathbf{D} . The secondary factors, which amount to $(m-d)$, contain the experimental error and can be removed from the matrices $\mathbf{R}_{\text{abs.}}$ and $\mathbf{C}_{\text{abs.}}$. To determine d – the rank of \mathbf{D} – the importance of the factors on the abstract data reproduction must be investigated. For this purpose we used the eigenvalues λ , the semi empirical indicator function (IND) developed by MALINOWSKY [14], and the function of residual-percent-variance (RPV) [15]. If d is determined, the dimensionality of the matrices $\mathbf{R}_{\text{abs.}}$ and $\mathbf{C}_{\text{abs.}}$ reduces to (n,d) and (d,m) , respectively. To obtain physical interpretable spectra and concentrations for the metal complexes, $\mathbf{R}_{\text{abs.}(n,d)}$ and $\mathbf{C}_{\text{abs.}(d,m)}$ must be transformed. We use the iterative targettest (ITT) with concentration testvectors $\mathbf{c}_{i,\text{test}}$ to transform the abstract factor solution. Each $\mathbf{c}_{i,\text{test}}$ contains an incomplete concentration profile for the i 'th factor in the measured spectra. All unknown values are set to zero. Known values are held constant during the iteration. In each cycle between eq. (2) and eq. (3)

$$\mathbf{t}_i = \mathbf{c}_{i,\text{test}} \mathbf{C}_{\text{abs.}}^i \quad (2)$$

$$\hat{\mathbf{c}}_{i,\text{test}} = \mathbf{t}_i \mathbf{C}_{\text{abs.}} \quad (3)$$

(t for transpose), a new concentration vector $\hat{\mathbf{c}}_{i,\text{test}}$ is generated for the factor i . $\hat{\mathbf{c}}_{i,\text{test}}$ is then put into eq. (2) as new $\mathbf{c}_{i,\text{test}}$. If the values in $\mathbf{c}_{i,\text{test}}$ converge to $\hat{\mathbf{c}}_{i,\text{test}}$, the iterative cycle between eq. (2) and (3) is stopped. During the iteration, negative elements in $\mathbf{c}_{i,\text{test}}$ are set to zero. Elements greater than one are set to one. For the creation of the concentration test vectors, we used the qualitative interpretable concentration profiles of the factors determined by VARIMAX rotation [16, 17]. After the ITT procedure, the real spectra (in \mathbf{R}_{real}) of the metal complexes can be calculated using eq. (4):

$$\mathbf{R}_{\text{real}} = \mathbf{R}_{\text{abs.}} \mathbf{T}^{-1} \quad (4)$$

The transformation matrix \mathbf{T} is simply a combination of the transformation vectors \mathbf{t}_i , which are calculated according to eq. (2).

In comparison to other techniques, the ITT procedure has the advantage that the concentration distributions of the factors are determined independently from each other. We used the described ITFA technique also for the investigation of the UV-vis spectra.

4. Results and discussion of the EXAFS investigations

The data matrix \mathbf{D} contains the raw uranium L_{III}-edge k^3 -weighted EXAFS spectra of the uranium(VI)/PCA mixtures at seven different pH values. The eigenanalysis of \mathbf{D} yields maximum seven eigenvalues λ and eigenvectors, which are contained in $\mathbf{C}_{\text{abs.}}$ and $\mathbf{R}_{\text{abs.}}$. For the first four factors the eigenvalues and the values of the *IND* function are listed in Table 1. The abstract spectra of the first four factors and their abstract concentration distributions are shown in Fig. 1.

Table 1: Eigenanalysis results of \mathbf{D} .

n ^{a)}	λ_i	$IND_i \cdot 10^3$ ^{b)}
1	4931.44	15.0
2	215.72	12.5
3	31.99	17.2
4	20.33	27.4

a: number of factor; b: indicator function

The eigenvalues measure the amplitude of the abstract spectra of the factors. Factors with large eigenvalues influence the data more than factors with small eigenvalues. Beginning with the third eigenvalue, the eigenvalues are small and do not change significantly (Table 1). This indicates that only two primary factors contribute to the variation in the data. To check whether the third or a following factor contains only the experimental error, it is instructive to look at the abstract spectra of the factors (Fig. 1, left). Only the abstract spectra of the first two factors show EXAFS-like oscillations and contain usable information. The following factors contain the experimental noise.

The *IND* function should reach a minimum when the correct number of primary factors is employed for the abstract data reproduction [14]. As one can see from Table 1, the *IND* function reaches a minimum at the second factor. The eigenvalues, the abstract spectra, and the *IND* function show clearly that two structural different spectral components exist in the pH range 4.0–6.8. Fig. 2 compares the raw k^3 -weighted EXAFS spectra and their abstract reproductions using the first two factors.

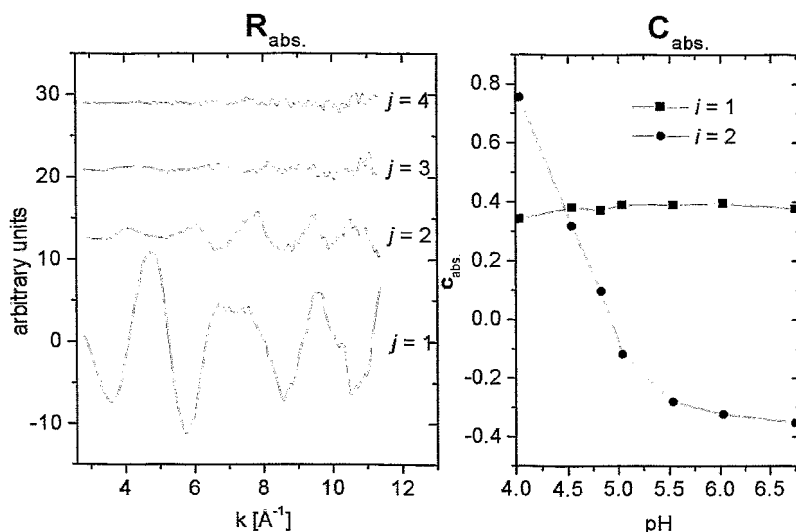


Fig. 1: The first four abstract spectra (eigenvectors) of the factors (left) and the abstract concentration distribution of the first two factors (right); i – number of factor.

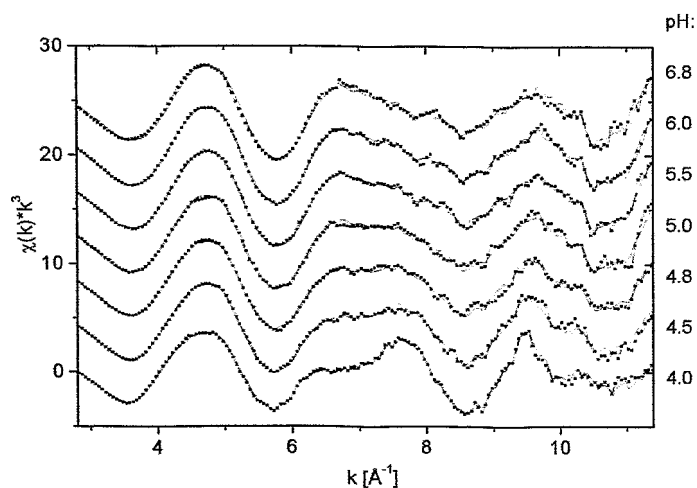


Fig. 2: Raw uranium L_{III} -edge k^3 -weighted EXAFS spectra of the aqueous uranium(VI)/PCA mixtures at different pH values (dotted line) and their abstract reproductions (solid line).

The VARIMAX rotation of the abstract concentration distributions in $\mathbf{C}_{abs.}$ yields that the first and the second factors have their maximum concentration at pH 4.0 and pH 6.8, respectively. Using this additional information, the concentration test vectors were created for the ITT. The spectral components correspond to the EXAFS spectra of the two structural different uranium(VI)/PCA complexes. Therefore, the ITT results in the speciation of the uranium(VI)/PCA complexes as a function of pH (Fig. 3).

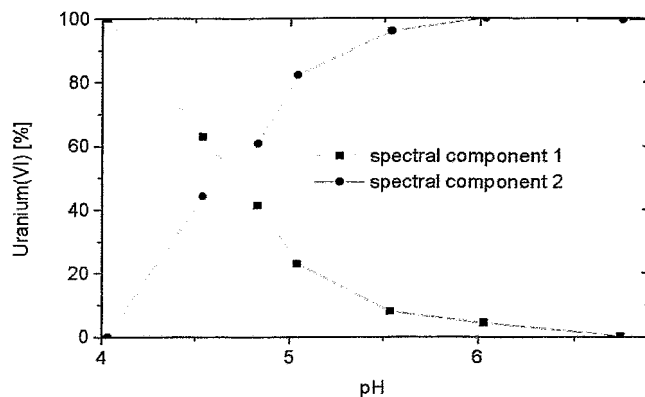


Fig. 3: The pH speciation of the uranium(VI)/PCA complexes.

After the ITT, the real EXAFS spectra of the two spectral components were calculated using eq. (4). In the following analysis, the chemical nature of the spectral components will be identified using conventional EXAFS data analysis. Results of fits to the spectral components are shown in Fig. 4 and listed in Table 2. The coordination number (N) of the axial oxygen of the uranyl unit was held constant at two in all fits.

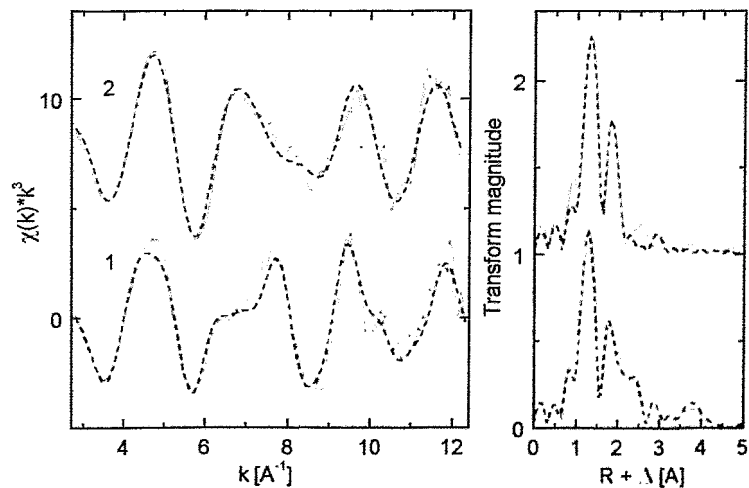


Fig. 4: Uranium L_{III}-edge k³-weighted EXAFS spectra of the spectral components 1 and 2 (left) and their corresponding Fourier transforms (right). Dashed line – best theoretical fit to the data.

Table 2: EXAFS structural parameters for the spectral components 1 and 2. (N – coordination number, R – radial distance in Å with an uncertainty of ± 0.02 Å, σ^2 – Debye-Waller factor in Å², ΔE_0 – energy shift in eV). Standard deviations of the variable parameters as estimated by EXAFSPAK are given in parenthesis.

spectral component	U-O _{axial(ax.)}		U-Atom _{equatorial(eq.)}				ΔE_0
	R	$\sigma^2 \cdot 10^3$	Atom	N	R	$\sigma^2 \cdot 10^3$	
1	1.780(2)	1.9(2)	O _{eq.}	6.4(9)	2.450(6)	11(1)	-7.6(6)
			C ₍₁₎	3.1(9)	2.876(6)	3(2)	
			C ₍₂₎	3.1	4.38(1)	3	
2	1.803(2)	1.8(1)	O _{eq.}	5.3(3)	2.362(4)	7.7(6)	-7.4(5)

Within the experimental uncertainty of 0.02 Å, the determined U-O_{eq.}, U-C₍₁₎, and U-C₍₂₎ bond distances are similar to those found for uranyl(VI)-triacetate [10]. In this compound the carboxylic group coordinates in a bidentate mode to the uranyl(VI) ion. According to the EXAFS structural parameters, we identify spectral component 1 as the EXAFS spectrum of a uranium(VI)/PCA complex where the carboxylic group forms a bidentate complex with the uranyl ion. For the second spectral component the U-O_{ax.} bond distance of 1.80 Å is slightly higher than the corresponding value for spectral component 1 (Table 2). A similar trend of increasing U-O_{ax.} bond distances with increasing pH was also observed in a previous investigation of uranium(VI) complexes with PCA [18]. The short U-O_{eq.} bond distance of 2.36 Å indicates that the coordination of uranium(VI) occurs via the neighboring phenolic OH groups of the PCA under formation of a five-membered ring [18]. The EXAFS spectrum and the EXAFS structural parameters of spectral component 2 are similar to those observed for an aqueous uranium(VI)/PCA solution at pH 10.0 [18]. From this we deduce that the o-diphenolic uranium(VI)/PCA complex exists in the pH range of 6.8 to 10.0.

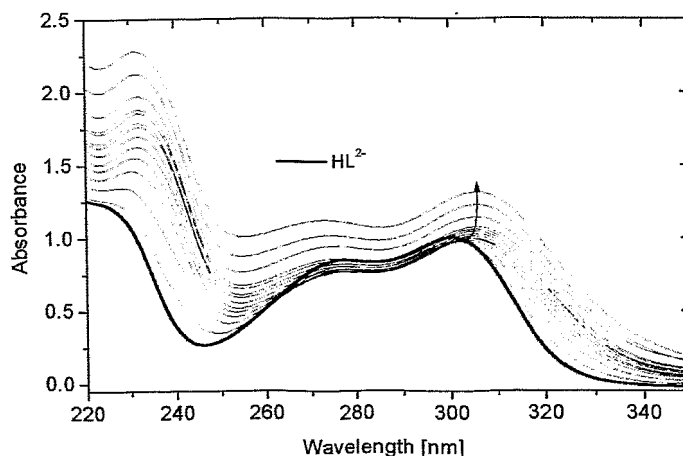


Fig. 5: UV-vis spectra of a series of uranium(VI)/PCA mixtures with variable uranium(VI) concentration. The arrow shows the shift of the absorption maximum with increasing uranium(VI) concentration.

5. Results and discussion of UV-vis investigations

The UV-vis spectra of $1.0 \cdot 10^{-4}$ mol/L PCA solutions at pH 11.0 as a function of uranium(VI) concentration are shown in Fig. 5. The arrow in Fig. 5 indicates the shift in the absorption maximum. The UV-vis spectrum of the twofold deprotonated PCA (HL^{2-}) without any uranium(VI) added to the solution was also measured (thick solid line in Fig. 5).

Before the VARIMAX rotation and ITT could be performed, the eigenanalysis of the 14 UV-vis spectra was carried out. The eigenvalues of the factors were used to calculate the *RPV* function, which allows to determine the number of chemical species causing the variance in the UV-vis spectra. If the correct number of factors for the data reproduction is employed, the *RPV* function should reach zero [15]. For this series of UV-vis spectra, the *RPV* function reach zero at three factors, i.e., chemical species. The result of the VARIMAX rotation is shown in Fig. 6.

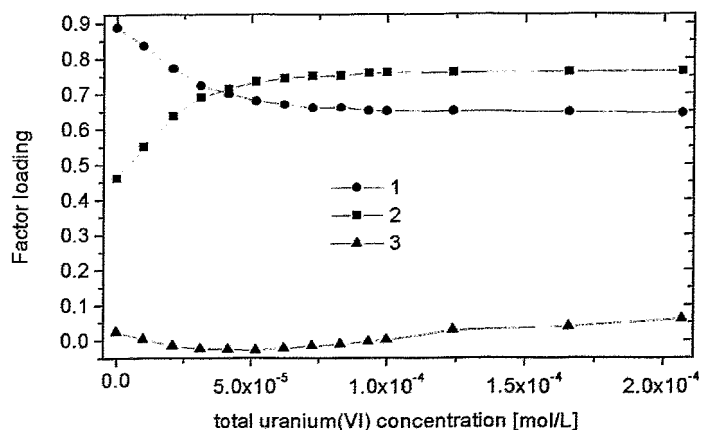


Fig. 6: The abstract concentration distribution of the spectral components 1-3 as a result of the VARIMAX rotation.

With the help of the abstract concentration distribution given in Fig. 6, it is possible to identify the chemical species. Spectral component 1 has its largest concentration in the solution without uranium and is, therefore, the spectrum of HL^{2-} . Up to a concentration of $0.5 \cdot 10^{-4}$ mol/L uranium(VI), the concentration of spectral component 2 increases with decreasing HL^{2-} concentration. Therefore, spectral component 2 corresponds to the uranium(VI)/PCA complex. When the uranium(VI) concentration is larger than $0.5 \cdot 10^{-4}$ mol/L, the concentration of spectral component 3 increases. Although uranium(VI) is being added to the solution, the concentrations of HL^{2-} and of the uranium(VI)/PCA complex remain constant and only the concentration of spectral component 3 increases. Therefore, spectral component 3 is the spectrum of noncomplexed uranium(VI). For the ITT procedure, the concentration test vectors were created according to the result of the VARIMAX rotation (Fig. 6) as in case of the EXAFS measurements. The ITT procedure yields the uranium(VI) speciation in $1.0 \cdot 10^{-4}$ mol/L PCA at pH 11.0 as a function of the total uranium(VI) concentration (Fig. 7).

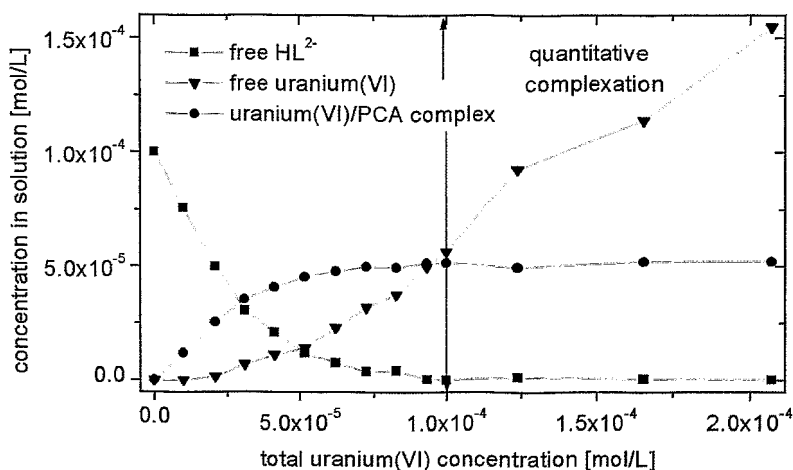


Fig. 7: The determined concentration of the chemical species at pH 11.0 by application of the ITT to UV-vis spectra of uranium(VI)/PCA mixtures. The twofold deprotonated protocatechuic acid (HL^{2-}) is quantitatively complexed above $1.0 \cdot 10^{-4}$ mol/L uranium(VI) (right side from the arrow).

As discussed in section 4, we conclude that the uranium(VI) complex with an o-diphenolic coordination of the PCA molecule exists in the pH range of 6.8 to 10.0. We assume that the same uranium(VI)/PCA complex exists also at pH 11.0 where the UV-vis measurements were done. Because no uranium-uranium scattering interaction was observed in the EXAFS spectra at pH 6.8 and 10.0, the existence of polynuclear uranium(VI) complexes can be excluded. Therefore, the determined concentration of complexed uranium(VI) is equal to the concentration of the uranium(VI)/PCA complex. The stability of the uranium(VI)/PCA complex is very high since the PCA is completely complexed at a total uranium(VI) concentration of $1.0 \cdot 10^{-4}$ mol/L (Fig. 7). By using the determined concentrations of the chemical species in Fig. 7 for each sample, the stoichiometry of the uranium(VI)/PCA complex can be calculated. The resulting average ratio of uranium(VI) to PCA is one to 1.95 ± 0.04 . This allows to conclude that a 1:2 uranium(VI)/PCA complex exists at pH 11.0.

6. Conclusions

The EXAFS spectra corresponding to two different uranium(VI)/PCA complexes were extracted from the series of EXAFS measurements using iterative transformation factor analysis. At pH 4.0 the carboxylic group of two or three PCA molecules binds to the uranyl unit in a bidentate fashion. EXAFS structural parameters of the uranium(VI)/PCA complex at pH 6.8 are similar to those observed at pH 10.0. In this pH range the coordination occurs via the two neighboring phenolic OH groups of PCA under formation of a five-membered ring. The stoichiometry of this uranium(VI)/PCA complex is 1:2 according to the UV-vis measurements at pH 11.0. The speciation diagram of the uranium(VI)/PCA complexes as a function of pH is given in Fig. 3. Note that this speciation is based solely on the structural differences in the near-neighbor surrounding of the uranium atoms that can be observed by EXAFS. For the implementation of our proposed factor analysis algorithm, we wrote a computer code in the programming language FORTRAN90.

Acknowledgement

We thank L. Baraniak and H. Neubert for their support during the sample preparation for the EXAFS measurements and K. Krogner for performing the ICP-MS measurements. H. Funke and C. Hennig are thanked for their assistance in the EXAFS measurements.

References

- [1] C.H. Ludwig, K.V. Sarkanen, *Lignins – occurrence, formation, structure and reactions*, Wiley-Interscience 1971, p. 773
- [2] M. Cresser, K. Killham, T. Edwards, in P.G.C. Campbell, J.N. Galloway, R.M. Harrison (Eds.): *Soil chemistry and its applications*, Cambridge Environmental Chemistry Series, Cambridge University Press 1993, p. 34
- [3] W. Fritsche, *Umwelt-Mikrobiologie*, Akademie-Verlag, Berlin 1985, p. 52
- [4] G. Ebert, *Biopolymere - Struktur und Eigenschaften*, B.G. Teubner, Stuttgart 1993, p. 442
- [5] S. Masselter, A. Zemann, O. Bobleter, *Analysis of lignin degradation products by capillary electrophoresis*, *Chromatographia* **40** (1995) 51
- [6] L. Baraniak, M. Schmidt, G. Bernhard, H. Nitsche, Forschungszentrum Rossendorf, Institut für Radiochemie, Annual Report 1996, p. 28
- [7] W. Matz, N. Schell, G. Bernhard, F. Prokert, T. Reich, J. Claussner, W. Oehme, R. Schlenk, S. Dienel, H. Funke, F. Eichhorn, M. Betzel, D. Proehl, U. Strauch, G. Hüttig, H. Krug, W. Neumann, V. Brendler, P. Reichel, M.A. Denecke, H. Nitsche, *ROBL - a CRG beamline for radiochemistry and materials research at the ESRF*, *J. Synchrotron Rad.* **6** (1999) 1076
- [8] G.N. George, I.J. Pickering, Stanford Synchrotron Radiation Laboratory, Stanford, CA. USA. 1995
- [9] S.I. Zabinsky, J.J. Rehr, A. Ankudinov, R.C. Albers, M.J. Eller, *Multiple-scattering calculations of x-ray-absorption spectra*, *Phys. Rev. B* **52** (1995) 2995
- [10] D.H. Templeton, A. Zalkin, H. Ruben, L.K. Templeton, *Redetermination and absolute configuration of sodium uranyl(VI) triacetate*, *Act. Cryst.* **C41** (1985) 1439
- [11] M. Acker, *Zeitaufgelöste laserinduzierte Fluoreszenzspektroskopie mit ultrakurzen Anregungsimpulsen und ihre Anwendung zur Untersuchung der Fluoreszenzeigenschaften von gelösten Huminstoffen, Protocatechusäure und deren Uran(VI)komplexen*, doctoral thesis, Technical University Dresden, Dresden (*in preparation*)
- [12] I. Grenthe, J. Fuger, R.J.M. Konings, R.J. Lemire, A.B. Muller, C. Nguyen-Trung, H. Wanner, *Chemical thermodynamics of uranium*, Elsevier Science, North-Holland, Amsterdam 1992
- [13] T.J. Wolery, part I. Lawrence Livermore National Laboratory 1992
- [14] E.R. Malinowski, *Determination of the number of factors and the experimental error in a datamatrix*, *Analytical Chemistry* **49** (1977) 612
- [15] E.R. Malinowski, *Factor analysis in chemistry*, John Wiley & Sons, New York 1991
- [16] H.F. Kaiser, *The VARIMAX criterion for analytic rotation in factor analysis*, *Psychometrika* **23** (1958) 187
- [17] M. Fernandez-Garcia, C. Marquez Alvarez, G.L. Haller, *XANES-TPR study of Cu-Pd bimetallic catalysts: application of factor analysis*, *J. Phys. Chem.* **99** (1995) 12565
- [18] A. Roßberg, L. Baraniak, T. Reich, C. Hennig, G. Bernhard, H. Nitsche, *EXAFS structural analysis of aqueous uranium(VI) complexes with lignin degradation products*, *Radiochim. Acta* **88** (2000) 593

EXAFS studies of reactions of neptunyl(V) with mackinawite

F.R. Livens¹, M.J. Jones¹, L.N. Moyes¹, R.A.D. Patrick², W.A. Reed¹, D.J. Vaughan²

¹Centre for Radiochemistry Research, Department of Chemistry

²Department of Earth Sciences

University of Manchester, Manchester M13 9PL, United Kingdom

J.M. Charnock, J.F.W. Mosselmans

CLRC Daresbury Laboratory, Warrington, Cheshire WA4 4AD, United Kingdom

C. Hennig

Institut für Radiochemie

Forschungszentrum Rossendorf, PO Box 51 01 19, 01314 Dresden, Germany

1. Introduction

The redox transformations of uranium and the early transuranium elements are of environmental interest because of the very different environmental mobilities of the tri- and tetravalent ions and the actinyl ($[\text{AnO}_2]^{n+}$, $n = 1, 2$) ions [1, 2]. In near-surface environments isolated from the atmosphere, microbial activity can lead to the development of reducing conditions as terminal electron acceptors other than oxygen are used (Fig. 1).

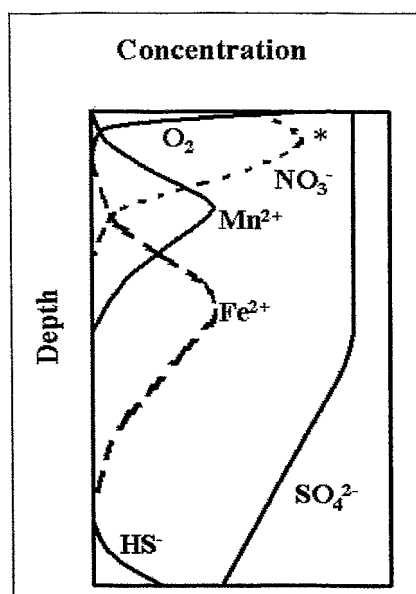


Fig. 1: Idealised sequence of changes in dissolved species concentrations in sediment porewaters with depth. The changes arise from successive exploitation of O_2 , NO_3^- , Mn(IV) , Fe(III) and SO_4^{2-} as terminal electron acceptors in microbial metabolism. FeS precipitation occurs at depths where both Fe(II) and HS^- are present in solution (adapted from reference [3]).

In sulfate reducing conditions, the presence of both Fe(II) and HS^- in solution leads to the precipitation of mackinawite, a microcrystalline FeS mineral. This is important both because it is a key intermediate in the low temperature Fe-S system (Fig. 2) and it has a reactive surface with high specific area. Mackinawite is capable of interacting with trace elements through a variety of mechanisms, including surface precipitation, surface complexation and surface-mediated redox reactions [4, 5]. In addition, mackinawite is unstable in aerobic conditions, oxidising readily to form poorly crystalline goethite, and the speciation of the associated trace elements may also change [5]. Mackinawite readily removes UO_2^{2+} from solution and EXAFS spectroscopy [6] showed that, at low surface loadings, a UO_2^{2+} surface complex formed but, as the surface loading increased, a mixed oxidation state uranium oxide, such as U_3O_8 or U_4O_9 , formed. It was suggested that the

formation of the surface complexes occurred through coordination of UO_2^{2+} ions to low concentrations of pre-existing oxidised zones on the surface. Once these are saturated, the uranium acts as an oxidant, oxidising the surface and generating U(IV), which becomes incorporated in the surface precipitate. Since neptunium, as the NpO_2^+ ion, is expected to be amongst the most mobile of the actinides, the interactions of NpO_2^+ with mackinawite are of interest. Batch sorption experiments showed that, in contrast to UO_2^{2+} , NpO_2^+ is only removed from solution to a limited extent, around 10% at all Np concentrations. The speciation of Np on the mackinawite surface was therefore investigated.

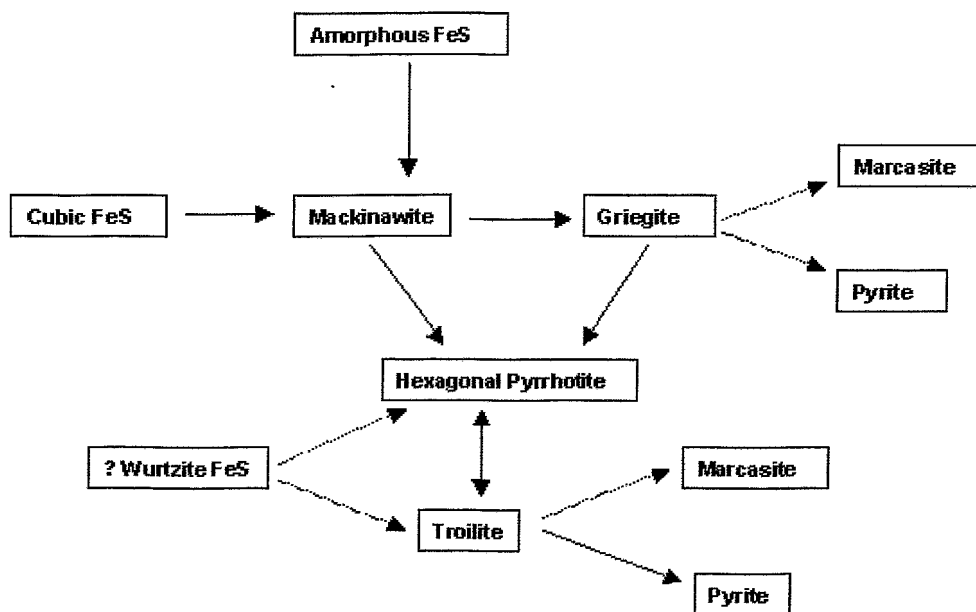


Fig. 2: Low temperature phase relations in the Fe-S system. Solid arrows indicate transformations which have been experimentally demonstrated, while broken arrows indicate those which have not yet been (adapted from reference [7]).

2. Materials and methods

Mackinawite is air-sensitive and all steps in its preparation and handling were carried out under an Ar atmosphere. Synthetic mackinawite was prepared by reacting equal volumes of solutions of Fe(II) (as ferrous ammonium sulfate) and sulfide (as sodium sulfide). Both solutions were prepared at 0.1 M concentrations in $\text{CH}_3\text{CO}_2\text{H}/\text{CH}_3\text{CO}_2\text{Na}$ buffer adjusted to pH 4 and pre-equilibrated overnight with Fe wire to ensure reducing conditions. The resulting precipitate was centrifuged, washed with water, resuspended and reacted with a solution of NpO_2Cl (AEA Technology, Harwell; final $[\text{Np}] = 17, 43$ and 170 kBq l^{-1}). After equilibration, the FeS was centrifuged and mounted in triple-contained cells for XAS analysis. The supernatant was retained and analysed by γ -spectroscopy, allowing Np uptake to be determined by difference. Two separate inert atmosphere gloveboxes were used, a "hot" box for manipulation of the Np-containing mackinawite and packing in the primary containment, after which the samples were bagged out in Ar and transferred to a "cold" box for final packaging. Three samples were prepared, containing $650, 1650$ and $6500 \mu\text{g g}^{-1}$ Np.

Np L_{III} -edge x-ray absorption spectroscopy was carried out at the ROBL beamline in fluorescence mode, collecting multiple scans to improve data quality. The data were transferred to Daresbury Laboratory and analysed using the Daresbury programs EXCALIB, EXBACK and EXCURV98 [8]. The occupancy of each shell was fixed at the integral value which gave the best fit, then the Fermi energy, interatomic distance and Debye-Waller factor refined. Shells were included in the final analysis only if they improved the overall goodness of fit (R-factor) by $>5\%$.

3. Results

The XANES spectra of the Np/FeS samples, together with the spectrum of a NpO_2^+ reference solution, are illustrated in Fig. 3. The spectra of all three FeS samples are identical, are very similar to the published spectrum of Np(IV) [9] and are clearly different from the spectrum of NpO_2^+ , suggesting that the surface species is Np(IV). The EXAFS spectra of the Np/FeS samples and the associated Fourier transforms are illustrated in Fig. 4, respectively. All three samples give very similar spectra, and EXAFS fitting parameters are presented in Table 1. The fitting parameters are essentially the same for all three samples, and suggest a mixed S/O coordination environment.

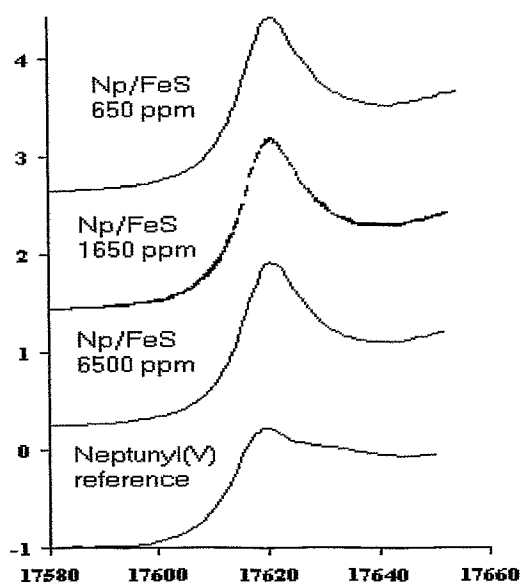


Fig. 3: Normalised XANES spectra of Np/FeS samples, together with that of a NpO_2^+ reference sample.

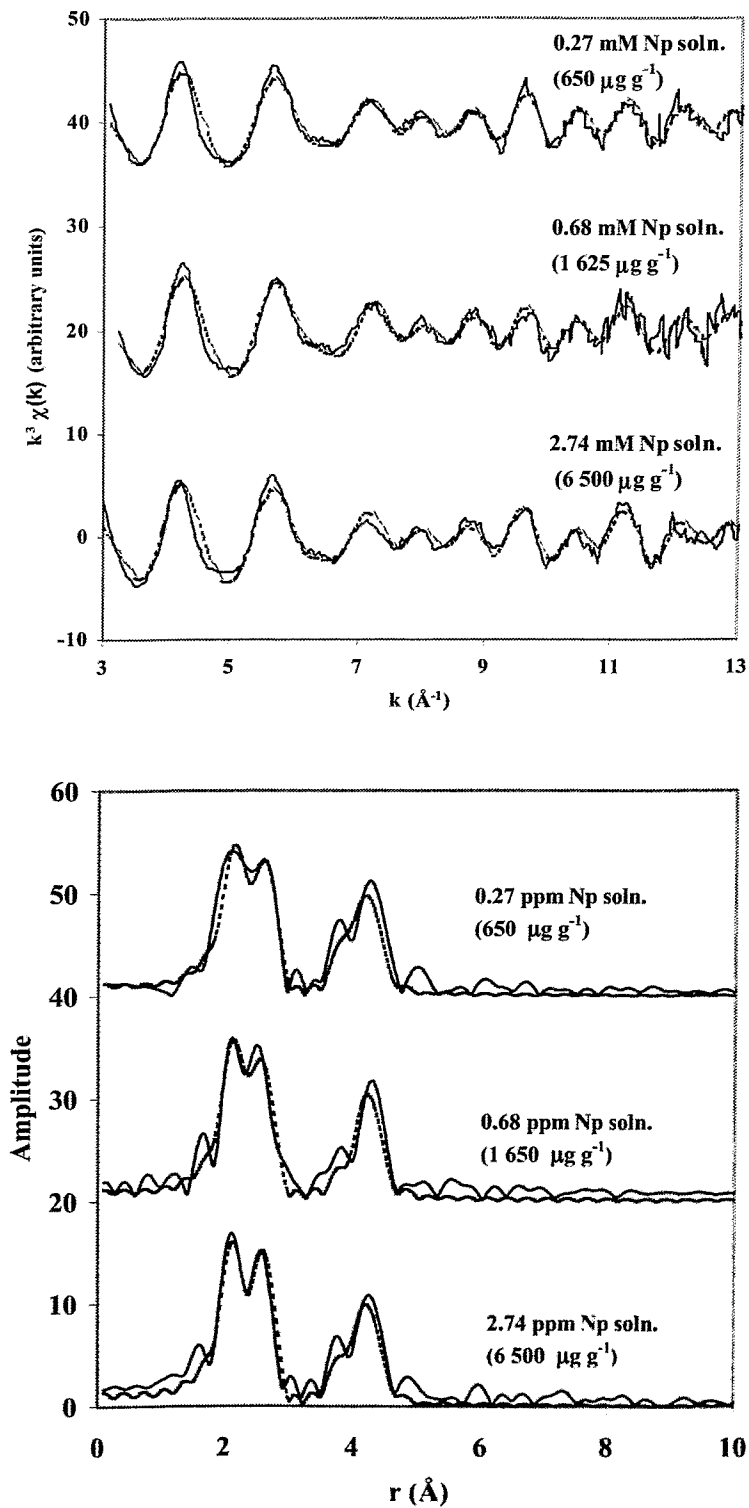


Fig. 4: Background subtracted, k^3 -weighted EXAFS spectra for Np/FeS samples and associated Fourier transforms (phase-shifted). Solid lines show experimental data and broken lines the model fit.

Table 1: EXAFS fitting parameters for Np/FeS samples. Uncertainties in occupancy are $\pm 25\%$ and in interatomic distance are $\pm 0.02 \text{ \AA}$.

Np Concentration	Occupancy, Type	Distance (\AA)	Debye-Waller Factor ($2\sigma^2/\text{\AA}^2$)
$650 \mu\text{g g}^{-1}$	4 O	2.25	0.016
	3 S	2.63	0.016
	2 Fe	3.92	0.009
	6 Fe	4.15	0.014
$1625 \mu\text{g g}^{-1}$	4 O	2.25	0.017
	3 S	2.61	0.019
	2 Fe	3.95	0.012
	5 Fe	4.16	0.010
$6500 \mu\text{g g}^{-1}$	4 O	2.26	0.017
	3 S	2.64	0.019
	2 Fe	3.91	0.009
	5 Fe	4.95	0.012

4. Discussion

On reaction with the mackinawite surface, NpO_2^+ is reduced to give a Np(IV) species. The EXAFS fitting parameters suggest coordination of the Np(IV) product to surface sulfur atoms. The Np-O distance of 2.25 \AA is consistent with the presence of oxygen in the primary coordination sphere of the Np centre. These results are interpreted as being due to the formation of a Np(IV) surface complex, with water or hydroxide ions filling the remainder of the Np coordination sphere (Fig. 5).

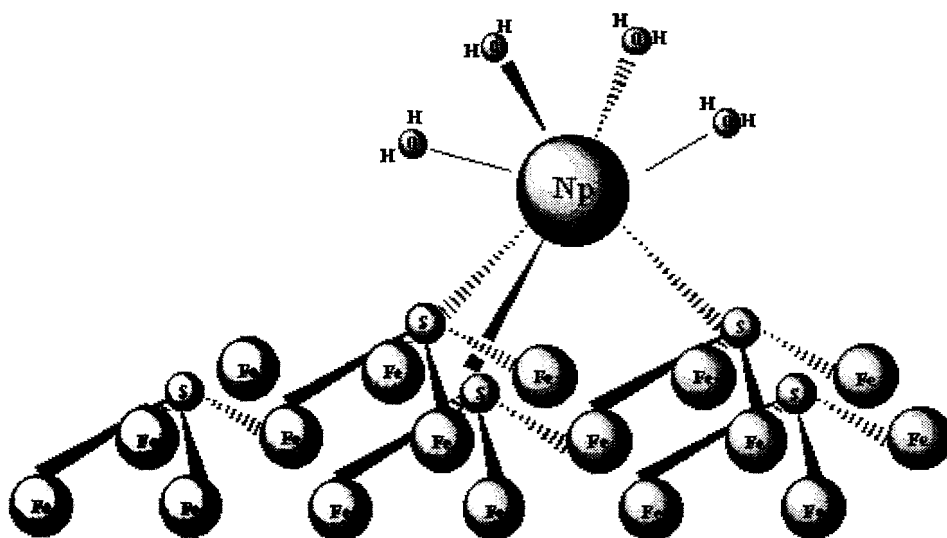


Fig. 5: Schematic diagram illustrating a possible Np coordination environment on the mackinawite surface.

While coordination of chalcophile elements such as Cu or Cd with surface S atoms is well established [4], direct interaction of an actinide with sulfur ligands is unusual since these ions are often viewed as archetypal "hard" cations, although Np-S complexes are known in solution [10]. The low uptake of NpO_2^+ from solution may arise from the inefficiency of reduction since UV-visible-near IR spectroscopy of the supernatant solution showed that the Np remaining in solution was still in oxidation state V. However, longer contact times, up to 48 hours, did not increase Np uptake onto FeS, nor was there any further change in the oxidation state of Np in solution.

5. Conclusions

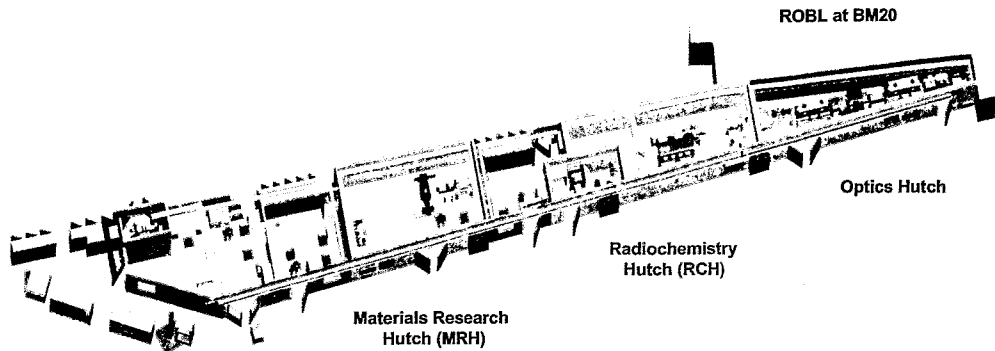
The mechanisms of reaction of UO_2^{2+} and NpO_2^+ with the surface of mackinawite are entirely different. The surface complex with sulfur atoms formed by Np(IV) is unusual and suggests that other actinides in low oxidation states (U(IV), Pu(IV), Pu(III)) may also coordinate directly to the mackinawite surface. It would be interesting to study the chemistry of these ions in the presence of mackinawite, and also to compare the reactivity of synthetic mackinawite with that of biogenic FeS.

References

- [1] D.L. Clark, D.E. Hobart, M.P. Neu, *Chem. Rev.* **95** (1995) 25
- [2] M. Dozol, R. Hagemann, *Pure Appl. Chem.* **65** (1993) 1081
- [3] K.O. Konhauser, K. Morris, *The role of microorganisms during sediment diagenesis – implications for radionuclide mobility*, chapter 3 in: *Interactions of microorganisms with radionuclides*, Eds. M.J. Keith-Roach, F.R. Livens (Elsevier, 2002)
- [4] R.H. Parkman, J.M. Charnock, N.D. Bryan, F.R. Livens, D.J. Vaughan, *Amer. Min.* **84** (1998) 407
- [5] M. Wharton, B. Atkins, J.M. Charnock, F.R. Livens, R.A.D. Patrick, D. Collison, *Appl. Geochem.* **15** (2000) 347
- [6] L.N. Moyes, R.H. Parkman, J.M. Charnock, D.J. Vaughan, F.R. Livens, C.R. Hughes, A. Braithwaite, *Environ. Sci. Tech.* **34** (2000) 1062
- [7] A.R. Lennie, D.J. Vaughan, *Min. Mag.* **59** (1995) 677
- [8] N. Binsted, *Daresbury Laboratory EXCURV98 Program*, CLRC Daresbury Laboratory, Warrington (1998)
- [9] S. Bertram, G. Kaindl, J. Jové, M. Pagès, J. Gal, *Phys. Rev. Lett.* **63** (1989) 2680
- [10] K.L. Nash, J.M. Cleveland, J.C. Sullivan, M. Woods, *Inorg. Chem.* **25** (1986) 1169

Overview of the technical characteristics of ROBL

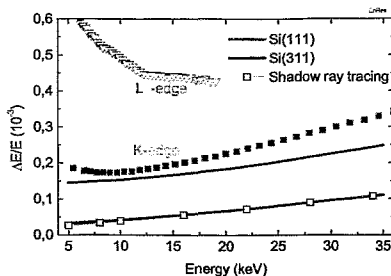
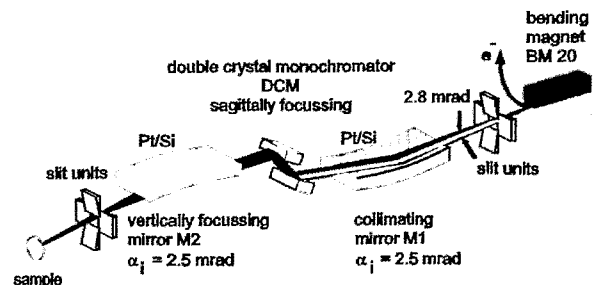
At the web-site http://www.esrf.fr/exp_facilities/BM20/ a detailed description of the beamline, its experimental possibilities, and the way to access beamtime is given. The following three pages give an abbreviated version about the beamline characteristics and its current technical status.



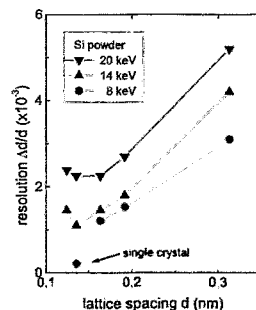
Characteristics of the beamline optics

The optics of ROBL has to serve two independent stations (working alternatively) with different needs to satisfy, i.e. spectroscopy with energy scanning (XAS) and diffraction with high angular resolution (XRD)¹.

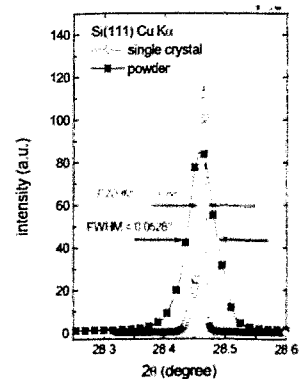
energy range	5 – 35 keV
with Si-mirrors	5 – 12 keV
energy resolution Si(a11)	$1.5 - 2.5 \times 10^{-4}$
energy resolution Si(311)	$0.5 - 1.0 \times 10^{-4}$
integrated flux (calc.)	$6 \cdot 10^{11}$ ph./s @ 20 keV and 200 mA
standard beam size	20 mm (w) x 3 mm (h)
focussed beam size	< 0.5 mm x 0.5 mm



Comparison of the calculated energy resolution and natural line widths of the absorption edges of the elements



Experimental resolution with Si(111) from silicon powder

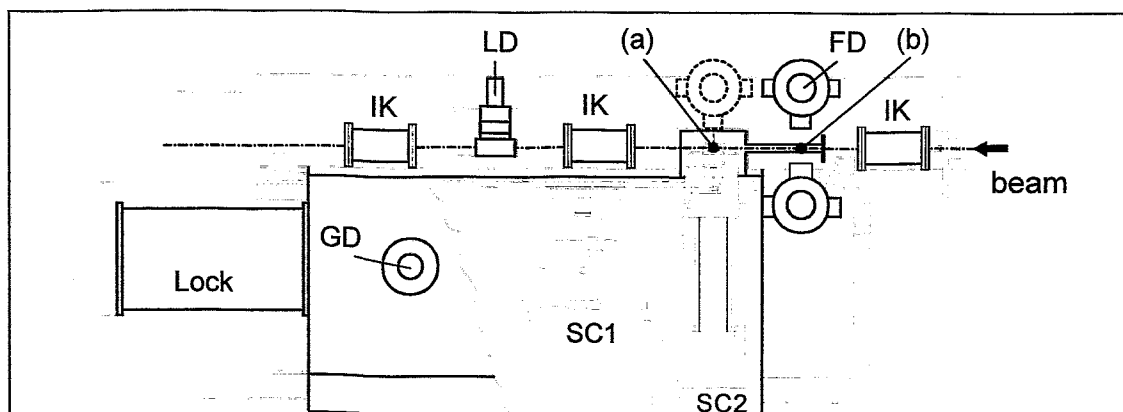


FWHM comparison

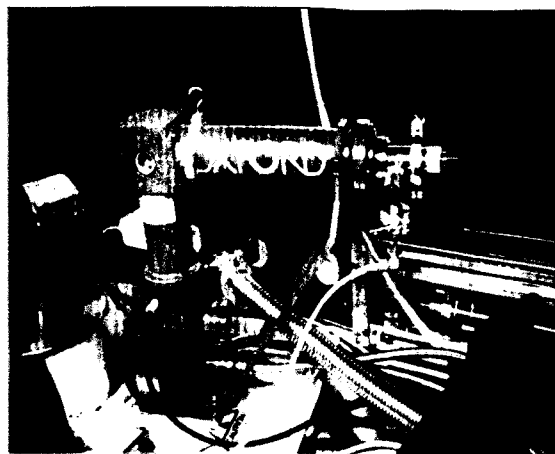
¹ Matz, W., Schell, N., Bernhard, G., Prokert, F., Reich, T., Claußner, J., *et al.* (1999). ROBL – a CRG Beamline for Radiochemistry and Materials Research at the ESRF. Journal of Synchrotron Radiation, 6, 1076-1085.

Technical characteristics of the radiochemistry experimental station

The radiochemistry experimental station RCH is a highly specialized *unique radiochemical laboratory* designed for **radioecological research** (determination of chemical speciation of radionuclides interacting with geological material, natural and anthropogenic organics, and micro-organisms) using x-ray absorption spectroscopy (XAS) in transmission and fluorescence (i.e. element specific, giving oxidation states, bond lengths, and the number of neighbouring atoms in the first few coordination shells) for solid and **liquid samples** with an activity of up to 185 MBq (5 mCi). A **multi-barrier safety concept** with separate ventilation, constant radiation monitoring and redundancy of all essential components was developed to satisfy all legal requirements.

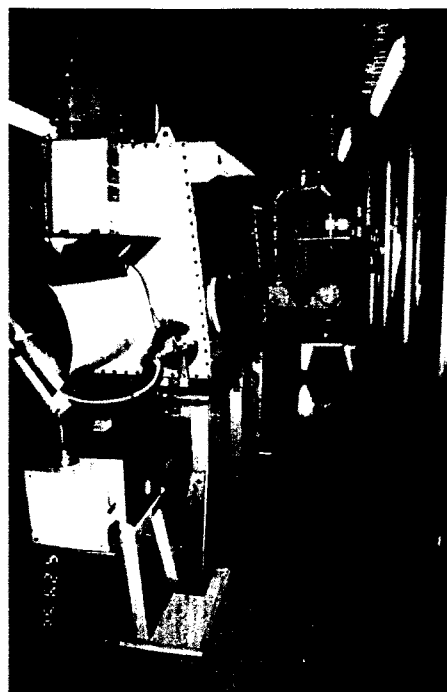


Principal layout of the glovebox. (a) standard sample position for XAFS experiments; (b) sample position for fluorescence radiation detection from dilute samples. The **ionisation chambers (IK)** are mounted on an optical bench and can also be used for non-radioactive samples while the box is moved out of the beam. **FD** – fluorescence detector; **LD** – Lytle detector; **GD** – gamma detector for measurement of sample activity; **SC1, SC2** – sample changers.



He cryostat (15 K) inside the glove box

Inside the experimental hutch →



Technical characteristics of the materials research experimental station

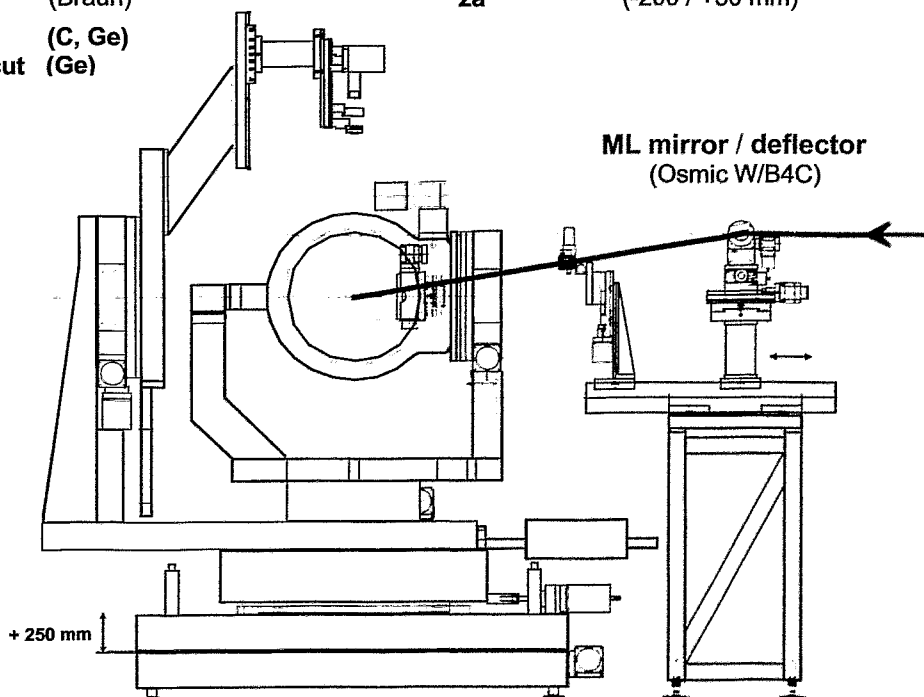
The materials research station (MRH) is designed for the **structural identification and characterisation of modifications of surfaces and interfaces produced by ion beam techniques** (e.g. hard covers, biocompatible materials, or for semiconductor technology) and the study of interfaces in thin films and nanometer-multilayers using various x-ray diffraction techniques (XRD, GIXS) and reflectometry (XRR).

detectors

scintillators (Bede ERD)
PIN-diodes (AMPTEK XRT-110T)
2-dim. CCD (Bruker SMART)
lin. PSD (Braun)
analyzer (C, Ge)
channel-cut (Ge)

diffractometer (HUBER)

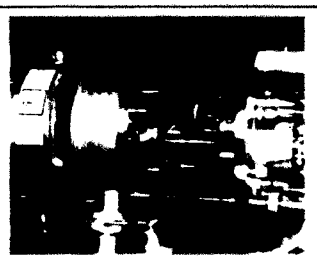
6 circles (0.001°)
x-y-z table ($\pm 75/75/12$ mm; 10/10/1 μ m)
15 kg load (at sample position)
za (-200 / +50 mm)



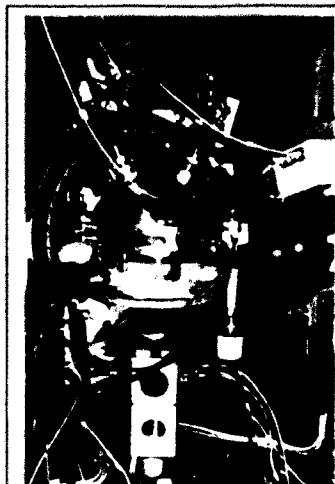
sample chambers annealing
 sputter deposition



In-house designed chamber for moderate annealing (<900°C) with **hemispherical Be-window**, i.e. 2π x-ray access for GIXS



Commercial **high temperature** chamber (Otto) for annealing up to 2000°C in vertical scattering geometry



In-situ two magnetrons sputter deposition chamber (Aarhus collaboration)

Overview of the beamtime distribution at ROBL

During the actual report period **35 scheduled experiments** were performed at **ROBL-MRH**. The overall number of shifts (each 8 hours) delivered for those experiments is given in the first table below. The shifts are divided into experiments allocated in the CRG beamtime and such allocated in the ESRF time (maximum 1/3 of user beamtime). Additionally, about **100 technical shifts** are used for methodical in-house experiments during the report period. The table also contains the number of **different user groups** (including FZR groups) – multiple visits of the same groups are thus not counted. The **total number of users** having visited ROBL for materials research experiments (again including FZR users permanently working in Rossendorf), is given in the last column.

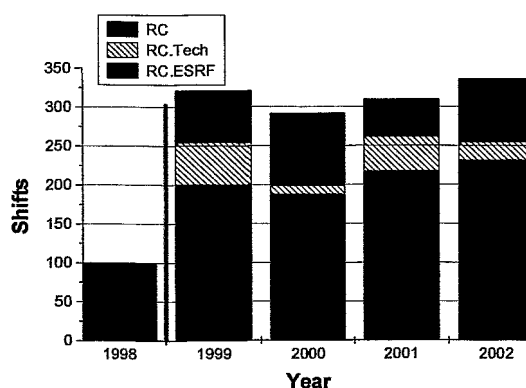
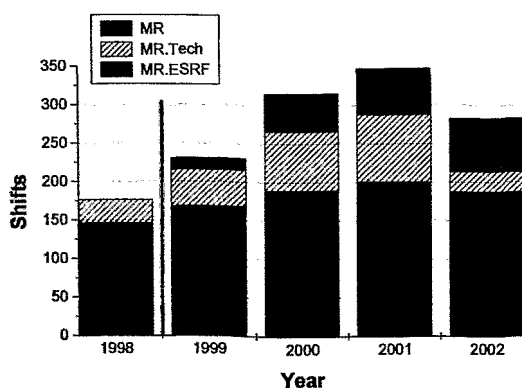
MRH	CRG shifts In-house / EU	ESRF shifts	technical shifts	User groups In-house / EU / ESRF	Users (different persons)
2001	146 / 54 = 200	60	88	8 / 5 / 4 = 17	16 / 12 / 11 = 39
2002	136 / 51 = 187	69	27	6 / 4 / 2 = 12	11 / 9 / 8 = 28

The second table below gives the corresponding statistics for the **64 scheduled radiochemistry experiments** done at **ROBL-RCH**.

RCH	CRG shifts In-house / EU	ESRF shifts	technical shifts	User groups In-house / EU / ESRF	Users (different persons)
2001	169 / 48 = 217	48	45	7 / 5 / 5 = 17	16 / 25 / 18 = 59
2002	153 / 78 = 231	81	24	8 / 7 / 6 = 21	17 / 26 / 19 = 62

The numbers together demonstrate that the ROBL team in Grenoble has to make a significant organisational effort for running the experiments.

The two figures below show the development of shift allocation from the end of the construction period (1998) up to December 2002 (the first year of full operation was 1999).

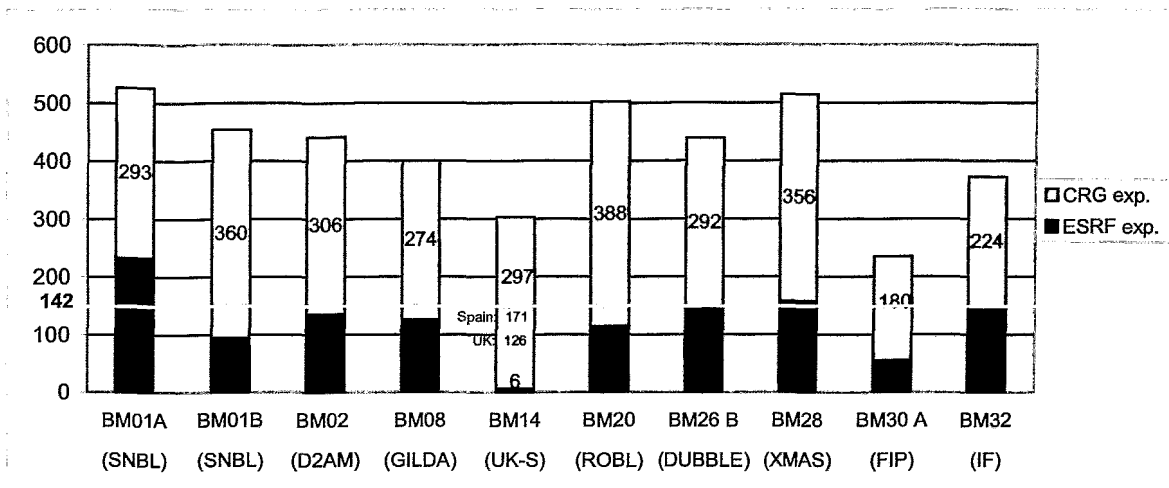


ROBL has to deliver 142 user shifts for ESRF users in every scheduling period. The two viewgraphs on the next page^{*} show the total number of scheduled **experimental shifts** and the ESRF part **for all CRG beamlines**. As the statistical period of the ESRF of each year extends to January/February of the next year (first run) the viewgraphs slightly differ from the tables above.

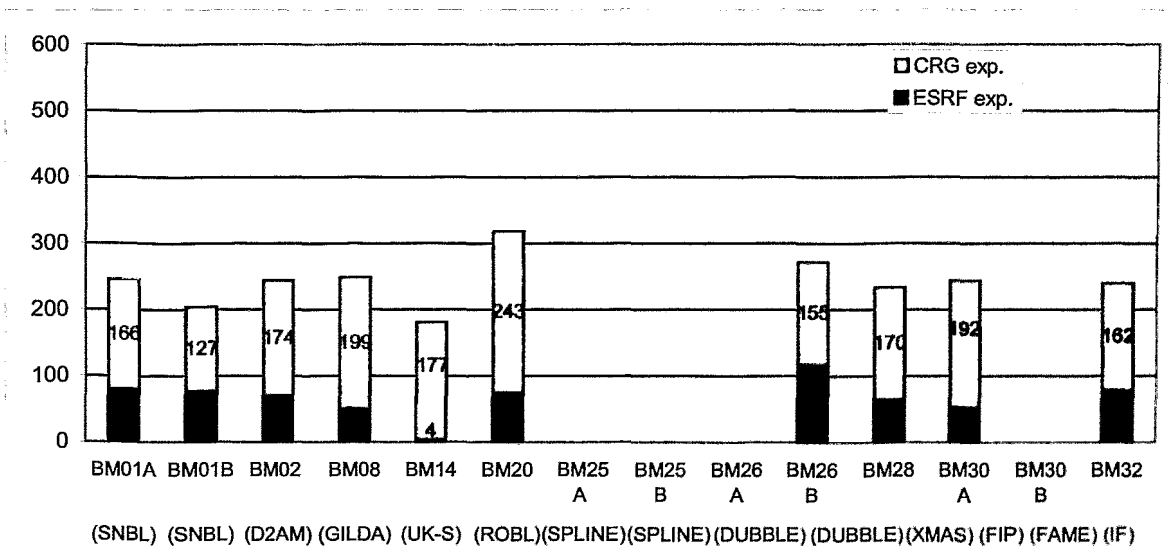
^{*} supplied by the CRG-office of the ESRF

Both viewgraphs show that ROBL is performing quite well with users' request for beamtime comparable to most other CRG beamlines.

CRG-shifts in 2001:



CRG-shifts in the first half of 2002:



The following pages first give information on **EC supported access to ROBL** with the corresponding user list and then the **tables "Scheduled Experiments ..."** and **"Allocated Times ..."** which list in detail all experiments performed. There are some with a high number of shifts (>18) and split into various periods which are part of *long term* research programmes of the FZR or connected to the work of Ph.D. students. From the tables one can also extract the **collaborating institutions** using the experimental possibilities of ROBL (in-house and external).

The **experimental reports** were provided by the users. The responsibility for the communicated results lies with them, ROBL made only minor changes concerning exclusively the layout. All reports received until December 2002 are reproduced here.

Support of user groups by the European Commission

In the 5th framework programme "Improving Human Research Potential" of the European Commission (EC) ROBL has been supported under the programme "Access to Research Infrastructures" since February 2000. Under the three year contract HPRI-CT-1999-00077 research groups from member and associated states of the EU could obtain a grant for experiments at ROBL.

ROBL published calls for proposals where the deadline for submission was given (April 2001, October 2001, April 2002). A user selection panel established with approval of the EC decided which experiments were to be performed at ROBL. At maximum 15 % of the beamtime is available for the EC supported user groups.

More information about this access can be obtain by contacting our Web-site: <http://www/fz-rossendorf.de/FEW/> (see under: EC supported access).

The performed experiments are included in the tables below and indicated by a second number, i.e. the project number, beginning with EU #xx.

List of EC supported users of ROBL

- A. Andrejczuk** 20_02_064 (EU #30)
University at Bialystok, Institute of Experimental Physics, Bialystok, Poland
- N. Baclet** 20_01_057 (EU #14)
CEA, Centre de Valduc, Is sur Tille, France
- T. Bertrand** 20_01_067 (EU #25)
CNRS, Laboratoire Chimie Nucleaire et Analitique, Gradignan, France
- I. Billard** 20_01_600 (EU #32)
IRES, Strasbourg, France
- A. Bhatt** 20_01_609 (EU #40)
University of Manchester, Department of Chemistry, Manchester, United Kingdom
- F. Braz-Fernandes** 20_02_061 (EU #31)
CENIMAT F.C.T./Universidade Nova de Lisboa, Monte da Caparica, Portugal
- J. Bruno** 20_01_049 (EU #18)
Polytechnical University of Catalonia UPC, Barcelona, Spain
- R. Cordeiro Silva** 20_02_061 (EU #31)
CENIMAT F.C.T./Universidade Nova de Lisboa, Monte da Caparica, Portugal
- G. Deves** 20_01_067 (EU #25)
CNRS, Laboratoire Chimie Nucleaire et Analitique, Gradignan, France
- L. Diehl** 20_02_058 (EU #11)
Johannes Kepler Universität, Institut für Halbleiterphysik, Linz, Austria
- T. Donchev** 20_02_047 (EU #12)
Institute of Electronics, Bulgarian Academy of Sciences, Sofia, Bulgaria
- W. Dong** 20_01_043 (EU #7)
Université Paris-Sud. IPN, Orsay, France

R. Drot 20_01_043 (EU #7)
 Université Paris-Sud, IPN, Orsay, France

L. Duro 20_01_049 (EU #18) 20_01_070 (EU #26)
 Universita Autonoma, Cerdanyola del Valles, Spain

F. Eichhorn 20_01_057 (EU #24)
 Forschungszentrum Rossendorf, Dresden, Germany

A. Frischbutter 20_02_048 (EU #23)
 Geoforschungszentrum Potsdam, Potsdam, Germany

A. Froideval 20_01_037 (EU #2)
 Université Louis Pasteur, Institut de Recherches Subatomiques, Strasbourg, France

C. Gaillard 20_01_600 (EU #32)
 IRES, Strasbourg, France

P. Gierlowski 20_02_043 (EU #13)
 Institute of Physics, Polish Academy of Sciences, Warsaw, Poland

S. Grandjean 20_01_607 (EU #38)
 C.E.A. Cadarache, Bagnols sur Cèze, France

K. Grigorov 20_02_047 (EU #12)
 Institute of Electronics, Bulgarian Academy of Sciences, Sofia, Bulgaria

M. Grivé 20_01_049 (EU #18) 20_01_070 (EU #26)
 Polytechnical University of Catalonia UPC, Barcelona, Spain

S. Hubert 20_01_602 (EU #34)
 Université Paris XI, Orsay, France

G. Heisbourg 20_01_602 (EU #34)
 Université Paris XI, Orsay, France

L. Joly 20_01_057 (EU #14)
 CEA, Centre de Valduc, Is sur Tille, France

A. Koster 20_01_068 (EU #28)
 University of Manchester, Department of Chemistry, Manchester, United Kingdom

R. Lechner 20_02_050 (EU #10)
 Johannes Kepler Universität, Institut für Halbleiterphysik, Linz, Austria

F. Livens 20_01_068 (EU #28)
 University of Manchester, Department of Chemistry, Manchester, United Kingdom

K. Lützenkirchen 20_01_037 (EU #2)
 Université Louis Pasteur, Institut de Recherches Subatomiques, Strasbourg, France

R. Martins 20_02_061 (EU #31)
 CENIMAT F.C.T./Universidade Nova de Lisboa, Monte da Caparica, Portugal

I. May 20_01_068 (EU #28) 20_01_609 (EU #40)
 University of Manchester, Department of Chemistry, Manchester, United Kingdom

K. Mazur 20_02_049 (EU #21) 20_01_057 (EU #24)
 Institute of Electronic Materials Technology, Warsaw, Poland

S. Mentese 20_02_058 (EU #11)
 Johannes Kepler Universität, Institut für Halbleiterphysik, Linz, Austria

P. Mikula 20_02_048 (EU #23)
Nuclear Physics Institute, Academy of Sciences of the Czech Republic, Rez, Czech Republic

R. Ortega 20_01_067 (EU #25)
CRNS – U.M.R., Gradignan, France

W. Paszkowicz 20_02_043 (EU #13)
Institute of Physics, Polish Academy of Sciences, Warsaw, Poland

J. Pelka 20_02_043 (EU #13) 20_02_064 (EU #30)
Institute of Physics, Polish Academy of Sciences, Warsaw, Poland

T. Petit 20_01_607 (EU #38)
C.E.A. Cadarache, Saint Paul lez Durance, France

J. Purans 20_01_602 (EU #34)
Université Paris XI, Orsay, France

I. Puigdomenech 20_01_048 (EU #20)
Royal Institute of Technology (KTH), Department of Chemistry, Stockholm, Sweden

H. Reniewicz 20_02_064 (EU #30)
University at Bialystok, Institute of Experimental Physics, Bialystok, Poland

S. Rihs 20_01_062 (EU #19)
Université Louis Pasteur, Centre de Geochimie de la Surface, Strasbourg, France

J. Riotte 20_01_062 (EU #19)
Université Louis Pasteur, Centre de Geochimie de la Surface, Strasbourg, France

C. Robisson-Thomas 20_01_607 (EU #38)
C.E.A. Cadarache, Bagnols sur Cèze, France

J. Sass 20_02_049 (EU #21) 20_01_057 (EU #24)
Institute of Electronic Materials Technology, Warsaw, Poland

F. Seco 20_01_070 (EU #26)
Centro Tecnológico de Manresa, Manresa, Spain

L. Sémon 20_01_037 (EU #2)
Université Louis Pasteur, Institut de Recherches Subatomiques, Strasbourg, France

E. Simoni 20_01_043 (EU #7)
Université Paris-Sud, IPN, Orsay, France

J. Stangl 20_02_050 (EU #10) 20_02_058 (EU #11)
Johannes Kepler Universität, Institut für Halbleiterphysik, Linz, Austria

Z. Szabo 20_01_048 (EU #20)
Royal Institute of Technology (KTH), Department of Chemistry, Stockholm, Sweden

C. Valot 20_01_057 (EU #14)
CEA, Centre de Valduc, Is sur Tille, France

V. Volkovich 20_01_609 (EU #40)
University of Manchester, Department of Chemistry, Manchester, United Kingdom

M. Vrana 20_02_048 (EU #23)
Nuclear Physics Institute, Academy of Sciences of the Czech Republic, Rez, Czech Republic

Z. Zhong 20_02_050 (EU #10)
Johannes Kepler Universität, Institut für Halbleiterphysik, Linz, Austria

Scheduled experiments at ROBL-RCH

number	title	proposer	institution	experimentator	shifts
20_01_019	EXAFS measurements at low temperature	Hennig, Reich, Rossberg, Amayri, Funke	FZR	Hennig, Funke, Reich, Rossberg, Stumpf, Falkenberg	2
20_01_022	Structural investigation of complexes between actinides (Np(IV/V), U(IV/VI), Th(IV)) and humic substances, BioRex70 and ATP	Schmeide, Sachs, Funke, Reich, Hennig, Rossberg	FZR	Funke, Reich, Hennig, Rossberg, Moll, Walter	6 + 1
20_01_024	Polarized EXAFS measurements at uranyl sorbed montmorillonite	Hennig, Reich, Funke, Rossberg	FZR	Funke, Rossberg, Reich, Hennig, Raff, Merroun, Moll, S. & T. Stumpf	6 + 8 + 5 + 6 + 6
20_01_027	Structural Investigation of Pu(III) complexes with humic substances, BioRex70	Schmeide, Sachs, Funke, Reich, Hennig, Rossberg	FZR	Funke, Hennig, Reich, Rossberg, Stumpf, Falkenberg	3
20_01_030	EXAFS investigation on uranium uptake by plants	Günther, Bernhard, Geipel, Reich	FZR	Hennig, Moll, Reich, Funke, Rossberg, Walter, Amayri	3 + 6
20_01_031	X-ray absorption spectroscopy investigation on uranyl complexes with α -substituted carboxylic acids	Moll, Reich	FZR	Hennig, Moll, Reich, Funke, Rossberg, Walter	6
20_01_033	EXAFS Study of U(VI) Sorption onto Birnessite	Manceau, Reich	LGIT Grenoble	Tournassat, Rihs, Sarret, Reich	9
20_01_034	Sorption of Am onto smectite	Stumpf, Fanghänel, Hennig	FZR	Reich, Rossberg, Hennig, Funke, Moll, Walter, Schmeide, Sachs	3 + 6 + 5
20_01_035	Complexation of Am and Er with glycolic acid	Stumpf, Fanghänel, Funke	FZR	Stumpf, Funke, Hennig, Rossberg, Falkenberg	2 + 3
20_01_036	Uranium sorption onto schwertmannite, muscovite, and goethite	Walter, Funke, Bernhard, Arnold, Hennig	FZR	Walter, Funke, Hennig, Moll, Reich, Rossberg	6
20_01_037 EU #2	Adsorption of actinide ions on (hydr-) oxide and clay minerals: Influence of the solution chemistry	Lützenkirchen, Billard, Del Nero, Rossini, Semon, Mignon	IRES, Strasbourg	Froideval, Lützenkirchen, Del Nero, Semon, Rossini, Bauer	9
20_01_038	Structural studies of uranyl phosphates including adenosine phosphates using EXAFS	Reich, Geipel, Hennig, Bernhard, Günther	FZR	Reich, Hennig, Merroun, Funke, Rossberg, Kunicke, Stumpf, Falkenberg	3 + 3
20_01_039	EXAFS investigation of uranium complexation with hydroxo benzoic acids	Reich, Geipel, Sachs, Rossberg, Schmeide, Vulpius	FZR	Reich, Rossberg, Hennig, Merroun, Funke, Kunicke	3

20_01_040	X-ray absorption spectroscopy investigation on solid uranyl complexes with α -substituted carboxylic acids	Reich, Moll	FZR	Reich, Hennig, Merroun, Funke, Rossberg, Stumpf, Kunicke, Falkenberg, Merroun, Walter	6 + 3 + 6
20_01_041	Uranium sorption onto aluminosilicates and ferric oxides	Reich, Walter, Arnold, Hennig, Bernhard, Funke	FZR	Reich, Hennig, Funke, Rossberg, Kunicke	3
20_01_042	Interaction of <i>Acidithiobacillus ferrooxidans</i> with uranium - an EXAFS study	Reich, Hennig, Selenska-Pobell, Merroun	FZR	Reich, Merroun, Hennig, Funke, Rossberg, Merroun, Walter	6 + 6 + 6
20_01_043 EU #7	Uranyl sorption on zirconium and titanium oxides: EXAFS study	Drot, Simoni, Dong	Uni Paris, Orsay	Drot, Simoni, Dong, Bauer	12
20_01_044	Uranium sorption onto chlorite	Reich, Hennig, Krawczyk-Bärsch, Funke, Bernhard, Arnold	FZR	Reich, Funke, Hennig, Stumpf, Rossberg, Falkenberg	3
20_01_045	EXAFS investigation of neptunium complexation with hydroxo benzoic acids	Reich, Sachs, Schmeide, Geipel, Rossberg	FZR	Funke, Hennig, Reich, Rossberg, Stumpf, Sachs Schmeide, Falkenberg	3 + 6 + 6
20_01_046	Cm(III) aquo ion	Stumpf	FZR	Hennig, Reich, Funke, Rossberg, Schmeide, Sachs	3
20_01_047	XAFS spectroscopic study of neptunium(V) sorption onto mineral surfaces	Schmeide, Hennig, Reich, Rossberg, Funke	FZR	Hennig, Reich, Funke, Rossberg, Schmeide, Sachs	3
20_01_048 EU #20	Solution structures of U(VI); Th(IV) and Dy(III) complexes with α -hydroxycarboxylates and phosphonic acids	Grenthe, Szabo, Stumpf	KTH, Stockholm, FZR	Szabo, Puigdomenech Sitja, Bauer	6
20_01_049 EU #18	Surface complexes of uranium onto magnetite and olivine	De Pablo, Duro, El Aamrani, Bruno	Uni Cerdanyola	De Pablo, Duro, Grivé, Bruno, Bauer, Rossberg, Hennig, Reich	12
20_01_050	U(VI)-benzoat and U(VI)-phenolat complexes	Rossberg, Vulpius, Reich, Hennig, Funke	FZR	Reich, Hennig, Rossberg, Funke, Merroun, Walter	3
20_01_051	Interaction between bacteria and uranium using EXAFS	Merroun, Reich, Tzvetkova, Selenska-Pobell	FZR	Reich, Hennig, Rossberg, Funke, Merroun, Walter	3
20_01_052	Uranium sorption onto ferric oxides	Walter, Reich, Funke, Hennig, Rossberg	FZR	Reich, Hennig, Rossberg, Funke, Merroun, Walter	3
20_01_053	Uranium sorption onto muscovite	Walter, Reich, Hennig, Funke, Rossberg	FZR	Reich, Funke, Rossberg, Hennig, Moll, Merroun, Walter	3 + 1 + 6
20_01_054	Interaction between bacterial S-layers and uranium using EXAFS	Raff, Selenska-Pobell, Funke, Reich, Hennig, Rossberg	FZR	Reich, Hennig, Rossberg, Funke, Merroun, Walter	3

20_01_055	Uranium complexation by hydroxybenzoic acids	Geipel, Sachs, Rossberg, Vulpius, Bernhard	FZR	Reich, Hennig, Rossberg, Funke, Merroun, Walter	6
20_01_056	EXAFS and XANES studies of technetium and rhenium complexes with relevance to radiopharmaceutical chemistry	Künstler, Seifert, Reich, Funke	FZR	Seifert, Künstler, Rossberg, Hennig	6
20_01_057 EU #14	δ -phase stabilisation in $Pu_xAm_{(1-x)}$ alloys as studied by EXAFS	Baclet	CEA Valduc	Baclet, Valot, Aubert, Joly, Ravat, Gogolusko, Bauer, Hennig	9
20_01_058	Uranium sorption onto chlorite	Krawczyk-Bärsch, Hennig, Bernhard, Arnold, Funke	FZR	Reich, Rossberg, Funke, Hennig	5
20_01_059	EXAFS study of thorium coordination in aqueous perchlorate, chloride, and nitrate solutions	Reich, Tsushima	FZR	Reich, Rossberg, Funke, Hennig	6
20_01_060	EXAFS investigations of uranium complexation by sugar phosphates	Günther, Reich, Rossberg, Koban	FZR	Reich, Rossberg, Funke, Hennig, Walter	2 + 5 + 3
20_01_061	EXAFS investigations of uranium complexation by peptides	Günther, Reich, Rossberg	FZR	Reich, Rossberg, Funke, Hennig	1 + 6
20_01_062 EU #19	Interaction of radionuclides (U, Th, Ra) with natural and synthetic birnessite. Application to radionuclides mobility in natural systems	Manceau, Rihs	LGIT-IRIGM Grenoble	Rhis, Reich	15
20_01_063	EXAFS investigation of Np(V) Carbonato complexes	Reich, Sachs, Schmeide	FZR	Reich, Rossberg, Hennig, Funke, Merroun, S. & T. Stumpf	3
20_01_064	Americium sorption onto ferrihydrite	S. Stumpf, T. Stumpf, Hennig, Funke, Reich, Rossberg	FZR	Reich, Rossberg, Hennig, Funke, Merroun, Moll, S. & T. Stumpf	6 + 3 + 6
20_01_065	Interaction between <i>Pseudomonas sp.</i> and uranium using EXAFS	Merroun, Selenska-Pobell, Reich	FZR	Reich, Rossberg, Hennig, Funke, Merroun, Walter	6 + 3 + 6 + 3
20_01_066	EXAFS investigation of uranium(VI) complexation with phenolic OH groups and carboxylic groups	Rossberg, Geipel, Reich, Hennig, Funke	FZR	Reich, Rossberg, Hennig, Funke, Merroun, Walter	3 + 4 + 6
20_01_067 EU #25	Characterization of uranium oxidation state in calcite and aragonite speleotherms from Aranzadi gallery (La Pierre-Saint-Martin, Pyrénées)	Ortega, Deves, Maire	CNRS Gradignan	Ortega, Deves, Maire, Thomas, Bauer, Rossberg	9
20_01_068 EU #28	EXAFS investigation into the interaction of Ra and Ba with synthetic and biogenic mackinawite	Livens	Uni Manchester	Livens, Charnock, May, Koster, Winkley, Hennig, Bauer	6
20_01_069	Uranium binding of sol-gel immobilised cells and S-layers of <i>Bacillus sphaericus</i> JG-A12 and NCTC9602	Raff, Selenska-Pobell, Funke, Reich, Hennig, Rossberg	FZR	Funke, Rossberg, Reich, Hennig, Raff, Walter, Merroun	6 + 6 + 5

20_01_070 EU #26	Study of the surface complexes formed between uranium and magnetite and between lanthanides and hydroxyapatite	Duro, de Pablo, Bruno, Grivé, Seco	Uni Cerdanyola	Duro, Ferran, Grivé, Bauer, Hennig	12
20_01_600 EU #32	Structural investigation of uranyl in ionic liquids	Gaillard, Billard, Lützenkirchen	IRES, Strasbourg	Billard, Gaillard, Bauer, Rossberg	9
20_01_602 EU #34	Identification of secondary phases formed onto leached ThO ₂ and Th _{1-x} U _x O ₂ solid solutions	Hubert, Purans, Heisbourg	Uni Paris, Orsay	Hubert, Purans, Heisbourg, Bauer, Funke, Hennig	12
20_01_606	Study of the surface complexes formed between uranium and magnetite and between lanthanides and hydroxyapatite	Duro, de Pablo, Bruno, Grivé, Ferran	Uni Cerdanyola	Grivé, Ferran, Funke, Hennig	6
20_01_607 EU #38	XAS study of the PuO _{2+x} oxides	Ripert, Martin, Grandjean, Robisson-Thomas, Petit	CEA Cadarache	Grandjean, Robisson-Thomas, Petit, Rousselle, Bauer, Hennig	6
20_01_609 EU #40	Uranium(III) speciation in ionic liquids	May	Uni Manchester	May, Bhatt, Volkovich, Charnock, Dadds, Bauer, Hennig	9
20_01_610	Grazing incidence XAS measurements of uranium sorbed onto α -Al ₂ O ₃	Hennig, Denecke	FZR, FZK	Hennig, Denecke, Rothe, Rossberg	12
20_01_611	Interaction of actinides with predominant bacteria isolated at nuclear waste repositories using x-ray absorption spectroscopy	Moll, Hennig, Rossberg, Funke, Merroun	FZR	Hennig, Funke, Rossberg, Moll	3
20_01_612	Uranium sorption onto leached layers of feldspar	Walter, Reich, Funke, Hennig, Rossberg	FZR	Hennig, Funke, Rossberg, Moll	12

ESRF allocated time for ROBL-RCH

number	title	proposer	institution	experimentator	shifts
ME-240	Sorption of trivalent lanthanides (Ln(III)) onto hydrous ferric oxide (HFO) and evolution of the sorbed species upon FHO aging	Denecke, Rothe	FZK	Dardenne, Rothe, Rossberg	12
CH-1050	EXAFS/XANES studies on speciation of Tc-99 under reducing conditions	Maes, Van Loon	Uni Leuven	Geraedts, Van Loon, Maes, Bruggeman, Roßberg	9
ME-246	Study of peroxide co-ordination in aqueous sol-gel processing of Ta(V) and Nb(V)	Van Bael, Van Poucke, Mullens, Van Wrede, Nelis, Vanhoyland, Mondelaers	Uni Diepenbeek	Van Bael, Van Wrede, Nelis, Vanhoyland, Mondelaers, Hardy, Bauer	12

ME-312	XAS study of uranium and plutonium local environment in (U,Pu)O ₂ solid solution	Ripert, Martin, Petit, Granjean, Beres, Blanc	CEA Cadarache	Ripert, Carlot, Grandjean, Martin, Robisson-Thomas, Bauer, Roßberg, Hennig	12
HS-1626 <i>coupled with MR</i>	Short range order investigations in the Fe ₇₂ Cr ₂₈ solid solution by combination of EXAFS and differential anomalous x-ray wide-angle scattering	Lauter-Passiouk, Lauter, Kravtsov, Babanov, Sidorenko, Romashev	TU München	Babanov, Reich, Hennig	3 + 9 MRH
ME-308	Uranyl speciation in cement phases	Bonhoure, Tits, Scheidegger, Dähn, Wieland	PSI Villingen	Dähn, Tits, Wieland, Hennig	18
CH-1264	Uranium complexation by adenosine phosphates	Geipel, Bernhard, Hennig	FZR	Geipel, Reich, Funke, Rossberg, Merroun, Hennig	9
ME-394	Solid speciation of plutonium in radioactive particles	Salbu, Janssens, Reich, Lind	Agricultural Univ. Norway	Salbu, Janssens, Lind, Reich, Hennig	12
SI-790	EXAFS/XANES studies on the speciation of reduced technetium-99 in presence of humic substances	Maes, Geraedts, Bruggeman, Van Loon	Uni Leuven	Maes, Bruggeman, Geraedts, Rossberg, Funke	9
CH-1357	Plutonium and neptunium speciation in anaerobic natural groundwater rich in humic substances	Denecke	FZK	Denecke, Panak, Seibert, Dardenne, Rossberg	9
ME-479	EXAFS investigation of the interaction of europium(III) with polyacrylic acid either free or sorbed on alumina	Montavon, Grambow	Subatech	Montavon, Poineau, Rossberg	6
ME-475	Determination of U(VI) uptake mechanisms onto purified Na-illite	Dähn, Bradbury, Bayens	PSI Villingen	Daehn, Wieland, Tits, Kunz, Funke	18

Scheduled experiments at ROBL-MRH

number	title	proposer	institution	experimentator	shifts
20_02_031 long term	Structural changes in N ⁺ -ion implanted Ti-6Al-4V alloys during annealing by <i>in situ</i> x-ray diffraction	F. Berberich, W. Matz, N. Schell	FZR (FWIS)	Berberich, Schell, Klimenkov, Prokert, Scholz	... + 11 + 9
20_02_041	<i>In-situ</i> x-ray diffraction during sputter deposition of TiN and CrN	J. Böttiger, N. Schell	University of Aarhus, FZR (ROBL)	Böttiger, Pakh Andreasen, Petersen, Schell, Rasmussen, Matz	15 + 16
20_02_042	Investigation of the shape of the chemical composition profile in InGaAs/GaAs heterostructures	J. Gaca, M. Wójcik, J. Sass	ITME Warsaw	Gaca, Wójcik, Bauer, Schell	9
20_02_043 EU # 13	Structural study of self-assembled film systems composed of metallic nano-clusters by x-ray grazing-incidence methods	J. B. Pelka, M. Brust, W. Paszkowicz	University of Warsaw (ifpan), University of Liverpool	Pelka, Brust, Paszkowicz, Bauer, Schell	9

20_02_044	SiC synthesis by dual beam ion implantation into silicon: crystallite formation studied by x-ray diffraction	F. Eichhorn, N. Schell, W. Matz, R. Kögler	FZR (FWIS, FWIM)	Eichhorn, Kaschny, Schell	8
20_02_045	Influence of dopant atoms in cubic boron nitride (c-BN) thin films on lattice parameters and intrinsic stress investigated by x-ray diffraction	Th. Halm, V. Linß, T. Pfeifer, W. Hoyer, F. Richter	TU Chemnitz	Halm, Linß, Schell	9
20_02_046	Identification of carbon phases formed by high dose carbon implantation into single crystalline silicon carbide at elevated temperatures	F. Eichhorn, V. Heera, N. Schell, W. Matz	FZR (FWIS, FWIM)	Eichhorn, Schell	12
20_02_047 EU # 12	Phase transformations of multi-layered HTS / dielectric / manganate and HTS / manganate / HTS structures in real-time synchrotron x-ray scattering study	K. Grigorov, A. Spasov, D. Donchev	Institute of Electronics, BAS, Bulgaria	Grigorov, Donchev, Bauer, Berberich	12
20_02_048 EU # 23	Texture measurement on tourmaline	P. Mikula, A. Frischbutter	Nuc. Phys. Inst. (Prague), Geo-for.-zen. Potsdam	Walther, Mikula, Frischbutter, Schell, Bauer	9 + 9
20_02_049 EU # 21	Investigation of the shape of the chemical composition profile in InGaAs/GaAs heterostructures	K. Wieteska, W. Wierzchowski, J. Gaca, M. Wójcik, J. Sass	Inst. Atomic Energy (Swierk), ITME Warsaw	Sass, Mazur, Bauer, Eichhorn, Schell	9
20_02_050 EU # 10	<i>In-situ</i> annealing studies of SiGe nanostructures: x-ray diffraction and GISAXS studies	G. Bauer, V. Holý	University of Linz	Lechner, Zhong, Stangl, Bauer	15
20_02_051	<i>In-situ</i> x-ray diffraction during reactive magnetron sputter deposition of Ti and Cu nanocomposites	J. Böttiger, N. Schell	University of Aarhus, FZR (ROBL)	Böttiger, Pakh Andreassen, Petersen, Jensen, Schell	18 + 18
20_02_052	Phase formation processes in nanoscale nickel layers during heat treatment on different silicon substrates	J. Rinderknecht, Th. Kammler	AMD Saxony Manufacturing Dresden	Rinderknecht, Prinz, Berberich	12
20_02_053	Waveguide-enhanced scattering from thin macromolecular films	T. Salditt, N. Schell	University of Saarland, FZR, FWIS	Jarre, Ollinger, Salditt, Schell	12
20_02_054 long term	Structure investigation of embedded nanoclusters in SiO ₂ films by x-ray diffraction	J. v. Borany, N. Schell	FZR, FWIS	Borany, Eichhorn, Shevchenko, Schell	9
20_02_055	<i>In situ</i> diffraction during high energy sputter deposition of TiAlN and TiN multilayers	S. Mukherjee, N. Schell	FWII, FWIS	Mukherjee, Schell	15
20_02_056	Structural studies of materials for quantum cascade lasers	T. Dekorsy, A. Bauer, F. Eichhorn, N. Georgiev	FWIH, FEW, FWIS	Bauer, Eichhorn, Georgiev	12 + 18
20_02_057 EU # 24	Structural studies of highly strained In _x Ga _{1-x} As/GaAs hetero-structures	J. Sass, K. Mazur, F. Eichhorn	ITME Warsaw, FWIS	Sass, Mazur, Eichhorn, Bauer	9 + 6
20_02_058 EU # 29	Annealing study of SiGe quantum cascade structures grown on relaxed SiGe buffer layers	G. Bauer, J. Stangl, S. Mentese	University of Linz, PSI Villigen	Stangl, Mentese, Diehl, Bauer	18

20_02_059 long term	Influence of interface structure on GMR and magnetic behaviour of Fe/Cr multilayers	F. Prokert, N. Shevchenko	FWIS	Prokert, Shevchenko, Schell	12 + 9
20_02_060 20_02_601	Study of the high temperature stability of a strange titanium-hydrogen phase induced by ion beam implantation	T. Wang, F. Eichhorn	FWIS	Wang, Eichhorn, Schell, Wunderlich (F. & B.)	12
20_02_061 20_02_602 EU # 31	Crystallisation of Ni-Ti thin film Shape Memory Alloy (SMA)	F. M. Braz Fernandes, R. J. Cordeiro Silva, R. Martins, N. Schell	CENIMAT, Campus FCT/UNL, Monte da Caparica, FWIS	Braz Fernandes, Cordeiro Silva, Martins, Schell	12
20_02_062 20_02_600	Structure of organic films grown on semiconductors	A. Das, W. Hoyer, W. Zahn	TU Chemnitz	Das, Halm, Schell	6
20_02_063 20_02_604	<i>In-situ</i> x-ray diffraction during magnetron sputter deposition of nanocrystalline metals (nc Au, Ag, Cu)	N. Schell, J. Böttiger	FWIS, University of Aarhus,	Böttiger, Pakh Andreasen, T. & M. Jensen, Schell, Beckers	25
20_02_064 20_02_605 EU # 30	Structure modifications in materials irradiated by ultra-short pulses of VUV free electron laser	J. Pelka	University of Warsaw (ifpan)	Pelka, Andrejczuk, Reniewicz, Bauer, Schell	12

Beamtime allocation for commissioning at ROBL-MRH

test no.	topic	institute	responsible	experimentator	shifts
01/1	Detector calibration (commissioning)	FWIS	N. Schell, P. Reichel	Schell, Reichel, Kreher	8
01/2 20_02_059	Specular and diffuse reflectivity of single and double layers of Fe, Cr/Co, Cu MBE/PLD-deposited on sapphire/silicon single crystal substrates	FWIS	F. Prokert	Prokert, Schell	9 + 3 + 5
01/3	Commissioning of sputter deposition chamber	FWIS, University of Aarhus	N. Schell, J. Böttiger	Schell, Böttiger, Petersen, Matz, Rasmussen	6
01/4 20_02_IH6	Powder diffraction on uranyl compounds	FWIS, FWRS	Ch. Hennig, F. Prokert, N. Schell	Ch. Hennig, N. Schell	3 + 2 + 6
01/5 20_02_IH5	Structure refinement of 4H-SiC	FWE	A. Bauer	Bauer, Schell	4 +10 + 9
01/6 20_02_057 20_02_IH5	Structure investigations of implanted InGaAs wafers, Ti-Al-V alloys and 4H-SiC	FWE, FWIS	N. Schell, A. Bauer	Bauer, Schell	6
01/7 20_02_056	Investigations of III-V and IV-IV semiconductors	FWE, FWIS, FWIH	A. Bauer	Bauer, Schell, Georgiev	9
01/8 20_02_056	Structural investigations on III-V semiconductors (InGaAs, GaSb)	FEW, FWIS	A. Bauer	Bauer, Schell	5 + 3
02/1	Commissioning of linear PSD	FWIS	N. Schell	Schell	9

02/2 20_02_048	CCD camera tests on tourmaline, quartzite and TiAl	Geo.-For.-zen. Potsdam, FWIS	K. Walther, N. Schell, M. Beckers	Walther, Schell, Beckers, Strauch	18
-------------------	---	------------------------------------	---	--------------------------------------	----

ESRF allocated time for ROBL-MRH

number	title	proposer	institution	experimentator	shifts
SI-622	X-ray investigation of silicon/germanium nanocrystals on silicon carbide	G. Heß, K. Goetz, J. Kräußlich	FSU Jena	Heß, Kräußlich, Wunderlich, Bauer, Schell	12
ME-217	Reflectometry on FeCo single and multilayer	S. Dieter, D. Dantz, A. Pyzalla, W. Reimers	HMI Berlin	Dieter, Poeste, Pyzalla, Schell, Bauer	9
SI- 685	Strain in Si/Ge-nanocrystals	G. Heß, J. Kräußlich, B. Wunderlich	FSU Jena	Heß, Kräußlich, Bauer, Schell, Wunderlich	15
ME-311	Influence of dopant atoms in cubic boron nitride (c-BN) thin films on lattice parameters and intrinsic stress investigated by x-ray diffraction	F. Richter, Th. Halm, W. Hoyer, V. Linss, Th. Pfeifer	TU Chemnitz	Halm, Peter, Schell	15
HS-1626 <i>coupled with RC</i>	Short range order investigations in the Fe ₇₂ Cr ₂₈ solid solution by combination of EXAFS and differential anomalous x-ray wide-angle scattering	V. Lauter- Passiouk, H. Lauter, Y. Babanov, E. Kravtsov, A. Sidorenko, L. Romashev	TU München, ILL, Inst. Met. Phys. (Ekaterin- burg)	Lauter-Passiouk, Babanov, Prokert, Schell	9 + 3 RCH
ME-309	X-ray investigation of Ge- nanocrystallites implanted in SiC	G. Heß, J. Kräußlich, B. & F. Wunderlich	FSU Jena	Kräußlich, Wunderlich, Bauer	12
ME-395	Scanning XRD investigations of strain-induced martensite contribution in fatigued austenitic steel 321	M. Grosse	PSI Villigen	Grosse, Niffenegger, Schell	12
HS-1774	Deformation induced change of grain structure and internal strains in micro-, submicro- and nanocrystalline nickel	E. Thiele, C. Holste, R. Klemm	TU Dresden (IPMK)	Thiele, Klemm, Hollang, Schell	15
ME-393	Characterisation of the oxide layers on bond coats of thermal barrier coatings	W. Reimers, A. Pyzalla, H. Freydank	TU Berlin	Dieter, Freydank, Camin, Bauer, Schell	18
SI-851	XRD of modified Ge- nanocrystals	B. & F. Wunderlich, J. Kräußlich	FSU Jena	Kräußlich, Wunderlich, Bauer	12

List of publications which contain results from experiments at ROBL

2001

Arnault, J.C., Knoll, A., Smigiel, E., and Cornet, A.

Roughness fractal approach of oxidised surfaces by AFM and diffuse x-ray reflectometry measurements

Applied Surface Science **171** (2001) 189-196

Bauer, A., Reischauer, Ph., Kräußlich, J., Schell, N., Matz, W., and Goetz, K.

Structure refinement of the silicon carbide polytypes 4H and 6H: unambiguous determination of the refinement parameters

Acta Cryst. **A57** (2001) 60-67

Berberich, F., Matz, W., Kreißig, U., Schell, N., Richter, E., and Möller, W.

Structural characterisation of hardening of Ti-Al-V alloys after nitridation by plasma immersion ion implantation

Applied Surface Science **179** (2001) 13-19

Bernhard, G., Geipel, G., Reich, T., Brendler, V., Amayri, S., Nitsche, H.

Uranyl(VI) carbonate complex formation: validation of the $\text{Ca}_2\text{UO}_2(\text{CO}_3)_3(\text{aq.})$ species

Radiochim. Acta **89** (2001) 511-518

Bolvin, H., Wahlgreen, U., Moll, H., Reich, T., Geipel, G., Fanghänel, T., and Grenthe, I.

On the structure of Np(VI) and Np(VII) species in alkaline solution studied by EXAFS and quantum chemical methods

J. Phys. Chem. **A 105** (2001) 11441-11445

Dardenne, K., Schaefer, T., Denecke, M. A., Rothe, J., and Kim, J. I.

Identification and characterization of sorbed lutetium species on 2-line ferrihydrite by sorption data modeling, TRLFS and EXAFS

Radiochim. Acta **89** (2001) 469-479

Funke, H., Bernhard, G., Claussner, J., Jansen, K., Matz, W., Nitsche, H., Oehme, W., Reich, T., and Röllig, D.

Technical description of the radiological safety system for X-ray absorption spectroscopy on radioactive samples at the Rossendorf Beamline

Kerntechnik **66** (2001) 195-201

Guerman, K., Reich, T., Sergeant, C., Ortega, R., Tarasov, V., and Simonoff, M.

Technetium metal and pyrometallurgically formed sediments: Study and speciation by Tc NMR and EXAFS/XANES

Pyrochemical Separations: **Workshop Proceedings**, Avignon; France, 14-16 March 2000, OECD/NEA Paris, France (2001) 233-241

Hecker, M., van Loyen, L., Tietjen, D., Schell, N., and Schneider, C. M.

Influence of annealing on structural properties of metallic multilayers

Materials Science Forum **378-381** (2001) 370-375

Hennig, C., Panak, P.J., Reich, T., Roßberg, A., Raff, J., Selenska-Pobell, S., Matz, W., Bucher, J.J., Bernhard, G., and Nitsche, H.

EXAFS investigation of uranium(VI) complexes formed at Bacillus cereus and Bacillus sphaericus surfaces

Radiochim. Acta **89** (2001) 625-631

- Hennig, C., Reich, T., Funke, H., Rossberg, A., Rutsch, M., and Bernhard, G.
EXAFS as a tool for bond-length determination in the environment of heavy atoms
 J. Synchrotron Rad. **8** (2001) 695-697
- Holý, V., Stangl, J., Springholz, G., Pinczolits, M., and Bauer, G.
High-resolution x-ray diffraction from self-organized PbSe/PbEuTe quantum dot superlattices
 Journal of Physics D (Appl. Phys.) **34** (2001) A1-A5
- Matz, W., Schell, N., Neumann, W., Böttiger, J., and Chevallier, J.
A two magnetrons sputter deposition chamber for in situ observation of thin film growth by synchrotron radiation scattering
 Review of Scientific Instruments **72** (2001) 3344-3348
- Moll, H., Reich, T., and Szabó, Z.
The hydrolysis of dioxouranium(VI) investigated using EXAFS and ¹⁷O-NMR
 ESRF Highlights 2000 (2001) 21-22
- Prokert, F., Noetzel, J., Schell, N., Wieser, E., Matz, W., and Gorbunov, A.
Reflectivity and diffraction stud of cross-beam pulsed laser deposited Co/Cu multilayers
 Thin Solid Films **394** (2001) 164-173
- Reich, T., Rossberg, A., Hennig, C., and Reich, G.
Characterization of chromium complexes in chrome tannins, leather, and gelatin using extended X-ray absorption fine structure (EXAFS) spectroscopy
 J. Am. Leather Chem. Assoc. **96** (2001) 133-147
- Schell, N., Matz, W., Prokert, F., Eichhorn, F., and Berberich, F.
Synchrotron radiation studies of thin films and implanted layers with the materials research endstation of ROBL
 Journal of Alloys and Compounds **328** (2001) 105-111
- Schweitz, K.O., Chevallier, J., Böttiger, J., Matz, W., and Schell, N.
Hardness in Ag/Ni, Au/Ni and Cu/Ni multilayers
 Philosophical Magazine A **81** (2001) 2021-2032
- Seifert, S., Künstler, J.-U., Gupta, A., Funke, H., Reich, T., Hennig, C., Rossberg, A., Pietzsch, H.-J., Alberto, R., and Johannsen, B.
EXAFS analyses in radiopharmaceutical research: stability studies of technetium(I) carbonyl complexes in solution
 ESRF Highlights 2000 (2001) 22-23
- Seifert, S., Künstler, J.-U., Gupta, A., Funke, H., Reich, T., Pietzsch, H.-J., Alberto, R., and Johannsen, B.
Reactivity of technetium(I) thioether carbonyl complexes towards histidine – an EXAFS study in solution
 Inorg. Chim. Acta **322** (2001) 79-86
- Sémon, L., Boehme, C., Billard, I., Hennig, C., Lützenkirchen, K., Reich, T., Roßberg, A., Rossini, I., and Wipff, G.
Do perchlorate and triflate anions bind to the uranyl cation in an acidic aqueous medium? A combined EXAFS and quantum mechanical investigation
 Chem. Phys. Chem. **2** (2001) 591-598

Vallet, V., Wahlgren, U., Schimmelpfennig, B., Moll, H., Szabó, Z., and Grenthe, I.
Solvent effects on Uranium(VI) Fluoride and Hydroxide Complexes Studied by EXAFS and Quantum Chemistry
Inorg. Chem. **40** (2001) 3516-3525

2002

Berberich, F., Matz, W., Kreißig, U., Schell, N., and Mücklich, A.
Mechanism of degradation of surface hardening at elevated temperature in TiAlV-alloys by in situ synchrotron radiation diffraction
Nuclear Instruments and Methods B **XX** in press (2002) xx-xx

Böttiger, J., Chevallier, J., Petersen, J.H., Schell, N., Matz, W., and Mücklich, A.
Observation of the growth mode of TiN during magnetron sputtering using synchrotron radiation
Journal of Applied Physics **91** (2002) 5429-5433

Bolvin, H., Wahlgren, U., Moll, H., Reich, T., Geipel, G., Fanghänel, T., and Grenthe, I.
Structure of neptunium(VII) complexes at high pH
ESRF Highlights 2001 (2002) 33-34

Dähn, R., Scheidegger, A.M., Manceau, A., Curti, E., Baeyens, B., Bradbury, M.H., and Chateignert, D.
Th uptake on montmorillonite: a powder and polarized extended x-ray absorption fine structure (EXAFS) study
Journal of Colloid and Interface Science **249** (2002) 8-21

Eichhorn, F., Schell, N., Mücklich, A., Metzger, H., Matz, W., and Kögler, R.
Structural relation between Si and SiC formed by carbon implantation
J. Appl. Phys. **91** (2002) 1287-1292

C. Hennig, G. Reck, T. Reich, A. Roßberg, W. Kraus, and J. Sieler
EXAFS and XRD investigations of zeunerite and meta-zeunerite
Zeitschrift für Kristallographie **217** (2002) 1-9

C. Hennig, T. Reich, R. Dähn, and A.M. Scheidegger
Structure of uranium sorption complexes at montmorillonite edge sites
Radiochim. Acta **90** (2002) 1-5

Klemm, R., Thiele, E., Holste, C., Eckert, J., and Schell, N.
Thermal stability of grain structure and defects in submicrocrystalline and nanocrystalline nickel
Scripta Materialia **46** (2002) 685-690

Linss, V., Halm, T., Hoyer, W., Richter, F., and Schell, N.
Analysis of the biaxial strain state of Al-doped c-BN films using diffraction experiments with synchrotron radiation
Vacuum **XX** in press (2002) xxx-yyy

Martin, P., Ripert, M., Petit, T., Reich, T., Hennig, C., D'Acapito, F., Hazemann, J.L., and Proux O.
A XAS study of the local environments of cations in (U, Ce)O₂
Journal of Nuclear Materials **XX** in press (2002) xxx-yyy

- Merroun, M.L., Hennig, C., Rossberg, A., Geipel, G., Reich, T., and Selenska-Pobell, S.
Molecular and atomic analysis of the uranium complexes formed by three eco-types of Acidithiobacillus ferrooxidans
 Biochem. Sc. Trans. **30** (2002) 669-672
- Merroun, M.L., Hennig, C., Rossberg, A., Reich, T., Nicolai, R., Heise, K-H., and Selenska-Pobell, S.
Characterization of uranium (VI) complexes formed by different bacteria relevant to uranium mining waste piles. In *Uranium in the aquatic environment*, Proceedings of the International Conference Uranium Mining and Hydrogeology III. Merkel, B., Planer-Friedrich, and Wolkersdorfer C. (eds.) Springer Verlag, p. 505-511 (2002)
- Moyes, L.N., Jones, M.J., Reed, W.A., Livens, F.R., Charnock, J.M., Mosselmans, J.F.W., Hennig, C., Vaughan, D.J., and Patrick, R.A.D.
An X-ray absorption spectroscopy study of neptunium(V) reactions with mackinawite (FeS)
 Environ. Sci. Technol. **36** (2002) 179-183
- Pfeiffer, F., Mennicke, U., and Salditt, T.
Waveguide-enhanced scattering from thin biomolecular films
 Journal of Applied Crystallography **35** (2002) 163-167
- Pfeiffer, F., Salditt, T., and David, C.
Reflection of waveguided x-rays in two-dimensional nanostructures
 Journal of Applied Crystallography **35** (2002) 430-433
- Prokert, F., Kravtsov, E., Milayev, M., Romashev, L., Ustinov, V., and Schell, N.
Reflektivitätsuntersuchungen mittels Synchrotronstrahlung an durch MBE erzeugten Fe/Cr-Multischichten
 Zeitschrift für Kristallographie, **Suppl. Issue No. 19** (2002) 58
 Referate (10. Jahrestagung der DGK, 04.-07.03.2002 in Kiel)
- Prokert, F., Noetzel, J., Schell, N., Wieser, E., and Gorbunov, A.
Effect of annealing on the interface structure of cross-beam pulsed laser deposited Co/Cu multilayers
 Thin Solid Films **416/1-2** (2002) 114-121
- Prokert, F., Schell, N., and Gorbunov, A.
Use of anomalous scattering for synchrotron x-ray reflectivity studies of Fe-Cr and Co-Cu double layers
 Nuclear Instruments and Methods B **XX** (2002) xx-xx in press
- Rinderknecht, J., Prinz, H., Kammler, T., Berberich, F., and Zschech, E.
In situ high temperature synchrotron radiation diffraction studies of Ni and Co-Ni silicidation processes
 Microelectronic Engineering **XX** in press (2002) xxx-yyy
- Schell, N., Böttiger, J., Matz, W., and Chevallier, J.
Growth mode and texture development in TiN films during magnetron sputtering – an in situ synchrotron radiation study
 Nuclear Instruments and Methods B **XX** in press (2002) xx-xx
- Schell, N., Matz, W., Böttiger, J., Chevallier, J., and Kringhøj, P.
Development of texture in TiN films by use of in situ synchrotron x-ray scattering
 J. Appl. Phys. **91** (2002) 2037-2044

Schell, N., Böttiger, J., Matz, W., Chevallier, J., Petersen, J., Andreasen, K.P., and Jensen, T. (2002). *New possibilities of characterizing growing sputter-deposited thin films*. Proceedings of the ninth annual international conference on composite engineering (ICCE/9) in San Diego, CA, July 1-6 2002, (sponsored and organized by: International Community for Composites Engineering and College of Engineering, University of New Orleans), ed. Hui, D., p. 697-698

Schell, N., Petersen, J.H., Böttiger, J., Mücklich, A., Chevallier, J., Andreasen, K.P., and Eichhorn, F.

On the development of texture during growth of magnetron-sputtered CrN

Thin Solid Films **XX** in press (2002) xxx-yyy

Sztucki, M., Metzger, T.H., Milita, S., Berberich, F., Schell, N., Rouvière, J.L., and Patel, J

Depth resolved investigations of boron implanted silicon

Nuclear Instruments and Methods B **XX** in press (2002) xx-xx

Thiele, E., Bretschneider, J., Buque, C., Schell, N., Schwab, A., and Holste, C.

Internal strains in single grains of fatigued polycrystalline nickel

Materials Science Forum **404-407** (2002) 823-828

Turos, A., Gaca, J., Wojcik, M., Stonert, A., and Groetzschel, R.

Strain and compositional profile determination in ion bombarded heterostructures by the complementary use of RBS/channeling and high resolution X-ray diffraction

Nuclear Instruments and Methods B **XX** in press (2002) xxx-yyy

Zänker, H., Moll, H., Richter, W., Brendler, V., Hennig, C., Reich, T., Kluge, A., and Hüttig, G.

The colloid chemistry of acidic rock drainage solution from an abandoned Zn-Pb-Ag mine

Applied Geochemistry **17** (2002) 633-648

Personnel of the Project Group ESRF-Beamline

The personnel of the project group comes from different institutes and departments of the FZR.

Head of the Project Group / Spokesperson of the CRG ¹ :	Dr. N. Schell
Local contact at ESRF and responsible for MRH:	Dr. N. Schell
Responsible for RCH at ESRF and for radiation protection ² :	Dr. Ch. Hennig

Staff at ESRF in Grenoble

A. Bauer (-2849)	F. Berberich until 04.2001	Dr. H. Funke from 07.2002 (-2339)
Dr. Ch. Hennig (-2005)	Dr. T. Reich until 03.2002	Dr. A. Roßberg (-2747)
Dr. N. Schell (-2367)	U. Strauch (-2372)	

Postal address:

ROBL-CRG
ESRF / sector 21
BP 220
F-38043 Grenoble Cedex, France

Phone: +33 (0)4 76 88 xx xx
Fax: +33 (0)4 76 88 25 05
e-mail: *surname@esrf.fr*

FZR-personnel working regularly at ROBL

Institute for Ion Beam Physics and Materials Research

M. Beckers from 08.2002	Dr. J. v. Borany	W. Boede
Dr. F. Eichhorn	J. Kreher	Dr. W. Matz until 09.2001
Dr. F. Prokert	A. Scholz	Dr. N. Shevchenko

Institute of Radiochemistry

Dr. S. Amayri	Prof. G. Bernhard	Dr. G. Geipel
Dr. A. Günther	Dr. A. Koban	Dr. E. Krawczyk-Bärsch
Dr. M. Merroun	Dr. H. Moll	Dr. J. Raff
Dr. S. Sachs	Dr. K. Schmeide	Dr. T. Stumpf until 11.2002
S. Stumpf until 11.2002	Dr. J. Tutschku	M. Walter

Institute of Bioanorganic and Radiopharmaceutical Chemistry

Dr. S. Seifert J.-U. Künstler

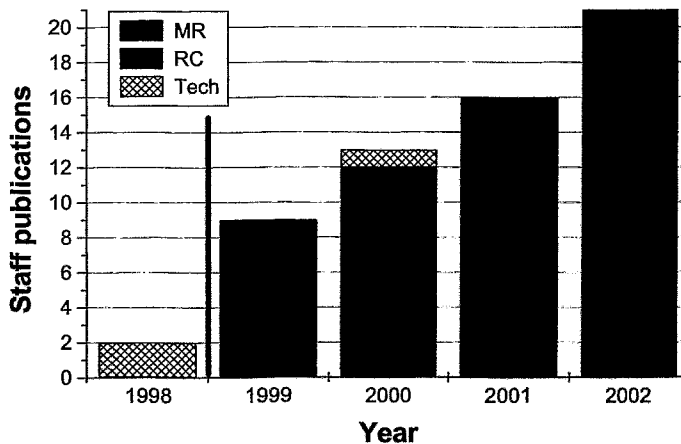
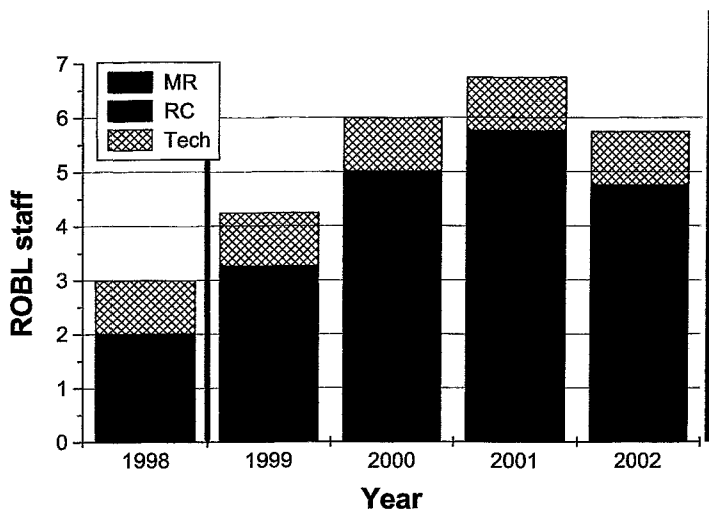
Central Department Experimental Facilities and Information Technology

J. Claußner	S. Dienel	Dr. H. Krug
W. Neumann	Dr. W. Oehme	Dr. D. Pröhl
T. Riedel	R. Schlenk	S. Winkelmann
Y. Zimmermann		


¹ Dr. W. Matz until August 2001 and Dr. T. Reich from September 2001 until March 2002

² Dr. T. Reich until March 2002

The first figure below shows the development of the number of permanent ROBL staff during the last years (and the planned staff for 2003 with three new members to be welcomed in the beginning of the new year 2003). The second figure below gives the number of publications³ with staff (co)authorship (there are additional ones resulting from experiments by external groups and also several internal and highlight reports, for that see the complete publication list above).



³ Due to the deadline of this bi-annual report in mid December 2002, not only published papers but also papers *in press* (2002) are included. Here, as publication is regarded a peer reviewed contribution printed (to be printed) in a scientific journal.

	Experiment title: EXAFS measurements at low temperature	Experiment number: 20_01_19
	Beamline: BM 20	Date of experiment: from: 10.06.2001 to: 11.06.2001
Shifts: 2	Local contact(s): Christoph Hennig	<i>Received at ROBL:</i> 22.11.2002
Names and affiliations of applicants (* indicates experimentalists): C. Hennig*, T. Reich*, H. Funke*, A. Roßberg*, T. Stumpf*, D. Falkenberg* Forschungszentrum Rossendorf e.V., Institute of Radiochemistry, D-01314 Dresden		

Report:

The EXAFS amplitude is influenced by disorder effects, described by the term $\exp(-2\sigma^2 k^2)$ summarising thermal and structural contribution $\sigma^2 = \sigma_{therm}^2 + \sigma_{stat}^2$. Low temperature reduces the temperature dependent part of EXAFS amplitude damping and allows the extension of measurements to a higher k range. As result the Fourier transform shows more backscattering shells and reveals additional details of the structure. This effect was studied on 1 : 1 and 1 : 2 uranyl arsenates.

The As K-edge k^3 -weighted EXAFS spectra of $\text{UO}_2[\text{H}_2\text{AsO}_4]_2 \cdot \text{H}_2\text{O}$ (Fig. 1) at room temperature (298 K) shows that As is surrounded by 4 oxygen atoms in an average distance of 1.69 Å indicating a $[\text{AsO}_4]$ tetrahedron. The measurement at 15 K shows that each $[\text{AsO}_4]$ tetrahedron is surrounded by two uranium atoms at a distance of 3.71 Å, not clear visible at 298 K. The observed bond length proofs a monodentate connection between the arsenate and the uranyl polyhedra. The EXAFS spectra of $\text{H}[\text{UO}_2\text{AsO}_4] \cdot 4\text{H}_2\text{O}$ (Fig. 2) shows already at room temperature an As backscattering shell. With a reduced temperature of 41 K there are indicated 4 uranium atoms at a As-U distance of 3.71 Å around the $[\text{AsO}_4]$ tetrahedron [1,2].

[1] Hennig, C. et al., J. Synchrotron Rad. **8** (2001) 695-697

[2] Hennig, C. et al., Z. Krist., in press

Tab. 1: EXAFS parameters of As K-edge measurements

	Shell	R [Å]	N	σ^2 [Å ²]	ΔE [eV]
$\text{UO}_2[\text{H}_2\text{AsO}_4]_2 \cdot \text{H}_2\text{O}$	As-O	1.69	4.2(1)	0.0016	-4.9
	(T = 15 K) As-U	3.71	1.9(2)	0.0029	-11.0
$\text{H}[\text{UO}_2\text{AsO}_4] \cdot 4\text{H}_2\text{O}$	As-O	1.69	3.8(1)	0.0017	-5.1
	(T = 41 K) As-U	3.71	4.2(1)	0.0021	-9.7
	As-As	5.06	3.7(1)	0.0029	-6.6

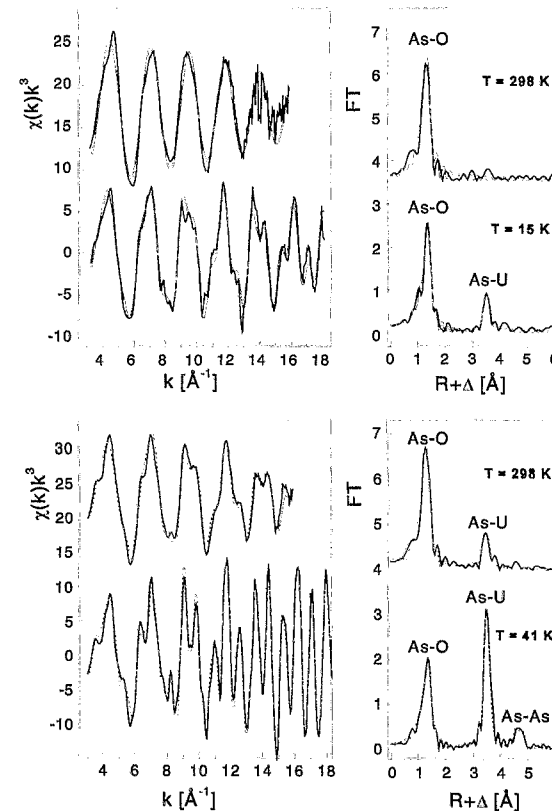



Fig. 1: As K-edge EXAFS spectra of $\text{H}[\text{UO}_2\text{AsO}_4] \cdot 4\text{H}_2\text{O}$ (on the left) and their Fourier transform (on the right).

Fig. 2: As K-edge k^3 -weighted EXAFS spectra of $\text{UO}_2[\text{H}_2\text{AsO}_4]_2 \cdot \text{H}_2\text{O}$.

 ROBL-CRG	Experiment title: EXAFS Study on Np(V) Complexes with Humic Acids of Different Functionalities	Experiment number: 20_01_22
	Beamline: BM 20	Date of experiment: from: 17.02.01 to: 19.02.01 from: 20.02.02 to: 21.02.02
Shifts: 7	Local contact(s): Tobias Reich	<i>Received at ROBL:</i> 17.10.2002
Names and affiliations of applicants (* indicates experimentalists): S. Sachs, K. Schmeide, T. Reich*, C. Hennig*, H. Funke*, A. Roßberg*, H. Moll*, M. Walter*, K.H. Heise, G. Bernhard Forschungszentrum Rossendorf e.V., Institute of Radiochemistry, P.O. Box 510 119, D-01314 Dresden		

Report:

In continuation of our studies described in /1/, we investigated Np(V) complexes with humic acids (HA) of different functionalities by EXAFS. We studied Np(V) complexes from commercially available natural HA from Aldrich (AHA), synthetic HA type M42, which shows a carboxyl group content comparable to natural HA /2/ and synthetic HA type M1 which has a low amount of carboxyl groups, however, a high ratio of phenolic OH to carboxyl groups /2/. In order to elucidate the influence of phenolic/acidic OH groups on the interaction between HA and Np(V), we studied Np(V) humates of modified HA Aldrich (AHA-PB), M42 (M42-PB) and M1 (M1-PB) with blocked phenolic/acidic OH groups /3/. The modified HA show phenolic/acidic OH group contents that are 62-75 % smaller than those of the original HA. Np(V) humate solutions were prepared under N₂ at pH 7 with Np and HA concentrations of 0.88–1.04 mmol/L and 8.1–27.5 g/L, respectively (0.1 M NaClO₄). Np L_{III}-edge EXAFS spectra were recorded at ROBL at room temperature in fluorescence mode.

Tab. 1: Structural parameters of Np(V) samples. (N_{ax}=const during fit).

Sample	Np-O _{ax}			Np-O _{eq}			ΔE ₀ (eV)
	N	R (Å)	σ ² (Å ²)	N	R (Å)	σ ² (Å ²)	
Np(V)-AHA	2	1.85 ± 0.01	0.0023	2.6 ± 0.8	2.49 ± 0.01	0.0040	-8.1
Np(V)-AHA-PB	2	1.85 ± 0.01	0.0030	2.7 ± 0.8	2.49 ± 0.01	0.0048	-8.1
Np(V)-M1	2	1.85 ± 0.01	0.0044	2.4 ± 0.8	2.49 ± 0.01	0.0050	-6.8
Np(V)-M1-PB	2	1.85 ± 0.01	0.0033	2.5 ± 0.8	2.50 ± 0.01	0.0040	-7.8
Np(V)-M42	2	1.84 ± 0.01	0.0029	2.4 ± 0.7	2.49 ± 0.01	0.0023	-9.2
Np(V)-M42-PB	2	1.84 ± 0.01	0.0026	2.7 ± 0.7	2.50 ± 0.01	0.0030	-9.6
Np(V)-Bio-Rex70 /1/	2	1.85 ± 0.01	0.0032	2.8 ± 0.5	2.50 ± 0.01	0.0044	-8.2
NpO ₂ (H ₂ O) ₂ ⁺ /4/	2	1.81 ± 0.01	0.0034	3.3 ± 0.4	2.49 ± 0.01	0.0051	-9.7

The Np L_{III}-edge k³-weighted EXAFS oscillations of Np(V) humates and their Fourier transforms (FT) are shown in Fig. 1 in comparison to a Np(V) sorbate with Bio-Rex70 (cation exchange resin having only carboxyl groups as proton exchanging sites) /1/ and Np(V) hydrate /4/. The EXAFS oscillations were fitted to the EXAFS equation with two oxygen coordination shells and including multiple scattering along the NpO₂⁺ unit. The data are summarized in Tab. 1.

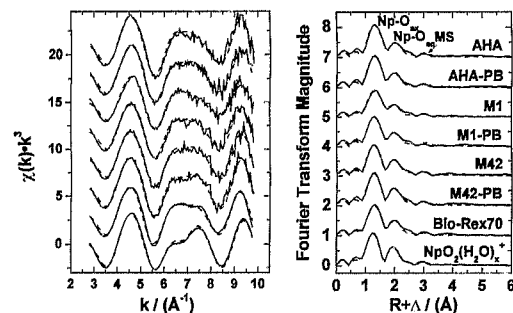


Fig. 1: Np L_{III}-edge k³-weighted EXAFS spectra and FT of Np(V) samples. Solid lines: experiment, dashed lines: fit, MS: multiple scattering.


The axial (ax) and equatorial (eq) coordination numbers (N) and bond lengths (R) for all Np(V) humates are comparable with each other as well as with the data of Np(V)-Bio-Rex70. Within the experimental error the equatorial data of Np(V) humates are also comparable to those of Np(V) hydrate. For all samples, also for Np(V) hydrate, we obtained smaller N_{eq} values compared to the theoretically expected value of 5, which cannot be explained up to now.

From our results we conclude, that the complexation of Np(V) by HA, which was confirmed by NIR spectroscopy, induces no shortening of R_{Np-O_{eq}}. The blocking of HA phenolic/acidic OH groups has no influence on coordination numbers and bond lengths in Np(V) humates. The similar structural parameters of Np(V) humates and Np(V)-Bio-Rex70 indicate that HA carboxylate groups dominate the interaction between HA and Np(V). However, the determined parameters represent averages over all interactions between HA and Np(V). Phenolic OH groups interacting with Np(V) could show R_{Np-O_{eq}} values similar to those of carboxylate groups. Thus, a contribution of phenolic/acidic OH groups to the complexation of Np(V) by HA cannot entirely be excluded.

Acknowledgment: This work was supported by BMWi (no. 02E9299).

References

- /1/ Pompe, S. et al., Report FZR-322, Rossendorf 2001, p. 62
- /2/ Pompe, S. et al., Report FZR-290, Rossendorf 2000.
- /3/ Pompe, S. et al., Radiochim. Acta **88**, 553 (2000).
- /4/ Reich, T. et al., Radiochim. Acta **88**, 633 (2000).

 ROBL-CRG	Experiment title: Polarized EXAFS measurements at uranyl sorbed montmorillonite	Experiment number: 20_01_24
	Beamline: BM 20	Date of experiment: from: 06.07.01 to: 08.07.01 from: 03.12.01 to: 04.12.01 from: 30.03.02 to: 31.03.02 from: 11.05.02 to: 12.05.02 from: 23.06.02 to: 23.06.02 from: 26.06.02 to: 28.06.02 from: 15.09.02 to: 17.09.02
Shifts: 31	Local contact(s): Christoph Hennig	<i>Received at ROBL:</i> 24.1.2002
Names and affiliations of applicants (* indicates experimentalists): C. Hennig*, T. Reich*, H. Funke*, A. Roßberg*, T. Stumpf*, S. Stumpf*, H. Moll*, M. Merroun*, J. Raff* Forschungszentrum Rossendorf e.V., Institute of Radiochemistry, D-01314 Dresden		

Report:

Variations in pH affect both the uranyl solution speciation and the preferred type of sorption sites on the montmorillonite surface. Exchange processes with interlayer cations are evoked by permanent negative layer charge. Al and Si atoms exposed to the crystallite edges are partially hydrolyzed to silanol (SiOH) and aluminol (AlOH) groups. These unsaturated edge sites are much more reactive than the saturated basal sites.

Uranium L_{III} -edge EXAFS spectra of the uranyl treated montmorillonite are shown in Fig. 1. Depending on the reaction conditions, the distances between the $U-O_{ax}$ pair vary slightly between 2.34 Å and 2.37 Å. These distances are far from values for mononuclear outer-sphere uranyl aquo-complexes with $U-O_{eq}$ distances between 2.41 Å–2.43 Å obtained at lower pH values.

The FT of all samples shows a peak at $R_{+1} \approx 3.0$ Å. This peak has the characteristic shape of the Al or Si amplitude function, but it is impossible to distinguish between Al and Si because of their similar scattering amplitude functions. Furthermore, this peak is a superposition of multiple-scattering effects of the $U-O_{ax}$ shell and single scattering contribution from the substrate. The best approach is a fit with Si or Al including fixed Debye-Waller factors together with the constrained parameters of the $U-O_{ax}$ MS contribution. This procedure gives distances of approximately 3.40–3.44 Å and a coordination number between 0.5

and 0.8 (Tab. 1). Calculations of structure models show that this peak originates from a preferred sorption to the aluminol edge sites by an inner-sphere, mononuclear complexation mechanism in bidentate fashion [1]. The polarization dependency of this EXAFS signal is weak [2].

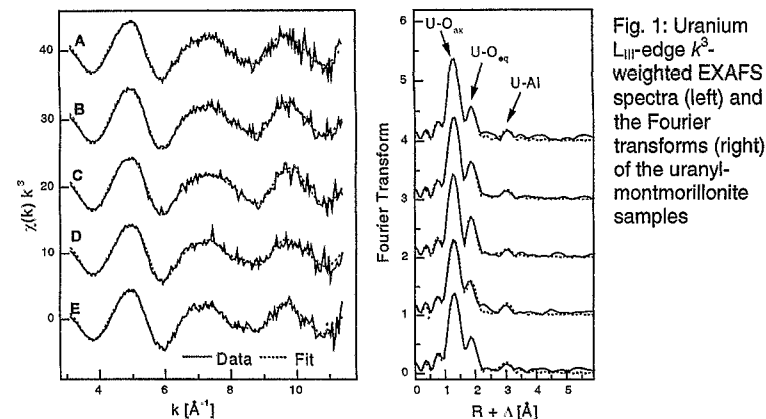



Fig. 1: Uranium L_{III} -edge k^3 -weighted EXAFS spectra (left) and the Fourier transforms (right) of the uranyl-montmorillonite samples

Tab. 1: EXAFS structural parameters

	pH _{final}	[NaClO ₄]	[UO ₂ ²⁺] _{init}	Shell	R [Å]	N	σ ² [Å ²]	ΔE ₀	Error
A	5.02	0.1	5.04·10 ⁻⁵	U-O _{ax}	1.78	2.0(2)	0.0026	0.4	0.50
				U-O _{eq}	2.36	6.2(15)	0.017		
				U-Al	3.43	0.6(2)	0.003*		
B	5.14	0.1	8.40·10 ⁻⁵	U-O _{ax}	1.78	2.0(2)	0.0022	0.2	0.26
				U-O _{eq}	2.36	6.1(8)	0.015		
				U-Al	3.43	0.5(2)	0.003*		
C	5.17	0.01	5.04·10 ⁻⁵	U-O _{ax}	1.77	1.9(2)	0.0016	0.5	0.34
				U-O _{eq}	2.37	5.7(8)	0.014		
				U-Al	3.44	0.5(2)	0.003*		
D	5.98	0.1	5.04·10 ⁻⁵	U-O _{ax}	1.77	2.0(2)	0.0033	0.4	0.41
				U-O _{eq}	2.35	5.9(7)	0.015		
				U-Al	3.41	0.8(2)	0.003*		
E	7.08	0.1	5.04·10 ⁻⁵	U-O _{ax}	1.78	1.9(2)	0.0021	-0.1	0.33
				U-O _{eq}	2.34	5.8(9)	0.013		
				U-Al	3.40	0.6(2)	0.003*		

[1] Hennig, C., Reich, T., Dähn, R., Scheidegger, A.M., Structure of uranium sorption complexes at montmorillonite edge sites, Radiochim. Acta, in press

[2] Hennig, C., et al., FZR Bi-Annual Report 1999/2000, p. 65

 ROBL-CRG	Experiment title: Structural Study of Pu(III) Complexes with Humic Substances and BioRex70	Experiment number: 20_01_27
	Beamline: BM 20	Date of experiment: from: 06.06.2001 to: 07.06.2001
Shifts: 3	Local contact(s): Tobias Reich	<i>Received at ROBL:</i> 17.10.2002
Names and affiliations of applicants (* indicates experimentalists): K. Schmeide, S. Sachs, G. Geipel, T. Reich*, C. Hennig*, H. Funke*, A. Roßberg*, T. Stumpf*, D. Falkenberg*, K.H. Heise, G. Bernhard Forschungszentrum Rossendorf e.V., Institute of Radiochemistry, P.O.Box 510119, D-01314 Dresden, Germany		

Report:

The near-neighbor surrounding of Pu(III) sorbed onto humic substances was studied at pH 1 by XAFS spectroscopy. The results are compared with literature data of Pu(III) and Pu(IV) hydrates.

Introduction: The objective was to investigate the structure of Pu(III) in complexes with humic substances. Our previous XAFS study /1/ had shown that part of the Pu(III) humate was oxidized to Pu(IV). Therefore, we repeated this experiment under improved conditions. For the sample preparation, the pH value was lowered from 2 to 1. The samples were sealed in PE cuvettes and transported to Grenoble under N₂ atmosphere.

Experimental: Pu(IV) was electrochemically reduced to Pu(III). Pu(III) samples were prepared from Kranichsee fulvic acid (KFA) and from synthetic humic acid type M42 at pH 1 (0.1 M HClO₄) under inert gas conditions. The Pu loading of the resulting wet pastes of KFA and M42 was 11.6 and 10.7 mg Pu per g sorbent, respectively. Pu L_{III}-edge XAFS spectra were collected in fluorescence mode at the Rossendorf Beamline at the ESRF in Grenoble.

Results: The trivalent oxidation state of Pu and its stability in the complexes with humic substances within the time of the experiment is verified by XANES spectroscopy. In Fig. 1, the XANES spectra of Pu(III)-KFA and Pu(III)-M42 are shown in comparison to that of Pu(III) hydrate. The energy scale of the spectra was calibrated with a Zr metal foil (Zr K edge at 17998 eV). The edge energy of the three spectra is identical (Pu(III) hydrate: 18059.0 eV, Pu(III) humates: 18059.2 eV). This confirms that the humate complexes contain exclusively Pu(III). The Pu L_{III}-edge k²-weighted EXAFS spectra of the Pu(III) humates and corresponding Fourier transforms (FTs) are shown in

Fig. 2. Both the EXAFS oscillations and the FTs of the samples are similar. The FTs indicate a single coordination shell (Pu-O) arising from the ligands.

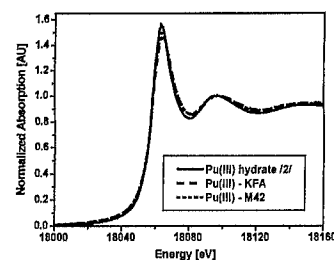


Fig. 1: Normalized Pu L_{III}-edge XANES spectra.

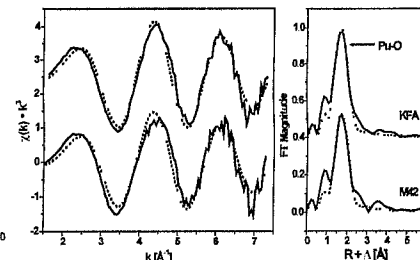


Fig. 2: Raw Pu L_{III}-edge k²-weighted EXAFS spectra and corresponding Fourier transforms of Pu(III) samples (without phase corrections). Solid lines: experiment, dashed lines: fit.

The structural parameters given in Tab. 1 agree with the conclusion drawn from the XANES spectra. The Pu-O bond length in the Pu(III) humate complexes is significantly longer than that of Pu(IV) hydrate. Furthermore, no evidence for the formation of polynuclear Pu(IV) species was found in the EXAFS spectra.

Tab. 1: Structural parameters of Pu samples

Sample	Shell	N	R [Å]	σ ² [Å ²]	E ₀ [eV]
Pu(III)-KFA	Pu-O	7.3±1.2	2.45±0.02	0.0150	-17.3
Pu(III)-M42	Pu-O	6.1±1.4	2.45±0.02	0.0137	-17.0
Pu(III)-nH ₂ O /2/	Pu-O	7.6±0.6	2.48±0.01	0.0102	-16.8
Pu(IV)-nH ₂ O /3/	Pu-O	8	2.39	0.0118	

The 95 % confidence limits are given for N and R as estimated by EXAFSPAK.

Within the experimental error, the coordination numbers determined for the Pu-O shell of the humate complexes agree well with the value reported for the hydrated Pu(III) aquo ion in 1 M HClO₄ /2/. The bond lengths determined for the Pu(III) humate complexes are 0.03 Å shorter than for the Pu(III) hydrate. A similar shortening of the bond length has been observed for U(VI) and Np(IV) humates /4, 5/ upon complexation of these actinides with the functional groups (predominantly -COOH) of the humic substances.

Acknowledgment: This work was supported by the BMWI (No. 02 E 9299).

References: /1/ Schmeide, K., et al., Report FZR-318, 16 (2001); /2/ Reich, T., et al., Report FZR-285, 72 (2000); /3/ Ankudinov, A.L., et al., Phys. Rev. B57, 7518 (1998); /4/ De-necke, M., et al., Radiochim. Acta 82, 103 (1998); /5/ Schmeide, K., et al., Report FZR-318, 14 (2001).

	Experiment title: EXAFS investigation on uranium uptake by plants	Experiment number: 20_01_30
	Beamline: BM 20	Date of experiment: from: 24.02.01 to: 25.02.01 from: 04.07.01 to: 06.07.01
Shifts: 9	Local contact(s): Tobias Reich, André Roßberg	Received at ROBL: 06.11.2002
Names and affiliations of applicants (* indicates experimentalists): A. Günther ¹ , G. Bernhard ¹ , G. Geipel ¹ , T. Reich ^{*2} , A. Rossberg ^{*2} , C. Hennig ^{*2} , H. Funke ^{*2} , H. Moll ^{*1} , S. Amayri ^{*1} , M. Walter ^{*1} ¹ Forschungszentrum Rossendorf e.V., Institute for Radiochemistry, P.O. Box 510119, 01314 Dresden, Germany ² ESRF-ROBL/CRG, Avenue des Matyrns, B.P. 220, 38043 Grenoble Cedex, France		

Report:

Experimental: For the determination of the uranium speciation in plants we have investigated fresh hydroponic samples of lupine after uptake of uranium (VI). The lupine plants, grown in uncontaminated soil, were transferred to uranium containing hydroponic solutions (pH 3 and 5). The uranium concentration in these solutions was $1.0 \cdot 10^{-3}$ M. After harvesting, the plants were washed, separated into roots, shoot axis, leaves and cut into small pieces. The U L_{III}-edge EXAFS spectra of the plant samples were recorded in fluorescent mode using a 4-pixel-germanium detector. The EXAFS spectra were analyzed according to standard procedures using the suite of programs EXAFSPAK /1/. The theoretical scattering phases and amplitudes were calculated with the scattering code FEFF8 /2/.

Results and discussion: The figure shows the raw U-L_{III}-edge k^3 -weighted EXAFS spectra and their corresponding Fourier transforms (FT) of the plant samples. Four peaks are visible in the FT. The fit results are listed in tables 1 and 2. The first and the second peak correspond to the scattering contribution of the two axial oxygen atoms (O_{ax}) of the uranium(VI) ion and the scattering contribution of the equatorial oxygen atoms ($O_{eq(1)}$) (major components). The data are comparable with structural parameters of meta- autunite and of the uranium biomass system too /3/. For the determination of structural parameters of the minor components (third and fourth peak in the spectra) we used the difference technique described in /4/. We assume for the third peak a backscattering equatorial oxygen atom $O_{eq(2)}$. The more important result of these measurements is the identification of the uranyl-phosphorus-

coordination in combination of a multiple scattering path (fourth peak) in the U(VI)-species in the plant samples. The uranium-phosphorus distance is in the range of 3.6 Å and corresponds to those observed for uranyl phosphates and uranium/bacillus sphaericus biomass system /3/.

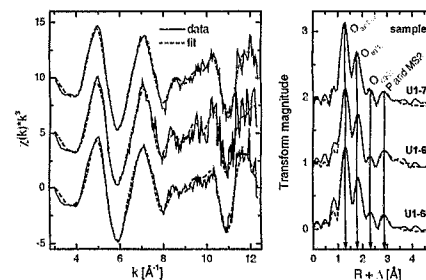


Fig.

Raw U L_{III}-edge k^3 -weighted EXAFS spectra (left) and their corresponding Fourier transform (right) of the fresh lupine samples (hydroponics)

Tab. 1: EXAFS structural parameters of the major components (O_{ax} , $O_{eq(1)}$) of the uranium species in fresh lupine samples

Sample	U - O_{ax}		U - $O_{eq(1)}$		$-\Delta E_0$		
	R	σ^2	N	R			
Hydroponics $1.0 \cdot 10^{-3}$ M U(VI), pH 3.0	U1-68 root	1.788(3)	2.1(2)	3.4(3)	2.302(4)	3.1(6)	16.7(8)
	U1-69 shoot axis	1.771(5)	2.9(3)	4.7(6)	2.283(7)	5.3(9)	20(1)
Hydroponics $1.0 \cdot 10^{-3}$ M U(VI), pH 5.0	U1-70 root	1.769(3)	2.6(2)	4.2(3)	2.278(4)	4.3(5)	20.3(8)


Tab. 2: EXAFS structural parameters of the minor components ($O_{eq(2)}$, P, MS2: U- $O_{eq(2)}$ -P) of the uranium species in fresh lupine samples

Sample	U - $O_{eq(2)}$		U - P		MS2: U - $O_{eq(1)}$ - P			
	N	R	N_p	R	σ^2	2- N_p	R	
U1-68	0.90(4)	2.863(3)	4.5(6)	3.632(4)	3.9(4)	9	3.746(7)	3.7(4)
U1-69	0.76(7)	2.820(5)	5.4(9)	3.623(4)	3.3(4)	10.8	3.734(9)	3.9(6)
U1-70	0.59(5)	2.868(5)	5.0(8)	3.604(4)	5.3(4)	10	3.716(9)	6.6(7)

(Table 1 and 2: Standard deviations are given in parenthesis)

References

- George, G. N., Pickering, I. J.: EXAFSPAK - A Suite of Computer Programs for Analysis of X-Ray Absorption Spectra, Stanford Synchrotron Radiation Laboratory, Stanford, CA, USA, (1995)
- Ankudinov, A.L. et al.: Real-space multiple scattering calculation and interpretation of x-ray absorption near-edge structure, Phys. Rev. B 58 7565-7576 (1998)
- Hennig, C. et al.: EXAFS investigation of uranium(VI) complexes formed at Bacillus cereus and Bacillus sphaericus surfaces, Radiochimica Acta 89, 625 (2001)
- Teo, B. K.: EXAFS - Basic Principles and Data Analysis, Springer-Verlag, New York 1986

	Experiment title: X-ray absorption spectroscopy investigation on uranyl complexes with α -substituted carboxylic acids	Experiment number: 20_01_31
	Beamline: BM 20	Date of experiment: from: 22.02.01 to: 24.02.01
Shifts: 6	Local contact(s): Tobias Reich	<i>Received at ROBL:</i> 29.10.2002
Names and affiliations of applicants (* indicates experimentalists): H. Moll*, T. Reich*, C. Hennig*, H. Funke*, S. Amayri*, A. Rossberg*, M. Walter*, Th. Fanghänel		

Report:

The aim of this EXAFS investigation was to study the structural changes of aqueous uranium(VI) complexes with glycolic acid and α -hydroxyisobutyric acid as a function of pH. It is known that organic ligands having an α -OH-group can form chelates even at low pH. Details of sample preparation and complementary investigations using UV-vis and TRLSFS can be found in /1/.

Table Summary of sample conditions and EXAFS structural parameters. H₂Gly: glycolic acid, H₂I_BA: α -hydroxyisobutyric acid, †: fixed during the fit.

Sample	Shell	N	σ^2 (Å ²)	R (Å)
A 0.01M U(VI), 1M H ₂ Gly, pH=3.7	U-O _{ax}	2 [†]	0.0014	1.78
	U-O _{eq}	5.4	0.0124	2.38
B 0.02M U(VI), 0.25M H ₂ Gly, pH=5.0	U-O _{ax}	2 [†]	0.0015	1.79
	U-O _{eq1}	4.8	0.0098	2.37
	U-C	1.5	0.0035	3.24
C 0.02M U(VI), 0.25M H ₂ Gly, pH=8.0	U-O _{ax}	2 [†]	0.0015	1.80
	U-O _{eq}	5.5	0.0150	2.37
	U-C	1.7	0.0046	3.25
	U-U	1.4	0.0037	3.81
D 0.01M U(VI), 0.6M H ₂ I _B A, pH=4.0	U-O _{ax}	2 [†]	0.0017	1.78
	U-O _{eq}	5.4	0.0115	2.43
	U-C	2.7	0.0082	2.89
E 0.01M U(VI), 0.6M H ₂ I _B A, pH=6.5	U-O _{ax}	2 [†]	0.0014	1.79
	U-O _{eq}	4.7	0.0137	2.37
	U-C	1.8	0.0020	3.25
F 0.01M U(VI), 0.6M H ₂ I _B A, pH=8.0	U-O _{ax}	2 [†]	0.0012	1.80
	U-O _{eq}	4.4	0.0127	2.36
	U-C	2.6	0.0023	3.25

The U-O_{eq} distance is an indicator for the coordination mode of carboxylate ligands to the uranyl center. For sample A at pH 3.7 (see Table) we

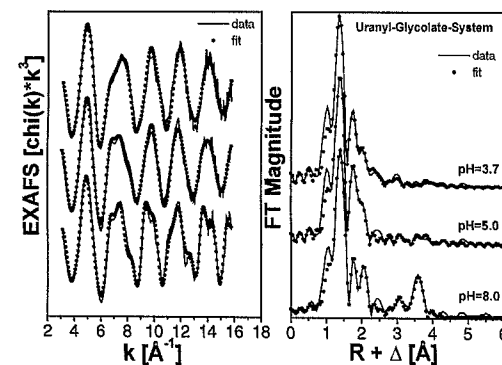
measured a U-O_{eq} distance of 2.38 Å. This value is shorter than expected for a bidentate coordination of the carboxylic group via both carboxylate oxygens. An additional indicator of unidentate coordination is the absence of a carbon shell around 2.90 Å. In contrast to the glycolate system, we observed a longer U-O_{eq} bond distance of 2.43 Å and a U-C interaction at 2.87 Å at pH 4 in the α -hydroxyisobutyrate system (sample D). Furthermore, we found evidence for a multiple-scattering path, presumably U-C-C, at 4.4 Å. The U-O_{eq} distance, 2.36 – 2.37 Å, measured in the near neutral and alkaline pH region for samples B, E, and F is a strong indication for the formation of chelate complexes due to the deprotonation of the α -OH-group of the ligand. In contrast to the α -hydroxyisobutyrate system, the EXAFS data from the glycolate system in the pH range 5.5 to 11 contain a feature at 3.81 Å which could be fit as U-U interaction (see Figure). This implies formation of a dimeric species, most likely similar to $[(\text{UO}_2)_2(\text{OCH}_2\text{COO})_2\text{F}_4]^{4-}/2$, where the oxo-group is bridging two uranium atoms and where the fluorides are replaced by a chelated $(\text{OCH}_2\text{COO})^{2-}$.

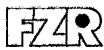
Acknowledgements. This work was supported by the European Commission within the Human Potential Program under contract number HPMF-CT-1999-00342.

References

- /1/ Moll, H., et al., *Uranyl complexes with alpha-substituted carboxylic acids in aqueous solution*, Radiochim. Acta, in press (2002).
 /2/ Farkas, I., et al., Acta Chem. Scand. **53**, 1009 (1999).

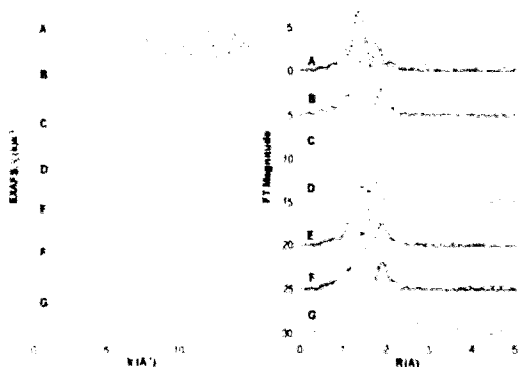
Figure Raw U L_{III}-edge k³-weighted EXAFS spectra and corresponding Fourier transforms measured in the uranyl glycolate system (sample A – C) including the best theoretical fits.



 ROBL-CRG	Experiment title: Interaction of radionuclides (U, Th, Ra) with natural and synthetic birnessite. Application to radionuclides mobility in natural systems.	Experiment number: 20_01_33 20_01_62 EU #19
	Beamline: BM 20	Date of experiment: from: 31.01.02 to: 05.02.02
Shifts: 15	Local contact(s): Tobias Reich	<i>Received at</i> ROBL:03.10.2002
Names and affiliations of applicants (* indicates experimentalists): *Sophie Rihs – Centre de Géochimie de la Surface - Strasbourg *Jean Riotte – Centre de Géochimie de la Surface - Strasbourg Alain Manceau – Laboratoire Géophysique interne et tectonophysique - Grenoble		

Report: Our long-term objective is to study in detail the adsorption processes of several radionuclides (U, Th, Ra) on birnessite, the most common Mn-oxides in soils. Indeed, the affinity of these nuclides for Mn-oxides has been widely reported. Thus, neglecting their influence in natural systems would yield to significant errors in predicting radionuclides transport. Among these nuclides, focus has been placed first on U in 2001 and 2002.

EXAFS measurements on U^{VI} sorbed synthetic birnessites were performed at the ESRF beamline BM20. These birnessites were reacted with U^{VI} solutions for various experimental conditions (see the table caption). Birnessite is a phyllosilicate characterized by edge-sharing Mn octahedra layers, separated by interlayer spaces filled with cations. A change in the interlayer spacing from 10Å to 7Å occurs when the solution pH decreases from basic to acidic [1]. For all except one experiments, U^{VI} was added to the solutions after the birnessite equilibration at pH 4 or 6, i.e. when mineral interlayer space = 7Å. For one experiment (sample A), U^{VI} was added before this equilibration (i.e. when mineral interlayer space = 10Å), then interlayer space decreased when decreasing the pH to 4.



U-L_{III} EXAFS spectra and their Fourier Transforms for U^{VI} sorbed on birnessite. Aqueous initial [U] concentration = $1.2 \cdot 10^{-5}$ M. Unless notified, U^{VI} was added to the solution after the birnessite equilibration to the aimed pH. Dashed lines are fits.

(A) pH 4, 0.1M $NaClO_4$, U^{VI} added before birnessite equilibration, [U]_{sorbed} = 867 ppm; (B) pH 4, 0.1M $NaClO_4$, [U]_{sorbed} = 500 ppm; (C) pH 6, 0.1M $NaClO_4$, [U]_{sorbed} = 980 ppm; (D) pH 6, 0.1M Na_2CO_3 , [U]_{sorbed} = 830 ppm; (E) pH 6,

0.1M $NaNO_3$, [U]_{sorbed} = 1230 ppm; (F) pH 4, 0.1M $NaNO_3$, [U]_{sorbed} = 1200 ppm; (G) $UO_2(NO_3)_2 \cdot 6H_2O$ model compound.

Fitting of the two first shells of U neighbors (axial and equatorial Oxygen atoms) of these spectra was performed. The theoretical modelling code FEFF8 was used to calculate the backscattering phases and amplitudes of the individual neighboring atoms. Results of these fits show a U-O_{eq} distance ranging from 2.31 to 2.35 Å, apart from the sorption experimental conditions. Analysis of the contribution from more distal neighbours has not been completed yet.


The distinct FTs shapes, and different sorbed [U^{VI}] concentrations shown by samples for which the same U^{VI} amount was added before or after birnessite equilibration (samples A and B), suggest that at least two different types of sorption sites are available on birnessite: within the cationic interlayer space and on edge sites. However, U^{VI} seems less able to enter the 7Å interlayer space sites (after low-pH mineral equilibration), and hence edge sites are probably the main sites during sorption at low pH. This is in agreement with complementary sorption experiments performed in our lab. The inability to fit our experimental sorption data with a Langmuir type isotherm (which assumes a single sorption site with a finite concentration) also suggests that the surface sites available for U^{VI} on birnessite are heterogeneous and/or not of finite concentration.

Another striking feature of our results is the influence of electrolyte background. Samples C and D show no difference in FTs distribution, despite completely different aqueous U^{VI} speciation ($\geq 96\%$ uranyl-hydroxyl complexes in sample C and 100% uranyl-carbonate complexes in sample D). In contrast, samples in $NaNO_3$ media (E and F) shows a consistent difference (whatever the pH), with disappearance of the peak at $R+\Delta R = 3.2$ Å, although the main U^{VI} dissolved species are similar than in $NaClO_4$ samples (uranyl-nitrate complexes represent less than 7% in $NaNO_3$ media). Complete analysis of the more distal neighbour will be needed to elucidate this feature, but possible minority uranyl-nitrate outer-sphere sorption will be tested. In contrast, the U-O_{eq} distance of 2.33 Å calculated for sample D (dissolved carbonates media) suggests U^{VI} inner-sphere complexation for this sample. Indeed, based on the bond-valence theory, this distance corresponds to an equatorial coordination number of 5 [2], whereas aqueous uranyl-carbonates complexes display equatorial CN of 6. The implied change in the geometrical configuration of the equatorial O atoms during sorption suggests that dominant inner-sphere complexation occurs for U^{VI} sorption onto birnessite in carbonate media.

Finally, further analyses will carefully focus on the peak at $R+\Delta R = 2.3$ Å contains in FTs of all samples. Previous studies [3-5] showed strong evidences for the presence of ternary uranyl-carbonates complexes sorbed on various mineral surfaces, and peaks at 2.3Å, which corresponds to a shell of neighboring atoms at 2.9 Å, seem typical of an U-C interaction [6]. Various experimental conditions were retained in the present study, in order to highlight this U-C interaction, but unexpected results appear. In experiments conducted at pH 4, a constant flux of Ar was held in the solutions, in order to definitively prevent some hypothetical carbonate-complexes formation (although these complexes are thermodynamically unexpected at this pH). In contrast, U^{VI} dissolved species were 100% uranyl-carbonate complexes in sample D. Despite these opposite conditions, all spectra show the same peak at 2.3Å in FTs, whatever the pH or the aqueous media. Moreover, no significative variation of this peak height occurs between samples with 0% and 100% of dissolved U-carbonates species. Ternary uranyl complexes with nitrate ligands could produce a similar contribution at 2.3Å, however no such contribution can be involved in $NaClO_4$ media.

References:

- [1] Giovanoli R., Stähli E. & Feitknecht W. (1970) Helvetica Chimica acta 53, 454-464.
- [2] Burns P.C., Ewing R.C. & Hawthorne F.C. (1997). Can. Mineral. 35, 1551-1570.
- [3] Reich T., Moll H., Arnold T., Denecke M.A., Henning C., Geipel G., Bernhard G., Nitsche H., Allen P.G., Bucher J., Edlestein N. & Shuh D.K. (1998). J. Electron Spectr. Rel. Phen. 96, 237-243.
- [4] Bargar J.R., Reitmeyer R. & Davis J.A. (1999). Environ. Sci. Technol. 33, 2481-2484.
- [5] Bargar J.R., Reitmeyer R., Lehman J. & Davis J. (2000) Geochim. Cosmoch. Acta 64, 2737-2749.
- [6] Coda A., Giusta A. & Tazzoli V. (1981) Acta Crystallogr. B37, 1496-1500.

 ROBL-CRG	Experiment title: Sorption of Am onto smectite	Experiment number: 20_01_34
	Beamline: BM 20	Date of experiment: from: 15.02.01 to: 16.02.01 30.08.01 01.09.0 16.02.02 17.02.02
Shifts: 14	Local contact(s): Christoph Hennig	<i>Received at ROBL:</i> 22.11.2002
Names and affiliations of applicants (* indicates experimentalists): Th. Stumpf*, C. Hennig*, H. Funke*, S. Stumpf*, T. Reich*, A. Rossberg*		

Report:

Motivation

Sorption to mineral surfaces is a major process controlling the concentration, mobility and bioavailability of radionuclides in nature. Oxides and clay minerals are the main constituents in the groundwater and soil systems and therefore they are responsible for metal ion sorption. In case of the release of actinides in a nuclear waste repository, clays as back-fill material will be the technical barrier for their spreading. Consequently it is essential for the long-term performance assessment of nuclear waste repositories to know about the interactions of actinide ions with clay minerals. Therefore it is necessary to identify the surface species that are formed during the sorption process. For this purpose, the sorption process of a trivalent actinide ion onto smectite and kaolinite was studied by X-ray absorption fine structure (XAFS) spectroscopy, as a function of pH.

Experimental

Well crystallized, fine grained kaolinite ($\leq 2 \mu\text{m}$) from St. Austell (UK) and smectite ($<0.1 \mu\text{m}$ fraction of the Ceca bentonite separated by sedimentation technique) were used for the experiments. The cation exchange capacity (CEC) of the initial products was found to be 3.7 meq/100 g for kaolinite and 75 meq/100 g for smectite. Each sample contained 0.1 g clay which was equilibrated at pH 6.7 for one week in the dark. As background electrolyte we used NaClO_4 solutions ($I = 0.025 \text{ M}$). The long-lived americium isotope Am-243 ($t_{1/2} = 7370$ years) was provided from the Oak Ridge National Laboratory. The initial americium concentration was adjusted to $1 \times 10^{-3} \text{ mol/L}$. The EXAFS samples were prepared at room temperature in a glove box under

nitrogen atmosphere. To avoid Am(III) precipitation the actinide was added to the clay suspensions in the acidic range (pH 3.5). Then the pH was increased in small steps to reach the final value of each sorption sample after 2-4 weeks. The suspensions (40 mL each) were centrifuged (6000 rpm; 10 min) and the received wet pastes were transported into polypropylene vessels.

Results

The EXAFS spectra and the corresponding Fourier transforms of Am(III) sorbed onto smectite and kaolinite at different pH are shown in figure 1. In all Fourier transformed spectra one peak dominates which can be attributed to an average Am/O distance composed out of Am/water and out of Am/O-mineral surface distances. A further signal that could be an indication for an Am/Al distance was not obtained. The EXAFS parameter derived from these spectra together with values found for the Am aquo ion are listed in table 1. As expected the accordance between the parameter found for the Am^{3+} aquo ion and obtained for the Am/smectite outer-sphere complex at pH 4 (Am-03) is very high.¹ With Am/clay inner-sphere complex formation at higher pH (6, 8) a slight shortening of the Am-O distance can be obtained. The reduction of the Am(III) coordination number with pH might be an indication for the formation of a ternary $\text{OH}^-/\text{Am}/\text{clay}$ surface complex.

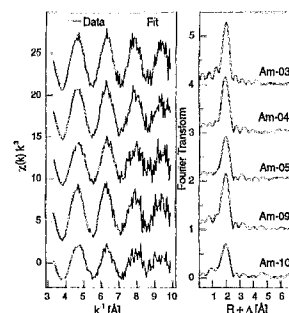



Figure 1: Am(III) sorbed onto smectite (03-05) and kaolinite (09, 10) at pH 4, 6, 8 and 6, 8; L_{III} -edge k^3 -weighted EXAFS spectra and corresponding Fourier transforms. (Solid line - experiment; dashed line - theoretical fit.).

1	R [Å] ^a	N ^b	σ^2 [Å ²] ^c	ΔE [eV]
Am^{3+}	2.494(2)	7.0(2)	0.0058 (3)	-1.8
03	2.486(4)	6.7(4)	0.0047 (6)	-2.1
04	2.480(5)	7.5(4)	0.0074 (6)	-2.5
05	2.475(7)	6.3(5)	0.008 (1)	-2.0
09	2.487(5)	7.8(5)	0.0077 (7)	-2.0
10	2.479(6)	5.5(4)	0.0097 (9)	-1.7

Table 1: EXAFS parameter of the Am(III) aquo ion and the Am(III)/clay sorption samples.

¹ Stumpf, Th.; Bauer, A.; Coppin, F.; Kim, J. I. *Environ. Sci. Technol.* **2001**, *35*, 3691-3694

	Experiment title: Uranium sorption onto muscovite	Experiment number: 20_01_36 20_01_53
	Beamline: BM 20	Date of experiment: from: 25.02. to: 26.02.01 from: 05.10. to: 06.10.01 from: 01.12. to: 01.12.01 from: 18.09. to: 20.09.02
Shifts: 16	Local contact(s): T. Reich, C. Hennig	<i>Received at ROBL:</i> 4.11.2002
Names and affiliations of applicants (* indicates experimentalists): M. Walter*, T. Arnold, G. Bernhard, H. Funke*, C. Hennig*, M. Merroun*, H. Moll*, T. Reich*, A. Rossberg* Forschungszentrum Rossendorf e.V., Institut für Radiochemie, P.O. Box 510119, D-01314 Dresden		

Report:

One of the most common minerals in granitic rocks, sediments, and soils is muscovite. Therefore, muscovite surfaces may influence the mobility of uranium(VI) in the environment (waste deposits, mining sites). The aim of the present project is to investigate the sorption of uranium(VI) on muscovite.

Experimental

Samples for EXAFS spectroscopy were prepared under ambient conditions using 200 mg of fine grained muscovite, dispersed in 1000 ml of 0.01 N NaClO₄ solution. The suspensions were equilibrated for two weeks to adjust the pH value of 5.8 or 8.0, respectively. The initial uranium(VI) concentrations were 1*10⁻⁴ M U(VI) for pH 5.8 samples, and 6*10⁻⁴ M U(VI) for pH 8.0 samples. In addition, two samples were prepared under N₂-atmosphere with an initial uranium(VI) concentration of 2*10⁻⁵ M. After a sorption period of approximately 40 hours, the suspensions were centrifuged and the sorption samples were prepared as wet pastes in Teflon sample holders for XAS measurements.

The X-ray absorption measurements were performed at the ROBL-CRG in fluorescence mode using a 4-element germanium solid state detector. The EXAFSPAK program was used to extract and fit the EXAFS data. The

theoretical phase shifts and backscattering amplitudes were calculated with FEFF8.

Results

Figure 1 shows the X-ray absorption spectra before and after preedge subtraction for U(VI) adsorbed on muscovite at pH 5.8 in a 2·10⁻⁵ M U(VI) solution. The high absorbance in the preedge region is caused by Rb K_{α1} fluorescence radiation (Rb K_{α1} 13395 eV), which was simultaneously recorded with U L_{III} (U L_{III} 13615 eV) by the germanium solid-state detector. The extracted U L_{III} edge EXAFS shows a large noise and is not evaluable. However, the Rb is located within the structure of muscovite (1700 mg/kg) and cannot be removed by sample preparation procedures.

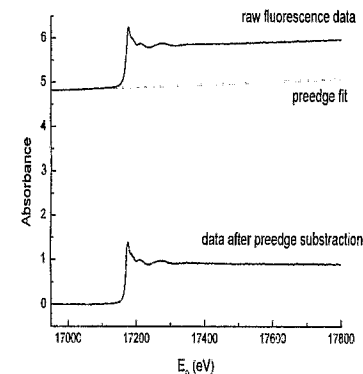


Fig 1.: X-ray absorption spectrum of U(VI) adsorbed on muscovite at pH 5.8 in a 2*10⁻⁵ M U(VI) solution.

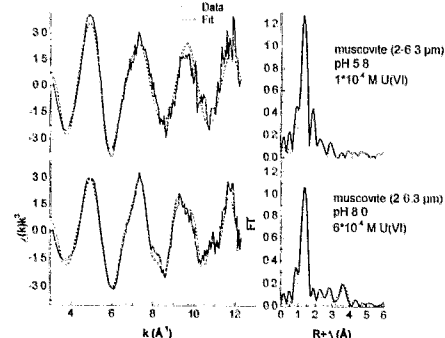



Fig 2.: U L_{III}-edge k³-weighted EXAFS spectra and related Fourier Transforms of uranium(VI) sorbed on muscovite

The U L_{III}-edge EXAFS of the uranium(VI) sorption sample prepared in 1*10⁻⁴ M U(VI) solution indicates that the equatorial oxygens shell (R = 2.37±0.02 Å) is strongly disordered, which can be interpreted as inner-sphere surface complexation. In contrast, at a higher uranium(VI) concentration of 6*10⁻⁴ M a uranium-uranium backscattering at a distance of 3.87±0.02 Å suggest the (surface) precipitation of uranium(VI).

	Experiment title: Adsorption of actinide ions on (hydr-) oxide and clay minerals : Influence of the solution chemistry	Experiment number: 20_01_37
	Beamline: BM 20	Date of experiment: from: 31.03.2001 to: 03.04.2001
Shifts: 9	Local contact(s): Andreas Bauer, Christoph Hennig	<i>Received at ROBL:</i> 30.02.2002
Names and affiliations of applicants (* indicates experimentalists): Clotilde Gaillard, Isabelle Billard, Mireille Del Nero*, Annick Froideval*, Klaus Lützenkirchen*, Gwanaelle Mignot, Isabelle Rossini*, Laurent Sémon* Institut de Recherches Subatomiques Chimie Nucléaire F-67037 STRASBOURG cedex 2		

Report:

The aim of the present experiment was to gain insights into the coordination of U(VI) -the most stable oxidation state in oxidizing aqueous medium- on two mineral phases (an alumina gel $Al_2O_3 \cdot nH_2O$ and a kaolinite $Al_2Si_2O_5(OH)_4$) under chemical conditions relevant to groundwaters (near-neutral pH values and presence of aqueous carbonate ligands). We investigated the influence of an aqueous carbonate complexation of U(VI) on the uranyl surface species by varying the initial uranyl concentration ($[U]_i = 5 \cdot 10^{-4}$ M or 10^{-4} M) and the carbonate concentration ($C_C = 10^{-2}$ M or $C_C \approx 0$ using CO_2 -free solutions under a N_2 -atmosphere) of the aqueous phase used in our batch sorption experiments. A list of the samples is given in table 1.

Uranium L_{III} -edge EXAFS spectra were recorded in transmission and fluorescence mode. The results of the fits are summarized in table 2 for the uranyl species on the alumina gel. A small contribution at 2.7 Å (on the FT) was attributed to a U-C single scattering contribution. A surprising feature is that the presence of carbon is observed not only for the A75C sample ($C_C = 10^{-2}$ M) but also for all samples maintained under a N_2 -atmosphere. This indicates either carbonate impurities on solids -that could not be removed by our minerals pre-treatments- and / or a carbonate contamination of the samples during the sorption experiments or their conditioning for EXAFS analyses. Indeed the formation of uranyl carbonate species is favoured in uranyl solutions at $C_C = 10^{-2}$ M or at equilibrium with atmospheric CO_2 at pH ≈ 7.5 . Uranium is found surrounded by an average of 2 carbon atoms, at a distance of 2.92-2.94 Å. This distance is typical of the formation of a bidentate

surface complex [1]. No evidence of an U-Al interaction was found, leading us to assume that an outer-sphere complexation mechanism is responsible for the formation of a carbonate-uranyl surface species at near-neutral pH values. The signal for the k75 sample (uranyl sorbed on kaolinite) was very weak, due to the low kaolinite specific surface. We however can notice that the O_{eq} contribution is diminished when compared with that obtained on the alumina gel samples. This suggests different chemical environments for uranium sorbed on a kaolinite and on an alumina gel respectively.

Table 1: Summary of samples preparation

Name	$[UO_2^{2+}]$ (M)	$[CO_3^{2-}]$ (M)	pH	Mineral phase
A75	$5 \cdot 10^{-4}$	* N_2 -atm	7.5	Alumina gel
A75C	$5 \cdot 10^{-4}$	10^{-2}	7.5	Alumina gel
a75	10^{-4}	* N_2 -atm	7.5	Alumina gel
k75	10^{-4}	* N_2 -atm	7.5	Kaolinite

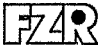
*sorption experiments using CO_2 -free solutions under a N_2 -atmosphere

Table 2 : Best fit parameters of the U L_{III} -edge EXAFS spectra for U(VI) sorbed on alumina. Distances are given in Å and Debye-Waller factors in Å². The O_{av} coordination number was held constant ($N = 2$) for all fits.

	O_{av}	O_{eq}	C
A75	R = 1.80 $\sigma^2 = 0.002$	N = 5.2 R = 2.44 $\sigma^2 = 0.007$	N = 1.7 R = 2.94 $\sigma^2 = 0.002$
A75C	R = 1.81 $\sigma^2 = 0.002$	N = 5.3 R = 2.46 $\sigma^2 = 0.005$	N = 2.3 R = 2.92 $\sigma^2 = 0.001$
a75	R = 1.80 $\sigma^2 = 0.004$	N = 6.8 R = 2.45 $\sigma^2 = 0.009$	N = 2.7 R = 2.92 $\sigma^2 = 0.003$

Reference:

[1] R.J. Reeder, M. Nugent, G.M. Lamble, C.D. Tait, D.E. Morris, Environ. Sci. Technol. 2000, 34, 638.

 ROBL-CRG	Experiment title: Uranium complexation by adenosine phosphates	Experiment number: 20_01_38 CH-1264
	Beamline: BM 20	Date of experiment: from: 25.04.01 to: 26.04.01 from: 09.06.01 to: 10.06.01 from: 27.02.02 to: 02.03.02 from: 24.01.02 to: 31.01.02
Shifts: 15 + 9	Local contact(s): Christoph Hennig	<i>Received at ROBL:</i> 28.11.2002
Names and affiliations of applicants (* indicates experimentalists): C. Hennig*, G. Geipel*, T. Reich*, A. Günther, G. Bernhard Forschungszentrum Rossendorf e.V., Institute of Radiochemistry, D-01314 Dresden		

Report:

Uranium(VI) can be bound to phosphoryl groups in microorganisms [1]. The most important phosphoryl containing enzymatic compounds are the adenosine phosphates which are able to transfer the phosphate groups from one to another molecule [2]. Heavy metal ions fixed onto adenosine phosphates can be transported into living cells and then deposited. Possible complex formation between adenosine phosphate and heavy metal ions therefore can be the pathway to understand the mechanisms of transportation. The fluorescence properties of uranium are changed upon complex formation in shifting of the emission bands of about 6 nm and in an increase of the fluorescence lifetime to more than 20 μ s. Additionally the adenosine molecule shows a dynamic quench effect onto the fluorescence. As example, the formation of 1:1 U(VI) adenosine triphosphate complex with a formation constant of $\log K = -3.8$ was determined using laser spectroscopy [3].

The complex compounds were prepared by mixing 1 M uranyl nitrate solution with 1 M adenosine triphosphate and adenosine monophosphate stock solutions at pH 1.8 - 2.5 and room temperature. The precipitate was filtered, washed and dried.

At Fig. 1 are shown the U L_{III} -edge EXAFS spectra of U(VI) adenosine monophosphate (U-AMP) and U(VI) adenosine triphosphate (U-ATP). The first Peak at the Fourier transform (FT) originates from the uranyl oxo group. The second shell of U-ATP comprises nitrogen and/or oxygen atoms at a distance of 2.36 \AA whereas the equatorial shell of U-AMP shows a splitting of bond distances into 2.36 \AA and 2.54 \AA . The phosphoryl groups of U-AMP and U-ATP are coordinated

in a monodentate fashion proofed by the U-P distance of 3.87 \AA (U-AMP) and 3.61 \AA (U-ATP).

Tab. 1: EXAFS parameters of U L_{III} -edge measurements.

sample	shell	R [\AA]	N	σ^2 [\AA^2]	ΔE [eV]
U-AMP	U-O _{ax}	1.791(2)	2.2(1)	0.0021(2)	-9.7
	U-MS	3.58	2.2	0.0042	
	U-N/O _{eq1}	2.356(4)	2	0.0061(5)	
	U-N/O _{eq2}	2.541(8)	3	0.0055(6)	
	U-P	3.871(6)	0.9(4)	0.0024(2)	
U-ATP	U-O _{ax}	1.773(1)	1.9(1)	0.0019(2)	-12.9
	U-MS	3.546	1.9	0.0038	
	U-N/O _{eq}	2.361(4)	4.1(3)	0.0073(6)	
	U-P	3.606(7)	1.0(3)	0.002(1)	

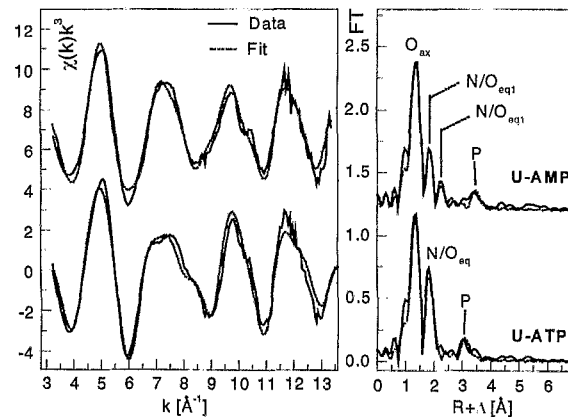



Fig. 1: U L_{III} -edge EXAFS spectra (left) and their Fourier transform (right) of U-AMP and U-ATP.

[1] Hennig, C. et al.: EXAFS investigation of uranium(VI) complexes formed at *Bacillus cereus* and *Bacillus spæricus* surfaces, *Radiochim. Acta* **89** (2001) 625

[2] Mildvan, A.S. et al.: The role of divalent cations in the mechanism of enzyme catalyzed phosphoryl and nucleotidyl transfer reactions, *Structure and bonding*, **20** (1974) 2

[3] Geipel, G. et al.: Complex formation between uranium(VI) and adenosine triphosphate; NRC5, 5th International Conference on Nuclear and Radiochemistry, Pontresina, Switzerland, Sept. 3-8, 2000, Extended Abstracts, Vol. 2, p.473

	Experiment title: EXAFS investigation of uranium complexation with hydroxo benzoic acids	Experiment number: 20_01_39
	Beamline: BM 20	Date of experiment: from: 26.04.01 to: 27.04.01
Shifts: 3	Local contact(s): T. Reich	<i>Received at ROBL:</i> 05.12.2002
Names and affiliations of applicants (* indicates experimentalists): A. Roßberg ^{*2} , T. Reich ^{*2} , H. Funke ^{*2} , C. Hennig ^{*2} , S. Sachs ¹ , M. Merroun ^{*1} , M. Kunicke ^{*1} ¹ Forschungszentrum Rossendorf e.V., Institute for Radiochemistry, P.O. Box 510119, 01314 Dresden, Germany ² ESRF-ROBL/CRG, Avenue des Matryrs, B.P. 220, 38043 Grenoble Cedex,		

Report:

Experimental:

The U L_{III} -edge X-ray absorption spectra of the aqueous solutions of U(VI) with 2,3-2,4- 2,5- and 2,6-dihydroxybenzoic acids (n,m-DIBA) were measured using the Si(111) double-crystal monochromator in channel cut mode [1]. The spectra were recorded in transmission mode. For each solution the U(VI) concentration and the ligand concentration was 0.01 M. The pH of the solutions was in the range of 2.5 - 2.1 (Tab. 1) and the ionic strength was 0.1 M (NaClO₄). The energy scale was calibrated using an Y foil. For EXAFS analysis the theoretical scattering phases and amplitudes were calculated with the scattering code FEFF6 [2] using the crystal structure of sodium uranyl(VI)-triacetate [3].

Results and Discussion:

The U L_{III} -edge k^3 -weighted EXAFS spectra are shown in Fig. 1 and the EXAFS structural parameters in Tab. 1. As one can see from Tab. 1 and Fig. 1 the EXAFS structural parameter of the n,m-DIBA samples are in agreement with those observed for U(VI) hydrate. From this we conclude that at pH 2.5 - 2.1 no interaction between U(VI) and the n,m-DIBA is present.

Tab.1: EXAFS structural parameters of the system U(VI)/n,m-DIBA.

n,m	pH	O _{axial(ax)}		O _{equatorial(eg)}		
		R [Å]	$\sigma^2 \cdot 10^3$ [Å ²]	N	R [Å]	$\sigma^2 \cdot 10^3$ [Å ²]
2,3	2.3	1.769(2)	1.2(1)	5.5(5)	2.407(6)	9.0(1)
2,4	2.5	1.763(1)	1.4(1)	5.4(3)	2.401(3)	7.9(5)
2,5	2.4	1.758(2)	1.8(1)	5.5(3)	2.395(4)	7.7(6)
2,6	2.1	1.760(1)	1.8(1)	5.0(2)	2.394(3)	6.8(4)
U(VI) hydrate	0.0	1.767(1)	1.28(6)	5.3(3)	2.408(3)	7.2(4)

N - coordination number; R - radial distance with an uncertainty of ± 0.02 Å; σ^2 - Debye-Waller factor; during the fitting procedure N of O_{ax} was held constant at N=2; the standard deviations are given in parenthesis.

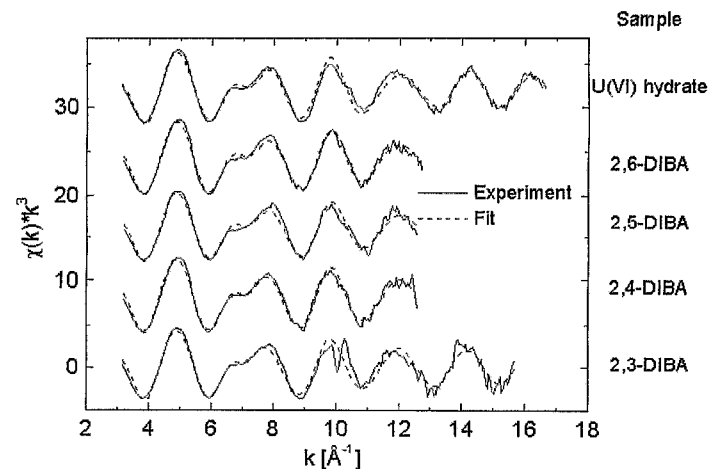


Fig. 1: Raw U L_{III} -edge k^3 -weighted EXAFS spectra of the aqueous solutions of U(VI)/n,m-dihydroxybenzoic acids and U(VI) hydrate.

References:

1. Matz, W., et al., J. Synchrotron Rad. **6**, 1076 (1999).
2. Zabinsky, S., et al., Phys. Rev. B **52**, 2995 (1995).
3. Templeton, D. H., et al., Act. Cryst. **C41**, 1439 (1985).

	Experiment title: X-ray absorption spectroscopy investigation on solid uranyl complexes with substituted carboxylic acids	Experiment number: 20_01_40
	Beamline: BM 20	Date of experiment: from: 28.09. to: 30.09.2001
Shifts: 6	Local contact(s): Tobias Reich	<i>Received at ROBL:</i> 23.10.2002
Names and affiliations of applicants (* indicates experimentalists): H. Moll*, T. Reich*, Ch. Hennig*, M. Merroun*, H. Funke*, A. Rossberg*, Th. Stumpf*, M. Kunicke*, D. Falkenberg*, M. Walter*		

Report:

Experimental. The aminoacids (HL) used were α -aminoisobutyric acid (HL¹), β -aminobutanoic acid (HL²), and γ -aminobutanoic acid (HL³). The reactions were performed in aqueous solution, in different molar ratios (UO₂:HL = 1:1, 1:2, 1:3) and the products were isolated by slow evaporation of the solvent. The samples used to measure the EXAFS from the precipitates were prepared by mixing appropriate amounts of the solid with teflon and then pressing to give pellets with a diameter of 13 mm.

Results. As a continuation of our project 20-01-31 we investigated the structure of solid complexes of uranyl with selected aminoacids. The aim of this EXAFS study was the investigation of structural changes of solid uranium(VI) complexes with selected aminoacids.

Table EXAFS structural parameters. f: fixed during the fit.

Sample	Shell	N	R (Å)	σ (Å ²)
A UO ₂ [HL ¹] ₁ (NO ₃) ₂	U-O _{ax}	2f	1.76	0.0017
	U-O _{eq}	5.0	2.39	0.0126
B UO ₂ [HL ¹] ₂ (NO ₃) ₂ ·H ₂ O	U-O _{ax}	2f	1.77	0.0017
	U-O _{eq1}	3.0	2.31	0.0059
	U-O _{eq2}	3.1	2.49	0.0071
C UO ₂ [HL ¹] ₃ (NO ₃) ₂ ·H ₂ O	U-O _{ax}	2f	1.77	0.0016
	U-O _{eq1}	3.0	2.34	0.0052
	U-O _{eq2}	1.9	2.48	0.0062
D UO ₂ [HL ³] ₃ (NO ₃) ₂ ·H ₂ O	U-O _{ax}	2f	1.77	0.0022
	U-O _{eq}	5.7	2.47	0.0058
	U-C	3.0	2.87	0.0034

Indications were obtained for the formation of three types of complexes of uranium(VI) and α -aminoisobutyric acid (1:1, 1:2, 1:3). Only tris complexes

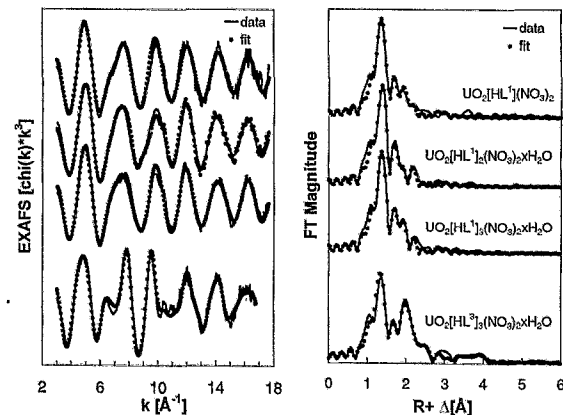
were observed with γ -aminobutanoic acid (HL³). This is in agreement with the findings of Bismondo et al. /1/. Whereas no solid complexes could be obtained with β -aminobutanoic acid (HL²). The U-O_{eq} distance can be used as an indicator for the coordination mode of carboxylate ligands to the uranyl center (see Table). For sample A we measured an U-O_{eq} distance of 2.39 Å. This value is shorter than expected for a bidentate coordination of the carboxylic group of the aminoacid. Most likely the α -aminoisobutyric acid is coordinated in the 1:1 complex via one oxygen of the carboxylic group to the uranyl center. If more than one aminoacid ligand are coordinated we observed a splitting of the U-O_{eq} shell. This might indicate a coordination of the aminoacid molecules either in monodentate and/or in a bidentate fashion. The EXAFS spectrum of UO₂[HL³]₃(NO₃)₂·H₂O looks different compared to the other data (see Figure). The U-O_{eq} distance of 2.47 Å is typical for bidentate coordinated COO⁻ groups, as indicated by the presence of an U-C contribution at 2.87 Å. The structural parameters determined are in agreement with those reported by Bismondo et al. /1/. Based on the presented experimental results we found no evidence for the formation of chelate species involving the amino group.


Acknowledgements. This work was supported by the European Commission within the Human Potential Program under contract number HPMF-CT-1999-00342.

Reference

/1/ A. Bismondo et al., Inorg. Chim. Acta **110**, 205 (1985).

Figure U L_{III}-edge k³-weighted EXAFS spectra (left) and corresponding Fourier transforms (right) of the synthesized solids. Solid line – experiment; dots – theoretical fit.



	Experiment title: Uranium sorption onto ferric oxides	Experiment number: 20_01_41 20_01_52
	Beamline: BM 20	Date of experiment: from: 29.04. to: 30.04.01 from: 04.10. to: 05.10.01
Shifts: 6	Local contact(s): T. Reich, C. Hennig	<i>Received at ROBL:</i> 4.11.2002
Names and affiliations of applicants (* indicates experimentalists): M. Walter*, T. Arnold, G. Bernhard, H. Funke*, C. Hennig*, M. Merroun*, H. Moll*, T. Reich*, A. Rossberg* Forschungszentrum Rossendorf e.V., Institut für Radiochemie, P.O. Box 510119, D-01314 Dresden		

Report:

Schwertmannite ($\text{Fe}_{16}\text{O}_{16}(\text{OH})_{12-9}(\text{SO}_4)_{2-3,5} \cdot n\text{H}_2\text{O}$, $n \sim 10$) and goethite are commonly found in acid mine drainage (AMD) systems. Such AMD waters can contain high uranium(VI) concentration, e.g. as a result of in situ leaching of uranium by sulfuric acid. Therefore, the sorption of uranium(VI) on schwertmannite surfaces may influence the migration of uranium under AMD conditions. The aim of the present project is to investigate the structure of uranium(VI) adsorbed on schwertmannite and goethite.

Experimental

Samples for EXAFS spectroscopy were prepared under N_2 -atmosphere using 200 mg of synthetic schwertmannite or goethite, dispersed in 1000 ml of 0.02 N Na_2SO_4 or 0.01 N NaClO_4 solution, respectively. The suspensions were equilibrated for two days to adjust the pH value of 4.2. The initial uranium(VI) concentration was $5 \cdot 10^{-5}$ M U(VI). In addition, one uranium(VI) sorption sample on goethite was prepared in 0.02 N Na_2SO_4 solution at pH 6.5 using an initial uranium(VI) concentration of $1 \cdot 10^{-5}$ M. After a sorption period of approximately 24 hours, the suspensions were centrifuged and the sorption samples were prepared as wet pastes in Teflon sample holders for XAS measurements.

The X-ray absorption measurements were performed at the ROBL-CRG in fluorescence mode using a 4-element germanium solid-state detector. The

EXAFSPAK program was used to extract and fit the EXAFS data. The theoretical phase shifts and backscattering amplitudes were calculated with FEFF8.

Results

All distances of the equatorial oxygens are about 2.37 Å (Table 1). They are significantly shorter than the typical values for the aquatic UO_2^{2+} ion of 2.41 Å /1/, which indicates strong interactions. An iron backscatterer was clearly found for uranium(VI) sorbed onto goethite at pH 4.2 and 6.5 in a sulfate-rich solution as well as for schwertmannite at pH 4.2 in perchlorate solution. Such a uranium - iron distance is indicative of a bidentate inner sphere complexation /2/. In contrast, the EXAFS of uranium(VI) sorbed onto schwertmannite at pH 4.2 in sulfate-rich solutions shows only a sulfur backscatterer at a distance of 3.67 Å, indicating a monodentate uranium(VI) - sulfate coordination. This could be interpreted either as uranium(VI) - surface complexes with the structural sulfate of the schwertmannite lattice ($\equiv\text{SO}-\text{UO}_2$, $\equiv(\text{SO})_2-\text{UO}_2$). A light backscatterer, like carbon, at a distance of 2.9 Å improves the fit. Although this uranium(VI) - carbon interaction is typical of a bidentate complexation /3/, ternary uranium(VI) - carbonate complexes are ruled out by the sorption conditions (pH, high sulfate concentration).

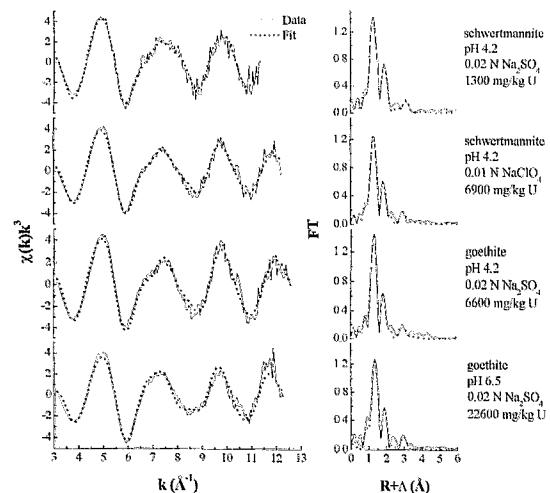



Fig. 1: k^3 -weighted uranium L_{III} edge EXAFS and corresponding Fourier transforms

/1/ Dent A. J., et al., J. Colloid Interface Sci. 150, 45-60 (1992)

/2/ Reich T., et al., J. Elec. Spec. Rel. Phe. 96, 237-234 (1998)

/3/ Bargar J. R., et al., Geochim. Cosmochim. Acta 64, 2737-2749 (2000)

	Experiment title: Interaction of <i>Acidithiobacillus ferrooxidans</i> with uranium - an EXAFS study	Experiment number: 20_01_42
	Beamline: BM 20	Date of experiment: from: 30.04.01 to: 02.05.01 from: 08.07.01 to: 10.07.01 from: 30.09.01 to: 02.10.01
Shifts: 18	Local contact(s): Christoph Hennig	<i>Received at ROBL:</i> 22.11.2002
Names and affiliations of applicants (* indicates experimentalists): M. Merroun*, S. Selenska-Pobell, T. Reich*, C. Hennig*, A. Rossberg*, H. Funke*, M. Walter*		

Report:

Bacteria express a wide variety of complex molecules on their surfaces which at physiological pH values, contain numerous charged chemical groups (such as phosphoryl, carboxyl, and amino groups) that usually gives the cell surface a net of anionic (negative) charge density. Since the cell surface is in direct contact with the environment, the charged groups within the surface layers are able to interact with ions or charged molecules present in the external milieu. The implication of one or other chemical group in the interaction with metals depends on different factors, e.g. pH of the metal solution, time contact, etc.

In this work, X-ray absorption fine structure (XAFS) measurements was used at the U L_{III} -edge to directly determine the pH (2, 3 and 4.5) and time contact (2, 4, 7, 14 days) dependence of the cell functional groups responsible for the absorption of aqueous uranyl ions to *Acidithiobacillus ferrooxidans*.

Uranium L_{III} -edge EXAFS spectra of the uranium species formed by different types of *A. ferrooxidans* at pH 3 and 4.5 and their corresponding Fourier Transforms (FT) are shown in Figure 1.

Fits to EXAFS spectra indicate that no structural differences were observed between the uranium complexes formed by the 3 types of *A. ferrooxidans* at pH 3 and 4.5 and also to pH 2 //1. In all samples the uranium is coordinated to phosphate groups in a monodentate fashion with an average distance between the U atom and the P atom of $3.62 \pm 0.02 \text{ \AA}$. The U-O_{eq} bond distances of the complexes formed by different types at different pH values ($2.36 \pm 0.02 \text{ \AA}$) are within the range of previously reported values for the oxygen atom of the phosphate bound to uranyl. However, Kelly *et al.*[2] studying the pH dependence of the cell wall functional groups of *Bacillus subtilis* responsible for the absorption of uranium, demonstrated that at low pH value (1.67) the EXAFS data indicate uranyl binding to a phosphoryl functional group, with

an average distance between the uranium atom and the phosphorus atom of approximately 3.6 \AA . At the higher pH values (3.22 and 4.80), the carboxyl groups and phosphates groups are implicated in the interaction with uranium. However, studying the time contact dependence (2, 4, 7 and 14 days) we have found that there are some structural difference concerning the U-P₁ bond distance (data not shown).

The U-P₁ bond distance of the *A. ferrooxidans* uranium complexes after 2, 4, 7 and 14 days contact with the metal are respectively 3.64 , 3.62 , 3.61 , $3.58 \pm 0.02 \text{ \AA}$. Thus, this bond distance decreases with the increasing of the time of the contact between bacteria and uranium. These results indicate probably the formation of short molecules of uranyl phosphates with increasing the time contact as a result of degradation of long molecules.

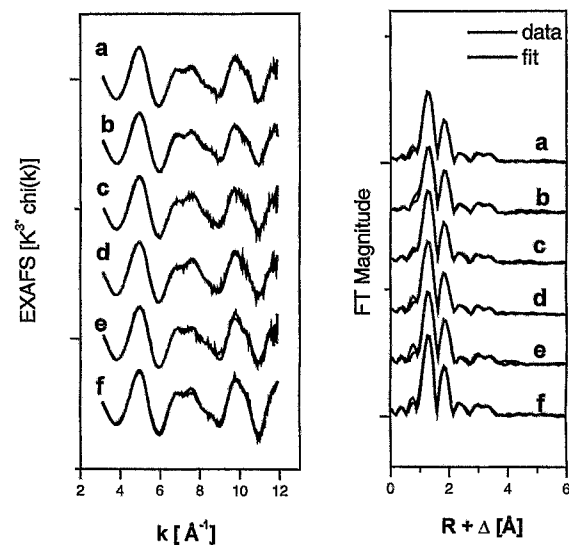



Figure 1: Uranium L_{III} -edge k^3 -weighted EXAFS spectra (left) and corresponding FT (right) of the *A. ferrooxidans* uranium complexes (type I, type II and type III at pH 4.5, (a), (c) and (e), and type I, type II and type III at pH 3 (b), (d) and (f), respectively.

References:

- [1] M. Merroun *et al.* Radiochim. Acta (submitted).
- [2] Kelly *et al.* 2002 Geochim. Cosmochim. Acta

 ROBL-CRG	Experiment title: Uranyl sorption titanium oxide: EXFAS study	Experiment number: 20_01_43 EU #7
	Beamline: BM 20	Date of experiment: from: 01/06/01 to: 04/06/01
Shifts: 12	Local contact(s): Andreas Bauer	
Names and affiliations of applicants (* indicates experimentalists): R. DROT*, IPN, Université Paris-Sud Orsay, 91406 Orsay cedex, France W. DONG*, IPN, 91406 Orsay cedex, France E. SIMONI*, IPN, Université Paris-Sud Orsay, 91406 Orsay cedex, France		

Report:

The aim of this work is to identify the uranium species sorbed onto the titania surface in order to define the sorption equilibria involved in the retention experiments. The sorbed samples have been first studied by spectrofluorimetry and XPS spectroscopy in order to determine the number of complexes on the surface. They have been prepared using the classical batch procedure at room temperature by mixing a weighed amount of powdered titania with an uranyl solution. After 24 hours stirring, the solution is removed and the solid is washed with distilled water at equilibrium pH value, and dried at room temperature. The concentration of uranyl ions on the surface has been determined directly on the solid by PIXE experiment and by measuring the uranyl concentration in solution after centrifugation as well.

Different samples have been analysed depending on the background salt (KNO_3 - NaClO_4 0.5 M) and on the solution equilibrium pH values (2.97 - 4.09). Under these conditions, the sorption rate ranges from 12 to 35 %. Moreover, by comparison between dried and wet samples, any effect of the drying step has been detected.

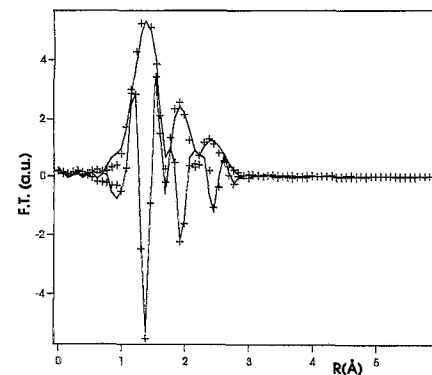
We have obtained the following results:


$\text{TiO}_2 / [\text{UO}_2^{2+}] = 10^{-3} \text{ M}$ $[\text{NaClO}_4] / [\text{KNO}_3] = 0.5 \text{ M}$ $\text{pH} = 3.05$	Axial Oxygens	Equatorial Oxygens	Equatorial Oxygens
N	2.0 / 2.0	2.0 / 2.0	2.9 / 3.1
σ (Å)	0.068 / 0.068	0.070 / 0.070	0.070 / 0.068
R (Å)	1.80 / 1.80	2.31 / 2.33	2.41 / 2.45
ΔE (eV)	7.2 / 7.2	7.0 / 7.0	7.0 / 7.0

In both media, there are two equatorial oxygens contributions at 2.31 and 2.41 Å. The 2.31 Å distance is too short to correspond to the uranyl hydration sphere and then arises from the link between the surface oxygen atoms and the uranyl ions, which means that the uranyl ions form an inner-sphere complex on the TiO_2 surface. Moreover, this surface complex is probably bidentate, considering the two oxygen atoms at this distance. The three oxygens at 2.41 Å belong to hydroxyl groups or water hydration molecules.

The third peak of the Fourier transform could be interpreted as the contribution of one or two titanium atoms at 2.68 Å. This value seems reasonable if we consider for example the distances Ti-O in the (110) face that corresponds to the easiest cleavage of the crystal. In order to check this model, we are performing the same studies (XPS, grazing EXAFS) on an uranyl sorbed TiO_2 single crystal.

The following figure shows the experimental data and the simulation of the Fourier transform of the first three contributions:



 ROBL-CRG	Experiment title: Sorption of U(VI) on chlorite	Experiment number: 20_01_44
	Beamline: BM 20	Date of experiment: from: 08.06.01 to: 09.06.01
Shifts: 3	Local contact(s): Christoph Hennig	<i>Received at ROBL:</i> 18.11.2002
Names and affiliations of applicants (* indicates experimentalists): E. Krawczyk-Bärsch, T. Arnold, T. Reich*, C. Hennig*, G. Bernhard Forschungszentrum Rossendorf e.V., Institute of Radiochemistry, P.O. Box 51 01 19, 01314 Dresden, Germany		

Report:

Introduction:

During the weathering of an iron-rich chlorite Fe-oxyhydroxides are formed in the neutral pH-range. Scanning electron microscopy (SEM) studies showed that the precipitated Fe-oxyhydroxides, probably ferrihydrite, formed heterogenous and homogenous colloids. The homogenous colloids are left in the aqueous solution and transported away from the mineral, while the heterogenous collids are sorbed on the chlorite faces, especially on the edges of the mineral /1/. Due to the high specific surface area /2/ ferrihydrite is dominating the sorption of U(VI) during the weathering of chlorite /3/. In EXAFS investigations the influence of the newly formed colloidal ferrihydrite on the sorption behavior should be confirmed.

Experimental:

A chlorite sample with a grain size of 2 - 6,3 μm was altered in a 0.01 M NaClO_4 -solution during 2 months supposing that ferrihydrite is forming and precipitating on the mineral faces. After alteration a uranyl solution was added with an U(VI)-concentration of $8.6 \cdot 10^{-6}$ M. After 6 hours of sorption duration the sample was prepared for EXAFS investigation. A second chlorite sample was taken without a previous alteration. In order to prevent the formation of ferrihydrite the sorption duration of the added U(VI)-concentration of $8.6 \cdot 10^{-6}$ M was limited to 6 hours.

Results and discussion:

The spectra of the samples are dominated by two peaks, which can be referred to the axial (O_{ax}) and equatorial (O_{eq}) coordination numbers (N). The short bond lengths (R) refer to an innerspere surface complex. The U- O_{eq} bond length with 2.34 Å of the first sample is shorter than the bond length for

ferrihydrite received in previous studies /4/. Furthermore no comparable peak of the U-Fe interaction of ferrihydrite is observed. Compared to the second sample no significant differences are visible.

Tab. 1: EXAFS structural parameter

sample	shell	R [Å] ^a	N ^b	σ^2 [Å ²] ^c	E [eV]	k [Å ⁻¹]	error
U1-48	U- O_{ax}	1.794(4)	2.1	0.0033(4)	1.3	3.1-11.5	0.16
	U- $\text{O}_{ax/MS}$	3.59	2.1	0.0067	/		
	U- O_{eq}	2.34(1)	4.7	0.021(4)	/		
U1-49	U- O_{ax}	1.787(4)	2.1	0.0032(4)	0.2	3.1-11.5	0.16
	U- $\text{O}_{ax/MS}$	3.57	2.1	0.0064	/		
	U- O_{eq}	2.35(1)	5.4	0.019(3)	/		

Standard deviation in brackets, ^a errors in distance ± 0.02 Å, ^b errors in the coordination number ± 25 %, ^c Debye-Waller-Faktor.

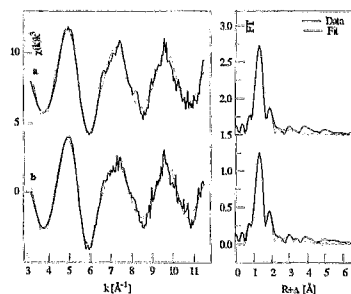



Fig. 1:

We assume that the duration of the alteration of about 2 months was too short for forming a ferrihydrite concentration that will significantly influence the sorption behavior of U(VI) on the chlorite sample.

Acknowledgment: This work was supported by DFG (BE 2234/4-1)

References:

- /1/ Krawczyk-Bärsch, E. et al. (2002): *Chemical Geology* (submitted)
- /2/ Cornell, R.M. and Schwertmann, U. (1996):
- /3/ Arnold, T. et al. (1998): *Chemical Geology* 151, 129-141
- /4/ Reich, T. et al. (1998): *J. Electron Spectroscopy* 96, 237-243

 ROBL-CRG	Experiment title: EXAFS investigation of neptunium with hydroxo benzoic acids	Experiment number: 20_01_45
	Beamline: BM 20	Date of experiment: from: 07.06.01 to: 08.06.01 from: 02.08.01 to: 04.08.01 from: 22.09.02 to: 24.09.02
Shifts: 15	Local contact(s): C. Hennig	<i>Received at ROBL:</i> 29.11.2002
Names and affiliations of applicants (* indicates experimentalists): A. Roßberg* ² , T. Reich* ² , H. Funke* ² , C. Hennig* ² , Th. Stumpf* ¹ , D. Falkenberg* ¹ , K. Schmeide* ¹ , S. Sachs* ¹ , G. Geipel ¹		
¹ Forschungszentrum Rossendorf e.V., Institute for Radiochemistry, P.O. Box 510119, 01314 Dresden, Germany ² ESRF-ROBL/CRG, Avenue des Matyrns, B.P. 220, 38043 Grenoble Cedex,		

Report:

Experimental:

We have investigated the interaction of Np(V) with 2,3- 2,4- 2,5- and 2,6-dihydroxybenzoic acid (n,m-DIBA) in aqueous solution at pH 4. Np(V) was used in a concentration of 5 mM and the ligand concentration was 50 mM. The ionic strength was adjusted to 0.1 M with NaClO₄. The Np L_{III}-edge EXAFS spectra were measured in fluorescence mode using a 4-pixel-germanium detector. The EXAFS spectra were analyzed according to standard procedures using the suite of programs EXAFSPAK [1]. The theoretical scattering phases and amplitudes were calculated with the scattering code FEFF 8 [2] using the atom coordinates of sodium uranyl(VI) triacetate [3]. For FEFF input U was exchanged by Np and the radial distance between Np and the axial oxygen atoms (O_{ax}) was changed to 1.84 Å.

Results and discussion:

The Np L_{III}-edge k³-weighted EXAFS spectra are shown in Fig. 1 and the EXAFS structural parameters in Tab. 1. Except for the Debye-Waller factors all EXAFS structural parameters for the 2,4- 2,5 and 2,6-DIBA/Np(V) solutions and those observed for Np(V) hydrate [4] are equal (Tab. 1). For the O_{ax} and equatorial oxygen atoms (O_{eq}) the largest Debye-Waller factors arise for the 2,3-DIBA/Np(V) solution. In the special case of the 2,3-DIBA ligand two neighboring phenolic OH groups exist. The considered phase and amplitude functions (single scattering Np-O_{ax}, Np-O_{eq}, and multiple scattering Np-O_{ax(1)}-Np-O_{ax(2)}) describe the EXAFS spectra of all mentioned samples

completely. In the FT no backscattering carbon around 2.3+ΔÅ is visible (Fig.1). Therefore we suppose, that the carboxylic group of the n,m-DIBA ligands interact not in a bidentate bonding mode with Np(V). Further investigations on simplest organic ligands such as acetic acid, benzoic acid and catechol are necessary to interpret the coordination.

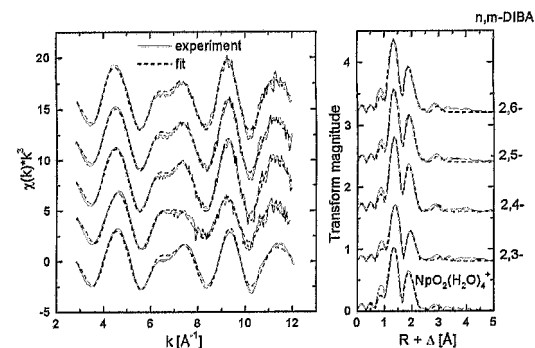


Fig. 1: Raw Np L_{III}-edge k³-weighted EXAFS spectra of the Np(V)/DIBA samples and Np(V) hydrate (NpO₂(H₂O)₄⁺) (left) and their corresponding Fourier transforms (FT) (right).


Tab.1: EXAFS structural parameters of the Np(V)/n,m-DIBA solutions at pH 4 and Np(V) hydrate.

n,m	Np-O _{ax}			Np-O _{eq}		
	N	R [Å]	σ ² ·10 ³ [Å ²]	N	R [Å]	σ ² ·10 ³ [Å ²]
2,3-	1.9(1)	1.861(2)	2.5(4)	3.2(3)	2.502(5)	7(1)
2,4-	2.00(7)	1.840(2)	0.2(2)	3.7(2)	2.500(3)	3.8(5)
2,5-	2.04(7)	1.838(2)	0.6(2)	3.6(2)	2.498(3)	3.3(4)
2,6-	2.03(7)	1.838(2)	0.7(2)	3.6(2)	2.501(3)	3.6(5)
NpO ₂ (H ₂ O) ₄ ⁺	2.03(6)	1.827(1)	1.6(2)	3.6(2)	2.489(3)	4.8(4)

N – coordination number, R - radial distance with an uncertainty of ± 0.02 Å, σ² - Debye-Waller factor; the standard deviations are given in parenthesis.

References:

- George, G. N., Pickering, I. J.: EXAFSPAK, Stanford Synchrotron Radiation Laboratory, Stanford, CA, USA., 1995.
- Ankudinov, A. L., Ravel, B., Rehr, J. J., Conradson, S. D., Phys. Rev. B, 7565 (1998).
- Templeton, D. H., Zalkin, A., Ruben, H., Templeton, L. K., Act. Cryst. C41, 1439 (1985).
- Reich, T., Bernhard, G., Geipel, G., Funke, H., Hennig, C., Roßberg, A., Matz, W., Schell, N., Nitsche, H., Radiochimica Acta 88, 633 (2000).

	Experiment title: Cm(III) Aquo ion	Experiment number: 20_01_46
	Beamline: BM 20	Date of experiment: from: 29.08.01 to: 30.08.01
Shifts: 3	Local contact(s): Christoph Hennig	Received at ROBL: 26.11.2002
Names and affiliations of applicants (* indicates experimentalists): Th. Stumpf*, C. Hennig*, H. Funke*, T. Reich*, A. Rossberg*		

Report:

Motivation

Besides plutonium, the long-lived isotopes of americium and curium play a crucial role for long-term performance assessment of nuclear waste repositories. In order to predict the mobilization and retardation of these nuclides, it is necessary to know the structures of the inorganic and organic actinide species that are involved in the process of migration. Thereby, the characterization of the Am^{3+} and Cm^{3+} aquo ions forms the base for further investigations.

In the literature only few measurements can be found of coordination numbers of trivalent actinides in aqueous solutions. By using UV/Vis spectroscopy, a co-ordination number of 9 was calculated for Am^{3+} aq [1]. The complexation behavior of curium is often investigated by time-resolved laser-induced fluorescence spectroscopy (TRLFS) [2,3]. In analogy to trivalent lanthanides, a coordination number of nine is assumed for Cm^{3+} aq. An extended X-ray absorption fine structure (EXAFS) spectroscopy investigations of Am^{3+} and of Cm^{3+} in 0.25 M HCl obtained coordination numbers of 10.3(0.3) and 10.2(0.3), respectively [4].

Experimental

In order to determine a reliable reference value for the coordination number of Cm^{3+} and Am^{3+} aquo ions, the samples used in our EXAFS measurements were prepared in non-complexing 1.0 M perchloric acid. High actinide concentrations (1×10^{-3} mol/L) were used in order to achieve low-noise EXAFS spectra, which enable a precise determination of bond lengths and coordination numbers of the Am^{3+} and Cm^{3+} aquo ions. EXAFS spectra were collected in transmission mode at the americium L_{III} edge at 18504 eV ($E_0=18520$ eV) and at the curium L_{III} -edge at 18970 eV ($E_0=18990$ eV), respectively. Zr and Nb metal foils were measured and the first inflection point

of the X-ray absorption spectra (Zr K edge at 17998 eV, Nb K edge at 18986 eV) were used for energy calibration. EXAFS data treatment and fit were done using the EXAFSPAK program package. Parameters for the backscattering phase and amplitude, the mean free path, and the reduction factor were calculated using the FEFF8 code.

Results

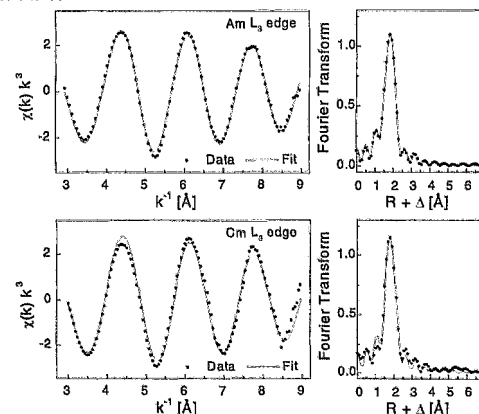



Figure 1.: Raw Am^{3+} and Cm^{3+} L_{III} -edge k^3 -weighted EXAFS spectra and corresponding Fourier transforms. (Points - experiment; dashed line - theoretical fit.)

	Shell	R [Å]	N	σ^2 [Å ²]	ΔE [eV]	k [Å ⁻¹]
Am1-6	Am-O	2.494(2)	7.8(2)	0.0075(2)	-1.8	3.3-9.0
Cm1-1	Cm-O	2.462(3)	7.9(3)	0.0070(4)	-12.5	3.3-9.0

Table 1.: EXAFS structural parameters for the Am^{3+} and Cm^{3+} aquo ions. The standard deviations as estimated by EXAFSPAK are given in parenthesis.

The measured bond distances, $R \pm 0.03$ Å, and coordination numbers, $N \pm 1$, are the same for the Am^{3+} and Cm^{3+} aquo ions and agree with the results of [4]. In the EXAFS analysis with $S_0^2 = 0.9$, the coordination numbers of the Am^{3+} and Cm^{3+} in 0.1 M HClO_4 are smaller by two atoms as compared to those in 0.25 M HCl [4].

1. Carnall, W. T., *J. Less-Common Met.*, **1989**, *156*, 221
2. Beitz, J. V., *Radiochim. Acta*, **1991**, *52/53*, 35
3. Kimura, T.; Choppin, G. R. J., *Alloys Comp.*, **1994**, *213/214*, 313
4. Allen, P. G.; Bucher, J. J., et al., *Inorg. Chem.*, **2000**, *39*, 595

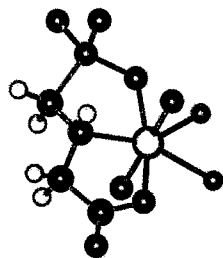
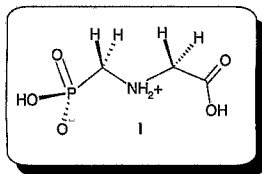
	Experiment title: Solution structures of U(VI); Th(IV) and Dy(III) complexes with α -hydroxy-carboxylates and phosphonic acids	Experiment number: 20_01_48 EU #20
	Beamline: BM 20	Date of experiment: from: 05.09.01 to: 07.09.01
Shifts: 6	Local contact(s): Andreas Bauer	<i>Received at ROBL:</i> 08.04.2002
Names and affiliations of applicants (* indicates experimentalists): Ingmar Grenthe, Zoltán Szabó*, Ignasi Puigdomenech*		
Department of Chemistry, Inorganic Chemistry, Royal Institute of Technology (KTH) S-100 44, Stockholm, Sweden		

Report:

The experiments provided verification on the following two problems:

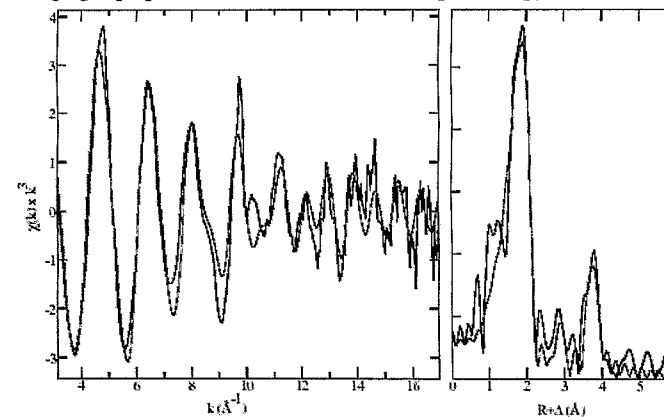
The first concern the structure of uranium(VI) complexes with N-phosphonomethyl glycine (I). This ligand is a commercial herbicide (Glyphosate), which exists in the zwitter-ionic form. Although complexation certainly must play role in its potency, easy transportation to each part of a plant, as well as its immobilization and degradation in the soil and, relatively little is known about the coordination behavior of this potentially tridentate ligand. From coordination chemical point of view, amino-phosphonic acids could be very effective ligands to certain metal ions and potent inhibitors of metallo-enzymes, blocking active metal centers.

The study of the complex formation of uranium(VI) offered not only the possibility to address its behavior in nature, but also to obtain new more fundamental information through the comparison with other elements. This depends partly on the unique coordination chemistry of the linear UO_2^{2+} ion.



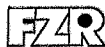
The EXAFS experiment confirmed the formation of mononuclear complexes in the ternary U(VI)-glyphosate-fluoride system with tridentate coordination mode for glyphosate. The structure is given above. Characteristic distances are as follows: U-O_{ax}: 1.79 Å, U-F: 2.25 Å and an average distance for the 3 donor atoms (two O and one N) in the equatorial plane: 2.38 Å.

The second part of this proposal dealt with the comparison of coordination geometry of actinide and lanthanide complexes. Potentiometric data indicate a dramatic change in the stability between the complexes of trivalent lanthanide ions and a dramatic difference in a comparison with uranium(VI). These differences may be used in separation technology. The complexation of Th(IV) and various Ln(III) by glycolic acid (HO-CH₂-COO⁻) has been investigated in 3.0 M NaClO₄ by potentiometry, ¹³C-NMR spectroscopy and EXAFS. Glycolate may be bonded in two ways: either through the carboxyl group or by formation of chelate. The formation of mononuclear complexes Th(HO-CH₂-COO)_n; n=1-4, were identified in the -log[H⁺] range 2.5-4.5. Multinuclear complexes Th₂(OH)₂(HO-CH₂-COO)_n were also determined from potentiometric results and ¹³C-NMR spectra. The chelate-bonded complexes, M₄(O-CH₂-COO)_n(OH-CH₂-COO)_{8-n}; n=6,8 for Th(IV) and 6-8 for Ln(III), were identified in the higher -log[H⁺] range. The structural model of these tetranuclear complexes having a tetranuclear core M₄(O-CH₂-COO)₄ with triple-bridging is proposed on the basis of ¹³C-NMR spectroscopy and EXAFS.



EXAFS spectrum for the Th-glycolate system. The concentration of Th(ClO₄)₄ is 50 mM in 1M sodium glycolate at pH=10.8. The measured Th-Th distance (3.98 Å) proves the formation of multinuclear complexes.

[1] T. Takashi *et al.*: Complexation of Th(IV) and various lanthanides(III) by glycolic acid; potentiometric, ¹³C-NMR and EXAFS studies (sent for publication).

 ROBL-CRG	Experiment title: Surface complexes of uranium onto magnetite and olivine	Experiment number: 20_01_49 EU #18
	Beamline: BM 20	Date of experiment: from: 07.09.01 to: 11.09.01
Shifts: 12	Local contact(s): Tobias Reich, Andreas Bauer	<i>Received at ROBL:</i> 09.04.2002
Names and affiliations of applicants (* indicates experimentalists): Joan de Pablo ¹ , Lara Duro ² , Mireia Grivé ^{2*} , Jordi Bruno ² ¹ ETSEIB, UPC, Avda. Diagonal 647, 08028-Barcelona (Spain); ² QuantiSci, S.L. Avda. Univ. Autònoma, 3, 08290-Cerdanyola del Vallés (Spain).		

Report:

The aim of this experiment is to examine the structure and the oxidation state of uranium sorbed onto the surface of magnetite (Fe₃O₄) and FeO-rich olivine. The U L₃-edge XANES spectra can be useful to derive information about the oxidation state of actinides on the solid surface (Morris et al., 1996; Conradson et al., 1998).

Four different uranium standards were analysed: U(VI): UO₃·2H₂O; U(IV) UO₂(s); U(VI) and U(IV): U₃O₈(s) and 50% UO₃·2H₂O + 50% of UO₂(s). Sorption of U(VI) onto the magnetite and the olivine samples was conducted at 25°C from a homogeneous solution containing 10⁻⁵ mole/dm³ of U(VI) at pH ranging from 6 to 7 and by continuous N₂ or H₂ (g) bubbling. XAS spectra of the samples were recorded by fluorescence detection, due to the low uranium content. We have proceeded in a manner similar to that of Conradson et al., 1998 and Morris et al., 1996 to deconvolute all the signals obtained for our samples and we have obtained a "calibration curve" (see Figure 1) of the oxidation state of uranium by using the data from our standards. We have then obtained the theoretical ratio U(VI) to U(IV) in the uranium-coated olivine and magnetite samples. Figure 1.a shows a typical XANES spectrum of our samples with the deconvolution of the signal in the different components previously mentioned. The resulting shifts of the standards and the samples analysed are presented in Figure 1.b. The parameters of the calibration curve are the following: %U(VI) = (12.459±0.869)·(SHIFT) - (124.37±12.465); with r² = 0.9808

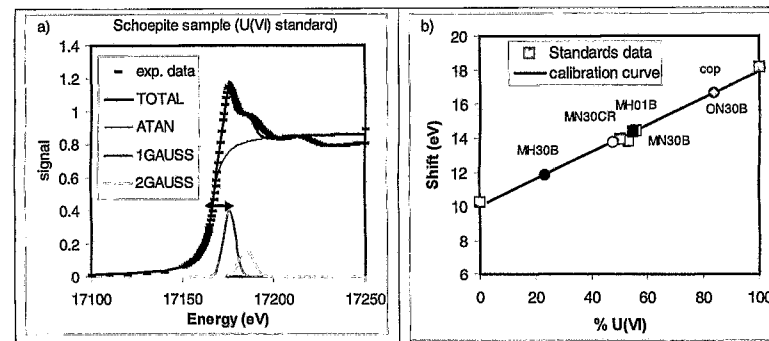



Figure 1(a). XANES spectrum of the U(VI) standard and de-convolution of the peak into an ATAN and two Gaussian functions. The arrow indicates the shift used for the determination of the U(VI) to U(IV) ratio in the sample. (b) Calibration curve of the shift over the percentage of U(VI) in the samples obtained by using data on the standards and data of the samples superimposed. M: magnetite; O: olivine; H and N indicates preparation under hydrogen (reducing) or nitrogen (anoxic) conditions; 01 and 30: days of contact between solid and U(VI) solution; "cop" sample prepared by coprecipitation of U(VI) with Fe(III), no U(VI) reduction to U(IV) is possible.

Sample MH30B, that was prepared under more reducing conditions and for which the interaction magnetite-Uranium was allowed to proceed for the longest time (30 days), plots at the lowest %U(VI), indicating that reduction of uranium has proceeded. Sample prepared with U(VI) and Fe(III) for which no reduction is feasible, plots in the highest range of the graph. There is some error in this analyses, given that this sample should plot on the right axis (U(VI) = 100%) and it behaves as if it had only a 83.5% of U(VI). This deviation can be also due to the different coordination environment of the samples, that is, the fact that the substrate in this case was ferrihydrite while in the other cases were either olivine, magnetite or uranium pure phases for the standards. In general, this analyses permits a rather good estimation of the percentage of reduction of U(VI) to U(IV).

References

- Conradson, S.D., Al Mahamid, I., Clark, D.L., Hess, N.J., Hudson, E.A., Neu, M.P., Palmer, P.D., Runde, W.H. and Tait, C.D. (1998). *Polyhedron*, vol.17, No.4, pp. 599-602.
- Morris, D.E., Allen, P.G., Berg, J.M., Chisholm-Brause, C.J., Conradson, S.D., Donohoe, R.J., Hess, N.J., Musgrave, J.A. and Tait, C.D. (1996). *Environ. Sci. Technol.*, 30, 2322-2331.

	Experiment title: U(VI)-benzoat and U(VI)-phenolat complexes	Experiment number: 20_01_50
	Beamline: BM 20	Date of experiment: from: 27.09.01 to: 28.09.01
Shifts: 3	Local contact(s): A. Roßberg	<i>Received at ROBL:</i> 29.11.2002
Names and affiliations of applicants (* indicates experimentalists): A. Roßberg* ² , T. Reich* ² , H. Funke* ² , C. Hennig* ² , D. Vulpius ¹ , M. Merroun* ¹ , M. Walther* ¹ ¹ Forschungszentrum Rossendorf e.V., Institute for Radiochemistry, P.O. Box 510119, 01314 Dresden, Germany ² ESRF-ROBL/CRG, Avenue des Matryrs, B.P. 220, 38043 Grenoble Cedex,		

Report:*Experimental:*

Our goal was to study the influence of a phenolic OH group on the interaction between U(VI) and a carboxylic group of an aromatic system. Two aqueous solutions were prepared with a U(VI) concentration of 1 mM at pH 4 and a ionic strength of 0.1 M (NaClO₄). One sample contains 10 mM benzoic acid (benz) and the other sample contains 20 mM 4-hydroxybenzoic acid (4-hybenz). According potentiometric titration investigations for each solution 20% U(VI) hydrate and 80% of the 1:1 U(VI)/ligand complex was expected. The U L_{III}-edge X-ray absorption spectra of the aqueous solutions were measured using the Si(111) double-crystal monochromator in channel cut mode [1]. We used a 4-pixel germanium solid-state detector to record the fluorescent signal. The energy scale was calibrated using an Y foil. The theoretical scattering phases and amplitudes were calculated with the scattering code FEFF6 [2] using the crystal structure of sodium uranyl(VI)-triacetate [3].

Results and Discussion:

The U L_{III}-edge k³-weighted EXAFS spectra are shown in Fig. 1 and the EXAFS structural parameters in Tab. 1. In the error limits for the O_{ax} atoms the radial distance and the Debye-Waller factor is equal for both samples (Tab. 1). The radial U-C distance of both samples (Tab. 1) points out, that the carboxylic group coordinates bidentate and not monodentate. In case of bidentate coordination the radial distance of the carboxylic O_{eq} atoms is 2.47±0.02 Å [3]. According to the determined coordination number of C (Tab. 1) U(VI) is coordinated by two ligands in case of benz and by three ligands in case of the 4-hybenz. If one assumes a six-fold coordination and that the radial U-O_{eq} distance of additional coordinated water molecules is 2.41±0.02 Å [4] then the

expected average radial U-O_{eq} bond distance for the U(VI)/benz complex is (4x2.46 Å+2x2.41 Å)/6 = 2.45±0.02 Å. For the U(VI)/4-hybenz complex the calculated radial U-O_{eq} distance is 2.47±0.02 Å. For both complexes the calculated radial U-O_{eq} distances are larger than the experimental determined radial U-O_{eq} bond distances (Tab. 1). The EXAFS structural parameters of O_{eq} and the carboxylic C show that neither a "classical" monodentate [5] coordination nor a "classical" bidentate [3] coordination of the carboxylic group at U(VI) is present. These results were the occasion for further fundamental investigations of the interaction between U(VI) with the carboxylic group in aqueous solution (see Proposal 20_01_55 and 20_01_66).

Tab.1: EXAFS structural parameters of the U(VI)/benz/4-hybenz complexes at pH 4.

sample	U-O _{axial(ax)}		U-Atom _{equatorial(eq)}			
	R [Å]	σ ² ·10 ³ [Å ²]	Atom	N	R [Å]	σ ² ·10 ³ [Å ²]
benz	1.778(3)	2.0(2)	O _{eq}	4.9(5)	2.409(6)	9(1)
			C	2.2(4)	2.91(1)	4
4-hybenz	1.774(3)	1.6(2)	O _{eq}	6.5(8)	2.427(7)	12(1)
			C	3.0(4)	2.882(8)	4

N – coordination number; R – radial distance with an uncertainty of ± 0.02 Å; σ² – Debye-Waller factor; during the fitting procedure N of O_{ax} was held constant at N=2; the standard deviations are given in parenthesis.

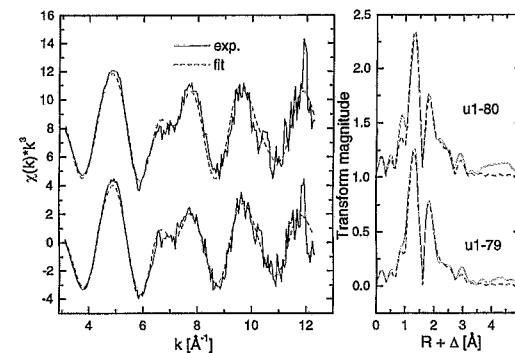



Fig. 1: Raw U L_{III}-edge k³-weighted EXAFS spectra of the aqueous solutions of U(VI)/benz (u1-79) and U(VI)/4-hybenz (u1-80) (left) and their corresponding Fouriertransforms (FT) (right).

References:

1. Matz, W., et al., J. Synchrotron Rad. **6**, 1076 (1999).
2. Zabinsky, S. I., et al., Phys. Rev. B **52**, 2995 (1995).
3. Templeton, D. H., et al., Act. Cryst. **C41**, 1439 (1985).
4. Thompson, H. A., et al., American Mineralogist **82**, 483 (1997).
5. Howatson, J., et al., J. inorg. nucl. Chem. **37**, 1933 (1975).

	Experiment title: Interaction between bacterial S-layers and uranium using EXAFS	Experiment number: 20_01_54
	Beamline: BM 20	Date of experiment: from: 06. 10. to: 07.10.01
Shifts: 3	Local contact(s): Christoph Hennig	Received at ROBL: 22.10.2002
Names and affiliations of applicants (* indicates experimentalists): J. Raff ¹ , T. Reich ^{*2} , C. Hennig ^{*2} , A. Rossberg ^{*2} , H. Funke ^{*2} , M.L. Merroun ^{*1} , M. Walter ^{*1} , S. Selenska-Pobell ¹ ¹ Institute of Radiochemistry, FZR e.V. P.O. Box 51 01 19, 01324 Dresden, Germany ² ESRF-ROBL/CRG, B.P. 220, 38043 Grenoble Cedex, France		

Report:

Introduction. The natural isolate *Bacillus sphaericus* JG-A12, recovered from a uranium mining waste pile, and the reference strain *B. sphaericus* NCTC 9602 possess surface layers (S-layer) as outermost cell wall components [1]. S-layers are highly ordered paracrystalline protein layers on the surface of many bacteria and archaea. It has been demonstrated that S-layers interact with different metal ions [2-4]. In this respect the S-layer of the uranium mining waste pile isolate *B. sphaericus* JG-A12 is of special interest because it may possess a high affinity to a large variety of toxic metals and may play an important role in uranium detoxification. In addition, the S-layer proteins of *B. sphaericus* JG-A12 and NCTC 9602 differ at their N-terminal domains significantly from all other S-layers studied up to date [1]. In this study we examined the interaction of uranium with native and recrystallised S-layers of *B. sphaericus* JG-A12 and NCTC 9602 to identify the chemical groups of the protein, which are responsible for metal binding.

Experimental. The incubation of the S-layers with uranium was carried out at pH 4.5. As S-layer lattices are not stable at pH values <5, the purified lattices were stabilized with 1-Ethyl-3-(N,N'-dimethyl-aminopropyl)-carbodiimid (EDC). 20 mg native or recrystallised S-layers were incubated with 9×10^{-4} M uranium nitrate in 0.9 % NaClO₄, pH 4.5. After incubation, the S-layers were washed in 0.9 % NaClO₄, pH 4.5 and in aqua. dest., pH 4.5. The pellets were resuspended in water, dried in a vacuum incubator at 30 °C and powdered.

Results and discussion. In all samples uranium is coordinated by two axial oxygen atoms (O_{ax}) at a distance of 1.77-1.78 Å. The second and the third shells are issue from the contribution of two oxygen at the equatorial plan. However the third one could be modeled to nitrogen atom, as well (EXAFS could not distinguish between O and N atoms). All FTs contain a shoulder at about 2.5 Å, which can be well fit by C neighbors at 2.89-2.91 Å. This distance is typical for carbonate groups coordinated to

U(VI) in a bidentate fashion. Moreover, if this FT peak originates from bidentate carboxyl ligands, the U-O_{eq} bond distance should be approximately 2.46-2.49 Å which is the case in this work. Fig. 1 and 2, a weak peak appears at about $R + \Delta R = 3$ Å (not corrected for phase shift) in the FT, which was modeled to the interaction of uranium with phosphorous giving a distance of 3.64-3.67 Å. A fifth peak at about 3.6 Å was modeled with a single scattering phosphorous shell giving a contribution at about 3.87-3.89 Å.

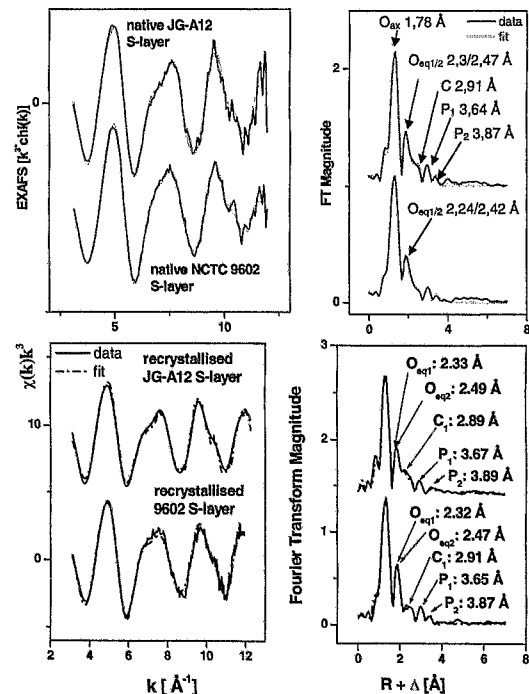



Fig. 1: Uranium L_{III}-edge k³-weighted EXAFS spectra (left) and corresponding FT (right) of the uranium complexes formed by native S-layers of *B. sphaericus* JG-A12 and *B. sphaericus* NCTC 9602

Fig. 2: Uranium L_{III}-edge k³-weighted EXAFS spectra (left) and corresponding FT (right) of the uranium complexes formed by recrystallised S-layers of the *B. sphaericus* strains JG-A12 and NCTC 9602

In summary, EXAFS analysis of the uranium complexes formed by native and recrystallised S-layers of *B. sphaericus* JG-A12 and *B. sphaericus* NCTC 9602 demonstrated the implication of carboxyl and phosphate groups in the interaction with uranium.

References

- 1/ Raff J., PhD Thesis, University of Leipzig (2002)
- 2/ Shenton W. et al., Nature 389, 585-587 (1997)
- 3/ Diehlweitt S. et al., Supramolecular Science 5, 15-19 (1998)
- 4/ Pompe W. et al., Metallkd. 90, 1085-1091 (1999)

 ROBL-CRG	Experiment title: EXAFS investigation of uranium(VI) complexation with phenolic OH groups and carboxylic groups	Experiment number: 20_01_55 20_01_66
	Beamline: BM 20	Date of experiment: from: 07.10.01 to: 09.10.01 from: 26.02.02 to: 27.02.02 from: 31.03.02 to: 02.04.02 from: 22.07.02 to: 23.07.02
Shifts: 19	Local contact(s): A. Roßberg C. Hennig H. Funke	<i>Received at ROBL:</i> 05.11.2002
Names and affiliations of applicants (* indicates experimentalists): A. Roßberg* ² , T. Reich* ² , H. Funke* ² , C. Hennig* ² , M. Merroun* ¹ , M. Walter* ¹ , G. Geipel ¹ , B. Bernhard ¹ , D. Vulpius ¹		
¹ Forschungszentrum Rossendorf e.V., Institute for Radiochemistry, P.O. Box 510119, 01314 Dresden, Germany ² ESRF-ROBL/CRG, Avenue des Martyrs, B.P. 220, 38043 Grenoble Cedex,		

Report:*Experimental:*

We have investigated the interaction between U(VI) and various simple organic aliphatic and aromatic model compounds in aqueous solution. The variation of the ligand permitted the investigation of the influence of the acidity of the functional groups (rest-COOH, rest-OH) on the U(VI)/ligand interaction. We have also investigated the U(VI)/ligand interaction as a function of pH. The ligands were 2,3-dihydroxybenzoic acid, 4-hydroxybenzoic acid, salicylic acid, formic acid, and monochlor acetic acid. In this report we show the results of the investigation of the system U(VI)/monochlor acetic acid. For each solution the U(VI) concentration was 75 mM and the monochlor acetic acid concentration was 1.0 M. The pH of the solutions was varied (Tab. 1). The U L_{III}-edge X-ray absorption spectra were measured using the Si(111) double-crystal monochromator in channel cut mode [1]. The spectra were recorded in transmission mode. The energy scale was calibrated using an Y foil. For EXAFS analysis the theoretical scattering phases and amplitudes were calculated with the scattering code FEFF6 [2] using the crystal structure of sodium uranyl(VI)-triacetate [3].

Results and Discussion:

The U L_{III}-edge k³-weighted EXAFS spectra are shown in Fig. 1 and the EXAFS structural parameters in Tab. 1. For O_{ax} the radial distances and the Debye-Waller factors increase slightly with pH. The coordination number of O_{eq} is nearly constant. With increasing pH for O_{eq} the radial distances decreases and the Debye-Waller factors increases. For pH 1.0 all EXAFS structural parameters agrees to those observed for U(VI) hydrate (see 20_01_39). From factor analysis results of the EXAFS spectra we can conclude that one species is the U(VI) hydrate and that for the other species U(VI) interact with the carboxylic group of monochlor acetic acid. The peak at 2.3 Å in the FT (Fig. 1) is a backscattering contribution of carbon and/or a oxygen atom of the carboxylic group.

Tab.1: EXAFS structural parameters of the aqueous U(VI)/monochlor acetic acid mixtures at different pH values.

pH	U-O _{axial(ax)}		U-Atom _{equatorial(eq)}		
	R [Å]	$\sigma^2 \cdot 10^3$ [Å ²]	N	R [Å]	$\sigma^2 \cdot 10^3$ [Å ²]
1.0	1.770(1)	1.47(6)	5.3(3)	2.402(3)	8.5(6)
2.3	1.773(1)	1.52(6)	5.6(4)	2.390(4)	11.5(8)
4.0	1.775(1)	1.60(6)	5.5(4)	2.378(4)	12.0(9)

N – coordination number; R – radial distance with an uncertainty of ± 0.02 Å; σ^2 – Debye-Waller factor; during the fitting procedure N of O_{ax} was held constant at N=2; the standard deviations are given in parenthesis.

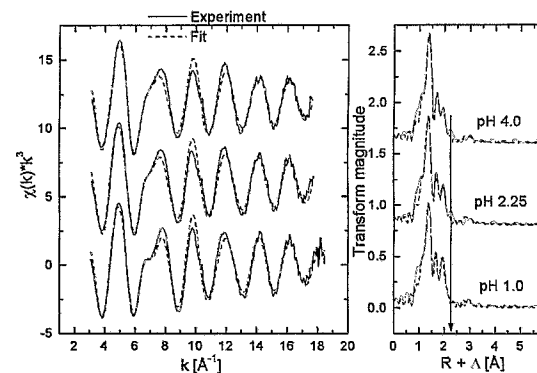


Fig. 1: Raw U L_{III}-edge k³-weighted EXAFS spectra of the aqueous solutions of U(VI)/monochlor acetic acid at different pH (left) and their corresponding Fouriertransforms (FT) (right).

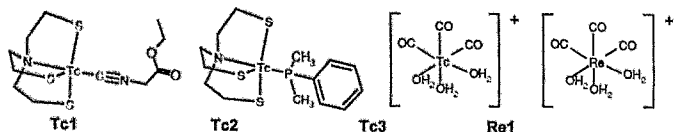
References:

- Matz, W., et al., J. Synchrotron Rad. **6**, 1076 (1999).
- Zabinsky, S. I., et al., Phys. Rev. B **52**, 2995 (1995).
- Templeton, D. H., et al., Act. Cryst. **C41**, 1439 (1985).

 ROBL-CRG	Experiment title: EXAFS studies of technetium and rhenium complexes with relevance to radiopharmaceutical chemistry	Experiment number: 20_01_56
	Beamline: BM 20	Date of experiment: from: 07.11.01 to: 09.11.01
Shifts: 6	Local contact(s): Christoph Hennig	Received at ROBL: 30.09.2002
Names and affiliations of applicants (* indicates experimentalists): J.-U. Kuenstler ^{*1)} , S. Seifert ^{*1)} , H.-J. Pietzsch, C. Hennig ^{*2)} , A. Rossberg ^{*2)} ¹⁾ Institute of Bioinorganic and Radiopharmaceutical Chemistry ²⁾ Institute of Radiochemistry Research Center Rossendorf P.O. Box 510119, 01314 Dresden, Germany		

Report:

In radiopharmaceutical chemistry, the most frequently used technetium compounds are complexes of the oxo ion $[\text{Tc}=\text{O}]^{3+}$. The applicability of such Tc(V) complexes is limited because of a possible instability and strong influence of the $[\text{Tc}=\text{O}]^{3+}$ unit on the biobehaviour. Thus, there is a considerable interest in alternative chelate systems that offer lower polarity and enhanced in vivo stability. We created a new type of Tc(III) chelate that should fulfill these requirements. We synthesized e. g. Tc1 and Tc2 as prototypic representatives of this novel class of Tc(III) compounds [1]. EXAFS analyses should be compared with results of single-crystal X-ray diffraction analyses. The detection of non-coordinated carbon atoms of the chelate ligand should be studied. Investigations of Tc and Re carbonyl chemistry has led to an organometallic M(I) aqua ion, $[\text{M}(\text{CO})_3(\text{H}_2\text{O})_3]^+$ ($\text{M} = \text{Tc}, \text{Re}$), as a precursor for the preparation of complexes containing the small $[\text{M}(\text{CO})_3]^+$ moiety. Tc(I) and Re(I) tricarbonyl complexes represent also a new and promising approach to low valent, non-polar and inert compounds [2]. Structural parameters of the precursor complexes Tc3 and Re1 which are available only in aqueous solution should be determined by EXAFS measurements.



Due to the extremely small concentration of the radionuclide present in the radiopharmaceutical preparation, XAS studies as well as most of chemical investigations employ the long-lived isotopes ^{99}Tc or inactive ^{187}Re .


We applied Tc K-edge (21.044 keV) and Re L_{III} -edge (10.535 keV) EXAFS measurements (transmission mode, room temperature, two or three scans averaged; Tc1, Tc2: solid, each sample contained 4 mg metal pressed into Teflon powder; Tc3, Re1: concentration ~ 0.01 to 0.02 M, 2 cm sample thickness). The data

were evaluated using the EXAFSPAK software. Effective scattering amplitude and wave phase-shift functions were calculated using FEFF6.

For Tc1 atomic distances of 2.22 Å (averaged distances for Tc-N and Tc-S), 1.94 Å (Tc-C_{CH}) and 3.13 Å (Tc-N_{CH}) were estimated. For the six carbon atoms included in the chelate system a Tc-C distance of 3.12 Å and a coordination number of 5.3 with a high standard deviation of ± 1.7 was obtained. For Tc2 atomic distances of 2.24 Å (averaged distances for Tc-N and Tc-S), 2.31 Å (Tc-P) and 3.19 Å (Tc-C, averaged value for six carbon atoms of the chelate system and two carbon atoms bound to phosphorous) were estimated. For the carbon coordination shell a coordination number of 7.4 was obtained but also with a high standard deviation of ± 1.6 . The estimated distances and coordination numbers for Tc1 and Tc2 are consistent with the data from X-ray crystal-structure analyses. The difference between the bond distances Tc-N and Tc-S obtained from X-ray crystal-structure data is distinct smaller than the expected resolution in distance of the EXAFS analysis, therefore only an averaged value was obtained. To get a satisfactory evaluation of the EXAFS spectra, nearly linear multiple-scattering paths along the isocyanide group were taken into account. The estimated atomic distances for Tc3 are 1.89 Å (Tc-C), 2.21 Å (Tc-O_{aq}) and 3.05 Å (Tc-O_{co}) and for Re1 1.91 Å (Tc-C), 2.19 Å (Tc-O_{aq}) and 3.07 Å (Tc-O_{co}). Thus no differences between the atomic distances of the analogous complexes were observed assuming an uncertainty of ± 0.02 Å. The estimated coordination numbers agree with the expected values. To obtain a satisfactory evaluation of the EXAFS spectra multiple-scattering paths to model the oxygen atom of the carbon monoxide had to be included.

References:

- [1] H.-J. Pietzsch et al., *Bioconj. Chem.*, **12**, 538 (2001).
 [2] R. Alberto et al., *Coordination Chem. Rev.*, **190-192**, 901 (1999).

	Experiment title: δ -phase stabilisation in $\text{Pu}_x\text{Am}_{(1-x)}$ alloys as studied by EXAFS	Experiment number: 20_01_57 EU #14
	Beamline: BM 20	Date of experiment: from: 8.12.01 to: 11.12.01
Shifts: 9	Local contact(s): T. Reich, C. Hennig, A. Bauer	<i>Received at ROBL:</i> 22.02.2002
Names and affiliations of applicants (* indicates experimentalists): N.Baclet*, B. Ravat*, L. Jolly*, C. Valot*, GL. Gogolusko* CEA-Centre de Valduc, F-21120 Is Sur Tille, France		

Report:

Introduction

The plutonium δ -phase (face-centered cubic) can be stabilized at room temperature with so-called deltagen elements such as Ga, Al, Am, Ce... While PuGa and PuAl alloys have been extensively studied, few works have been devoted to PuCe and PuAm alloys. A Ph.D. (initiated in 10/98) was devoted to a better understanding of the δ -phase stabilization in especially binary $\text{Pu}_{(x)}\text{Am}_{(1-x)}$ alloys [1]. Electronic and crystalline structure appeared to be strongly related in these alloys. Electronic effects have been suggested through a positive deviation from the Vegard's law, as shown by XRD [2]. A complete localization of the 5f electrons of Pu atoms has been indicated by electrical and magnetic measurements for an Am content of about 25 at% [1]. However, the techniques used until now gave only a general information whereas, as EXAFS measurements in $\text{Pu}_{(x)}\text{Ga}_{(1-x)}$ alloys revealed, important phenomena can happen at a short range order [3,4].

Experiment

EXAFS measurements have been performed at the LIII-edges of Pu (18057 eV) and Am (18504 eV) in the transmission mode on three alloys: $\text{Pu}_{0,95}\text{Am}_{0,05}$, $\text{Pu}_{0,85}\text{Am}_{0,15}$, and $\text{Pu}_{0,75}\text{Am}_{0,25}$. As the cryostat from the BM20 line was out of order, EXAFS spectra have been recorded at room temperature inducing a damping of the EXAFS oscillations due to thermal disorder; the information was then limited to the first

coordination shell. No EXAFS oscillation could be detected at the Am LIII-edge on the $\text{Pu}_{0,95}\text{Am}_{0,05}$ alloy.

Results and discussion

The results (Fig. 1) highlight an increase in both Am-Pu and Pu-Pu distances with the Am content. An increase in cell parameter with Am content has already been observed by XRD, technique which is sensitive to long range order. This can first be attributed to a steric effect, the Am atomic volume being more important than the Pu one. Even if only two experiments have been performed at the Am LIII-edge, we can note that the Am-Pu distances increase more than the Pu-Pu ones. This suggests that the localization of the 5f electrons appears preferentially on Pu atoms that are close to the Am ones. Interatomic distances obtained from EXAFS (Pu-Pu distance) are compared to those deduced from XRD ($a/\sqrt{2}$). For PuGa alloys, both techniques lead to the same interatomic values. For $\text{Pu}_{(x)}\text{Am}_{(1-x)}$ alloys, these distances are strongly different, as previously observed in PuCe alloys [1]; this is not explained yet.

In order to better understand whether the localization of the plutonium 5f electrons would happen preferentially around the Am atoms, it is necessary to perform new experiments at low temperature to extend the investigation to the higher coordination shells. Moreover, it is interesting to extend the study to a $\text{Pu}_{0,57}\text{Am}_{0,43}$ alloy, in which the localization of the Pu 5f electrons may be complete

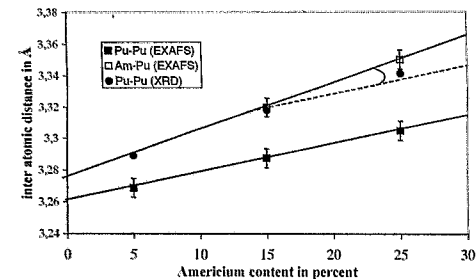



Fig. 1: Change in the Am-Pu and Pu-Pu interatomic distances with the Am content in the alloy

[1] M. Dorneval, "Structure électronique d'alliages Pu-Ce(-Ga) et Pu-Am(-Ga) stabilisés en phase δ ", thèse de l'Université de Bourgogne, septembre 2001.

[2] M. Dorneval, N. Baclet, "Plutonium Futures - the Science", July 2000, Santa-Fe, New Mexico.

[3] Ph. Faure, B. Deslandes, D. Bazin, C. Tailland, J.M. Fournier, J. Alloys and Comp., 244, p131 (1996).

[4] S. D. Conradson, "Where is the Gallium?", Los Alamos Science Number 26, 2000.

 ROBL-CRG	Experiment title: Uranium sorption onto chlorite	Experiment number: 20_01_58
	Beamline: BM 20	Date of experiment: from: 01.12.01 to: 03.12.01
Shifts: 5	Local contact(s): Christoph Hennig	<i>Received at ROBL:</i> 12.11.2002
Names and affiliations of applicants (* indicates experimentalists): E. Krawczyk-Bärsch, T. Arnold, T. Reich*, C. Hennig*, G. Bernhard Forschungszentrum Rossendorf e.V., Institute of Radiochemistry, P.O. Box 51 01 19, 01314 Dresden, Germany		

Report:

Introduction:

Fe-oxyhydroxides, probably ferrihydrite, are formed as heterogenous and homogenous colloids in the neutral pH-range during the weathering of an iron-rich chlorite /1/. Previous studies /2/ showed that ferrihydrite is dominating the sorption of U(VI) due to the high specific surface area during the weathering of chlorite /2/. In first EXAFS investigations (project no. 20-01-44) on the sorption behavior of U(VI) no significant structural difference was obtained by using a weathered and a less weathered chlorite sample. With respect to this results an iron-poor chlorite was used for further investigations to be compared to the iron-rich chlorite.

Experimental:

Both chlorite samples with a grain size of 2 - 6,3 μm were weathered in a 0.01 M NaClO_4 -solution during 2 months supposing that only the iron-rich chlorite is forming ferrihydrite. After addition of a $8.6 \cdot 10^{-6}$ M uranyl stock solution the pH were adjusted to pH 6.5 and the suspensions were stirred for 6 hours. The samples were subsequently prepared for EXAFS investigation as wet pastes. The L_{III} -edge EXAFS spectra were recorded at room temperature in fluorescence mode at ROBL.

Results and discussion:

Fig. 1 shows the U L_{III} -edge k^3 -weighted EXAFS oscillations and their corresponding Fourier transforms (FT). The EXAFS oscillations and the FT are comparable for both samples (U1-100, U1-101). Independent of the Fe content of the samples the axial (ax) and equatorial (eq) coordination numbers (N) and U-O bond lengths (R) for both samples are comparable (Fig. 1). In comparison to the results of ferrihydrite /3/ there is no difference in

the U-O_{eq} bond lengths. As shown in the previous EXAFS investigations (project no. 20-01-44) no comparable peak of the U-Fe interaction of ferrihydrite is observed.

Tab. 1: EXAFS structural parameters of the iron-rich (U1-100) and iron-poor (U1-101) chlorite.

sample	shell	R [\AA] ^a	N ^b	σ^2 [\AA^2] ^c	ΔE [eV]	k [\AA^{-1}]	error
U1-100	U-O _{ax}	1.78	1.8	0.0019	0.8	3.1-11.5	0.26
	U-O _{ax/MS}	3.57	1.8	0.0039	/		
	U-O _{eq}	2.36	4.7	0.013	/		
U1-101	U-O _{ax}	1.80	2*	0.0038	0.2	3.1-11.5	0.24
	U-O _{ax/MS}	3.59	2	0.0076	/		
	U-O _{eq}	2.39	5*	0.015	/		

Standard deviation in brackets, ^a errors in distance $\pm 0.02 \text{ \AA}$, ^b errors in the coordination number $\pm 25 \%$, ^c Debye-Waller-Faktor, *fixed during the fits

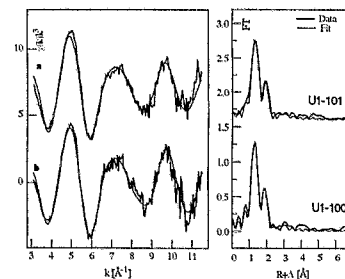



Fig. 1: U L_{III} -edge k^3 -weighted EXAFS oscillations and their corresponding Fourier transforms (FT)

We assume that the formation of ferrihydrite during the weathering of chlorite is too low in order to produce a significant EXAFS signal.

Acknowledgment: This work was supported by DFG (BE 2234/4-1)

References:

- /1/ Krawczyk-Bärsch, E. et al. (2002): *Chemical Geology* (submitted)
- /2/ Arnold, T. et al. (1998): *Chemical Geology* 151, 129-141
- /3/ Reich, T. et al. (1998): *J. Electron Spectroscopy* 96, 237-243

 ROBL-CRG	Experiment title: EXAFS investigations of uranium complexation by sugar phosphates	Experiment number: 20_01_60
	Beamline: BM 20	Date of experiment: from: 07.12.01 to: 08.12.01 from: 07.05.02 to: 09.05.02 from: 17.07.02 to: 18.07.02
Shifts: 10	Local contact(s): A. Roßberg, C. Hennig	<i>Received at ROBL:</i> 18.10.2002
Names and affiliations of applicants (* indicates experimentalists): A. Koban, A. Günther, T. Reich*, A. Roßberg*, H. Funke*, C. Hennig*, M. Walter* Forschungszentrum Rossendorf e.V., Institut für Radiochemie, P.O. Box 510119, D-01314 Dresden, Germany		

Report:

The complexation of U(VI) with glucose 1-phosphate (G1P), glucose 6-phosphate (G6P), and fructose 6-phosphate (F6P) was investigated by EXAFS.

Experimental: The EXAFS-measurements were carried out on solutions containing 10^{-3} M UO_2^{2+} , and 5×10^{-2} M sugar phosphate ($I=0.15$ M) at $\text{pH}=4.0$ in polyethylene tubes of 13 mm diameter. The U L_{III} -edge spectra were measured in fluorescence modus. The EXAFS spectra were analyzed using the suite of programs EXAFSPAK. The theoretical scattering phase and amplitude functions used in data analysis were calculated for the model compound $\text{Ca}(\text{UO}_2)_2(\text{PO}_4)_2 \times 6 \text{H}_2\text{O}$ [1] using the FEFF8.

Results and discussion: The raw U L_{III} -edge k^3 -weighted EXAFS spectra and the corresponding Fourier transform (FT) for the uranium solutions containing glucose 1-phosphate (U-G1P) and glucose 6-phosphate (U-G6P) are shown in Fig. 1 and the fit results are listed in Tab. 1. In the FT from the sample U-G1P four peaks are visible. The first and the second peak correspond to the scattering contribution of the two axial oxygen atoms (O_{ax}) of the uranyl ion and the scattering contribution of the equatorial oxygen atoms ($\text{O}_{eq(1)}$), respectively. The third peak is probably due to backscattering from a light element like carbon or oxygen. Because of the respectable possibilities in this molecule, we assumed an oxygen shell ($\text{O}_{eq(2)}$) in our fit. The fourth peak we interpret as a scattering contribution of phosphorus.

The main contributions to the total EXAFS amplitude are caused by the axial and the equatorial oxygen atoms. In comparison, the contributions of the

$\text{O}_{eq(2)}$ and P coordination shells are very small. Therefore, we consider the O_{ax} and $\text{O}_{eq(1)}$ shells as major and the $\text{O}_{eq(2)}$ and P shells as minor components in the EXAFS spectra, respectively. To increase the precision in determination of the EXAFS structural parameters for the minor components, we use the difference technique as described in [2]. Furthermore the twofold degenerated 3-legged MS path $\text{U-O}_{eq(1)}\text{-P}$ (MS2) had to be considered because its intensity is similarly to the backscattering of P.

The spectra of the sample U-G6P differs from those of U-G1P regarding to the minor components. Its FT contains a peak at $4.36 + \Delta\text{Å}$. This backscattering can be interpreted as an U-U interaction. But there is no scattering contribution of phosphorus visible.

The spectra of the uranium solution containing fructose 6-phosphate (U-F6P) are similar to those of U-G6P.

However, the interpretation of the data concerning the structure of the uranium sugar phosphate complexes needs any further investigations.

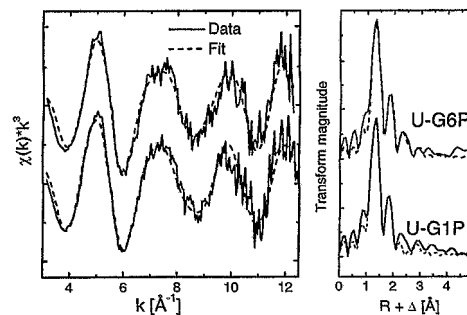


Fig. 1: Raw U L_{III} -edge k^3 -weighted EXAFS spectra (left) and the corresponding Fourier transform (FT) (right) of the samples U-G1P and U-G6P.

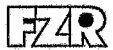
Table 1: Summary of the EXAFS structural parameters.

Sample	Shell	N	R	σ^2
U-G1P	U- O_{ax}	2	1.771(3)	0.0019(2)
	U- $\text{O}_{eq(1)}$	4.3(5)	2.336(7)	0.008(1)
	U- $\text{O}_{eq(2)}$	0.82(6)	2.864(5)	0.003
	U-P	$N_P=2.4(6)$	3.587(9)	0.0030(7)
	MS2	$2xN_P$	3.71(1)	0.0014(8)
U-G6P	U- O_{ax}	$2^{(2)}$	1.773(3)	0.0014(2)
	U- $\text{O}_{eq(1)}$	4.3(5)	2.326(7)	0.009(1)
	U- $\text{O}_{eq(2)}$	1.3(2)	2.87(1)	0.003
	U-U	0.77(3)	4.586(1)	0.0044(2)

Standard deviations of variable parameters are given in parenthesis; N - coordination number; R - Radial distance in Å with an uncertainty of ± 0.02 Å; σ^2 - Debye-Waller factor in Å²

References:

- [1] Makarov, E. S., et al., Doklady Akademii Nauk SSSR **132**, 673 (1960).
 [2] Teo, B. K.: EXAFS: Basic Principles and Data Analysis, Springer Verlag New York 1986.

 ROBL-CRG	Experiment title: EXAFS investigations of uranium complexation by peptides	Experiment number: 20_01_61
	Beamline: BM 20	Date of experiment: from: 07.12.01 to: 07.12.01 from: 09.05.02 to: 11.05.02
Shifts: 7	Local contact(s): Andre Roßberg	<i>Received at ROBL:</i> 25.11.2002
Names and affiliations of applicants (* indicates experimentalists): A. Günther ¹ , T. Reich ^{*2} , A. Roßberg ^{*2} , H. Funke ^{*2} , C. Hennig ^{*2}		
¹ Forschungszentrum Rossendorf e.V., Institute for Radiochemistry, P.O. Box 510119, 01314 Dresden, Germany ² ESRF-ROBL/CRG, Avenue des Matryrs, B.P. 220, 38043 Grenoble Cedex, France		

Report:**Experimental:**

We have investigated the complex formation of the U(VI) with the tripeptide glutathione and its basic components glycine, glutamic acid and cysteine (amino acids) at pH 4. The uranium concentration in the complex solutions was $1.0 \cdot 10^{-3}$ M. The concentration of the organic ligands was $2.5 \cdot 10^{-1}$ M (glycine, cysteine), $3.0 \cdot 10^{-2}$ M (glutamic acid) and $5.0 \cdot 10^{-2}$ M in the case of glutathione. The ionic strength of the complex solutions was adjusted to 0.1 M (amino acids) or 0.15 M (glutathione) with NaClO₄. The U L_{III}-edge EXAFS spectra were measured in fluorescence mode using a 4-pixel-germanium detector. The EXAFS spectra were analyzed according to standard procedures using the suite of programs EXAFSPAK /1/. The theoretical scattering phases and amplitudes were calculated with the scattering code FEFF 6 /2/ using the model compound sodium tris(acetato)dioxouranate /3/. The analysis of the minor component in the spectra was realized by the difference technique described in /4/.

Results and discussion:

The figure shows the raw U L_{III}-edge k^3 -weighted EXAFS spectra and their corresponding Fourier transforms (FT) of the investigated organic uranyl complex solutions. The fit results are listed in the table. The first and the second peak correspond to the scattering contribution of the two axial oxygen atoms (O_{ax}) of the uranium(VI) ion and the scattering contribution of the

equatorial oxygen atom (O_{eq}) (major components). The third peak in the spectra at 2.3 Å we interpret as a backscattering carbon atom (minor component).

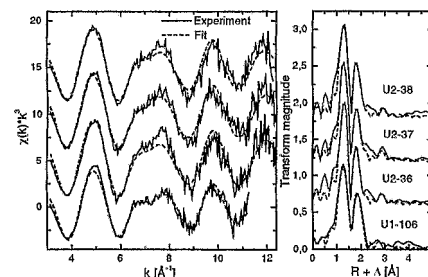


Fig.: Raw U L_{III}-edge k^3 -weighted EXAFS spectra (left) and its corresponding Fourier transform (right) of the complex solutions at pH 4:

U(VI)/glutathione (U1-106)
 U(VI)/glycine (U2-36)
 U(VI)/glutamic acid (U2-37)
 U(VI)/cysteine (U2-38)

From this EXAFS study we conclude, that the coordination of U(VI) to all these organic ligands is identical. There occurs an interaction between U(VI) and the carboxylic group of the corresponding bioligand.


Table: EXAFS structural parameters of several complex systems U(VI)/organic ligand at pH 4

System	U-O _{ax}		U-atom _{eq}			
	R [Å]	$\sigma^2 \cdot 10^3$ [Å ²]	atom	N	R [Å]	$\sigma^2 \cdot 10^3$ [Å ²]
U1-106 (glutathione)	1.771(3)	4.0(3)	O	4.7(4)	2.394(5)	8.6(9)
			C	0.93(6)	2.955(4)	
U2-36 (glycine)	1.771(3)	1.4(2)	O	6.5(9)	2.376(9)	1.2(2)
			C	1.34(7)	2.921(3)	
U2-37 (glutamic acid)	1.772(3)	1.7(2)	O	6.4(8)	2.388(8)	1.3(2)
			C	1.7(1)	2.878(4)	
U2-38 (cysteine)	1.776(3)	2.2(2)	O	5.4(6)	2.391(8)	1.1(1)
			C	1.19(6)	2.922(3)	

The standard deviations are given in parenthesis. During the fitting procedure the coordination number of O_{ax} was held constant at N=2. The shift of the binding energy ΔE_b was used for the fit of all coordination shells of the corresponding sample.

References:

- George, G. N., Pickering, I. J.: EXAFSPAK - A Suite of Computer Programs for Analysis of X-Ray Absorption Spectra, Stanford Synchrotron Radiation Laboratory, Stanford, CA, USA, (1995)
- Zabinsky, S. I., Rehr, J. J., Ankudinov, A., Albers, R. C., Eller, M. J.: Multiple-scattering calculations of x-ray-absorption spectra, Phys. Rev. B52, 2995 (1995)
- D. H. Templeton et al.: Acta Cryst. c41, 1439-1441 (1985)
- Teo, B. K.: EXAFS - Basic Principles and Data Analysis, Springer-Verlag, New York 1986

	Experiment title: Americium Sorption onto Ferrihydrite	Experiment number: 20_01_64
	Beamline: BM 20	Date of experiment: from: 17.02.02 to: 19.02.02 21.02.02 22.02.02 20.09.02 23.09.02
Shifts: 15	Local contact(s): Christoph Hennig	<i>Received at ROBL:</i> 13.11.2002
Names and affiliations of applicants (* indicates experimentalists): S. Stumpf ^a , Th. Stumpf ^a , C. Hennig ^a , H. Funke ^a , T. Reich ^a , A. Rossberg ^a Forschungszentrum Rossendorf, Institut für Radiochemie		

Report:

Motivation

For the long-term performance assessment of nuclear waste repositories, knowledge concerning the interactions of actinide ions with mineral surfaces is imperative. The mobility of released radionuclides is strongly dependent on the sorption/desorption processes at mineral surfaces and their incorporation into the mineral frame.

Hydrous iron oxides (ferrihydrite) are globally of great importance in the environment. Ferrihydrite is able to dominate the retardation of radionuclides in particular the actinides in the near-field as well as in the far-field of a nuclear waste repository¹. Upon heating pure ferrihydrite converts to crystalline goethite and hematite. This EXAFS study deals with the question if Am(III) can be immobilized by sorption onto ferrihydrite. Furthermore the interaction of Am(III) with the mineral surface after a thermal treatment is studied.

Experimental

The long-lived americium isotope Am-243 ($t_{1/2} = 7370$ years) was provided from the Oak Ridge National Laboratory. The preparation of the EXAFS samples (Am2-1/pH 5.5 and Am2-2/pH 8) was made at 25 ± 1 °C in a glove box under nitrogen atmosphere. After the samples were measured by EXAFS they were put into a water bath and heated at 85°C for 67 days. The transformation product (goethite) was characterized by IR and TEM after 67 days. After transformation the Am(III) samples (Am2-1T/pH 5.5 and Am2-2T/pH 8) were again measured by EXAFS.

Results

The Fourier transform of the EXAFS spectra at pH 5.5 and pH 8 show two peaks (Fig. 1). The first one can be attributed to a Am-O distance of 2.48 Å and agrees with the value cited in literature². This distance is comparable to the bond length that can be found for the Am(III) aquo ion determined either in transmission (Am1-6) and fluorescence (Am2-7). Moreover there is no significant change in the coordination number (Tab. 1). Surely the number of coordinating water overbalances the coordination by the substrate. The second peak can be attributed to a Am-Fe distance of 3.78 Å. This bond length indicates an inner sphere, bidentate coordination of Am(III) onto ferrihydrite. After transformation of the samples the question arises if Am is incorporated in the goethite crystal structure. The fourier transformed of the EXAFS spectra at pH 5.5 and pH 8 are also shown in figure 1. There is no increase of the Am-Fe peak intensity. Therefore we can conclude that Am is not incorporated after transformation but still surface coordinated.

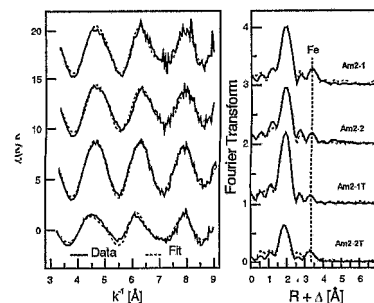



Figure 1: k^3 - weighted EXAFS spectra of the Am L_{III} -edge (left) and the according fourier transformed spectra (right) of the Am/ferrihydrite sorption samples before (Am2-1/2) and after the transformation (Am2-1T/2T) at pH 5.5 and 8.

Sample	Shell	R [Å] ^a	N ^b	σ^2 [Å ²] ^c
Am1-6	Am-O	2.494(2)	7.8(2)	0.0075(2)
Am2-7	Am-O	2.494(2)	7.0(2)	0.0058(3)
Am2-1	Am-O	2.489(6)	6.2(4)	0.0077(8)
	Am-Fe	3.78(3)	1*	0.004(2)
Am2-2	Am-O	2.480(5)	6.0(4)	0.0080(7)
	Am-Fe	3.79(2)	1*	0.010(2)
Am2-1T	Am-O	2.486(2)	6.7(2)	0.0083(4)
	Am-Fe	3.80(5)	0.5(2)	0.008*
Am2-2T	Am-O	2.477(6)	3.5(2)	0.0053(8)
	Am-Fe	3.74(3)	1.2(2)	0.008*

Table 1: EXAFS parameter of the Am(III) aquo ion (Am1-6, Am2-7) and the Am(III)/ferrihydrite sorption samples before (Am2-1/2) and after the transformation (Am2-1T/2T) at pH 5.5 and 8.

¹ Jambor, J.L.; Dutrizac, J.E. *Chem. Rev.* **1998**, *98*, 2549-2585.

² Allen, P.G., Bucher, J.J., Shuh, D.K., Edelstein, N.M., Craig, I.: Coordination chemistry of trivalent Lanthanide and Actinide ions in dilute and concentrated chloride solutions. *Inorg.Chem.*, **2000**, 595

	Experiment title: Interaction between <i>Pseudomonas</i> strains and uranium using EXAFS	Experiment number: 20_01_65
	Beamline: BM 20	Date of experiment: from: 22.02.02 to: 24.02.02 from: 23.06.02. to: 25.06.02 from: 22.07.02. to: 23.07.02 from: 08.12.02. to: 09.12.02
Shifts: 18	Local contact(s): Christoph Hennig	Received at ROBL: 24.11.2002
Names and affiliations of applicants (* indicates experimentalists): M. Merroun*, S. Selenska-Pobell, T. Reich*, A. Rossberg*, C. Hennig*, H. Funke*, M. Walter*		

Report:

Interactions between uranium and microorganisms have been intensively studied. Microbial cells are known to reduce, oxidize, biosorb, bioaccumulate, and bioprecipitate uranium. Living and dead microorganisms possess abundant functional groups, such as carboxyl, hydroxyl and phosphate that bind metal ions. In this paper, we present results of U L_{III} -edge Extended X-ray Absorption Fine Structure (EXAFS) spectroscopy of the uranium complexes formed by different reference strains of *Pseudomonas* which were demonstrated to be relevant to the bacterial populations in the uranium wastes [1].

For EXAFS sample preparation, the cells were resuspended for 48 h in 10 ml 0.5 mM solution of uranyl nitrate (pH 2 and 4.5). After the contact with uranyl, the cells were harvested and washed. The pellets were dried at 30 °C for 24 h and ground (dry samples). Uranium L_{III} -edge X-ray absorption spectra were collected at room temperature in fluorescence mode at the Rossendorf Beamline (ROBL).

Uranium L_{III} -edge EXAFS spectra of the uranium species formed by *P. stutzeri* DSMZ 7136, *P. stutzeri* ATCC 17588, *P. migulae* CIP 105470 at pH 2.5 and 4; and their corresponding Fourier Transforms (FT) are shown in Figure 1. The most prominent peak in all samples occurs at 1.3 Å and arises from the backscattering caused by the oxygen atoms which are the nearest to the uranium. They are identified as axial oxygens (O_{ax}) of the linear uranyl group. Backscatters from oxygen atoms laying in the equatorial plane of the uranyl ion appear as a single broad peak at 1.7-1.8 Å. The U- O_{eq} bond distances of *Pseudomonas*/ uranium complexes formed at pH

2 (2.33 ± 0.02 Å) are longer to of those formed by these strains at pH 4.5 (2.27 ± 0.02 Å). As evident from Figure 1 a weak peak appears in all samples at about $R + \Delta R = 3$ Å (not corrected from phase shift) in the FT, which was modelled to the interaction of uranium with phosphorous in a monodentate fashion giving a distance of 3.62 ± 0.02 Å. The fifth peak could arise from the two degenerated 3-legged MS path U- O_{eq1} -P₁ (model A) or from an additional SS path U-P₂ (model B). In order to resolve this problem, we use difference technique [2]. This method (data not shown) demonstrated that the model B provide best-fit model to the experimental data. Therefore, one may conclude that the phosphate groups of the bacterial strains studied are the main uranium binding sites.

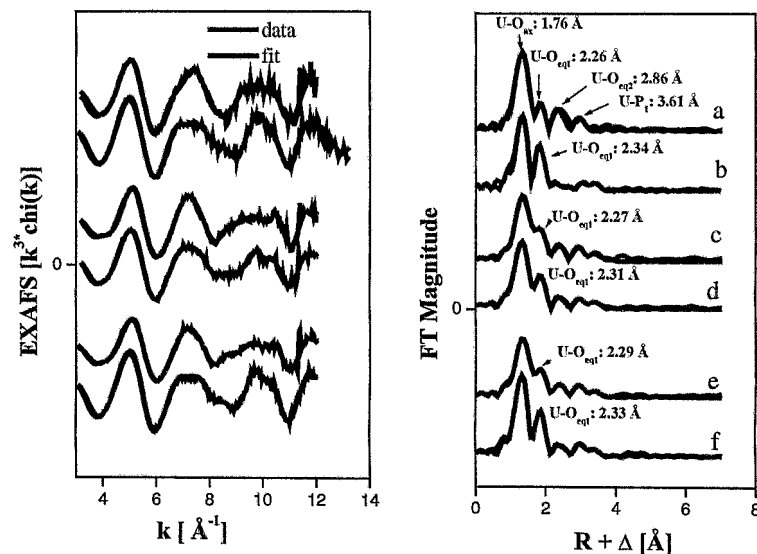



Fig. 1. Uranium L_{III} -edge k^3 -weighted EXAFS spectra (left) and corresponding FT (right) of the *P. stutzeri* DSMZ 7136 at pH 2 (b) and pH 4.5 (a), ATCC 17588 at pH 2 (f) and pH 4.5 (e); and *P. migulae* CIP 105470 at pH 2 (d) and pH 4.5 (c) uranium complexes.

References:

- [1] S. Selenska-Pobell. 2002 *In: Interactions of microorganisms with radionuclides.* (Keith-Roach and Livens, eds.) pp. 225-254.
- [2] M. Merroun *et al.* *Radiochim. Acta* (submitted).

	Experiment title: Characterization of uranium oxidation state in calcite and aragonite speleothems from the Aranzadi gallery	Experiment number: 20_01_67 EU #25
	Beamline: BM 20	Date of experiment: from: 02.03.02 to: 05.03.02
Shifts: 9	Local contact(s): Andreas Bauer	<i>Received at ROBL:</i> 17.10.2002
Names and affiliations of applicants (* indicates experimentalists): * ORTEGA Richard LCNAB, CNRS UMR5084 Université de Bordeaux 1; Gradignan, France * DEVES Guillaume LCNAB, CNRS UMR5084 Université de Bordeaux 1, 33175 Gradignan, France * MAIRE Richard DYMSET, CNRS UMR 5064, Université de Bordeaux 3, 33607 Pessac, France		

Project objectives

The aim of this experiment was to determine the oxidation state of uranium in subterranean concretions, or speleothems, formed of an unusual mixture of calcite and aragonite, using x-ray absorption near edge structure (XANES) spectroscopy.

The understanding of uranium chemistry in speleothems is of great interest because the U/Th method is generally used for the radiometric age dating of this objects. In addition, these samples constitute excellent models to study the geochemistry of uranium on environmental systems, such as natural calcium carbonates. The oxidation state determination of uranium is important to determine the stability of U storage in such natural systems over geological timescales.

The studied speleothems have been sampled in the cave of Pierre Saint-Martin located in the department of "Pyrénées-Atlantiques" (France). Aragonite and calcite speleothems contain significant amounts in uranium (up to 350 µg/g) and strontium (up to 18000 µg/g) measured spatially and chemically by nuclear microprobe analysis. These uranium and strontium

contents are the most important measured in supergene speleothems, connected with infiltration of meteoric waters.

Main achievements

X-ray absorption measurements were successfully performed at ROBL, BM-20, ESRF Grenoble, enabling the determination of uranium oxidation state in aragonite and calcite of speleothems from the Aranzadi gallery. Measurements were made in fluorescence mode at the U L2 edge (20498 eV) as interference from Sr K-edge fluorescence precluded the use of U L3 edge (17166 eV).

Xanes experiments revealed that uranium is present in its hexavalent form both in aragonite and in calcite (Fig. 1). This result confirms that aragonite structure can concentrate relatively large amounts of hexavalent U, hundreds of µg/g, in natural systems. Moreover, it suggests that the relatively high U content found into calcite from the Aranzadi gallery speleothems is not due to the sequestration of U in its tetravalent state.

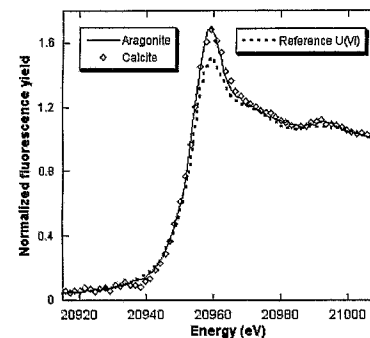
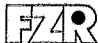
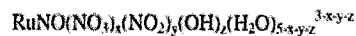


Figure 1. U-L2 edge XANES spectra of U(VI) standard, and from calcite and aragonite speleothems collected in the Aranzadi Gallery. The absorption edge energy of uranium in both samples, calcite and aragonite, is consistent with U(VI) oxidation state.

 ROBL-CRG	Experiment title: Ruthenium nitrosyl speciation in nuclear waste simulants	Experiment number: 20 01 68 EU #28
	Beamline: BM 20	Date of experiment: from: 12.05.2002 to: 14.05.2002
Shifts: 6	Local contact(s): Christoph Hennig	<i>Received at ESRF:</i> 02.12.2002
Names and affiliations of applicants (* indicates experimentalists): A.L. Koster, ¹ A.J. Hynes, ¹ I. May, ¹ J.M. Charnock, ² F.R. Livens. ¹ ¹ Centre for Radiochemistry Research, Department of Chemistry, The University of Manchester, Oxford Road, Manchester, M13 9PL, UK. ² CLRC, Daresbury Laboratory, Daresbury, Warrington, Cheshire, WA4 4AD, UK.		

Report:

Ruthenium is one of the most important fission products formed in the nuclear reaction by thermal fission of ^{235}U or ^{239}Pu . Upon dissolving spent nuclear fuel in nitric acid during fuel reprocessing numerous rutheniumnitrosylnitrate complexes are formed with the general formula¹:



These ruthenium species can cause problems in the reprocessing of spent nuclear fuel, because ruthenium partly coextracts with U and Pu by tri-n-butylphosphate (TBP). In addition, volatile ruthenium species may be produced in the high level waste vitrification process.²

The ruthenium speciation in nuclear fuel processing solutions is complex and is still not fully understood, although it is known that the ruthenium(II)nitrosyl moiety dominates in these solutions. Several techniques (e.g. UV-vis, IR, Raman, NMR) have been used in order to investigate the ruthenium speciation in various nitrite and nitrate containing aqueous solutions in which full characterisation is not possible. XAS could be a useful technique for

the characterisation of these solutions, because this technique can be used to determine local structural parameters of metal complexes.

This work is focussed on using EXAFS for the determination of the ruthenium speciation in nitric acid, NO_2^- and NO_3^- containing solutions. Ru K-edge spectra were recorded at ROBL at room temperature in the fluorescence mode for the solution samples. Also some solid samples (RuNOCl_3 and $\text{Na}_2[\text{RuNO}(\text{NO}_2)_4\text{OH}]$) have been measured to be able to interpret the results of the solution experiments. These solid samples were measured in the transmission mode.

A summary of the preliminary results is shown in table 1.

Sample	CN	Atom	R(Å)	$2\sigma^2$	Assignment
Ru stock in 6	1	O	1.70	0.017	Ru-O (hydroxide)
M NaNO_2	4	O	2.04	0.010	Ru-O (nitrate)
	4	N	3.01	0.004	Ru-N (nitrate)
	1	N	1.84	0.002	Ru-N (nitrosyl)
	1	O	3.13	0.003	Ru-O (nitrosyl)
Ru stock in 6	1	N	1.76	0.012	Ru-N (nitrosyl)
M HNO_3	4	O	2.04	0.013	Ru-O (nitrate)
	2	N	3.09	0.005	Ru-N (nitrate)
	2	O	3.97	0.002	Ru-O (nitrate)
0.01 M	1	N	1.76	0.017	Ru-N (nitrosyl)
$\text{RuNO}(\text{OH})_3$	4	O	2.05	0.007	Ru-O (nitrate)
in 6 M HNO_3	3	N	3.09	0.003	Ru-N (nitrate)


The ruthenium stock solution is a $\text{RuNO}(\text{NO})_x$ stock solution in dilute nitric acid (1.5% Ru). CN is the coordination number, R the interatomic distance, and $2\sigma^2$ is the Debye-Waller factor. The uncertainty in CN is ± 1 .

Table 1. EXAFS fitting parameters for some of the measured ruthenium solutions.

The ruthenium stock solution in a 6 M NaNO_2 solution indicates that a hydroxide group and a nitrosyl ligand are coordinated to the ruthenium metal centre and also four nitrate ligands are coordinated. Therefore the nitrate ligands have to be coordinated as monodentate ligands. The ruthenium stock solution in nitric acid and the 0.01 M $\text{RuNO}(\text{OH})_3$ solution in nitric acid both have two nitrate ligands coordinated to the metal centre. The nitrate ligands are coordinated as bidentate ligands. These preliminary results show that this technique can be very useful for the determination of the ligands bound, coordination modes and hence the ruthenium speciation in solution.

¹ T. Sato, *Radiochimica Acta*, 1989, 47, 219-228.

² J.M. Fletcher, I.L. Jenkins, F.M. Lever, F.S. Martin, A.R. Powell, R. Todd, *J. Inorg. Nucl. Chem.*, 1955, 47, 387-401.

	Experiment title: Uranium binding of sol-gel immobilized cells and S-layers of <i>Bacillus sphaericus</i> JG-A12 and NCTC 9602	Experiment number: 20_01_69
	Beamline: BM 20	Date of experiment: from: 28.03. to: 30.03.2002 from: 20.07. to: 22.07.2002 from: 07.12. to: 09.12.2002
Shifts: 17	Local contact(s): C. Hennig	Received at ROBL: 26.10.2002
Names and affiliations of applicants (* indicates experimentalists): J. Raff* ¹ , H. Funke* ² , A. Rossberg* ² , T. Reich* ² , C. Hennig* ² , M. Walter* ¹ , M.L. Merroun* ¹ , S. Selenska-Pobell ¹ ¹ Institute of Radiochemistry, FZR e.V. P.O. Box 51 01 19, 01324 Dresden, Germany ² ESRF-ROBL/CRG, B.P. 220, 38043 Grenoble Cedex, France		

Report:

Introduction. Vegetative cells of the natural *Bacillus sphaericus* isolate JG-A12, recovered from a uranium mining waste pile, accumulate selectively large amounts of U, Cu, Pb, Al, and Cd /1/. In addition, *B. sphaericus* JG-A12 possesses a surface layer (S-layer) as outermost cell wall component, which differs at its N-terminal domain significantly from all other S-layers studied up to date /2/. The geographic origin of *B. sphaericus* JG-A12 and the ability to interact with heavy metals makes it a good candidate for preparation of bacteria-based ceramics (biocers) for *in situ* bioremediation of uranium contaminated waste waters. Vegetative cells of *B. sphaericus* JG-A12 were embedded in a porous SiO₂ matrix using sol-gel techniques /3/. The aim of this experiment is to investigate the sorption of uranium by the biocer, the single biocomponent and the SiO₂ matrix itself.

Experimental. Sol-gel ceramics were prepared by dispersing vegetative cells in a aqueous silica nanosol, gelling and drying. 100 mg biocer consists of 81.8 mg SiO₂ and 18.2 mg cells. Before the experiments the pH of the biocer was adjusted to pH 4.5 by washing several times with 0.9% M NaClO₄, pH 4.5. For uranium sorption, all components were shaken 48 h in 30 ml 9x10⁻⁴ M uranium nitrate in 0.9% M NaClO₄, pH 4.5 at 30 °C and under air. After incubation, samples were washed with 30 ml 0.9% M NaClO₄ pH 4.5 and with 30 ml aqua dest., pH 4.5. The particles were dried in a vacuum incubator at 30 °C and powdered. Uranium L_{III}-edge (17185 eV) X-ray absorption spectra were collected at room temperature in fluorescence mode at the Rossendorf Beamline (ROBL) using the Si(111) double-crystal monochromator.

Results and discussion. The Fourier transforms (FT) of the EXAFS spectra of the JG-A12 cell-uranium complex show five significant peaks (Fig. 1). The most prominent peak is at 1.3 Å. It arises from the backscattering caused by oxygen atoms nearest to the uranium, which can be identified as the axial oxygens of the linear uranyl

groups (U-O_{ax}) with a distance of 1.76 ± 0.02 Å.

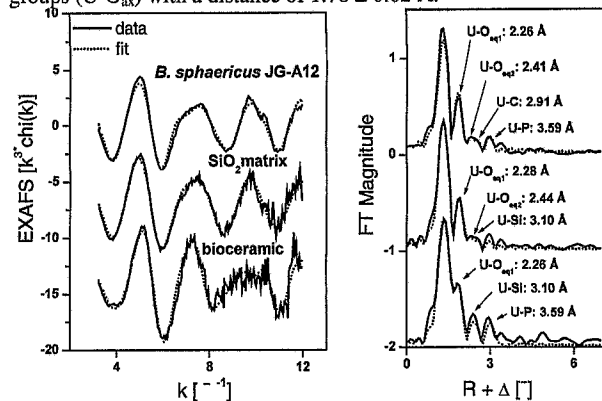



Figure 1: Uranium L_{III}-edge k³-weighted EXAFS spectra (left) and corresponding FT (right) of the uranium complexes formed by cells of *B. sphaericus* JG-A12, the SiO₂ matrix and by the bioceramic.

The second and third peak was modeled to 2 equatorial oxygen shells, which observed to have a radial distances of 2.26 and 2.41 ± 0.02 Å, respectively. All FTs contain a peak at about 2.3 Å, which can be well fit by C neighbours at 2.91 Å. This distance is typical for carbonate groups coordinated to U(VI) in a bidentate fashion. The FT peak between 2.7 and 3.9 Å could arise from a phosphorus and the twofold degenerated 3-legged multi scattering path U-O_{eq1}-P₁ or from a phosphorus and an additional single scattering path U-P₂ instead of the multi scattering path U-O_{eq1}-P₁. In the case of the SiO₂ matrix, the uranium is coordinated to 2 axial oxygen atoms at a distance of 1.77 ± 0.02 Å. The second shell corresponds to the coordination of uranium to 3 equatorial oxygen atoms at a distance of 2.28 ± 0.02 Å. The broad shell (third peak) could be splitted in two individual peaks, one could be modeled to interaction between uranium and a second equatorial oxygen (2.44 ± 0.02 Å). This oxygen atom arises from water molecules. The second peak could be modeled to interaction between uranium and silicon at distance of 3.10 Å. Using cell biocers uranium is coordinated to 2 axial oxygen atoms at a distance of 1.77 ± 0.02 Å. The second shell corresponds to the coordination of uranium to 5 equatorial oxygen atoms at a distance of 2.26 ± 0.02 Å. The third peak corresponds to interaction of uranium with silicon atom at a distance of 3.10 Å. The fourth peak is modelled to interaction between uranium and phosphorous atom at distance of 3.59 Å.

In summary, EXAFS analysis of the uranium complexes formed by *B. sphaericus* JG-A12 cells demonstrated the implication of carboxyl and phosphate groups and for the uranium complexes formed by the SiO₂ matrix the implication of silicate and hydroxyl (water molecules) groups in the interaction with uranium.

References

- /1/ Selenska-Pobell et al., FEMS Microbial. Ecol. 29, 59-67 (1999)
- /2/ Raff J., PhD Thesis, University of Leipzig (2002)
- /3/ Raff J. et al., Chem. Mater., accepted (2002)

	Experiment title: Study of the surface complexes formed between uranium and magnetite and between lanthanides and hydroxyapatite	Experiment number: 20_01_70 EU #26
	Beamline: BM 20	Date of experiment: from: 19.06.02 to: 23.06.02
Shifts: 12	Local contact(s): Andreas Bauer	<i>Received at ROBL:</i> 31.10.2002
Names and affiliations of applicants (* indicates experimentalists): Joan de Pablo, UPC, Avda. Diagonal 647, Barcelona Lara Duro*, QuantiSci, Avda Universitat Autònoma 3, Cerdanyola Mireia Grivé*, UPC, Avda. Diagonal 647, Barcelona Ferran Seco*, Centre Tecnològic de Manresa, Avda. Bases de Manresa, 1, Manresa		

Report:

INTRODUCTION

One of the aims of this work is to study the interactions between uranium and iron oxides that can act as retardation factor of the migration of contaminant metals in the geosphere. Coprecipitation of uranium (VI) with iron (III) can retard U transport in environments. Extended X-ray absorption structure (EXAFS) analysis at the U L_{III} edge showed that there is a rearrangement process of the different coprecipitates depending on the ageing time.

EXPERIMENTAL

Coprecipitation experiments were conducted under nitrogen atmosphere with the objective to avoid the introduction of CO₂(g) in the system. The three Fe-U coprecipitates were prepared with the same procedure at different ageing times by coprecipitation of iron (III) with U(VI) solutions, and pH was adjusted to pH=5.5 with a free carbonate NaOH solution. In order to have an homogeneous suspension the experiments were kept under vigorous stirring. The three suspensions prepared in the same way were aged for one week, three weeks and four weeks respectively, in order to study the ageing effect on these coprecipitation samples. After contacting time and for EXAFS measurements, samples were filtered and washed through 0.02 µm pore size filters.

RESULTS

Data analysis was performed using the EXAFSPAK software. Theoretical scattering amplitudes and phases for each adsorber and backscattered pair, U-O (axial and equatorial) and U-Fe, were calculated with the program FEFF8 (Zabinsky et al. (1995)). The contribution of a multiple scattering (MS) interaction within the uranyl unit to EXAFS signal was taken into account. A single value of the shift in threshold energy, ΔE_0 , was allowed to vary for all coordination shells of a given sample. The peak corresponding to a $R + \Delta = 2.3 \text{ \AA}$ is described as a U-C distance observed for a bidentate coordination of CO₃²⁻ group to UO₂²⁺. If we take into account that the experimental conditions were in a nitrogen atmosphere and that this peak decreases with ageing time, we can discard the presence of any uranium carbonate species in the sample. Then we can assume that this peak corresponds to an U-O_{eq} interaction at approximately $R = 2.9 \text{ \AA}$. In order to compare the fits and to follow the trend with time of the different coprecipitated samples, the Debye-Waller factor was held constant in the three and four weeks samples, with the values obtained in the fit of the one week sample. As we can observe from the values given in table 1, there is a decreasing of the Fe coordination number with ageing time which could be explained as a less adsorption capacity of the sample.

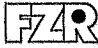
Table 1: EXAFS structural parameters for uranyl and iron coprecipitates

1 week ageing	Coordination number (N)	Distance (R) in Å	σ^2 in Å ²	ΔE_0 in eV
Oax	2.00	1.80	0.026	-2.5
Oeq	4.22	2.38	0.014	-2.5
Oeq	0.96	2.90	0.003	-2.5
Fe	1.11	3.47	0.058	-2.5
3 week ageing	Coordination number (N)	Distance (R) in Å	σ^2 in Å ²	ΔE_0 in eV
Oax	2.00	1.80	0.026	-1.6
Oeq	3.82	2.39	0.014	-1.6
Oeq	0.73	2.89	0.003	-1.6
Fe	0.95	3.46	0.058	-1.6
4 week ageing	Coordination number (N)	Distance (R) in Å	σ^2 in Å ²	ΔE_0 in eV
Oax	2.00	1.80	0.026	-3.4
Oeq	3.55	2.36	0.014	-3.4
Oeq	0.53	2.88	0.003	-3.4
Fe	0.73	3.44	0.058	-3.4

At this moment we are trying to improve the fitting by filtering the different EXAFS contributions in order to have more accurate parameters to elucidate the possible structure of these coprecipitation samples.

REFERENCES

- Zabinsky, S.J., Rehr, J.J., Ankudinov, A., Albers, R. C. and Eller, M. J. (1995) Multiple Scattering Calculations of X-ray Absorption Spectra. Phys. Rev. B 52, 2995

 ROBL-CRG	Experiment title: Identification of secondary phases formed onto leached pellets of ThO_2 and $\text{Th}_{1-x}\text{U}_x\text{O}_2$	Experiment number: 20_01_602 EU #34
	Beamline: BM 20	Date of experiment: from: 22.11.02 to: 26.11.2002
Shifts: 12	Local contact(s): A. Bauer, H. Funke, C. Hennig	<i>Received at ROBL:</i> 29.11.2002
Names and affiliations of applicants (* indicates experimentalists): Solange Hubert*, Guillaume Heisbourg*, and Juris Purans* Institut de Physique Nucléaire, 91406 ORSAY, FRANCE		

Report :

Introduction : The kinetics and the mechanism of dissolution of actinides from solid solutions $\text{Th}_{1-x}\text{M}_x\text{O}_2$ in oxidizing aqueous media is the purpose of this study. The capability of some actinides (U, Pu) to be oxidized in contact with aqueous media can influence the release of both actinides, release which is most of the time considered to be congruent with the dissolution of the matrix in the long term behaviour of spent-fuel modeling. Leaching test leads to conclude that in nitric solutions, both actinides are released congruently in solutions at pH <3, while for higher pH, precipitate of Th appears in the leachate. On the other hand, due to the oxidation of U(IV) at the surface, the dissolution of the ceramic increases with the increase of the Th substitution rate by U(IV) with different behaviour for $x < 0.5$ and $x > 0.5$. During leaching test, secondary phases are formed depending on the pH, and EXAFS and XANES studies are necessary to identify these new phases and oxidation state of uranium at the surface.

Experimental: XAFS data were recorded at the ESPF Rossendorf Beamline (ROBL BM-20) in Grenoble. The XAFS spectra of the Th L_3 -edge (16300 eV), and U L_3 -edge (17166 eV) have been performed in the transmission and fluorescence mode at room temperature. The mixed oxides were prepared through the coprecipitation of the mixed oxalates from nitrate solutions after calcination at 1300°C. The samples have been leached in HNO_3 solutions at different pH during 1 year at 90°C.

Two scan measurements have been measured at the L_3 -edges of Th (16300 eV) and U (17166 eV):

1. Sintered pellets of ThO_2 leached at pH 1 and pH 11; ThO_2 as prepared (ref. sample).
2. Sintered pellets of $\text{Th}_{0.75}\text{U}_{0.25}\text{O}_2$ leached at pH 1 and pH 11; $\text{Th}_{0.75}\text{U}_{0.25}\text{O}_2$ as prepared (ref. sample).
3. Sintered pellets of $\text{Th}_{0.5}\text{U}_{0.5}\text{O}_2$ leached at pH 1 and pH 11; $\text{Th}_{0.5}\text{U}_{0.5}\text{O}_2$ as prepared (ref. sample).
4. Reference powders of UO_2 and U_3O_8 .

Data analysis: The experimental XAFS data were treated by our software package "EDA" in the way similar to the one applied by us previously. The MS calculations were performed by FEFF8 code.

The origin of peaks in FT's of isomorphous ThO_2 and UO_2 was described previously using the multiple-scattering approach. The interpretation of XAFS in the stoichiometric $\text{Th}_{1-x}\text{U}_x\text{O}_2$ solid solutions is

analogous due to the very small differences in the scattering amplitude and phase shift functions of thorium and uranium atoms: here the visible differences are only caused by the change of the lattice constant with the composition, by the increase of disorder in the structure and by the very small differences in the scattering amplitude and phase shift functions of thorium and uranium. The first effect is responsible for the shift in the energy position of the features while the second one for the small decrease of the second peak amplitude.

We have focused our attention only on the two contributions located at 1.0-2.5 Å and 2.8-4.7 Å : they are mainly due to the first shell (O1) and the second shell (Th,U) contributions, respectively, however the outer 24 oxygen atoms of the third shell also produce some contribution to the second peak. Thus, the XAFS signals of the first peak at 1.8 Å and the second at 3.8 Å were singled out by the back FT procedure and were utilized in further analysis.

Results: For the first time the local structure of leached ThO_2 - UO_2 samples have been established. For the sample $\text{Th}_{0.50}\text{U}_{0.50}\text{O}_2$ leached at pH 1, we have observed a strong change of the XANES at the U L_3 -edge (see Fig.1 left). It corresponds to the oxidation in the bulk sample, of the valence state from U^{4+} (reference UO_2) to U^{5+} or U^{6+} (reference U_3O_8). The EXAFS analysis shows also strong modification of the local structure in the first and next coordination shell of uranium. The different ionic radii of U^{4+} and U^{5+} or U^{6+} gives strong beating in the EXAFS and two peaks in the FT (see Fig.1 right). At the same time the XANES at the Th L_3 edge is not so sensitive to the leaching procedure. For the sample $\text{Th}_{0.50}\text{U}_{0.50}\text{O}_2$ leached at pH 11, we have observed a small change of the XANES at the U L_3 -edge, which corresponds to small oxidation in the bulk sample. The EXAFS analysis shows the increase of the disorder in the local structure.

For the sample $\text{Th}_{0.75}\text{U}_{0.25}\text{O}_2$ leached at pH 1, we have observed a small change of the XANES at the U L_3 -edge. We suggest that the oxidation occurs only on the surface of the leached sample. These results are in a good agreement with our study on the dissolution kinetics of ThO_2 - UO_2 system at pH1 and pH11. Therefore we confirm the change in the mechanism of dissolution at 50%U.

We have not observed in transmission and fluorescence mode, the secondary phases on the surface of the leached samples. Only future XAFS measurements in a nearly grazing incidence configuration would allow a favoured characterization of minority secondary phases.

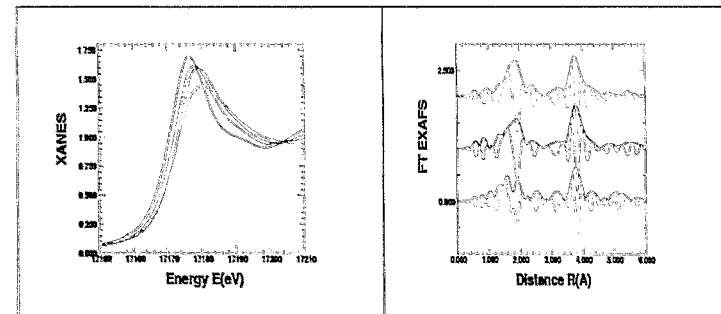



Fig1. (Left) : U L_3 -edge XANES spectra : UO_2 (left), $\text{Th}_{0.5}\text{U}_{0.5}\text{O}_2$ at pH11 and pH1, and U_3O_8 (right) (right) : FT of XAFS spectra: $\text{Th}_{0.5}\text{U}_{0.5}\text{O}_2$ (upper), $\text{Th}_{0.5}\text{U}_{0.5}\text{O}_2$ at pH11 and pH1 (lower).

	Experiment title: Study of the surface complexes formed between uranium and ferrihydrite in presence of phosphate and between uranium and hydroxyapatite	Experiment number: 20_01_606
	Beamline: BM 20	Date of experiment: from: 12.09.02 to: 14.09.02
Shifts: 6	Local contact(s): Christoph Hennig	<i>Received at ROBL:</i> 01.11.2002
Names and affiliations of applicants (* indicates experimentalists): Lara Duro, Mireia Grivé*, Ferran Seco* QuantiSci, Avada Universitat Autònoma 3, Parc Tecnològic del Valles, E-08290 Cerdanyola, Spain		

Report:

INTRODUCTION

The main objective in these series of experiments is the study of the interaction mechanism between uranium (VI) and hydroxyapatite ($\text{Ca}_5(\text{PO}_4)_3\text{OH}$) and ferrihydrite in presence of phosphate in solution by uranium LIII-edge extended X-ray absorption fine structure (EXAFS) analysis.

EXPERIMENTAL:

Uranium (VI) sorbed onto hydroxyapatite

A weighed amount of synthetic hydroxyapatite was equilibrated with a uranyl nitrate solution during 6 hours in an air atmosphere. After the contact time, the solution was removed, the solid was dried at room temperature and the final uranium concentration was measured by ICP-MS. The final pH was 6.4.

Uranium (VI) sorbed onto HFO in phosphate aqueous solution

The sorbed uranium onto ferrihydrite samples were prepared at room temperature by equilibrating a weighed amount of powdered ferrihydrite with an uranyl solution containing a well known phosphate concentration ($[\text{P}]=1 \cdot 10^{-4} \text{ mol} \cdot \text{dm}^{-3}$). This sorption experiments were carried out under $\text{N}_2(\text{g})$ atmosphere using a batch procedure. After 6 hours of equilibration, samples were filtered and washed through $0.02 \mu\text{m}$ pore size filters. The pH of the solution was adjusted to be 4.3.

Results:

The EXAFS spectra were collected in fluorescence mode at room temperature and the data analysis was performed using the EXAFSPAK software. Theoretical scattering amplitudes and phases for each adsorber and backscatterer pair, U-O (axial and equatorial) and U-Fe, were calculated with the program FEFF8. The contribution of a multiple scattering (MS) interaction within the uranyl unit to EXAFS signal was taken into account. A single value of the shift in threshold energy, ΔE_0 , was allowed to vary for all coordination shells of a given sample.

Uranium (VI) sorbed onto hydroxyapatite

For the equatorial oxygen shell we have obtained a large Debye-Waller factor value which indicates certain disorder among the distances. Two carbon atoms were fitted at a distance of 2.97 \AA which may suggest a bidentate coordination between carbonate groups and the uranium atom. Phosphorous atoms were fitted at 3.63 \AA , distance which may indicate a monodentate bonding to the hydroxyapatite surface.

Table 1. EXAFS structural parameters

	Coordination number (N)	Distance (R) in \AA	σ^2 in \AA^2	ΔE_0 in eV
Oax	2.0	1.80	0.0024	-2.5
Oeq	6.0	2.37	0.0181	-2.5
C	2.0	2.97	0.0042	-2.5
P	2.2	3.63	0.0020	-2.5
Ca	1.0	3.73	0.0047	-2.5

The fifth peak at 3.73 \AA was attributed to Ca atom contribution and is in agreement with the values found in the literature ($d_{\text{U,Ca}} = 3.72 - 4.26 \text{ \AA}$).

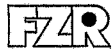
Uranium (VI) sorbed onto ferrihydrite in phosphate aqueous solution

The U-O_{eq} distance of 2.38 \AA is in agreement with the average value expected for a five fold coordination which has been reported to be 2.34 \AA (Bruns et al. (1996)) The high Debye-Waller factor observed for this oxygen equatorial shell might indicate some disorder in the structure. We can see in table 2 that we have a iron coordination number of 0.5 for iron at a distance of 3.41 \AA .

Table 2. EXAFS structural parameters

	Coordination number (N)	Distance (R) in \AA	σ^2 in \AA^2	ΔE_0 in eV
Oax	2.0	1.79	0.0024	-2.5
Oeq	5.1	2.38	0.0131	-2.5
Fe	0.5	3.41	0.0014	-2.5

At this moment we are trying to elucidate some type of structure corresponding to the adsorption of uranyl onto ferrihydrite.

 ROBL-CRG	Experiment title: XAS study of the PuO _{2+x} oxides	Experiment number: 20_01_607 EU #38
	Beamline: BM 20	Date of experiment: from: 20.11.02 to: 22.11.02
Shifts: 6	Local contact(s): Andreas BAUER	<i>Received at ROBL:</i> 29.11.2002
Names and affiliations of applicants (* indicates experimentalists): Michel RIPERT ¹ , Stéphane GRANDJEAN ^{2*} , Philippe MARTIN ¹ , Thierry PETIT ^{1*} , Charlotte ROBISSON-THOMAS ^{2*} , Jérôme ROUSSELLE ^{2*} ¹ CEA/CADARACHE, DEN/DEC/SESC/LLCC Bat 315 13108 Saint Paul Lez Durance Cedex, France ² CEA/VALRHO, DEN/DRCP/SCPS/LPCA, Bat 399 BP 17171 30207 Bagnols sur Cèze Cedex, France		

Report:

The aim of our measurements is to verify the existence of hyperstoichiometric PuO₂ and to characterise more precisely its structure using X-ray Absorption Spectroscopy. As described by Haschke *et al.*¹, PuO_{2+x} appears under specific conditions by reaction of PuO₂ with adsorbed water following the global scheme:

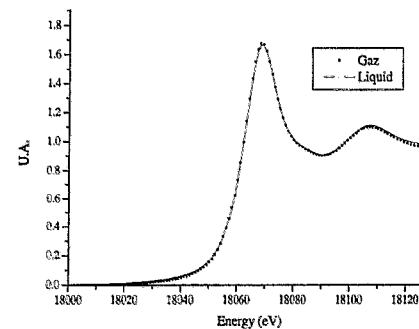
$$\text{PuO}_2(\text{s}) + x \text{H}_2\text{O}(\text{ads.}) \rightarrow \text{PuO}_{2+x}(\text{s}) + x \text{H}_2(\text{g})$$

Preliminary tests performed at CEA Marcoule, by prolonged action at 340°C of a PuO₂ powder obtained by oxalic conversion, with an inert gas saturated with water, did not reproduce the previous reaction. It seems that very specific physico-chemical conditions are required, in particular the PuO₂ powder surface state. The temperature and pressure conditions of the reaction also has to be precisely reproduced to reach the oxidation kinetics required to obtain a significant hyperstoichiometry and within a period of a few months.

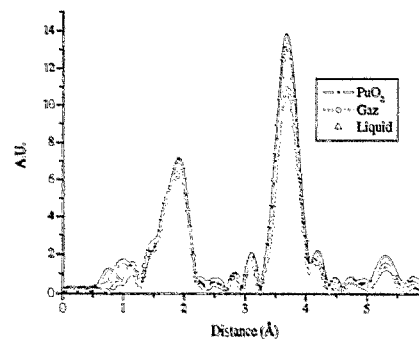
Two new samples were then prepared by total immersion and in water atmosphere during 2800 hours at temperatures between 130 and 180°C. They were conditioned in the Atalante facility at Marcoule in order to respect the standards of

protection against radiation of the BM20 line. They were encapsulated and sent to ESRF by special transportation according to the French regulations.

For each sample, the transmission and fluorescence signals were collected at the plutonium (18.056 keV) L_{III} edges. Energy calibration of the XANES data was achieved using the reference Zr foil (17.998 keV) positioned after the second ionisation chamber. As shown on the following figure, the XANES spectra are always the same, whatever the reaction conditions used.

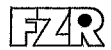


As observed on the Fourier Transforms, the position of the white line remains the same to the one of a PuO₂-reference compound. The oxidation state of plutonium remains equal to +IV in all our samples.



Further data analysis are conducted to confirm these results.

¹J. M. Haschke, T. H. Allen, L. A. Morales, Science, 287, 285 (2000).

 ROBL-CRG	Experiment title: Uranium (III) speciation in ionic liquids	Experiment number: 20 01 609 EU #40
	Beamline: BM 20	Date of experiment: from: 16.11.02 to: 19.11.02
Shifts: 9	Local contact(s): Andreas Bauer	<i>Received at ESRF:</i> 28.11.2002
Names and affiliations of applicants (* indicates experimentalists): A. I. Bhatt,* ¹ B. L. Dadds,* ¹ I. May,* ¹ V. A. Volkovich,* ¹ J. M. Charnock,* ² A. Bauer,* ³ C. Hennig,* ³ A. Rossberg,* ³		
¹ Centre for Radiochemistry Research, Department of Chemistry, The University of Manchester, Oxford Road, Manchester, M13 9PL, UK ² CLRC, Daresbury Laboratory, Daresbury, Warrington, Cheshire, WA4 4AD, UK. ³ ESRF, ROBL - CGR, BP 220, Grenoble Cedex, France		

Report:

Ionic liquids (ILs) are liquids composed of cations and anions only *e.g.* molten NaCl (801°C). Low temperature ionic liquids are usually comprised of organic cations and a variety of inorganic anions. The chemical and physical properties can be changed by varying the anions and/or cations.¹ These low vapour pressure salts are attracting considerable commercial and academic interest due to their use as solvents for catalysis, organic synthesis and separations.^{1,2}

Comparatively little is known about metal ions speciation in ILs, although several papers have previously reported the crystal structures of metal - IL anion complexes,³ this however only gives information regarding solid state behaviour. Solution speciation can be inferred from several spectroscopic techniques *e.g.* UV/vis, IR, Raman, NMR *etc.*, and with XAS (a powerful complementary technique to the more routine spectroscopies).

Due to large electrochemical windows IL's can in theory be used to electrodeposit actinides and lanthanides from solution⁴ and thus to develop alternative methods of

¹ T. Welton, *Chem. Rev.*, 1999, **99**(8), 2071-2084; P. Wasserchied and W. Kiem, *Angew. Chem. Int. Ed.* 2000, **39**, 3772-3789

² M. Freemantle, *Chem. Eng. News*, 1998, **76**(34),

³ (a) J. J. Golding, D. R. MacFarlane, L. Spiccia, M. Forsyth, B. W. Skelton, A. H. White, *Chem Commun.*, 1998, 1593-1594, (b) A. Haas, Ch. Klare, J. Bruckmann, C. Krüger, Y.-H. Tsay, F. Aubke, *Inorg. Chem.*, 1996, **35**, 1918-1925, (c) A. E. Bradley, J. E. Hatter, M. Nieuwenhuijzen, W. R. Pitner, K. R. Seddon, R. C. Thied, *Inorg. Chem.*, 2002, **41**, 1692-1694

⁴ A. I. Bhatt, I. May, V. A. Volkovich, M. Hetherington, R. C. Thied, B. Lewin, N. Ertok, *Dalton Comm.*, 2002, in press.

nuclear fuel processing.^{5,6} The key to understanding and optimising this electrodeposition process is the solution speciation of actinides in ionic liquids. This work has focused on the use of XANES and EXAFS to look at the speciation of uranium in selected quaternary ammonium bis((trifluoromethane)sulfonyl)amide (bistriflimide) ionic liquids (particularly U(III), due to the U(0)/U(III) couple being a crucial step in the electrodeposition reaction). U L_{III}-edge EXAFS spectra were recorded at ROBL at room temperature in transmission mode. UV/vis spectroscopy indicates that U(III) is stable in IL solutions and preliminary XANES spectra (see Figure 1) confirm this, showing an energy shift in the edge position from U(IV) and U(VI).

Initial theoretical fits show that the data obtained is of a high enough quality to show mixed ligand coordination, and oligomeric species that cannot otherwise be seen by conventional laboratory techniques (Table 1). Preliminary results for UCl₄ dissolved in a bis((trifluoromethane)sulfonyl)amide ionic liquid indicate a mixed Cl⁻ / [N(SO₂CF₃)₂]⁻ species (as has been previously been speculated⁷).

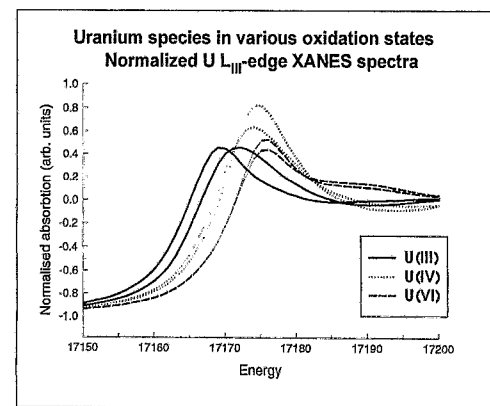


Figure 1: Normalized U L_{III}-edge XANES spectra


	R (Å)	Coordination Number	σ ² (Å ²)
U-O	2.220	2	0.011
U-Cl	2.614	4	0.022
U-S	3.330	2	0.038
U-U	3.701	2	0.009

Table 1: EXAF structural parameters for UCl₄ dissolved in [Me₃NBu][N(SO₂CF₃)₂]

⁵ K. Murase, K. Nitta, T. Hirato, Y. Awakura, *J. Appl. Electrochem.*, 2001, **31**, 1089-1094.

⁶ T. A. Hopkins, J. M. Berg, D. A. Costa, W. H. Smith and H. J. Dewey, *Inorg. Chem.*, 2001, **40**, 1820; W. H. Smith and D. Costa, *Los Alamos National Laboratory Report*, LA-UR 98-3669, 1999.

⁷ D. Costa, Oral presentation - Electrochemical Society Meeting - Philadelphia, 2002.

	Experiment title: Interaction of actinides with predominant bacteria isolated at nuclear waste repositories using X-ray absorption spectroscopy	Experiment number: 20_01_611
	Beamline: BM 20	Date of experiment: from: 14.09.02 to: 15.09.02
Shifts: 3	Local contact(s): Christoph Hennig	<i>Received at ROBL:</i> 29.10.2002
Names and affiliations of applicants (* indicates experimentalists): H. Möll*, C. Hennig*, M. Merroun*, H. Funke*, A. Rossberg*, G. Bernhard, S. Selenska-Pobell		

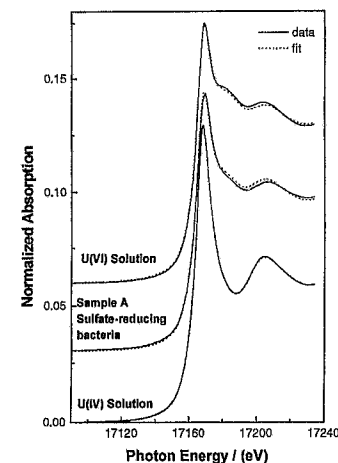
Report:

We are reporting the first preliminary results within this proposal. In this part of the project we are investigating the interaction of actinides with indigenous bacteria in Äspö aquifer (Sweden). The role of microorganisms in the migration behavior of actinides have not yet been studied in the Hard Rock Laboratory in Äspö. At this stage of the project the research will be focused on the recovered bacterial strain *Desulfovibrio äspöensis* which is indigenous at the Äspö site /1/. *Desulfovibrio* strains are widespread and have the ability to immobilize heavy metals, e.g. uranium by reduction.

Experimental. After culturing *Desulfovibrio äspöensis* in optimized growth medium, the bacterial cells were obtained by centrifugation. They were washed and re-suspended in a solution of 0.9% NaCl. Two samples were prepared. In sample A, the cells were incubated with 6.3×10^{-4} M U(VI) solution at pH 5. Whereas, in sample B the uranium concentration and pH used were 1.05×10^{-4} M and 6, respectively. After shaking the samples for 7 days under nitrogen atmosphere, the biomass was separated by centrifugation, washed with 0.9% NaCl solution, and sealed in polyethylene cuvettes.

Results. The Figure shows a comparison of the U L_{III}-edge XANES spectrum of the bacterial sample A with the spectra of the U(VI) and U(IV) reference solutions. The pattern of the XANES spectrum of sample A clearly indicates the presence of uranium in both oxidation states +4 and +6. We applied the Factor Analysis described in /2/ to determine the amounts of U(IV) and U(VI) present in sample A. The calculations revealed a mixture containing 20 % U(IV) and 80% U(VI). For the first time we could show that *Desulfovibrio äspöensis* are able to reduce U(VI) to U(IV).

Figure U L_{III}-edge XANES spectra of 0.03 M U(IV) and 0.04 M U(VI) reference solutions in 1 M HClO₄ and after bacterial reduction of U(VI) (sample A). Solid line – experiment; dots – calculated spectrum.




The localization of U(IV) in sample B failed. The XANES spectrum indicates that almost all of the uranium is present in the oxidation state +6. The reasons for this observation are not clear at the moment. The evaluation of the EXAFS data of sample B yielded an relatively short U-O_{eq} distance of 2.34 Å. This indicates an intensive interaction of uranyl with the surface of the bacteria. A detailed data evaluation is in progress. The interaction process of *Desulfovibrio äspöensis* with uranium could probably consists of a bio-sorption of uranyl onto the cell wall of the bacteria followed by an enzymatic reduction of uranyl to U(IV) and a slow precipitation of UO₂. Due to the experimental findings it seems that the enzymatic reduction is somehow inhibited in sample B. Another reason for the difficulties in detecting U(IV) in this sample could be a re-oxidation of U(IV) to U(VI). We have to point out that these are only preliminary conclusions. Further investigations to throw light on the interactions of uranium with *Desulfovibrio äspöensis* are needed and planned.

Acknowledgements. This work is supported by the BMWi (no. 02E9491).

Reference

- /1/ M. Motamedi, K. Pedersen: *Int. Syst. Bacteriol.* **48**, 311 (1998).
 /2/ A. Rossberg, Ph.D. Thesis, Technische Universität Dresden (2002).

	Experiment title: Uranium sorption onto leached layers of feldspar	Experiment number: 20_01_612
	Beamline: BM 20	Date of experiment: from: 30.10.02 to: 02.11.02
Shifts: 12	Local contact(s): Christoph Hennig	<i>Received at ROBL:</i> 28.11.2002
Names and affiliations of applicants (* indicates experimentalists): M. Walter*, T. Arnold, G. Bernhard, H. Funke*, C. Hennig*, H. Moll*, T. Reich*, A. Rossberg*, S. Stumpf*, T. Stumpf* Forschungszentrum Rossendorf e.V., Institut für Radiochemie, P.O. Box 510119, D-01314 Dresden		

Report:

The feldspar mineral albite is a common constituent of various rocks. Because the high occurrence, albite may influence the migration of uranium(VI) in the environment.

Experimental

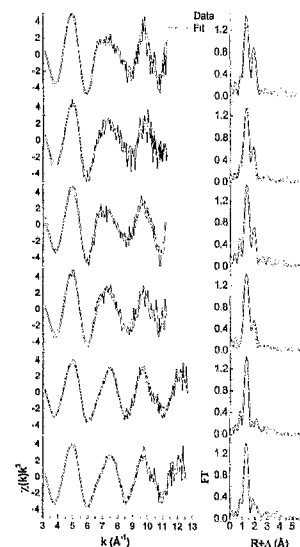
Two samples for EXAFS spectroscopy were prepared under ambient conditions (U1-35) and N₂-atmosphere (U1-34) using 200 mg of fine-grained albite, dispersed in 1000 ml of 0.01 N NaClO₄ solution. The suspensions were equilibrated for two weeks to adjust the pH value of 6.4. The initial uranium (VI) concentration was 1*10⁻⁵ M U(VI).

The surface of albite was modified by acid leaching at pH 2, resulting in a leached layer which is enriched on silanol surface groups [1]. Uranium(VI) was sorbed under ambient conditions on this leached albite at pH 5.0 (1*10⁻⁴ M U; U2-76) and pH 5.8 (2*10⁻⁵ M U; U2-77). After a reaction period of approx. 40 hours, the suspensions were centrifuged and the sorption samples were prepared as wet pastes in Teflon sample holders for XAS measurements.

In addition, two samples of 400 mg albite were altered under ambient conditions using a 0.01 N NaClO₄ solution with initial uranium(VI) concentrations of 5*10⁻⁶ M (U2-73) or 2*10⁻⁵ M (U2-74), respectively. The albite alteration and uranium(VI) sorption were performed over a period of 170 days. The flow rate of the uranium(VI) solution was approx. 20 ml/d.

The X-ray absorption measurements were performed at the ROBL-CRG in fluorescence mode using a 4-element germanium solid-state detector. EXAFS data analysis was performed using the EXAFSPAK program. The theoretical phase shifts and backscattering amplitudes were calculated with FEFF8.


Results



U(VI) - sample	Shell	N	R (Å)	σ ² (Å ²)	ΔE ₀
Albite (U1-34)	O _{ax}	2.5	1.79	0.0038	3 eV
pH 6.4 N ₂	O _{eq}	3.9	2.39	0.006	
1*10 ⁻⁵ M U(VI)					
Albite (U1-35)	O _{ax}	2.2	1.77	0.0038	-1 eV
pH 6.4 (air)	O _{eq}	5.5	2.34	0.014	
1*10 ⁻⁵ M U(VI)					
Albite (U2-73)	O _{ax}	1.9	1.79	0.0010	1 eV
pH 5.8	O _{eq}	5.4	2.36	0.012	
5*10 ⁻⁶ M U(VI)					
Albite (U2-74)	O _{ax}	2.5	1.78	0.0040	1 eV
pH 5.8	O _{eq}	5.2	2.35	0.015	
2*10 ⁻⁵ M U(VI)					
H-Albite (U2-76)	O _{ax}	1.8	1.76	0.0007	-2 eV
pH 5.8	O _{eq1}	2.6	2.23	0.005	
2*10 ⁻⁵ M U(VI)	O _{eq2}	2.8	2.44	0.005	
H-Albite (U2-77)	O _{ax}	2.1	1.76	0.0021	-2 eV
pH 5.0	O _{eq1}	2.6	2.22	0.009	
1*10 ⁻⁴ M U(VI)	O _{eq2}	3.8	2.43	0.009	

Two different types of U-L_{III} EXAFS spectra can be observed: spectra of uranium(VI) sorbed on albite indicate a distorted equatorial oxygen shell (O_{eq}). In contrast, for uranium sorbed on the modified surface, the equatorial oxygen shell is clearly splitted in silanol-group enriched albite. No further backscatterer contributions, which would indicate die coordination to Al- or Si-polyhedra, are detectable. However, the strong distortion of the equatorial oxygen shell indicates a inner-sphere surface complexation mechanism.

[1] Casey W. H., Westrich H. R., Arnold G. W. (1988) Surface chemistry of labradorite feldspar reacted with aqueous solution at pH = 2, 3, and 12., Geochim. Cosmochim. Acta 52, 2795-2807.

	Experiment title: Structural changes in N⁺-ion implanted Ti6Al4V alloys during annealing by <i>in-situ</i> x-ray diffraction (Depth resolved XRD analysis of nitrogen implanted Ti-6Al-4V alloys)	Experiment number: 20_02_031 (c) longterm
	Beamline: BM 20	Date of experiment: (long term) from: 26.01.01 to: 29.01.01 from: 04.03.01 to: 07.03.01
Shifts: 11 + 9	Local contact(s): Dr. N. Schell	<i>Received at ROBL:</i> 15.04.01
Names and affiliations of applicants (* indicates experimentalists): ** F. Berberich, *W. Matz † Forschungszentrum Rossendorf, Institute of Ion Beam Physics and Materials Research, P.O. Box 510119, D-01314 Dresden, Germany ‡ ROBL – CRG at ESRF		

Report:

With the x-ray diffraction analysis adapted for grazing incidence diffraction (GID) geometry it is possible to investigate depth distribution of crystalline phases. It is based on the changes the average penetration depth of the x-ray beam under variation of the incident angle (α_i). However, it is not easy to detect from such experiments the real depth distribution of a crystal structure. The scattering volume is not well defined because of the exponential attenuation of the x-ray intensity in the sample. The scattering is accumulative, so the signal from the surface will be present at all greater α_i . A difference method is not applicable because of different absorption coefficients. To find the real phase distribution the theory of the standing wave field was used. The scattered intensity is given by:

$$I(\alpha_i) = I_0 \int_{-\infty}^0 |E_i(r, k)|^2 g(z) dz$$

where I_0 is the normal intensity, E_i is the electrical field calculated from the standing wave field [1] and $g(z)$ is the distribution function of the scatterers. Thus, by fitting $I(\alpha_i)$ with a model function $g(z)$ to the measured values of a certain sample the depth distribution can be derived.

The aim of the experiment was to show the different phase distribution of TiN and Ti₂N in the nitrogen implanted Ti-6Al-4V alloys. The used samples were implanted with ion beam implantation technique at different energies (from 20 keV to 180 keV) and different fluences (1-6) $\times 10^{17}$ N⁺/cm². So, it was possible to compare in the GID implantation depth

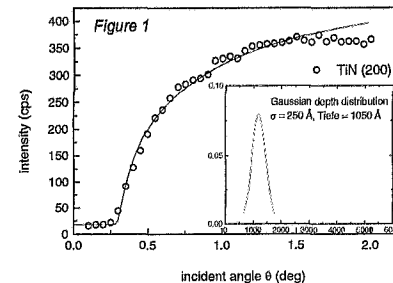


Fig. 1: Measured and simulated depth distribution of TiN(200) of an ion beam implanted Ti-6Al-4V sample (implanted fluence: 6×10^{17} N⁺/cm² with an implantation energy of 80 keV).

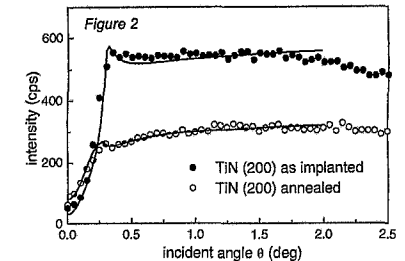
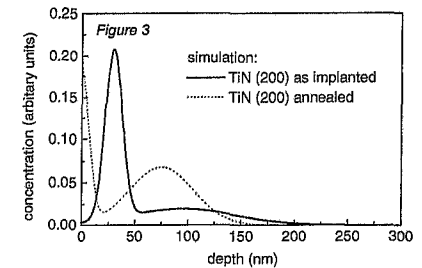


Fig. 2: Measured and **Fig. 3** simulated depth distribution of TiN(200) of a PII implanted Ti-6Al-4V sample (implanted fluence: 2×10^{17} N⁺/cm² with an implantation energy of 40 (20) keV).




profiles of 100 up to 200 nm. Further samples were implanted by plasma ion immersion (PII) with a fluence of 2.0×10^{17} N⁺/cm². With this technique, nitrogen is deposited only very near to the surface.

All samples were studied in the as-implanted and in the annealed state. For all samples the depth profile of characteristic Bragg reflections were recorded by varying the incident angle from 0° to 2° at a wavelength of $\lambda = 0.154$ nm.

The result for an ion beam implanted sample in the as-implanted state is given in Fig. 1. The simulation shows the maximum of the Gaussian depth profile at a depth of 135 nm. Former investigations with the elastic recoil detection analysis [2] have indicated that the maximum of the nitrogen concentration lies at a depth of 146 nm with also a Gaussian depth profile.

Fig. 2 depicts the result for a PII implanted sample in the as-implanted state and after annealing at 680°C for 2 h. Both curves show in principle the same behaviour: the occurrence of a resonance peak near the critical angle of Ti-6Al-4V of $\alpha_{crit} = 0.3^\circ$. For this example, it is only possible to get a well adapted curve if two Gaussian distributions are used as it is shown in Fig. 3. One at the surface, the second one in the deeper region of about 80 nm. The ratio of the two normalized concentrations gives a hint to a starting diffusion process and beyond to the phase formation in deeper regions.

- [1] D. Windt, Computers in Physics, IMD-Software for modeling the optical properties of multilayer films: 12(4) (1998) 360
- [2] F. Berberich, W. Matz, E. Richter, N. Schell, U. Kreißig and W. Möller, Surface and Coatings Technology **128-129** (2000) 450-454

	Experiment title: <i>In-situ</i> x-ray diffraction during sputter deposition of TiN and CrN	Experiment number: 20_02_041
	Beamline: BM 20	Date of experiment: from: 22.03.2001 to: 27.03.2001 (A) and from: 20.06.2001 to: 25.06.2001 (B)
Shifts: 15(A) + 16(B)	Local contact(s): Dr. Norbert Schell	<i>Received at ROBL:</i> 14.07.01
Names and affiliations of applicants (* indicates experimentalists): * J. Böttiger, University of Aarhus, Denmark * N. Schell, ROBL-CRG, Germany		

Report: (A)

The heteroepitaxial growth of TiN on MgO(001), deposited by reactive magnetron sputtering, has been studied *in situ*. Using real-time specular X-ray reflectivity, layer-by-layer growth was observed, with the surface-roughening decreasing with increasing deposition temperature. Higher temperatures also resulted in lower growth rates. The film thickness was measured with specular X-ray reflectivity. Using off-plane Bragg-Brentano as well as grazing incidence in-plane wide angle scattering, the pseudomorphic growth of TiN to the underlying MgO(001) was established. Transmission electron microscopy revealed atomic planes passing through the MgO-TiN boundary, thus confirming the heteroepitaxial growth. To the best of our knowledge, this is the first report [1] on *real-time* measurements of the surface morphology on an atomic scale during the growth of a film deposited by magnetron sputtering.

EXPERIMENTAL

The deposition chamber (together with the detailed scattering geometry and the quality of the data, like intensity, resolution, background, which can be obtained with the set-up) is described in detail in Ref. 2. The magnetrons, commercially available from AJA International, are placed at a distance of 100 mm from the substrates and tilted 30 degrees away from the substrate normal. To avoid cross contamination of the two targets, each with a diameter of 1 inch, chimneys are mounted on the magnetrons. Air-pressure-controlled shutters are placed in front of the chimneys. The base pressure was appr. 2×10^{-5} Pa. The reactive sputter gas was a mixture of Ar (99.9999%) and N₂ (99.9999%) with the ratio 4:1, at a total gas pressure of 0.3 Pa. Only one magnetron was used at the time. It was run at a de power of 80 W, resulting in a deposition rate of appr. 0.65 Å/s. The substrates were 1.5 x 1.5 cm² MgO(001) single crystals with a thickness of 1 mm. A resistive heater was mounted below the substrate so the temperature could be varied from room temperature up to 600 °C. The temperature was measured by use of a thermocouple. A negative bias voltage of 30 V was applied to the substrate. Before depositing TiN, the surface of the substrate was cleaned/annealed by heating it to 600 °C for 1 h.

The deposition chamber was mounted on the six-circle goniometer in MRH. The incident x-rays were monochromatized to 11.696 keV ($\lambda = 1.060$ Å). To study the growth of TiN films *in situ*, four different scattering geometries were used:

1. Vertical Bragg-Brentano large-angle scattering (XRD) revealing the texture. In addition, from the exact positions of the Bragg peaks, information on the out-of-plane lattice strain, and from their widths and shapes, out-of-plane grain sizes and microstrain (lattice defects) are obtained.
2. Grazing incidence and grazing exit in-plane large-angle scattering (GIXS). With an incident angle of 0.2°, the calculated penetration depth of the x-rays was about 100 Å, assuming a mass density of TiN of 5.43 g/cm³. Crystallographic planes perpendicular to the surface are identified and, from the positions and widths of the Bragg peaks, in-plane lattice parameters (strain), grain sizes and microstrain are calculated.
3. Low-angle specular reflectivity with information on film thickness and surface roughness.
4. Large-angle specular reflectivity to measure the crystal truncation rod (CTR) intensity in real time during film growth. The sample and detector were fixed at $\theta/2\theta = 3.596/7.192^\circ$, resp. The intensity was recorded in intervals of 1 second starting 5 to 55 seconds before the shutter of the magnetron was opened and the deposition began (comp. Fig. 1). The first three scattering geometries, on the contrary, were applied after growth.

By using a Philips CM300 transmission electron microscope, cross-sectional electron micrographs were obtained (comp. Fig. 2). The samples were cut perpendicular to the film surface and grinded mechanically. The final thinning was made by ion beam milling using Ar ions.

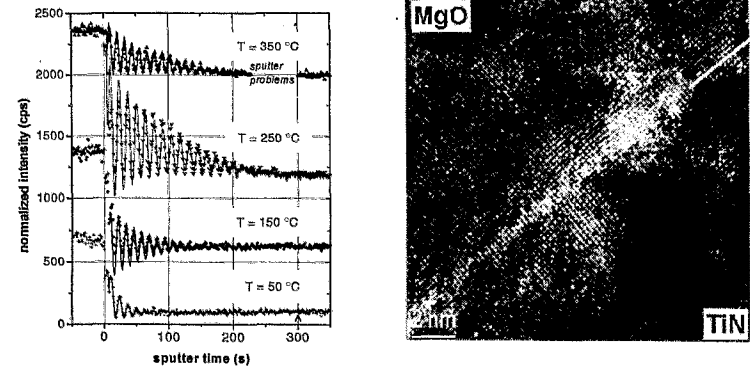
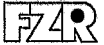


Fig. 1 (left: Oscillations in CTR intensity) and Fig. 2 (right: high resolution TEM micrograph from a 360 Å TiN film grown at 250 °C) are examples of the obtained data.

SUMMARY:

Using reactive magnetron sputtering, we studied the heteroepitaxial growth of seven TiN films deposited at different substrate temperatures: 50 °C, 150 °C, 250 °C, three films at 350 °C, and 450 °C, resp. XRD, GIXS and TEM measurements revealed that the TiN(001) films are pseudomorphic to the underlying MgO(001) substrates, whereby the films experience a compressive stress. Based on thickness measurements carried out using specular X-ray reflectivity, it was found that the growth rate decreased with increasing temperature. Measurements of the CTR intensity versus time showed oscillations which revealed that the TiN films grew in the layer-by-layer mode. The surface roughened faster during growth at lower temperatures. To the best of our knowledge, this is the first *real-time* measurements of the growth mode of a film deposited by magnetron sputtering.

- [1] J. Böttiger, N. Schell, J. Chevallier, W. Matz, J.H. Petersen, and A. Mücklich. *Submitted to J. Appl. Phys.*
 [2] W. Matz, N. Schell, W. Neumann, J. Böttiger, and J. Chevallier, *Rev. Sci. Instrum.* **72**, 3344 (2001).

 ROBL-CRG	Experiment title: <i>In-situ</i> x-ray diffraction during sputter deposition of TiN and CrN	Experiment number: 20_02_041
	Beamline: BM 20	Date of experiment: from: 22.03.2001 to: 27.03.2001 (A) and from: 20.06.2001 to: 25.06.2001 (B)
Shifts: 15(A) + 16(B)	Local contact(s): Dr. Norbert Schell	<i>Received at ROBL:</i> 13.02.02
Names and affiliations of applicants (* indicates experimentalists): * J. Böttiger, University of Aarhus, Denmark * N. Schell, ROBL-CRG, Germany		

Report: (B)

During growth of CrN films deposited by reactive magnetron sputtering, the development of the microstructure, especially the texture, was studied. *In situ* Bragg-Brentano x-ray diffraction and reflection measurements were carried out where the dynamic development of the microstructure was followed in real time. Below a transition deposition temperature of approximately 550°C, it was found that the <002> preferred orientation dominated, while a mixture of <111> and <002> preferred orientations was found above the transition temperature. The development of texture with film thickness was controlled by a recrystallization mechanism [1]. With increasing film thickness, the grain size increased while the microstrain decreased. The real-time measurements with synchrotron radiation revealed that several different dynamic processes took place both during and after depositions. After a long-time interruption of the growth, major changes in the texture were observed.

EXPERIMENTAL

The deposition chamber (together with the detailed scattering geometry and the quality of the data, like intensity, resolution, background, which can be obtained with the set-up) is described in detail in Ref. 2. The magnetrons, commercially available from AJA International, are placed at a distance of 100 mm from the substrates and tilted 30 degrees away from the substrate normal. To avoid cross contamination of the two targets, each with a diameter of 1 inch, chimneys are mounted on the magnetrons. Air-pressure-controlled shutters are placed in front of the chimneys. The base pressure was appr. 2×10^{-3} Pa. The reactive sputter gas was a mixture of Ar (99.9996%) and N₂ (99.99990%) with the ratio 2:3, at a total gas pressure of 0.35 Pa. Only one magnetron was used at the time. It was run at a dc power of 60 W, resulting in a deposition rate of appr. 0.8 Å/s. The substrates were 1.5 x 1.5 cm² silicon (100) wafers with a thickness of 1 mm and a 1800 Å amorphous oxide layer on top. A resistive heater was mounted below the substrate so the temperature could be varied from room temperature up to 600°C. The temperature was measured by use of a thermocouple. A variable negative bias voltage was applied to the substrate.

The deposition chamber was mounted on the six-circle goniometer in MRH. The incident x-rays were monochromatized to 11.696 keV ($\lambda = 1.045$ Å). To study the growth of CrN films *in situ*, two different scattering geometries were used:

1. Bragg-Brentano large-angle scattering (comp. Fig. 1). Such measurements reveal the texture. In addition, the exact positions of the Bragg peaks yield information on the out-of-plane lattice strain, and from the widths and shapes of the peaks, out-of-plane grain sizes and microstrain (lattice defects) are obtained.
2. Low-angle specular reflectivity. The film thickness and information on density and surface roughness are obtained.

By using a Philips CM300 transmission electron microscope, cross-sectional electron micrographs were obtained (comp. Fig. 2). The samples were cut perpendicular to the film surface and grinded mechanically. The final thinning was made by ion beam milling using Ar ions.

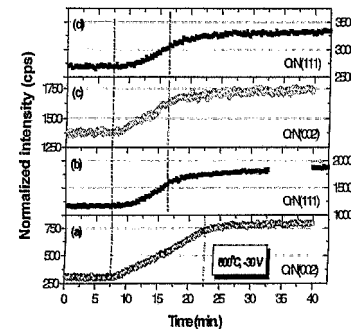
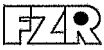


Fig. 1 (left: Bragg-Brentano diffraction-peak intensities versus time before, during and after deposition at a substrate temperature of 600°C and a bias voltage of -30 V. The deposition times are in between the dot-dashed vertical lines) and Fig. 2 (right: bright field TEM micrograph from a 2200 Å CrN film deposited *ex situ* at 600°C and with a bias of -30 V) are examples of the obtained data.

SUMMARY

Using reactive magnetron sputtering, we studied the development of texture of five CrN films deposited at different substrate temperatures (450°C, 600°C) and bias voltages (-30 V, -60 V, -100 V). XRD (also *ex situ*, including pole figure determination) and TEM measurements revealed columnar growth morphology of the CrN films. A recrystallization mechanism was found to control the change from <002> preferred orientation to <111> preferred orientation. The grain size increased and the microstrain decreased with film thickness. The real-time measurements with synchrotron radiation revealed that several different dynamic processes like annihilation of defects, recrystallization and grain growth took place both during and after deposition. Increasing the bias from -30 V to -100 V resulted in higher defect concentrations and, most likely, formation of complex defects after a relaxation period. These defects hindered recrystallization, whereby the <002> preferred orientation became more pronounced. After a long-time interruption of the growth, major changes in the texture were observed due to changes in the surface during the interruption.

- [1] N. Schell, A. Mücklich, F. Eichhorn, J.H. Petersen, J. Böttiger, J. Chevallier, and K.P. Andersen, *Thin Solid Films*, *in press*
 [2] W. Matz, N. Schell, W. Neumann, J. Böttiger, and J. Chevallier, *Rev. Sci. Instrum.* **72**, 3344 (2001).

 ROBL-CRG	Experiment title: Investigation of the shape of the chemical composition profile in InGaAs/GaAs heterostructures	Experiment number: 20_02_042
	Beamline: BM 20	Date of experiment: from: 18.04.2001 to: 21.04.2001
Shifts: 9	Local contact(s): Dr. Norbert Schell schell@esrf.fr	<i>Received at ROBL:</i> 11.12.01
Names and affiliations of applicants (* indicates experimentalists): Dr Jarosław Gaca gaca-j@sp.itme.edu.pl Dr Marek Wójcik wojcik-m@sp.itme.edu.pl Institute of Electronic Materials Technology (ITME), ul. Wolczynska 133, 01- 919 Warsaw, Poland		

Report:

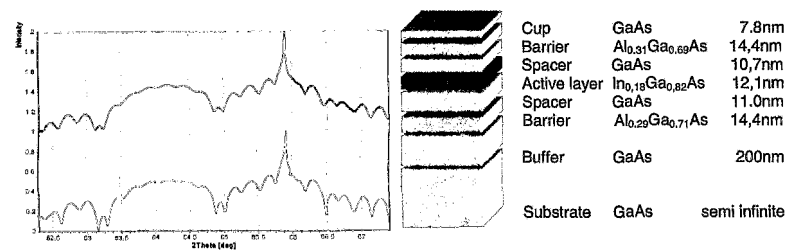
The ability of manufacturing heterostructures consisting of thin crystalline layers differing in their chemical composition and thickness is vital to the technology of semiconducting lasers and resonance diodes. In order to acquire laser action, it is essential to produce high quality multilayered crystals with sharp interfaces between succeeding layers. It is very difficult to accomplish this goal if there is a great lattice mismatch between layers, what refers especially to quantum wells applied to lasers and diodes, because in this case the lattice strain is often exploited to obtain a desired band structure. For such heterostructures the chemical composition profile undergoes the greatest disturbances in the vicinity of the interface in relation to the assumed one. The aim of this project was to investigate the chemical composition profile in the growth direction of heterostructures making quantum wells with very thin active $\text{In}_x\text{Ga}_{(1-x)}\text{As}$ layers. Since the total thickness of the heterostructure is very small ($d < 500\text{\AA}$) the synchrotron radiation was used.

Experimental method

Two kinds of heterostructures were investigated:

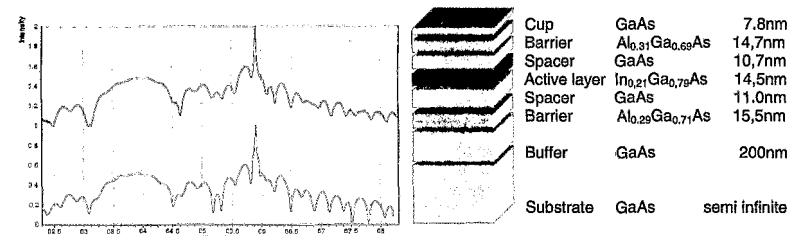
1. Laser structure as shallow and wide quantum well with wide barriers.
2. Structure of resonant tunneling diode (RTD) composed of deep and narrow quantum well with narrow barriers.

The determination of the chemical composition profile in the growth direction of the investigated heterostructures was carried on by means of the computer simulations based on Darwin dynamical diffraction theory.



Experimental (top) and calculated (bottom) diffraction profiles for heterostructure growth rate 2ML/s, T=700C

Diagram representation of the heterostructure




Experimental (top) and calculated (bottom) diffraction profiles for heterostructure growth rate 0,5ML/s, T=700C

Diagram representation of the heterostructure

Applying synchrotron radiation in the experiment it was possible to determine the real structure of the very thin buried active layer.

On the basis of the experimental results and conducted simulation the chemical composition profile of investigated heterostructures was determined as a function of a growth rate. It was found that lower growth rate results in greater discrepancy between obtained and expected results. It was also established that the symmetric AlGaAs barriers stabilize the profile of InGaAs active layer (there is greater discrepancy between the expected and real chemical composition profiles in case of heterostructure with only one barrier between active layer and substrate). These results allow us to draw conclusions concerning deposition of In and Ga atoms as a function of growth conditions and contribute to the program dedicated to producing laser and resonant diode structures.

	Experiment title: Structural study of self-assembled film systems composed of metallic nano-clusters by x-ray grazing-incidence methods	Experiment number: 20_02_43 EU #13
	Beamline: BM 20	Date of experiment: from: 12.04.2001 to: 15.04.2001
Shifts: 9	Local contact(s): Dr. Norbert Schell, Andreas Bauer	<i>Received at ROBL:</i> 12.12.01
Names and affiliations of applicants (* indicates experimentalists): Jerzy B. Pelka^{*a}, Mathias Brust^{*b}, Wojciech Paszkowicz^{*a}, Piotr Gierlowski^{*a} ^a Institute of Physics, Polish Academy of Sciences, Al. Lotnikow 32/46, 02-668 Warsaw, Poland ^b Department of Chemistry, University of Liverpool, Liverpool L69 7ZD, UK		

Report:

Multilayer thin films of gold nanoparticles on glass have been prepared via a step-by-step wet-chemical method using aliphatic dithiols of different length (3 to 9 C atoms) as inter-particle linker/spacer molecules. It has been shown by x-ray diffraction line broadening analysis that the gold particles within the films retain their original size of ca. 4-5 nm even in the case of the shortest aliphatic spacer molecule employed (1,3-propanedithiol). Thus, no significant particle destabilization and fusion occurs, and the typically observed spacer dependent differences in the electronic and optical properties of such films can be attributed confidently to the precisely controllable changes in inter-particle distance on a molecular size scale. Film thickness and density have been accurately determined by x-ray reflectometry confirming the previously suggested discrete layer-by-layer growth mechanism of the thin film structures. Preliminary in-plane diffraction

studies suggest the existence of only very small ordered domains of particles within the films. However, this point needs still further extensive studies.

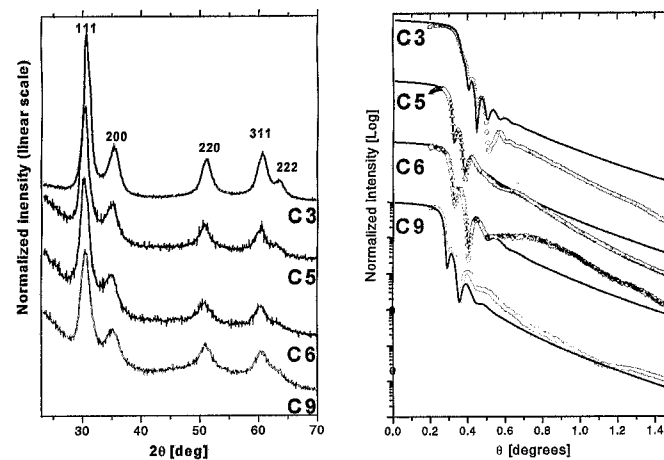



Fig. 1: *Left:* Recorded x-ray diffraction patterns of samples C3-C9. $\lambda=1.2398 \text{ \AA}$, angle of incidence: 0.7° . *Right:* Reflectivities of samples C3-C9 (points) as compared with simulated curves (solid lines). C_n symbols refer to number of carbon atoms in the dithiol spacer molecules.

Comparison of the reflectivity measurements with various models of the films arrangement revealed that the best fit is obtained for the simplest models, assuming homogeneous in-depth mass density distribution in all investigated nanocluster films. The single-layer model is compared with experimental data in Fig 1. This indicates that the deposition of subsequent cluster "monolayers" leads to a structure with a homogeneous cluster distribution rather than to a "multilayer" structure with a pronounced in-depth periodic structure.

The structural properties of the films obtained in this study form an excellent base to interpretation and calibration of transport measurements.

	Experiment title: SiC synthesis by dual beam ion implantation into silicon: crystallite formation studied by x-ray diffraction	Experiment number: 20_02_044
	Beamline: BM 20	Date of experiment: from: 21.04.2001 to: 23.04.2001
Shifts: 8	Local contact(s): Dr. N. Schell	<i>Received at ROBL:</i> 14.01.02
Names and affiliations of applicants (* indicates experimentalists): F. Eichhorn*, N. Schell* (a), J. Kaschny*, W. Matz, R. Kögler Forschungszentrum Rossendorf Institute of Ion Beam Physics and Materials Research P.O. Box 510119, 01314 Dresden, Germany (a) present address: ROBL-CRG at ESRF Grenoble		

Report:

The aim of the measurements was to analyze the effect of an additional (double) Si ion implantation on the growth of SiC crystallites in Si in comparison with the usual ion beam synthesis. Properties to be determined are the amount of grown SiC, the orientation of the crystallites in the Si matrix, the deformation in the SiC precipitates and in the surrounding Si matrix.

n-type Si(001) was implanted with $8.4 \times 10^{16} \text{ cm}^{-2}$ C ions of 360 keV at 450 °C (sample Z22). Additionally, the material was implanted with Si ions under conditions given in the following table.

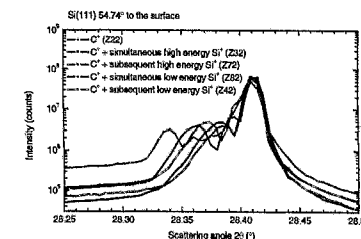
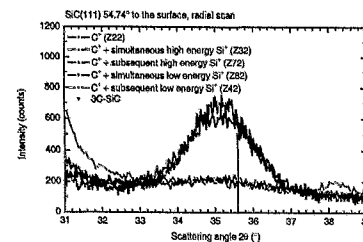
Sample name	Energy (keV)	Fluence (10^{16} cm^{-2})	Remarks
Z22	-	-	only C
Z32	1500	2.01	simultaneous implantation
Z72	1500	1.64	subsequent implantation
Z82	500	0.59	simultaneous implantation
Z42	500	0.54	subsequent implantation

Si ions with an energy of 1500 keV completely penetrate the layer of the implanted carbon atoms (maximum C concentration in a depth of 870 nm, maximum Si

concentration in a depth of 1770 nm), whereas Si ions with an energy of 500 keV are stopped in nearly the same depth (maximum Si concentration in a depth of 830 nm) like the C ions.

Typical results can be concluded from the figures with the 3C-SiC(111) diffraction line (the wavelength used was 0.15382 nm) characterizing the formation of 3C-SiC and the shape of the Si(111) diffraction line characterizing the deformation of the Si matrix:

- (1) In comparison with the pure carbon implantation (Z22, black symbols), SiC is formed in a higher amount if high energy Si ions which penetrate the carbon layer are simultaneously implanted (Z32, red symbols). The SiC crystallites are strained with $\Delta d/d = 0.012$ and have diameters of (4.5 ± 0.4) nm in sample Z22 and (4.9 ± 0.2) nm in sample Z32, respectively.
- (2) If the high energy Si implantation succeeds the C implantation, then the formerly grown SiC is obviously destroyed (Z72, green symbols). Furthermore, the Si matrix is deformed producing a considerable diffuse intensity.
- (3) By implantation of low energy Si ions (the Si atoms are stopped in nearly the same region as the C atoms) only a poor amount of SiC crystallites is formed. Their size seems to be smaller. A significant difference between the effect of a simultaneous (Z82, blue symbols) or subsequent (Z42, magenta symbols) Si implantation is not observed.
- (4) The grown 3C-SiC crystallites have the same crystallographic orientation as the Si matrix. Randomly oriented crystals or other SiC polytypes were not observed.



	Experiment title: Influence of dopant atoms in cubic boron nitride (c-BN) thin films on lattice parameters and intrinsic stress investigated by x-ray diffraction	Experiment number: 20_02_045
	Beamline: BM 20	Date of experiment: from: 14.06.2001 to: 17.06.2001
Shifts: 9	Local contact(s): Dr. N. Schell	<i>Received at ROBL:</i> 10.01.02
Names and affiliations of applicants (* indicates experimentalists): F. Richter, Th. Peifer, V. Linß* TU Chemnitz, Institut für Physik -123202- , D-09107 Chemnitz, Germany W. Hoyer, Th. Halm* TU Chemnitz, Institut für Physik -123402- , D-09107 Chemnitz, Germany		

Report:

First aim of this experiment was to study the reproducibility of the enlargement of cubic BN lattice constant by incorporation of Al. For this purpose a pure cubic BN and an Al-incorporated sample were measured. Secondly, the behaviour of a pure cubic BN layer on top of an Al-incorporated sublayer was investigated to study the influence of this sublayer on the biaxial stress value of the pure cubic BN-layer.

A preliminary study on such c-BN films revealed that the reflex of the (111) lattice planes is well pronounced, therefore this reflex was chosen to be studied. To obtain a great variety of different orientations of these (111) planes relative to the sample surface, a monochromatic beam of 1.1 Å was used. The angle between the incident beam and the sample surface was fixed at values of 0.3 ° (slightly above the angle of external total reflection). To access differently oriented planes, the detector was

moved either around a horizontal axis (2θ) or a vertical axis (2ω) while the remaining axis was held constant. The $\sin^2\Psi$ method (where Ψ is the angle between the vector normal to the lattice plane and the vector normal to the sample surface) was applied to analyze the biaxial stress state. Assuming a reliable value for the c-BN POISSON'S ratio from the literature, the spacing $d_{0(111)}$ of the unstressed lattice planes was obtained.

It comes out that the unstressed (111) lattice spacing of pure cubic BN depends on the preparation process. The relative enlargement of the lattice spacing due to Al incorporation remains nearly unchanged. As to the second study of the cubic BN layer on top of a Al-incorporated sublayer the contributions of the sublayer and top layer could not be resolved. The mean value of the lattice spacing lies between that of the pure cubic BN layer and that with incorporated Al described above.

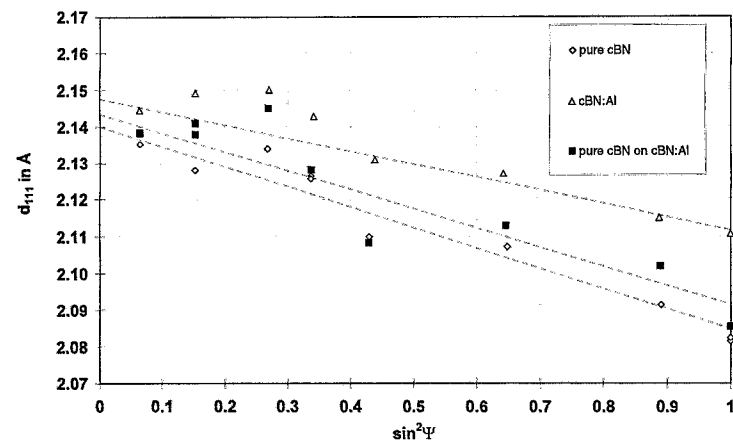



Fig. 1: Lattice spacing of (111) planes having different orientations with respect to the sample surface: a pure cubic BN layer, cubic BN layer with incorporated Al and a pure cubic BN-layer on top of a cubic BN-sublayer with incorporated Al.

 ROBL-CRG	Experiment title: Identification of carbon phases formed by high dose carbon implantation into single crystalline silicon carbide at elevated temperatures	Experiment number: 20_02_046
	Beamline: BM 20	Date of experiment: from: 19.09.2001 to: 22.09.2001
Shifts: 12	Local contact(s): Dr. N. Schell	<i>Received at ROBL</i> 05.09.02
Names and affiliations of applicants (* indicates experimentalists): F. Eichhorn*, V. Heera, N. Schell* (a) Forschungszentrum Rossendorf Institute of Ion Beam Physics and Materials Research P.O.B. 510119, 01314 Dresden, Germany (a) present address: ROBL-CRG at ESRF Grenoble		

Report:

SiC and diamond are semiconductor materials with unique physical properties for very promising applications for high frequencies, high power and extreme environment (radiation, high temperature). However, the possibility of doping these materials are limited and complementary to each other. Only n-doped SiC and p-doped diamond can be produced in a reliable way [1]. It is found that p-n-junctions can be formed by ion beam synthesis of buried nanocrystallites, especially diamond in SiC [2].

The material studied was 6H-SiC(0001) implanted with $1 \times 10^{18} \text{ cm}^{-2} \text{ C}^+$ (60 keV) at 900 °C. In this high temperature implantation process nanocrystals of diamond should grow in 6H-SiC at a depth of $(110 \pm 30) \text{ nm}$ below the surface. At lower implantation temperatures it was not possible to grow diamond in 6H-SiC.

Various x-ray scattering techniques like coplanar diffraction, grazing incidence diffraction (GID), texture studies, measurement of specular reflectivity, and reciprocal space mapping were used at laboratory and synchrotron sources to study structural details of the material.

The diamond crystallites are found to be completely aligned to the host lattice according to the relationship: diamond $\langle 111 \rangle \parallel$ substrate 6H-SiC $\langle 0001 \rangle$
 diamond $\langle 110 \rangle \parallel$ substrate 6H-SiC $\langle 11-20 \rangle$.

Fig. 1 shows the results obtained with the GID method. Here, the x-ray penetration depth Λ is controlled by the radiation incidence and exit angle near the critical angle in the range of 7 ... 1800 nm.

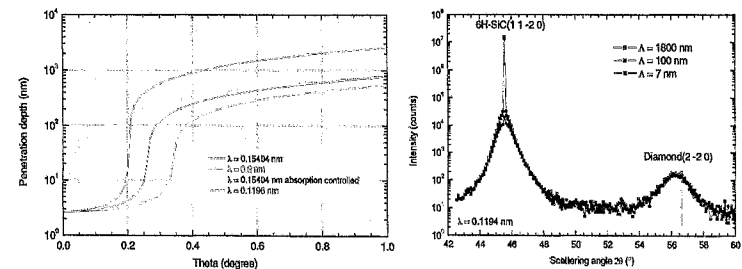


Fig. 1: Penetration depth of x-rays into crystalline SiC and a GID radial scan.


In detail, from the tails of the substrate reflection the nanocrystal diameter is determined to be 5 nm ... 10 nm.

Position and width of the diamond nanocrystal radial scan (particle size deconvoluted) give the strain and the strain fluctuation in the diamond crystals: $\Delta d/d = 0.01 \dots 0.02$, $\delta d/d \approx 0.01$. The width of the diamond nanocrystal angular scan (particle size deconvoluted) contains the orientation fluctuation with a FWHM = $2^\circ \dots 12^\circ$.

Furthermore, it is found that the nanocrystalline layer begins immediately at the surface (it is not buried!)

[1] R. Kalish, *Diamond and Related Materials* **10**, 1749 (2001)

[2] V. Heera *et al.*, *Applied Physics Letters* **76**, 2847 (2000)

 ROBL-CRG	Experiment title: Phase transformations of multi-layered HTS/dielectric/manganate and HTS/manganate/HTS structures in real-time synchrotron x-ray scattering study	Experiment number: 20_02_047 EU #12
	Beamline: BM 20	Date of experiment: from: 13.07.2001 to: 17.07.2001
Shifts: 12	Local contact(s): Andreas Bauer	<i>Received at ROBL:</i> 28.02.02
Names and affiliations of applicants (* indicates experimentalists): Todor Dochev, Kornely Grigorov Institute of Electronics, BAS, 72, Blvd. "Tzarigradsko Chaussee", 1784 Sofia, Bulgaria		

Report:

The goal of this project was to investigate the phase transformation of thin multilayer structures from High Temperature Superconductor - $Y_1Ba_2Cu_3O_{7.6}$ (YBCO) and manganate - $La_{0.7}Sr_{0.3}MnO_3$ (LSMO) both deposited on different substrates by means of real-time synchrotron X-ray scattering. The SR-XRD experiments are in pursuit of complex and fundamental questions concerning the development of new devices, which should encounter new demands.

We studied the temperature influence on the phase formation and phase interaction process. The latter was possible only using SR at ROBL, because the process demands short measuring times in order to follow the process adequately. Additionally, we found the temperature range of existence of the superconducting phase analyzing the lattice parameter and the peak evolutions. The formation of new unexpected phases was also registered. We established the general temperature range of the superconducting YBCO phase formation. To attain this purpose, a special chamber was constructed to fit the goniometer and to work in oxygen atmosphere at elevated temperatures.

The measured structure was 40 nm quenched in vacuum YBCO deposited on $SrTiO_3$ (STO) substrate. The experiment carried out was designed to simulate the process of oxygen uptake and superconducting phase formation such as it takes place in the deposition set-up. A set of scans was measured from 650°C to room temperature in oxygen pressure of 900 mbar. The oxygen content is correlated with the lattice constants of the YBCO layer. Its structure consists of three cubes, with yttrium or barium at the center, copper at the corners, and oxygen at the middle of each edge with the exception of the middle cube, which has oxygen vacancies at the outer edges. The critical feature in this structure is the presence of two sheets of copper-

oxygen ions, located above and below the oxygen vacancies, along which superconduction takes place. The transport of electrons perpendicular to these sheets is not favored, making the YBCO structure severely anisotropic. One of the challenges in fabricating crystalline YBCO ceramics capable of passing large currents is to align all the grains in such a manner that their copper-oxygen sheets line up. We calculated the lattice parameter "c" in function of the temperature, which is related with the oxygen content.

Fig. 1 displaces the one-to-one dependence, which is quasilinear from 600°C to 450°C and then leads to saturation. The relative peak shifts give valuable information concerning the lower temperature limit, which was found to range from 420-450°C – Fig. 2.

The peak amplitude was also studied due to its correlation with the coherent domain size of diffraction. The peak amplitude evolution, presented on Fig. 3, becomes significant from about 570°C and saturates at about 420°C. Taking account of all considered data we can deduce that the temperature range of phase formation ranges from 570°C to 420°C. It is worth noting here, that when a film is grown at insufficient oxygen supply other phases could be formed, such as e.g. $BaCuO_2$. This phase was confirmed both by SR-XRD and high precision RBS simulation. The latter method states that this layer is thick about 20 nm and lies on the interface. In Fig. 4 the beginning of the process of oxygen uptake is shown at the highest temperature. With red arrows the reflection from Y_2O_3 and $BaCuO_2$ phases are shown. Here, all the planes (00l) are shifted left (to lower 2 θ) in comparison with the orthorhombic superconducting phase. Moreover, peak (004) is missing. At the end of this process – Fig. 5, the reflections from the $BaCuO_2$ phase disappear and the (004) YBCO peak appears. The (00l) peak positions correspond to the peak reflections representative for $Y_1Ba_2O_7$.

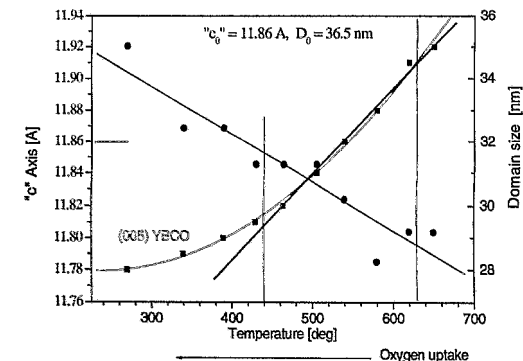


Fig. 1: The lattice parameter "c" as a function of the oxygen uptake. On the left axis, the domain size evolution is shown as a function of the temperature.

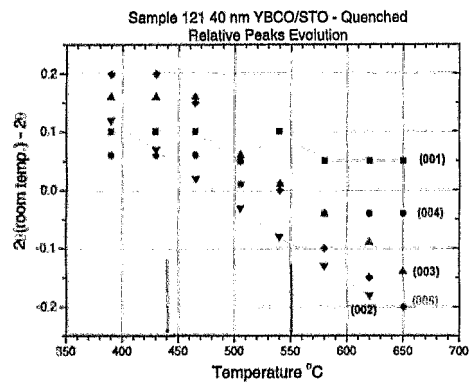


Fig. 2: The relative peaks evolution for 40 nm quenched YBCO/STO.

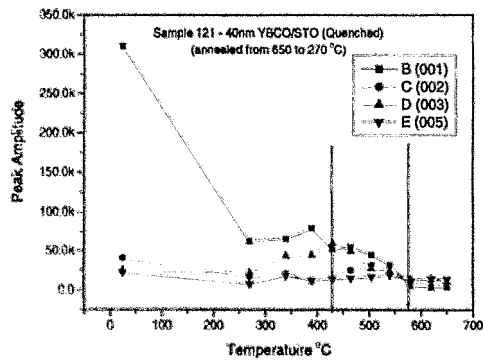


Fig. 3: Peak amplitude variations as a function of the temperature.

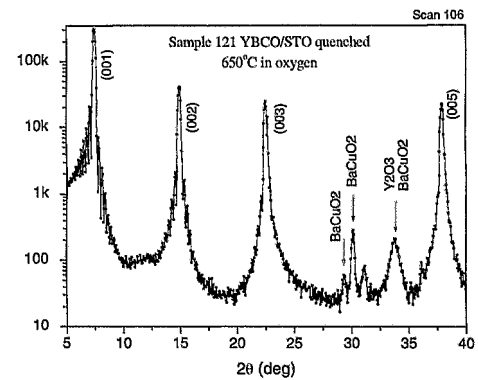


Fig. 4: YBCO/STO scan at the beginning of the oxygen uptake. Scan at 650°C.

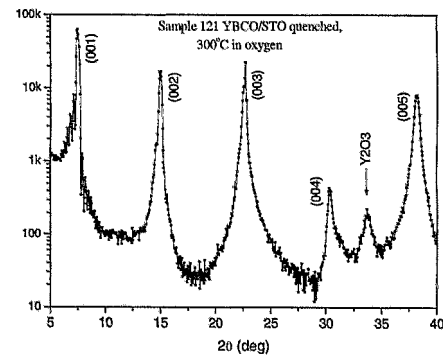


Fig. 5: YBCO/STO scan (at 300°C) at the end of the oxygen uptake process.

 ROBL-CRG	Experiment title: Texture measurement on tourmaline	Experiment number: 20_02_048 EU #23
	Beamline: BM 20	Date of experiment: from: 15.09.2001 to: 18.09.2001
Shifts: 9	Local contact(s): Andreas Bauer	<i>Received at ROBL:</i> 08.06.02
Names and affiliations of applicants (* indicates experimentalists): Dr. Pavol Mikula*, Nuclear Physics Institute ASCR, 250 68 Řež rear Prague, Czech Republic Dr. Kurt Walther*, GeoForschungsZentrum Potsdam, c/o FZ Rossendorf, PF. 51 01 19, 01314 Dresden, Germany Dr. Alexander Frischbutter*, GeoForschungsZentrum Potsdam, Telegrafenberg, 14473 Potsdam, Germany		

Report:

Tourmaline (ditrigoonal-pyramidal) is a characteristic mineralisation during the pneumatolytic state of the consolidation of granitic intrusions into the Earth's crust. It may be concentrated like planar, mostly spotlike distributed occurrences on joint planes within granitic bodies, but never reaches concentrations in nature required for diffraction experiments using neutron radiation. Therefore, textural information on tourmaline may be of interest analysing the latest states of granitic magma consolidation or even states of its earliest deformation.

Tourmaline occurs in several modifications depending on its contents on iron, sodium and others. The tourmaline under investigation was proved to be the iron-rich mineral *schoerl*.

Otherwise, the tourmaline spectrum is known to have many reflexes. The strongest peaks – determined from a powder sample – are: $(0\ 5\ \bar{5}\ 1)$, $(2\ 2\ \bar{4}\ 0)$, $(0\ 1\ \bar{1}\ 2)$, $(1\ 3\ \bar{4}\ 1)$, $(1\ 2\ \bar{3}\ 2)$ and $(2\ 1\ \bar{3}\ 1)$.

The texture of a tourmaline covered joint plane from a granodiorite was determined by measuring pole figures within steps of five degrees. The azimuth angle was measured in the interval $0...360^\circ$ and for the pole angle $0...70^\circ$. The number of pole figures should be not less than six. The wavelength of the incident beam was chosen to be $1.541\ \text{\AA}$.

A special computer code was written for the data handling, i. e. for the composing of the pole figures from the scans. The code makes a background correction and – if needed – adds some pole figures. Furthermore, the experimental data can be smoothed by several methods: binominal smoothing (including the next, the next but one, the next but two, the next but three and the next but five neighbours), fast Fourier transformation or cyclic cubic splines. Large crystallites give raise to strong, but narrow peaks. These peaks should be eliminated in the quantitative texture analysis because in other pole figures the corresponding peak would not be observed (they would occur between the neighbouring points of the measuring grid and, therefore, not be measured). The computer code indicates peaks with widths less than a preselected value.

For example, in Fig. 1 are shown the experimental $(2\ 2\ \bar{4}\ 0)$ and $(1\ 2\ \bar{3}\ 2)$ pole figures, respectively, and in Fig. 2 are shown the recalculated $(1\ 3\ \bar{4}\ 1)$ and $(2\ 2\ \bar{4}\ 0)$ pole figures. At present the coincidence between experimental and recalculated pole figures are poor due to the large pollution of the experimental pole figures with single grain orientation. Further investigations are on their way.

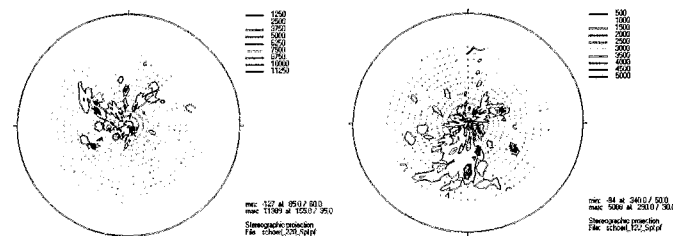


Fig. 1: Experimental pole figures. The pole figures are smoothed by cyclic cubic splines.

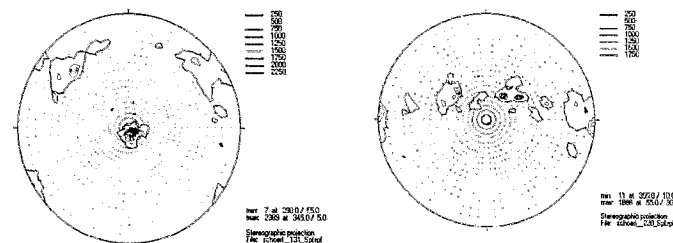



Fig. 2: Recalculated pole figures.

 ROBL-CRG	Experiment title: Investigation of the shape of the chemical composition profile in InGaAs/GaAs heterostructures	Experiment number: 20_02_049 EU #21
	Beamline: BM 20	Date of experiment: from: 22.09.2001 to: 25.09.2001
Shifts: 9	Local contact(s): Dr. Norbert Schell <u>schell@esrf.fr</u>	<i>Received at ROBL:</i> 12.12.01
Names and affiliations of applicants (* indicates experimentalists): Dr. Jerzy Sassi, ITME, Warsaw, Poland e-mail: sassi_j@sp.itme.edu.pl M. Sc. Krystyna Mazur, ITME, Warsaw, Poland e-mail: mazur_k@sp.itme.edu.pl		

Report:

The investigations of the laser structure active layer $\text{In}_{0.13}\text{Ga}_{0.87}\text{As}/\text{GaAs}$ were performed with samples with the same chemical composition but a range of layer thicknesses to estimate the range of the metastable equilibrium state. The value of the lattice misfit is equal to $\Delta a/a = 9.3 \times 10^{-3}$ which corresponds to a critical thickness of $t_c = 200 \text{ \AA}$. The layer thicknesses in the range of 80-1000 \AA (above and below the critical thickness) were investigated by means of high resolution x-ray diffractometry with synchrotron radiation ($\lambda = 1.5358 \text{ \AA}$) and in combination with a conventional x-ray source ($\lambda = 1.5405 \text{ \AA}$). All of the epitaxial layers were produced in ITME. The coplanar high-angle $\theta/2\theta$ -scans were performed for substrate and layer reflections. Additionally, the ω -scans (scan perpendicular to the diffraction plane) and reciprocal space mapping in the vicinity of the 004 layer node were done. The strain relaxation and the layer thickness were determined from $\theta/2\theta$ -scans, and the distribution of diffuse scattering related to misfit dislocation was measured by means of reciprocal space maps. The diffuse scattering intensity depends on the strain field, the microstructural arrangement and the density of the defects.

It was necessary to use the synchrotron radiation for the epitaxial layers with the thickness below 500 \AA to measure the diffuse scattering. The experimental results are presented in Table I.

Table I: Experimental results : $\theta/2\theta$ data of the laser structure active layer $\text{In}_{0.13}\text{Ga}_{0.87}\text{As}/\text{GaAs}$

No	sample	thickness [\AA]	$\Delta\theta$ synchr [deg]	layer thicken.(interf. fring.)
1	str2364	80	-	bufor thicken.1837 \AA
2	str2363	300	0.685	layer thicken.342 \AA
3	str2355	580	0.683	layer thicken.582 \AA
4	str2364a	800	0.612	relaxation

The diffuse scattering connected to the misfit dislocation is observed for the layer thickness exceeding 300 \AA (Table I). But the main relaxation process connected with the shift of layer reflection starts at an epi-layer thickness of 800 \AA . An example of the diffraction pattern of the metastable state is presented in Fig.1. In this figure one can see the diffuse spot characteristic for a small dislocation density ($\rho d \leq 1$) where ρ is the linear dislocation density and d the layer thickness [1]. Besides the diffuse spots in the reciprocal space map, also the thickness fringes are visible. As the dislocation density increases (the long range order is not retained), the layer reflection continuously transforms to an anisotropic Gaussian extended in a direction perpendicular to the diffraction vector and a layer peak shift is observed (see Table I, No 4). Our results are in agreement with the calculations and simulations presented in [1].

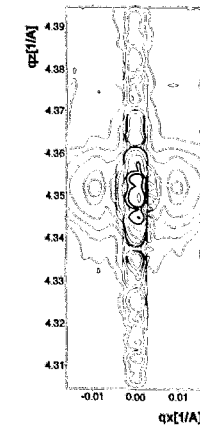
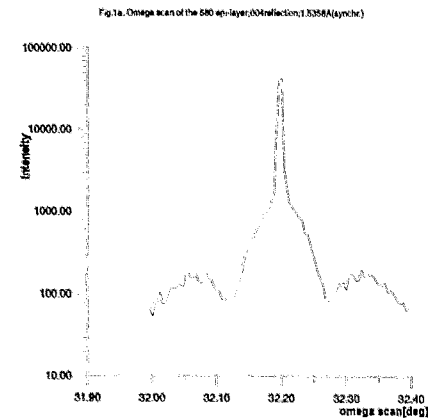



Fig.1b: Reciprocal space map of the 580A epi-layer, 004 reflection, 1.5358 \AA synchr.

References

- [1] V.M. Kaganer *et al.*, Phys. Rev. B, Vol. 55, No. 3 (1997) 1793-1810.

	Experiment title: <i>In-situ annealing studies of SiGe nano-structures: x-ray diffraction and GISAXS studies</i>	Experiment number: 20_02_050 EU #10
	Beamline: BM 20	Date of experiment: from: 25.10.2001 to: 30.10.2001
Shifts: 15	Local contact(s): Andreas Bauer	<i>Received at ROBL:</i> 14.02.02
Names and affiliations of applicants (* indicates experimentalists): Dr. Julian Stangl, University of Linz Dr. Zhenyang Zhong, University of Linz Mag. Rainer T. Lechner, University of Linz		

Report:

The intentions of this beamtime at ROBL were the investigations of SiGe-structures and nanostructures with the help of grazing incident small angle scattering (GISAXS) and conventional high angle diffraction. Si/SiGe cascade emission structures have been developed and manufactured recently, and for the first time with well-resolved electroluminescence in 10 μm wavelength range. The non-radiative lifetime is found to depend strongly on the design of the quantum well structure (layer thickness, Ge concentration and interface roughness). Using GISAXS we want to obtain more detailed information about the interface roughness correlation properties within one interface and from interface to interface. The self-organisation of pyramidal PbSe islands that spontaneously form during strained-layer epitaxial growth of PbSe/PbEuTe superlattices results in the formation of 3D dot crystals. Lateral and vertical ordering of these PbSe quantum dots have been studied recording reciprocal space maps around (111).

The Si/SiGe cascade structures were investigated using GISAXS geometry with a PSD. This geometry enables us to record a large range of momentum transfer in reciprocal space, i.e. small lateral structures. Thus, we achieved detailed information on the correlation spectrum of the interface morphology.

To obtain information on the vertical and lateral ordering of the PbSe dots, we measured reciprocal space maps (RSMs) in coplanar high-resolution x-ray diffraction

geometry. RSMs were measured in three different azimuths $[-1-12]$, $[-101]$ $[-211]$ within the (111) surface using a position sensitive detector (PSD). In the RSMs q_z is parallel to the [111] surface normal. A large number of satellite peaks is observed not only along q_z , but also in the q_x direction parallel to the surface (Fig. 1). The appearance of these peaks proves that the dot positions are highly correlated both laterally and vertically. This ordering shows a strong dependence on the PbEuTe spacer layer thickness; thus a whole sample series with the same growth parameters, but with varying spacer layer thicknesses, were investigated. We were able to show that a pronounced hexagonal lateral ordering tendency for vertical aligned dots exists around 160 \AA spacer layer thickness (Fig. 1a). Furthermore, the lateral dot spacing changes linearly with spacer thickness, as can be seen from the spacing of the lateral intensity maxima. As a comparison, we investigated also a sample with a spacer thickness of about 460 \AA , revealing a well ordered fcc-like dot stacking (Fig. 1c).

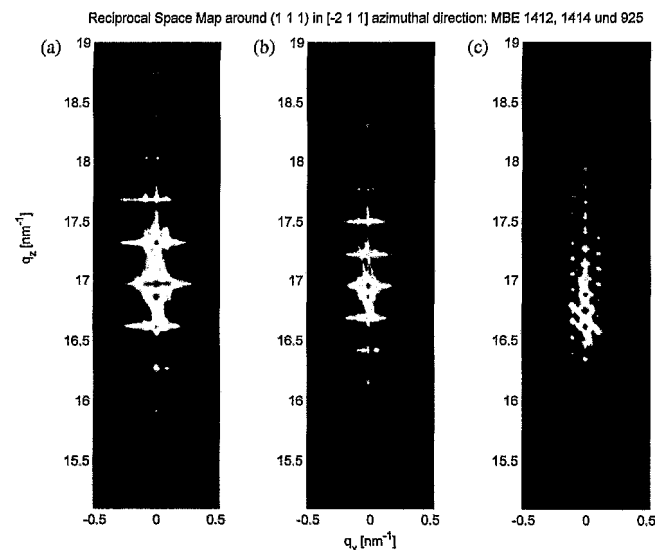



Fig. 1: Reciprocal space maps around (111): PbSe Dots with (a) 160 \AA , (b) 200 \AA and (c) 460 \AA PbEuTe spacer layer thickness.

	Experiment title: <i>In-situ</i> x-ray diffraction during reactive magnetron sputter deposition of Ti and Cu nanocomposites	Experiment number: 20_02_051
	Beamline: BM 20	Date of experiment: from: 14.11.2001 to: 20.11.2001 (A) and from: 24.04.2002 to: 30.04.2002 (B)
Shifts: 18(A) + 18(B)	Local contact(s): Dr. Norbert Schell	<i>Received at ROBL:</i> 01.03.02
Names and affiliations of applicants (* indicates experimentalists): * J. Böttiger, University of Aarhus, Denmark * N. Schell, ROBL-CRG, Germany		

Report: (A)

In recent years, nanocrystalline materials have been introduced as a new class of materials with unique properties and a great potential for industrial applications. These properties are connected with the small grain sizes down to a few nm whereby an appreciable fraction of the atoms is residing in grain boundaries, i.e. atoms are situated in defect environments. This can result in high catalytic activity and high corrosion resistance and also in highly beneficial magnetic or mechanical properties. However, single-phase nanocrystalline materials are not stable with respect to thermal grain growth, which results in deterioration of their properties. To avoid this grain growth at elevated temperatures and to build additional beneficial properties into the materials, two-phase nanocrystalline materials, nanocomposites, can be introduced. E.g., the combination of a ductile phase (Cu) and a hard and brittle phase (ZrN) in a ZrN-Cu nanocomposite results in mechanical properties, that make the nanocomposite very suitable for a variety of tribological applications [1].

Nanocrystalline materials, including nanocomposites, are produced by many different techniques, e.g. melt spinning and vapour phase sputtering. Frequently, an intermediate amorphous phase is produced, which is transformed by thermal annealing into a two-phase amorphous/nanocrystalline material. In our experiment we wanted to study the nanostructure and its development during deposition of TiN-Cu composites by reactive magnetron sputtering. This nanostructure depends on the deposition parameters, and such knowledge is required to tailor the nanostructure for optimum performance in specific applications. Before and after our experiments, we also did *ex-situ* x-ray diffraction measurements, additionally characterizing the phases appearing, the preferred orientation of the grains, the grain size and the microstrain as a function of the deposition temperature and the substrate bias voltage. At ROBL *in-situ* x-ray diffraction and reflection measurements were carried out, and, for various temperatures, the development of the nanostructure was followed as a function of film thickness, including in real-time. The nanostructure was also studied using a transmission electron microscope (TEM), while a scanning electron microscope (SEM) was used to measure the surface morphology. The film composition and thickness were obtained by Rutherford backscattering spectroscopy (RBS).

EXPERIMENTAL

The deposition chamber (together with the detailed scattering geometry and the quality of the data, like intensity, resolution, background, which can be obtained with the set-up) is described in detail in Ref. 2.

For the *in-situ* studies (incident x-rays monochromatized to 12.651 keV / $\lambda = 0.980 \text{ \AA}$), three different scattering geometries were used: (1) Bragg-Brentano large-angle scattering (XRD) revealing the texture, the out-of-plane lattice strain, grain sizes and microstrain (lattice defects). (2) Grazing incidence and grazing exit in-plane large-angle scattering (GIXS), with incident angle of 0.2° , i.e. a penetration depth of about 100 \AA , probing the crystallographic planes perpendicular to the surface. (3) Low-angle specular reflectivity giving film thickness and information on density and surface roughness.

Further experimental parameters were: base pressure 2×10^{-5} Pa, target material Ti₅₀Cu₅₀ (element mixture of 99.999% pure Ti and 99.999% pure Cu, manufactured by induction melting on a water-cooled Cu crucible under a Zr gettered Ar-atmosphere), reactive sputter gas a mixture of Ar (99.9996%) and N₂ (99.99990%) with the ratio 4:1 at a total gas pressure of 0.6 Pa. The magnetron (only one at the time) was run at a dc power of 70 W, resulting in a deposition rate of approximately 0.5 \AA/s on Si(100) with a 180 nm amorphous oxide layer on top. The temperature varied from room temperature up to 700°C, a negative bias voltage of -30 V was applied.

RESULTS

At low-temperature depositions, due to a high N concentration, only a small amount of the fcc Cu phase was observed while for higher temperatures a strong Cu(111) peak developed (Fig. 1). The texture changed with deposition temperature, and the grain size increased (no thermal grain growth) and the microstrain decreased with increasing deposition temperature. Plotting the microstrain as a function of grain size, we found the data points to be lying on a single line similar to the universal, empirical plots in the literature of microstrain versus grain size. From the real-time measurements, it was found that nanostructural changes only took place during growth, not in between depositions, where the temperature was kept at the deposition temperature (Fig. 2). By SEM and cross-sectional TEM, hillock-like protrusions at the surface (TiN-Cu and pure Cu, as revealed by energy dispersive x-ray analysis) were observed at deposition temperatures above 300°C (Fig. 3) driven most likely by mechanical stress.

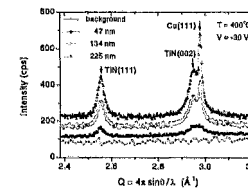


Fig. 1: Typical Bragg-Brentano x-ray diffractograms recorded *in situ* at 400°C with -30 V bias.

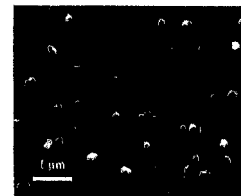


Fig. 3: SEM picture of the surface of a film deposited at 400°C with a bias of -30 V.

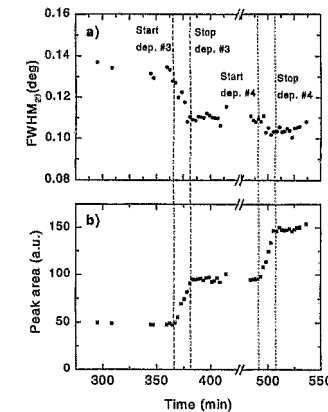


Fig. 2: FWHM_{2θ} and area of TiN(111) *in-situ* Bragg-Brentano diffraction peaks, recorded during and in between depositions of a TiN-Cu film at 25°C with a bias of -30 V versus time.

- [1] P. Zeman, R. Cervisy, P.H. Mayrhofer, C. Mitterer, and J. Musil, *Mat. Sci. & Eng. A* **289**, 189 (2000).
 [2] W. Matz, N. Schell, W. Neumann, J. Böttiger, and J. Chevallier, *Rev. Sci. Instrum.* **72**, 3344 (2001).

	Experiment title: <i>In-situ</i> x-ray diffraction during reactive magnetron sputter deposition of Ti and Cu nanocomposites	Experiment number: 20_02_051
	Beamline: BM 20	Date of experiment: from: 14.11.2001 to: 20.11.2001 (A) and from: 24.04.2002 to: 30.04.2002 (B)
Shifts: 18(A)+18(B)	Local contact(s): Dr. Norbert Schell	<i>Received at ROBL:</i> 20.08.02
Names and affiliations of applicants (* indicates experimentalists): * J. Böttiger, University of Aarhus, Denmark * N. Schell, ROBL-CRG, Germany		

Report: (B)

Introduced as a *new class of materials*, nanocrystalline materials are polycrystalline materials with grain sizes between a few nanometers and 100 nm. Because of the extremely small grain sizes, a large volume fraction of the atoms is located at the grain boundaries, i.e. atoms are sitting in defect environments. This confers to the materials *unique properties*, e.g. increased strength/hardness, enhanced diffusivity, improved ductility/toughness, reduced density, reduced elastic modulus, higher electrical resistivity, increased specific heat, higher thermal expansion coefficient, lower thermal conductivity, and superior soft magnetic properties [1]. These properties bear a great potential for industrial applications. Nanocrystalline materials are produced by many different techniques, including quenching from the liquid phase (melt spinning) and the vapour phase (sputtering). *Magnetron sputtering* has turned up to be a versatile technique for deposition of thin-film nanocrystalline materials. To tailor the nanostructure of magnetron-sputtered nanocrystalline thin films for specific applications, knowledge of the *dependence of the nanostructure on the deposition parameters* are required as is an *understanding of the mechanisms which control the formation and evolution of the nanostructure*. A general review dealing with the microstructure of polycrystalline films can be found in Ref. 2.

This report describes experimental studies at ROBL of the *evolution of the nanostructure of magnetron-sputtered gold films during the non-epitaxial growth and subsequent heat treatments*. More specifically, by *in-situ* x-ray diffraction and reflection measurements, the *preferred orientation of the grains (texture), the lattice constant (stress), the grain size and microstrain* were studied.

EXPERIMENTAL

The **deposition chamber** is described in detail in Ref. 3. For the *in-situ* studies (incident x-rays monochromatized to 13.120 keV / $\lambda = 0.945$ Å), three different scattering geometries were used: (1) Bragg-Brentano large-angle scattering (XRD) revealing texture, out-of-plane lattice strain, grain sizes and microstrain (lattice defects). (2) Grazing incidence and grazing exit in-plane large-angle scattering (GIXS), with incident angle of 1.8° (penetrating the whole film), probing the crystallographic planes perpendicular to the surface. (3) Low-angle specular reflectivity giving film thickness and information on density and surface roughness. To increase signal intensity and data taking speed, we used a *sagittally focussing 2nd DCM crystal* (leading to a focus spot of $400 \times 500 \mu\text{m}^2$ at the sample position) and a *1-dim. PSD*.

Further experimental parameters were: base pressure 5×10^{-4} Pa, target material Au, sputter gas Ar (99.9996%) at a pressure of 0.6 Pa. The magnetron (only one at the time) was run at a dc power of 10 W, resulting in a *deposition rate of approximately 1.3 Å/s* on Si(100) with a 180 nm amorphous oxide layer on top. The temperature varied from room temperature (deposition) up to 220°C (annealing), a negative bias voltage of -30 V was applied.

RESULTS

During growth, with Bragg-Brentano geometry (Fig. 1) only *(111) grains*, having a (111) plane parallel to the film surface, have been observed, while with GIXS geometry, *(111)* and (200)* grains*, having one of their (111) and (200) planes, respectively, perpendicular to the film surface, have also been observed. The *(111)* and (200)* grains were uniformly distributed* over the film thickness, while the *(111) grains were concentrated in the upper part of the film*.

The *(111) texture changed during annealing* (at temperatures of 95°C, 125°C, 150°C and 215°C) and *probably also during growth*. The GIXS Au(111) peak area decreased during annealing (Fig. 2) which we suggested was due to changes in the orientation of the individual (111)* grains and/or recrystallization. During growth, probably, an increase of the (111) grains relative to the (111)* grains took place. The *microstrain decreased strongly during the initial growth and in the beginning of an annealing period*, while the *grain size increased both during film deposition and during annealing*. A surprisingly *small activation energy of grain growth of 0.25 ± 0.02 eV* has been found. During the first few minutes of growth, the *compressive film stress was strongly reduced* due to a tensile contribution arising from the coalescence of the initially formed islands. *During annealing, stress relaxation* has also been observed.

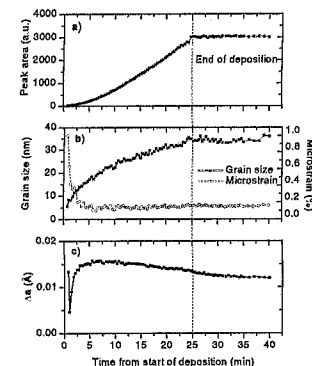


Fig. 1: The Bragg-Brentano Au(111) peak measured *in situ* during growth (room temperature, -30 V bias, deposition time 25 min., corresponding to 1900 Å film thickness): (a) peak area versus deposition time, the dashed curve is a power law fit with exponent 1.56; (b) drastically decreasing microstrain and increasing grain size versus deposition time; (c) deviation of lattice constant (from tabulated Au lattice constant) versus deposition time, revealing first tensile and later decreasing compressive contributions.

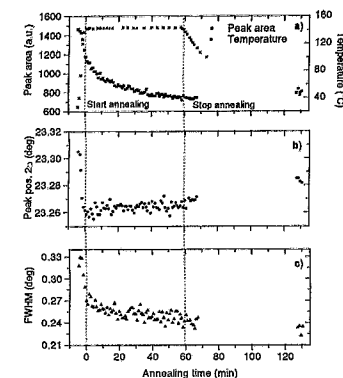



Fig. 2: The GIXS Au(111) peak with incidence angle 1.8° measured during annealing for 1 hr at 143°C of a 750 Å Au film deposited with standard parameters (see caption of Fig. 1): (a) peak area versus annealing time, revealing a decreasing intensity in contrast to what is found in Bragg-Brentano geometry; (b) peak position 2θ versus annealing time – almost constant during annealing; (c) decreasing FWHM versus annealing time, indicating grain growth and/or reduction of microstrain.

[1] C. Suryanarayana, Inter. Mater. Rev. **40** (1995) 41.

[2] C.V. Thompson, Ann. Rev. Mater. Sci. **30** (2000) 159.

[3] W. Matz, N. Schell, W. Neumann, J. Böttiger, and J. Chevallier, Rev. Sci. Instrum. **72** (2001) 3344.

	Experiment title: Phase formation processes in nanoscale Nickel layers during heat treatment on different silicon substrates	Experiment number: 20_02_052
	Beamline: BM 20	Date of experiment: from: 21.11.2001 to: 25.11.2001
Shifts: 12	Local contact(s): Dr. Norbert Schell, Florian Berberich	Received at ROBL: 26.06.02
Names and affiliations of applicants (* indicates experimentalists): Jochen Rinderknecht, AMD Saxony Manufacturing GmbH Dr. Hartmut Prinz, AMD Saxony Manufacturing GmbH Florian Berberich, IIM, FZR		

Report:

In press for Microelectronic Engineering

IN SITU HIGH TEMPERATURE SYNCHROTRON-RADIATION DIFFRACTION STUDIES OF NI AND CO-NI SILICIDATION PROCESSES

Silicidation processes in nanoscale Ni and Co(Ni) layers, i.e. Co with 5at.% Ni sputtered from an alloy target, on Silicon substrates were studied. These silicides are supposed to be future substitutes for CoSi₂ which is commonly used as contact material on active areas and poly gates of transistors in state-of-the-art ICs [1,2]. The phase formation sequences as well as the formation and transition temperatures in the temperature range between 160°C and 750°C were studied.

Thin film diffraction investigations were done using grazing incidence geometry at the Rossendorf Synchrotron Radiation Beamline at the ESRF, Grenoble. An energy just below the Co-K absorption edge was chosen to minimize Co fluorescence background. An evacuated high temperature diffraction chamber enabled us to perform *in situ* high temperature diffraction studies. The impact of different Silicon substrates, i.e. polycrystalline Si and (100) orientated Si single crystal substrates, as well as the impact of different species (As, P) and different doses of dopants on the phase formation and transition processes were analyzed.

The samples with a pure Ni layer on As or P doped single crystalline Silicon show first weak and very broad Ni₂Si diffraction maxima at 160°C. The amount of this phase increases up to 275°C. At this temperature the Ni₂Si → NiSi transition starts, which is completed at about 300°C. Further thermal treatment up to 650°C increases the amount of the NiSi phase, mainly due to Silicon substrate consumption. At 700°C the intensity of the NiSi diffraction peaks decreases significantly whereas no indications of NiSi₂, the high temperature phase of Nickel silicide, could be observed. No diffraction peaks are visible at 750°C which is due to an epitaxial growth of NiSi₂.

On polycrystalline Silicon Ni₂Si is stable up to 200°C for standard As doped substrates and up to 250°C for highly As doped substrates. The formation of NiSi starts at 200°C and 250°C, respectively. The intensities of NiSi diffraction maxima rise up to 475°C. The transition to NiSi₂ starts at 475°C. NiSi is present up to 650°C in case of standard As doped polycrystalline Si substrates and at 550°C where it also vanishes for highly As doped substrates.

In the case of the (Co, Ni) layers on Si (100) single crystal substrates very weak diffraction peaks of (Co,Ni)₂Si for the highly doped substrates become visible between 275°C and 300°C. There are also very broad diffraction maxima of the monosilicide phase (Co,Ni)Si visible at 275°C. (Co,Ni)Si reaches its maximal intensity of diffraction peaks at 350°C for standard As doped substrates, at 400°C for highly As doped substrates and 425°C for highly P doped substrates. In each case (Co, Ni)Si is stable up to 475°C, at which temperature it is transformed into (Co, Ni)Si₂ for both highly doped samples. For standard doped substrates the disilicide phase starts to form at 400°C.

The investigations further developed the knowledge of the silicidation process of thin films on different substrates.

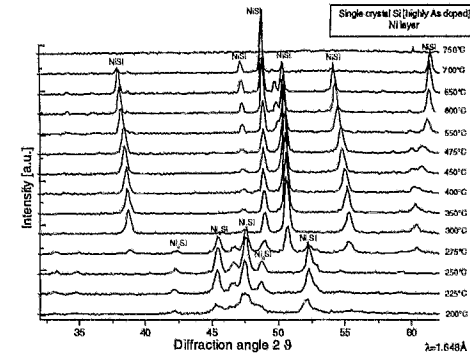


Fig. 1: Diffraction pattern of Ni layer on highly As doped single crystal Si.

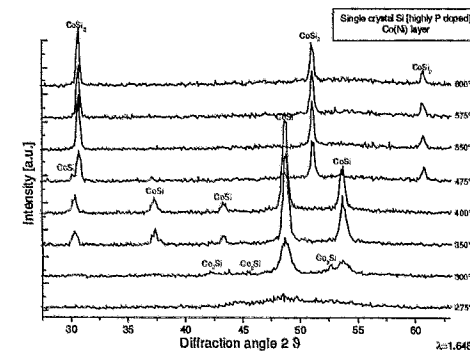



Fig. 2: Diffraction pattern of (Co,Ni) layer on highly P doped single crystal Si.

References

- [1] C. Detavernier, R.L. Van Meirhaeghe, K. Maex, F. Cardon, Mat. Res. Soc. Symp. 611 (2000)
- [2] O. Chamirani, A. Steegen, H. Bender, A. Lauwers, M. de Potter, F. Marabelli, K. Maex, Conference programme and abstracts of MAM2001

 ROBL-CRG	Experiment title: Waveguide enhanced scattering from thin macromolecular films	Experiment number: 20_02_053
	Beamline: BM 20	Date of experiment: from: 06.02.2002 to: 10.02.2002
Shifts: 12	Local contact(s): Dr. Norbert Schell	<i>Received at ROBL:</i> 19.11.02
Names and affiliations of applicants (* indicates experimentalists): Ansgar Jarre*, Christoph Ollinger*, T. Salditt* Universität des Saarlandes, 66048 Saarbrücken (present address: Gustav August Universität, 37073 Göttingen) N. Schell, ROBL-CRG		

Report:

Coherent x-ray scattering can be used as a novel tool to study the static and dynamic disorder in solid supported lipid bilayers. Lateral inhomogeneities in multilamellar stacks, due to a variation in the number of lipid bilayers N , inhomogeneities due to dewetted areas, or the strain field associated with inclusions are different examples of static disorder in lipid films. Thermal fluctuations due to bending and compressional modes are examples of dynamic disorder.

In the present experiment, the *suitability of the ROBL beamline for coherent scattering* has been investigated and a corresponding scattering setup was tested. This is a prerequisite for a possible future use of waveguides as coherence filters for coherent scattering experiments at ROBL (replacing conventional pinholes). In order to observe a static speckle pattern, the primary beam (11 keV, Si(111) monochromator) was defined by motorized slits (jj-xray) to $D = 50 \mu\text{m} \times 300 \mu\text{m}$ (vert. x horz.). Fig. 1a shows that the corresponding primary beam profile, measured with fixed detector slits of $D = 40 \mu\text{m}$ (vertical), exhibits the characteristic Fraunhofer fringes, reflecting the coherence of the beam.

At these settings, a multilamellar phospholipid sample (dimyristoylphosphatidylcholine, DMPC), deposited on a Si substrate in 10 mg/ml solution Isopropanol (see [1]), was aligned in reflection (see Fig. 2a). The sample was heated to $T = 50^\circ\text{C}$ in order to reach the fluid L_α -phase of the lipids, where thermal bilayer fluctuations are excited. The samples were only partially hydrated yielding a lamellar repeat distance of $d = 46.8 \text{ \AA}$, as determined from the Bragg peak positions in a reflectivity scan. As expected, the reflectivity curves do not exhibit speckles. This is understandable, since for specular reflectivity the reflected amplitudes across the sample all add up in phase. Contrarily, under the non-specular conditions of a rocking or a detector scan, the statistical nature of the large-scale film structure, which is dominant at small q_x should appear [2]. The speckles occur on a q_x -scale of $q_x \cong 5 \cdot 10^{-6} \text{ \AA}^{-1} = 2\pi/L$, corresponding to a lateral length scale of $L \cong 0.1 \text{ mm}$ (see Fig. 1b). On this scale defects are clearly visible in the optical microscope. Interestingly, the speckle pattern extends over the whole range of the rocking scan, in particular also close to the so-called Yoneda wing (see Fig. 1c), indicating that the source of diffuse scattering is of static rather than dynamic nature. Only at higher q_x we would expect that thermal fluctuations rather than the static disorder of the domain structure

dominates the diffuse scattering. In this case, a temporal averaging would result in a continuous curve like in conventional (non-coherent) x-ray scattering. However, due to the decay of the diffuse scattering with q_x , it is difficult to measure in this range with sufficient statistic to discriminate between speckle and photon shot noise (described by Poisson statistics).

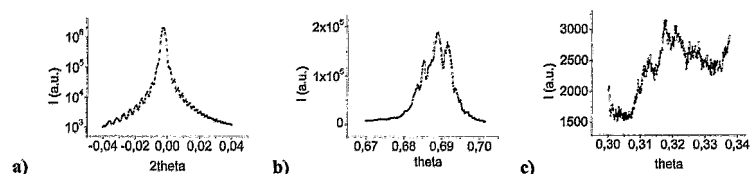


Fig. 1: Profile of the primary beam (a), Static speckle pattern observed in a rocking scan (b) around the specular 1st Bragg peak (2θ fixed at 1.363°), and (c) in the region of the Yoneda peak (2θ fixed at 1.37°).

In a second step we investigated the suitability of the beamline for x-ray photon correlation spectroscopy (XPCS). As a prerequisite for such studies, the temporal photon statistics of the primary beam as quantified by the intensity-intensity auto-correlation function $g(t) = \langle I(0)I(t) \rangle / \langle I \rangle^2$ must be measured and be sufficiently free of noise [3]. Fig. 2b shows a typical autocorrelation spectrum $g(t)-1$ of the primary beam (measured by an ALV-5000/EPP autocorrelator setup). Apart from the electron bunch structure of the ring ($2^*1/3$ fill) observed at small t of about $1 \mu\text{s}$, strong structures are observed in the range of 10 ms (plot a in Fig. 2b). These were found to result from the Piezo control of the second monochromator crystal (used for higher harmonic suppression). Shutting off these piezos (Queensgate) gives a much more stable (uncorrelated) temporal pattern, suitable for XPCS (plot b in Fig. 2b). Hence, we have shown, that *the ROBL beamline is in principle well suited for XPCS*, if the monochromator stabilization is shut off.

In the future, this may be used for different studies of soft-condensed matter, e.g. lipid membranes. We are also planning to replace the small entrance slits (or pinhole) by a planar x-ray waveguide, which acts like an efficient coherence filter [4].

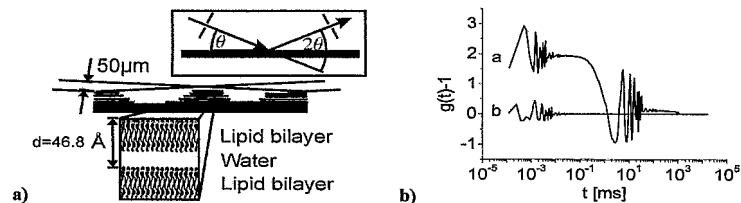



Fig. 2: Schematic setup of the experiment (a). Autocorrelation functions of the primary beam at ROBL (b).

References:

- [1] M. Vogel, C. Münster, W. Fenzl, T. Salditt, PRL **84**(2) (2000) 390-393
- [2] J.L. Libbert, R. Pindak, S.B. Dierker, I.K. Robinson, Phys. Rev. B **56**(11) (1997) 6454-6457
- [3] A. Fera, I.P. Dolbnya, G. Grübel, H.G. Müller, B.I. Ostrovskii, A.N. Shalaginov, W.H. de Jeu, PRL **85**(11) (2000) 2316-2319, and references therein
- [4] T. Salditt, F. Pfeiffer, H. Perzl, A. Vix, U. Mennicke, A. Jarre, A. Mazuelas, to be published

	Experiment title: Structure investigation of embedded nano-clusters in SiO₂ films by x-ray diffraction	Experiment number: 20_02_054
	Beamline: BM 20	Date of experiment: from: 6.03.02 to: 9.03.02
Shifts: 9	Local contact(s): Dr. Norbert Schell	Received at ROBL: 10.09.02
Names and affiliations of applicants (* indicates experimentalists): Dr. Johannes von Borany Forschungszentrum Rossendorf, Institute of Ion Beam Physics and Materials Research, PO. Box 51 01 19, 01314 Dresden, Germany Dr. Frank Eichhorn Forschungszentrum Rossendorf, Institute of Ion Beam Physics and Materials Research, PO. Box 51 01 19, 01314 Dresden, Germany Dr. Natalia Shevshenko Forschungszentrum Rossendorf, Institute of Ion Beam Physics and Materials Research, PO. Box 51 01 19, 01314 Dresden, Germany		

Report:

1. Nanoclusters in thin SiO₂ films

Ion beam synthesized Au, Ge, and Si nanoclusters embedded in SiO₂ films of 30 or 100 nm thickness onto a (100) Si substrate have been investigated by grazing incidence X-ray diffraction. The best experimental conditions have been found to use an incident angle of 0.3° and a Soller collimator in front of the scintillation detector. The results can be summarized as follows:

- Au nanoclusters can be clearly detected even in thin SiO₂ films < 100 nm. Depending on the Au impurity content in the oxide (7-20 at.%) and the annealing temperature of ion beam synthesis the nanocluster size varies between 1.5 and 3 nm which is in reasonable agreement with TEM results (Fig. 1).
- As derived from the existence of multi-reflexes [(111), (200), (220), (311)] the Au nanoclusters are nanocrystals with a random crystalline orientation within the matrix. The crystalline structure has been found even in the as-implanted state, which can be explained by the high mobility of gold under the beam during the synthesis process. No texture effects have been observed.
- From the comparison of Au, Ge and Si nanocrystals it has been found that Ge nanoclusters could be identified only for the highest impurity content of 20 at.%, whereas the detection of Si nanocrystals failed (Fig. 2).

- The use of an asymmetrical cut Ge crystal in front of the sample has only a minor influence on the SN-ratio of the diffraction reflexes (Fig. 3). The idea behind was to enlarge the divergence of the incoming beam to fulfil the condition for X-ray diffraction for an increased number of nanocrystals with respect to their random orientation within the SiO₂ film.

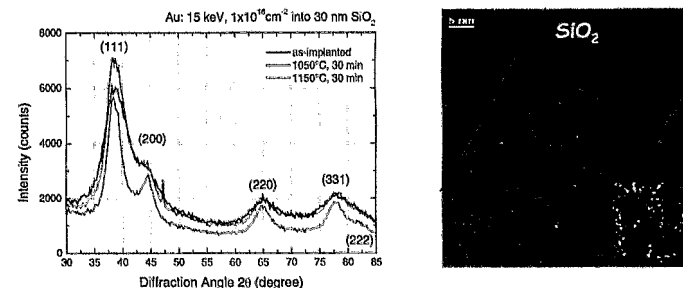


Fig.1: XRD pattern of Au nanocrystals embedded in a 30 nm SiO₂ film on (100) Si for different annealing conditions (left) and cross-sectional TEM micrographs of the film annealed at 1050°C for different magnifications (right) which enable information about the position of the nanoclusters in the oxide and their crystalline structure due to the identification of the lattice planes (inset).

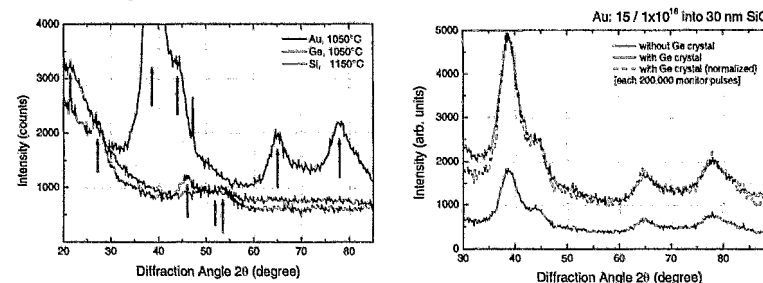


Fig. 2: Comparison of the XRD pattern of Au, Ge, and Si nanocrystals in thin SiO₂ films (Au, Ge for dox=30 nm; Si for dox=100 nm). Despite the higher annealing temperature and the larger oxide thickness no significant reflexes have been observed for Si.

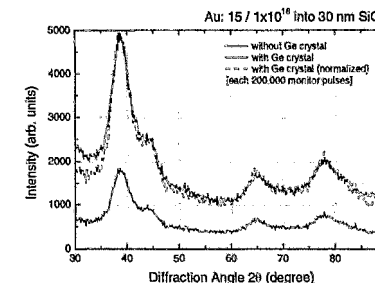



Fig. 3: Comparison of the XRD pattern of Au nanocrystals in SiO₂ films for different measuring modes. The use of an asymmetrical cut Ge crystal results in only a minor improvement in the SN-ratio (10-15%), whereas small angle scattering significantly reduces the intensity.

2. Investigation of Si/SiO₂ superlattices

In addition, X-ray reflectometry (XRR) has been successfully applied to determine the properties of superlattice structures made by ~ 45 periods of SiO₂ (5nm) and thin Si nanocrystal films (with variable nanocrystal size between 2-5 nm). The structures were produced by reactive physical vapour deposition. The evaluation of the XRR interference pattern gave information about the total thickness of the superlattice and allowed to determine independently the thickness of the SiO₂ layers and the mean nanocrystal size, which corresponds to the Si layer thickness. For these investigations the high angle resolution of the ROBL beamline enables considerably advantages in comparison to laboratory equipment.

 ROBL-CRG	Experiment title: <i>In situ</i> x-ray diffraction during high energy sputter deposition of TiAlN and TiN multilayers	Experiment number: 20_02_055
	Beamline: BM 20	Date of experiment: from: 01.05.2002 to: 06.05.2002
Shifts: 15	Local contact(s): Dr. Norbert Schell	<i>Received at ROBL:</i> 23.09.2002
Names and affiliations of applicants (* indicates experimentalists): * Dr. Subroto Mukherjee, FZR, IIM, FWII, PF 510119, D - 01314 Dresden, Germany * Dr. Norbert Schell, ROBL-CRG at ESRF		

Report:

TiN and $Ti_{1-x}Al_xN$ are commercially exploited hard coatings having been deposited on a wide variety of materials to enhance the surface properties like microhardness, wear resistance, etc. On the other hand, commercial Al alloys are widely used in the automobile and textile industry, because of its low mass density. A suitable surface hardening technique of Al is therefore desirable, as it improves the wear resistance of the Al maintaining its light mass density, suitable for industrial applications.

In the planned investigation, $Ti_{1-x}Al_xN$ was to be deposited on thermally amorphized Si(100) wafers biased at different pulsed negative voltages (up to -800 V) so as to change the deposition rate, growth pattern and crystallographic orientation during growth. The growth rate of the coating and its preferred orientation are known to depend on the film thickness and also on the substrate bias and the duration. In previous experiments at our institute involving the arc deposition with TiAl targets it was observed that the Ti to Al ratio of the film depends on the substrate bias. Also, the film thickness, phase formation, preferred orientation and chemical composition changes with the bias characteristics. The same experiment was now to be repeated with TiAl targets sputtered with magnetrons, in a reactive nitrogen environment so that the film texture evolution could be determined *in-situ*.

The role of pulsed bias is essential for deposition experiments as revealed by recent experiments by McKenzie and Bilek [1]. If a dc bias (~ -1 kV) is applied to the substrate, most of the deposited film will be resputtered, resulting in a film of very poor growth rate. Alternatively, if a pulsed bias is used then during the pulsing there will be considerable amount of stress release by a temperature rise in the implanted region. Simultaneously, there will be a significant reduction in (re)sputtering. This will lead to the possibility of growth of films of much larger thickness.

In continuation of earlier similar work done at ROBL [2, 3], the growth of $Ti_{1-x}Al_xN$ was to be studied by using *in-situ* X-ray diffraction, thereby monitoring the growth mode, the phase formation, and the development of the grain size, texture and stress during growth. The studies were carried out systematically with variations of the deposition parameters like temperature, bias voltage and sputtering gas pressure.

EXPERIMENTAL

The deposition chamber (together with the detailed scattering geometry and the quality of the data, like intensity, resolution, background, which can be obtained with the set-up) is described in detail in Ref. 4.

For the *in-situ* studies (incident x-rays monochromatized to 12.915 keV / $\lambda = 0.960$ Å), three different scattering geometries were used: (1) Bragg-Brentano large-angle scattering (XRD) with a lin. PSD revealing time-resolved the texture, the out-of-plane lattice strain, grain sizes and microstrain (lattice defects). (2) Grazing incidence and grazing exit in-plane large-angle scattering (GIXS), with incident angle of 0.2° , i.e. a penetration depth of about 200 Å, probing the crystallographic planes perpendicular to the surface. (3) Low-angle specular reflectivity giving film thickness and information on density and surface roughness.

Further experimental parameters were: a base pressure about 2×10^{-5} Pa, a reactive sputter gas as a mixture of Ar (99.9996%) and N_2 (99.99990%) with the ratio 4:1 and a total gas pressure of 0.3 Pa, the magnetron dc power of 80 W, leading to a deposition rate of about 1.4 Å/s. The samples were deposited at room temperature with later annealing up to 500°C , at 250°C , at 350°C and with various pulse bias characteristics (-25 V dc, $0/-200/-500$ V pulsed with 10 μs pulse-length and 500 Hz repetition rate).

RESULTS

Figs 1 and 2 show the slight effect – wished for at the outset of the experiment – of pulsed bias on the strain: putting on pulsed bias reduces the strain, thereby favoring the TiN(002) texture component [2, 5], i.e. reducing the TiN(111) and increasing the TiN(002) Bragg-reflections.

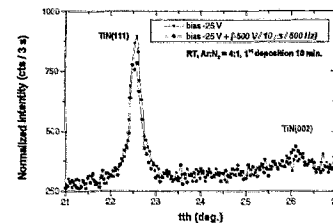


Fig. 1: Bragg-Brentano diffractograms for two depositions with and without pulsed bias as indicated in the inset.

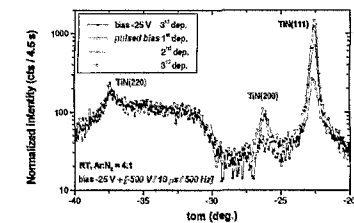



Fig. 2: In-plane GIXS diffractograms for two depositions with and without pulsed bias as indicated in the inset.

As observed, this effect would be too minute to improve the technological fabrication processes for an increase in film thickness by reducing (with moderate increase in deposition effort) film strain. Chemical composition tests of the samples with ERD and RBS back home in Rossendorf, however, showed a contamination of several per cent with Vanadium of the targets – the supplier had not kept the purity specifications, thereby invalidating the planned experiment. Further experiments with uncontaminated targets have to be repeated.

- [1] D.R. McKenzie, M.M.M. Bilek, Thin Solid Films 382 (2001) 280.
- [2] N. Schell, W. Matz, J. Böttiger, J. Chevallier, P. Kringhøj, J. Appl. Phys. 91 (2002) 2037.
- [3] J. Böttiger, J. Chevallier, J.H. Petersen, N. Schell, W. Matz, A. Mücklich, J. Appl. Phys. 91 (2002) 5429.
- [4] W. Matz, N. Schell, W. Neumann, J. Böttiger, J. Chevallier, Rev. Sci. Instrum. 72 (2001) 3344.
- [5] J. Pelleg, L.Z. Zevin, S. Lungu, N. Croitoru, Thin Solid Films 197 (1991) 117.

	Experiment title: Structural studies of materials for quantum cascade lasers	Experiment number: 20_02_056
	Beamline: BM 20	Date of experiment: from: 15.05.02 to: 19.05.02 and from: 03.07.02 to: 09.07.02
Shifts: 12 + 18	Local contact(s): Andreas Bauer (bauer@esrf.fr)	<i>Received at ROBL:</i> 22.11.02
Names and affiliations of applicants (* indicates experimentalists): T. Dekorsy; N. Georgiev*; F. Eichhorn*; A. Bauer* (a) Forschungszentrum Rossendorf Institute of Ion Beam Physics and Materials Research P.O.B. 510119, 01314 Dresden, Germany (a) present address: ROBL-CRG at ESRF, Grenoble		

Report:

There is considerable interest in developing shorter wavelength ($< 3 \mu\text{m}$) optical devices based on intersubband transitions (ISBT) such as ultrafast switches, modulators, and quantum cascade lasers. Pseudomorphic $\text{In}_x\text{Ga}_{1-x}\text{As}/\text{AlAs}$ heterostructures on InP or GaAs have emerged as excellent candidates for short-wavelength ISBT because of their large conduction band offset. However, the growth of appropriate structures on both GaAs or InP substrates requires to grow strained well and/or barrier layers, respectively. It was demonstrated that in ultrathin, strained $\text{In}_x\text{Ga}_{1-x}\text{As}/\text{AlAs}$ multiple quantum well (MQW) on GaAs substrate, x should be more than 0.4 in order to confine the carriers in the well region. However, island formation due to strain relaxation would be a problem in these MQW with high In content. The x-ray diffraction pattern of the MQW sample with 7 monolayer (ML) thick $\text{In}_x\text{Ga}_{1-x}\text{As}$ ($x \sim 0.7$) and AlAs layers, and 20 nm $\text{In}_y\text{Al}_{1-y}\text{As}$ ($y \sim 0.55$) layer is presented in Fig. 1. In this structure, we utilise the high barrier

provided by thin AlAs layers. An increased In content in the well and in the $\text{In}_y\text{Al}_{1-y}\text{As}$ barrier layers helps to compensate the large AlAs tensile strain.

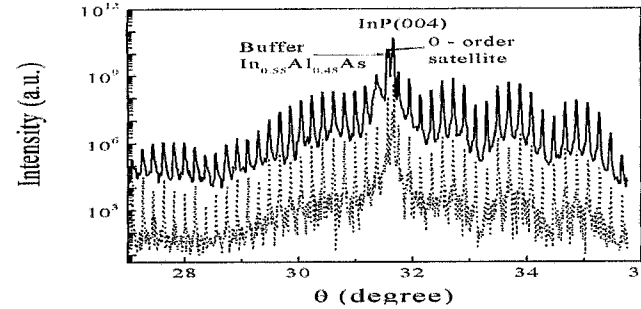
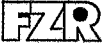


Fig. 1: XRD pattern of the $\text{In}_{0.7}\text{Ga}_{0.3}\text{As}/\text{AlAs}/\text{In}_{0.55}\text{Al}_{0.45}\text{As}$ MQW around the InP (004) reflex. Experimental data (solid line), and simulated (dotted line) using a model that includes interfacial compositional grading.

The main peak at the lower angle side of the InP(004) peak originates from the slight compressively strained $\text{In}_y\text{Al}_{1-y}\text{As}$ buffer layer. The zero-order peak of the MQW is located close to the substrate peak which indicates that compressive strain of the InGaAs and the InAlAs layers nearly compensate the tensile strain of the AlAs layers. In spite of the large misfit of the AlAs layers the average mismatch in the MQW is small, because the AlAs layers are much thinner than the InGaAs and InAlAs layers in the MQW. Note that the choice of an appropriately strained second barrier layer and buffer layer is essential for growing pseudomorphic QW structures. Indeed, if we grow these layers lattice matched we observe both a broadening and a reduced number of the satellite peaks. This is an indication for the deterioration of the crystalline and interfacial quality in MQW due to the increased strain from strongly mismatched AlAs layers. However, a model allowing 1-2 ML compositional grading at the interfaces provides an even better fit to the experimental data than the model assuming abrupt interfaces.

 ROBL-CRG	Experiment title: Structural studies of highly strained In_xGa_{1-x}As/GaAs heterostructures	Experiment number: 20_02_057
	Beamline: BM 20	Date of experiment: from: 19.05.2002 to: 22.05.02
Shifts: 9	Local contact(s): A. Bauer	<i>Received at ROBL:</i> 17.10.02
Names and affiliations of applicants (* indicates experimentalists): * J. Sass, ITME, Warsaw, Poland * K. Mazur, ITME, Warsaw, Poland * F. Eichhorn, FZ- Rossendorf, Dresden, Germany		

Report:

The objective of this study was to obtain information about the stress relaxation of the laser structure active layer In_{0.13}Ga_{0.87}As/GaAs in the range above the critical layer thickness. The experimental results were obtained with the asymmetric (224) reflections and non-specular reflectivity measurements as function of layer thickness (30-200 nm). The (224) reciprocal space mapping was performed using synchrotron radiation at a wavelength of 0.15406 nm. From the mutual position of the layer and substrate reflections in the (224) reciprocal space map for the layers in the range of thickness 30-58 nm one can state (i) that the coherency strain in the layer exists, (ii) that the concentration of indium in the layer is equal 0.13 (x=0.13). In the thickness range below 80 nm the misfit dislocation density can be calculated from the FWHM of the layer diffuse component (Fig. 3). In Fig. 1 the (224) reciprocal space map of the 58 nm layer thickness is shown.

In the case of the layer with 80 nm thickness, the shift of the layer reflection on the relaxation line in the (224) reciprocal space map (Fig. 2) was observed. This means that the relaxation process starts. From the modulus of momentum transfer, the relaxation degree of the layer stress and density of misfit dislocation were calculated. Besides, from the relaxation triangle in the (224) map it was stated that the concentration of indium in the layer was equal to 0.13 (x=0.13).

At the lattice mismatch close to 1%, the main relaxation mechanism is the slip of 60-degree dislocations. The normal component of the Burgers vector produces satellites in the layer reflection (Fig. 3) and steps on the layer surface. The surface layer micromorphology was measured by means of non-specular reflectivity and Normarski phase-contrast microscopy.

The bimodal reflection in reflectivity (Fig.4) suggests that the scale factor sq is much smaller than 1 (s-rms height of the surface step, q-momentum transfer). Besides, assuming a statistically isotropic and homogeneous Gaussian rough surface, the step correlation length was calculated from the FWHM of the diffuse component. Non-specular reflectivity results are well comparable with Normarski contrast phase microscopy results.

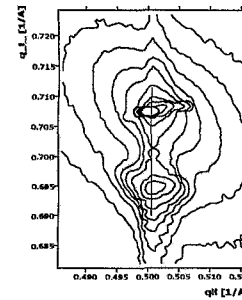


Fig.1: (224) reciprocal space map of the heterostructure (58 nm layer thickness).

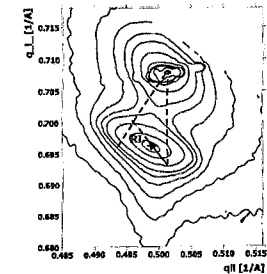


Fig.2: (224) reciprocal space map and relaxation triangle of the heterostructure (80 nm layer thickness).

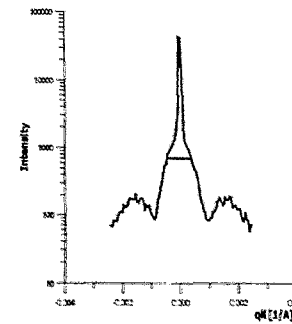


Fig.3: 002 and 004 omega scans (58 nm layer thickness).

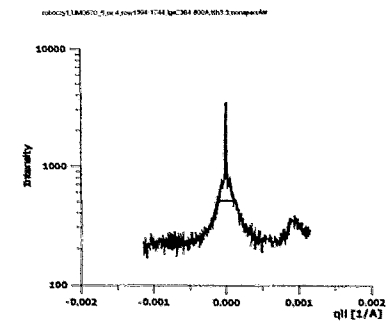
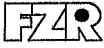


Fig.4: Non-specular diffuse scattering of the heterostructure (80 nm layer thickness).

 ROBL-CRG	Experiment title: Annealing study of SiGe quantum cascade structures grown on relaxed SiGe buffer layers	Experiment number: 20_02_058 EU #29
	Beamline: BM 20	Date of experiment: from: 12.06.2002 to: 18.06.2002
Shifts: 18	Local contact(s): Andreas Bauer	<i>Received at ROBL:</i> 25.11.02
Names and affiliations of applicants (* indicates experimentalists): Laurent Diehl *, Selcuk Mentese *, Julian Stangl * Johannes Kepler Universität, Institut für Halbleiterphysik, Linz, Austria		

Report:

The aim of the experiment was the investigation of plastic relaxation via the formation of dislocations in Si/SiGe multilayer structures. The samples have been grown at the PSI Villigen (Switzerland) and are so-called quantum cascade structures. A series of strained SiGe layers forms quantum wells for holes in the valence band. For especially designed quantum well widths and depths (the latter are determined by the Ge content of the wells and their strain status) minibands are formed under an applied bias, and electroluminescence can be observed. A particular problem of such structures in the SiGe system is the required large number of strained layers with a very high total thickness, which may lead to plastic relaxation. In order to enhance the design freedom for such structures, instead of growing them directly onto Si(001) wafers, they are grown onto a virtual substrate with a different lattice parameter than Si. For this purpose, Si wafers with a strain-relaxed SiGe buffer layer have been used.

For the investigated samples, the plastic relaxation of the remaining strain via formation or multiplication of dislocations during thermal treatment has been investigated, in order to obtain a measure for the thermal budget the structures may undergo during device processing without deterioration. It was planned to use a small furnace available at ROBL beamline to perform this annealing study *in-situ*, recording reciprocal space maps around selected reflections during annealing at temperatures between 450°C and 850°C. Due to a problem with the furnace, the annealing had to be carried out *ex-situ*, and the samples have been

measured after subsequent annealing steps. Fig. 1 shows several reciprocal space maps of sample J014 in the as-grown state as well as after annealing at 850°C for 30 minutes. As is obvious from the maps, the shape of the diffusely scattered intensity from the SiGe buffer as well as from the cascade multilayer shows small differences. Also, the average position with respect to the Si substrate is slightly changed, which might hint at a different strain state. It is, however, not clear, whether this is already an effect of annealing and a difference in the dislocation distribution in the samples, or whether the differences rather result from different measurement spots at the samples: as the annealing was *ex-situ* and the samples had to be aligned after each annealing step, it is likely that slightly different spots are illuminated.

As the samples are grown on a relaxed buffer containing already a high density of dislocations, the threading segments of dislocations penetrate the SiGe cascade structure already in the as-grown sample, leading to a peak broadening in reciprocal space maps. Hence small differences in the relaxation state are difficult to detect in the case of an *ex-situ* annealing study for samples exhibiting lateral inhomogeneities, as is the case here.

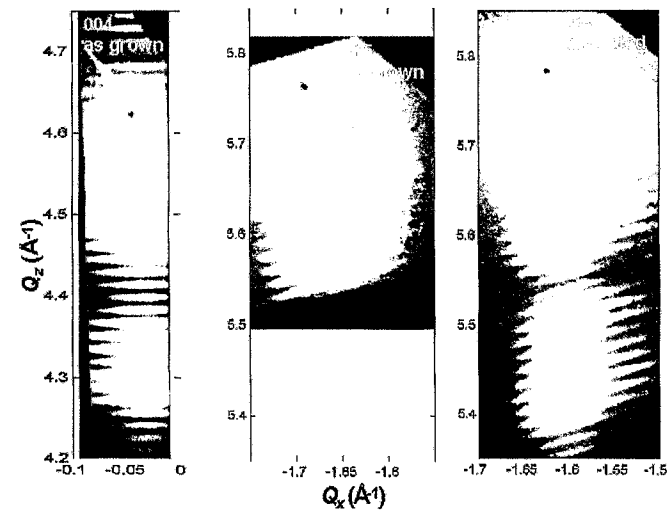



Fig. 1: Reciprocal space maps around (004) and (115) of sample J014 as grown and after annealing at 850°C for 30 min.

 ROBL-CRG	Experiment title: Influence of interface structure on GMR and magnetic behaviour of Fe/Cr multilayers	Experiment number: 20_02_059
	Beamline: BM 20	Date of experiment: from: 04.06.02 to: 08.06.02 and from: 29.08.02 to: 01.09.02
Shifts: 12 + 9	Local contact(s): Dr. Norbert Schell	<i>Received at ROBL:</i> 14.11.02
Names and affiliations of applicants (* indicates experimentalists): F. Prokert *, FZ Rossendorf, IIM, Dresden, Germany N. Shevchenko *, FZ Rossendorf, IIM, Dresden, Germany E.A. Kravtsov, Russian Academy of Science, IMP, Ekaterinburg, Russia M.A. Milyaev, Russian Academy of Science, IMP, Ekaterinburg, Russia		

Report:

The *interface structure of Fe/Cr multilayers* (MLs) was studied by x-ray reflectometry (XRR) and diffuse scattering using the contrast enhancement between Fe and Cr for measurements at energies in vicinity of the K-edges of these elements. The Fe/Cr MLs, UU9_3, UU9_1 and UU9_4, having the double layer structure $8 \times [^{57}\text{Fe}(2 \text{ nm})/\text{Cr}(1 \text{ nm})]$, were prepared by MBE on sapphire with a Cr buffer layer (7 nm) at different substrate temperatures of 60°C, 140°C and 240°C, respectively.

The data were received in the first run at energies *below* (5.95 keV) and *above* (6.05 keV) the *Cr K-edge* and in the second run *below* (7.10 keV) and *above* (7.15 keV) the *Fe K-edge*. Besides the measurements of the specular scattering also the diffuse scattering was studied by rocking and offset scans. Fig. 1 shows the plotted intensity of such scans taken at 7.10 keV.

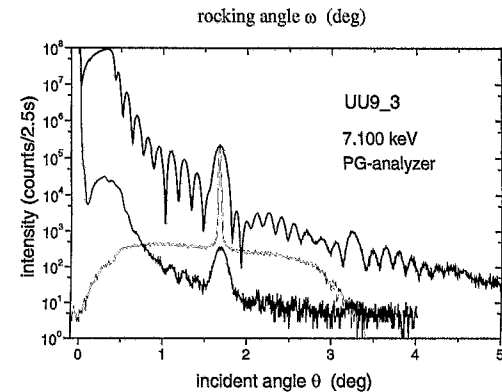


Fig. 1: Specular, longitudinal and transverse scans from the Fe/Cr ML UU9_3 measured below the Fe K-edge at 7.10 keV. The intensity of the transverse scan is plotted versus the rocking angle.

This study is a part of measurements on a series of this type of MLs. The MLs were grown on (1 0 -1 2) Al_2O_3 substrates, covered by 7 nm-Cr buffer layer, at different substrate temperatures in the range 20–480°C. Preceding investigations [1] have shown that the interface rms-roughness in these Fe/Cr-MLs strongly depends on the substrate temperature.

At present the evaluation of the measurements is not completed. Simulations using the REFS code (Bede Scientific software package) [2] are done only for the sample UU9_1. However, *first results* concerning the specular reflectivity have shown:


- The interface *rms-roughness*, σ_{rms} , of Fe-on-Cr ($\sigma_{\text{rms}}^{\text{Cr}}$) and Cr-on-Fe ($\sigma_{\text{rms}}^{\text{Fe}}$) are significantly different. The *interface width* $\sigma_{\text{rms}}^{\text{Cr}}$ is smaller compared to interface width $\sigma_{\text{rms}}^{\text{Fe}}$.

From the distribution of the diffuse scattering of this ML follows :

- The part of the vertically *correlated interface rms-roughness*, C_v does not exceed an amount of $C_v \approx (30 \pm 15)\%$.
- The MBE-grown Fe/Cr MLs of this type have an interface morphology with a short *lateral roughness correlation length* $\xi \approx 8 \pm 3 \text{ nm}$.
- The *Hurst parameter*, h , indicates with values of $h \approx 0.35 \pm 0.5$ a relatively high jaggedness of the interfaces. Based on the model of a self-affine interface morphology [3], this gives a *fractal dimension* $D=3-h$ of appr. 2.65.

References

- [1] V.V. Ustinov *et al.*, J. of Magnetism and Magnetic Materials 240 (2002) 511
- [2] B.K. Tanner *et al.*, Surface Invest. 12 (1997) 259
- [3] S.K. Sinha *et al.*, Phys. Rev. B 38 (1988) 2297

	Experiment title: Study of the high temperature stability of a strange titanium-hydrogen phase induced by ion beam implantation	Experiment number: 20_02_060 20_02_601
	Beamline: BM 20	Date of experiment: from: 06.09.2002 to: 10.09.2002
Shifts: 12	Local contact(s): Dr. Norbert Schell	<i>Received at ROBL:</i> 29.09.2002
Names and affiliations of applicants (* indicates experimentalists): * Prof. Tieshan Wang, FZR, IIM, PF 510119, D-01314 Dresden, Germany * Dr. Frank Eichhorn, FZR, FWIS, PF 510119, D-01314 Dresden, Germany		

Report:

A *strange hydrogen phase* has been found by the proposers in H_2^+ -implanted titanium samples. This phase is not yet characterized, but proved *stable under very high mechanical stress at room temperature*. It also showed very good *anti-oxidation stability at room temperature*. Therefore, this phase might be usable in hydrogen storage applications. A detailed study should characterize the temperature behaviour. In order to enhance the surface sensitivity, various samples were measured under grazing incidence in a high-temperature chamber at Cu-K α wavelength in vertical scattering geometry (*thermal in-situ XRD phase analysis*).

RESULTS

- The previously observed "strange" TiH_2 -phase has been *confirmed* and better *characterized* (Fig. 1).
- The thermal stability of this TiH_2 -phase has been studied carefully leading to a thermal *phase transition curve* as shown in Fig. 2 with a *critical temperature of $48 \pm 2^\circ C$* .
- The time dependence of the phase-transition has been determined at a fixed temperature of $65^\circ C$ (Fig. 3) showing that the transition, i.e. *dehydrogenation rate is temperature dependent*.
- The *hydrogen distribution* in the sample is *inhomogenous in respect to depth and H-concentration* (Figs 4, 5). After heating all the hydrogen is released (Fig. 4).
- Another *strange high-temperature-phase* was observed (under ongoing investigation); its peak position did almost not change under annealing up to $1.000^\circ C$, but it disappeared after the titanium phase transition.

Conclusions:

- The TiH_2 -phase observed has *features quite different from other well-known Ti/H-phases*.
- This phase is stable at room temperature, but with a critical temperature of only $48^\circ C$, the transformation can also be conducted by mechanical stress (former IBA work); so it has a potential to be used as an alternative phase for hydrogen storage media.
- This Ti/H-phase could be easily formed during mechanical and ion-implantation-processes.
- The dehydrogenation could be conducted by heating up to $100^\circ C$. It is useful for treating the hydrogenated Ti surface, esp. for driving out the H-contamination after modifications with ion beams.

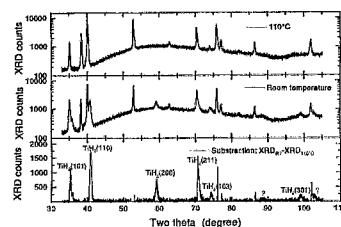


Fig. 1: XRD diagram of the "strange" TiH_2 -phase.

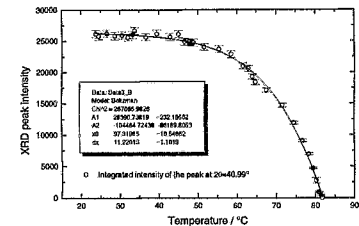


Fig. 2: The thermal transition curve of the TiH_2 phase.

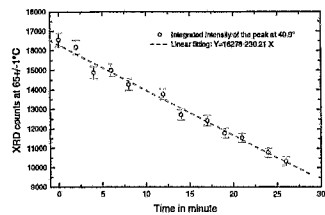


Fig. 3: The TiH_2 phase transition versus time at $65^\circ C$.

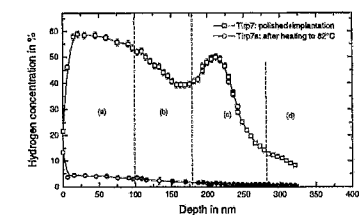


Fig. 4: Comparison of H-depth profiles before and after heating.

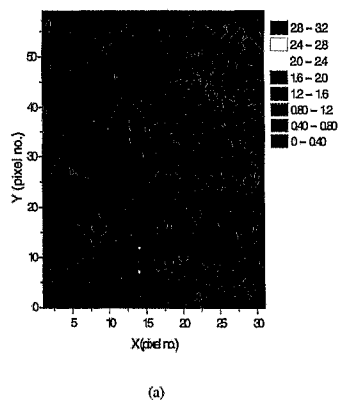



Fig. 5: Lat. distribution (res.: $3 \times 10 \mu m^2$) of hydrogen in different layers in depths (a) 181-280 nm and (b) >281 nm.

	Experiment title: Crystallisation of Ni-Ti thin film Shape Memory Alloy (SMA)	Experiment number: 20_02_061 20_02_602 EU #31
	Beamline: BM 20	Date of experiment: from: 25.09.2002 to: 29.09.2002
Shifts: 12	Local contact(s): Dr. Norbert Schell	<i>Received at ROBL:</i> 29.11.02
Names and affiliations of applicants (* indicates experimentalists): *Francisco M. Braz Fernandes, *Rui M. S. Martins, *Rui J. C. Silva CENIMAT – Centro de Investigação de Materiais Campus da FCT/UNL 2829-516 MONTE DE CAPARICA PORTUGAL		

1. Thin films production

NiTi thin films were deposited on Si(100) wafers using sputtering rf technique. The chemical composition of the target material was 44 wt% Ni – 56 wt% Ti, i.e. 49 at% Ni – 51 at%Ti. The sputter deposition performed, using the conditions described, gave rise to films with thickness ranges from 0.3 μm to 1 μm .

2. GIXRD *in situ* annealing

Samples of 10x10 mm² were cut to be analysed by GIXRD at ROBL. The annealing of the films took place under vacuum (pressures ranging from 5.7×10^{-6} to 1.4×10^{-5} mbar). Samples of NiTi thin films (0.3 μm to 1 μm thick) deposited on Si(100) wafers, with different sputtering conditions, were studied. The temperature range covered for the crystallisation studies was from room temperature to 520°C.

3. Results

The samples S8 and S11 (distance target-substrate during sputtering: 70 and 90 mm, respectively) showed, after annealing, the presence of the austenite phase (B2) of the Ni-Ti system and the intermetallic Ni₃Ti, as well as the presence of silicides (Figs 1 and 2). The sample S12 (distance target-substrate: 186 mm) only shows the presence of the Ni-rich solid solution (of Ti) and TiO₂.

Both S8 and S11 are not crystallised at 325°C, but they show a significant degree of crystallisation at 365°C. Increasing the temperature up to 445°C or 525°C, improves the degree of crystallisation.

Stress state determination by GIXRD was performed on the sample S8 at room temperature, after annealing at 445°C. The results (Fig. 3) show that the residual stress state is very low.

4. Discussion

- the greater distance target-substrate (186 mm) used for the sample S12 led to a significant Ti depletion on the sputtered thin film; during annealing a further depletion of Ti by the oxide formation led to the appearance of the Ni solid solution (Ti solute);

- the films S8 and S11 showed the formation of the B2 phase, the crystallisation temperature being comprised between 325°C and 365°C; the presence of Ni₃Ti intermetallic shows that the sputtered thin film is slightly enriched in Ni;
- the residual stress state of the S8 film after annealing appears to be very low.

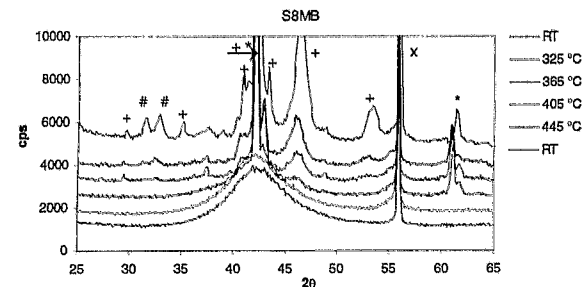


Fig. 1: GIXRD spectra of sample S8 at room temperature and different annealing temperatures (* B2, + Ni₃Ti, # Ni₂Si, x Si).

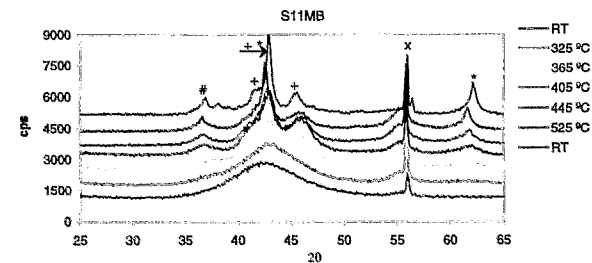


Fig. 2: GIXRD spectra of sample S11 at room temperature and different annealing temperatures (* B2, + Ni₃Ti, # Ti₅Si₃, x Si).

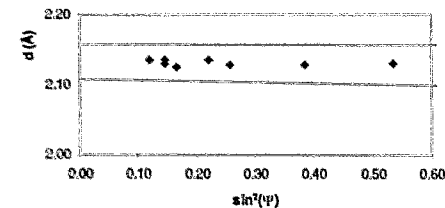



Fig. 3: GIXRD stress state determination on sample S8 at room temperature, after annealing at 445°C (the two lines show the limits of the 95% confidence interval).

	Experiment title: Structure of organic films grown on semiconductors	Experiment number: 20_02_062 20_02_600
	Beamline: BM 20	Date of experiment: from: 29.09.2002 to: 30.09.2002
Shifts: 6	Local contact(s): Dr. Norbert Schell	<i>Received at ESRF:</i> 25.11.02
Names and affiliations of applicants (* indicates experimentalists): Arindam Das*, Th. Halm*, W.Hoyer and D.R.T. Zahn TU-CHEMNITZ, Institute for Physics, Reichenhainer Str. 70, D-09107 Chemnitz, Germany		

Report:

Organic electronics exploits the outstanding properties of organic polymers and molecules that combine electrical conductivity with low weight, low cost and the ease of processing. Active layers from organic materials were e.g. successfully applied in organic light emitting diodes (OLED), solar cells, field effect transistors. The growth of organic films is an important step for the fabrication of these devices. This is due to the fact that physical properties such as opto-electrical characteristics depend on the surface and interface properties. Surface roughness is found to cause failure mechanisms that limit the lifetime of OLED.

With the advent of sophisticated organic thin film deposition techniques such as organic molecular beam deposition (OMBD), smooth and homogeneous organic films are easily prepared under well defined conditions. This development has further enhanced the great interest and drawn attention towards detailed investigations of surface and interface properties of organic films. This is not only for fundamental understanding of this subject but also for controlling interfacial properties so as to obtain desired electrical and optical parameters for a device [1, 2]. Many techniques such as scanning tunneling microscope (STM), ultraviolet photoelectron spectroscopy (UPS), low energy electron diffraction (LEED) are used to study the surface and interfaces properties of organic thin films [3-5]. Importantly, these techniques are suitable for very thin films and *in situ* investigations for obtaining structural and electronic properties of an organic film. However, employing these techniques on relatively thick organic films becomes difficult due to the limitation of these techniques, such as charging effects due to the low electrical conduction of the film. GIXRD is an ideal structural probe of such thin films and particularly for interfaces. It combines the power of conventional XRD for determining bulk structure with refraction effects at the interface to probe interfacial effects. By employing an angle of incidence α less than the critical angle α_c (typically of the order of 0.2°), the penetration of the x-ray beam can be limited to approx. 100 Å, giving surface sensitivity to the topmost molecules at the surface [6].

A conventional laboratory XRD facility has been used for x-ray reflectometry to obtain valuable information such as thickness, surface and interface roughness of organic thin films on GaAs or Si substrates. However, intensity less than 5 orders of magnitude was found as a limitation for detailing surface and interface properties. A synchrotron radiation source is considered to be suitable for these studies. Fig. 1 shows the reflectivity curves of a thin organic film deposited on GaAs substrate obtained using the laboratory XRD facility and synchrotron radiation facility. A saturation of the intensity at higher 2θ values for curves obtained using the laboratory XRD facility (40 V, 20 mA) clearly limits the information (Fig. 1b) as compared to the reflectivity curve received using the synchrotron facility (Fig. 1a). More than seven orders of magnitude in intensity is recorded when ROBL BM20 at ESRF is used. This is evidence of the usefulness of synchrotron radiation for such organic-inorganic systems.

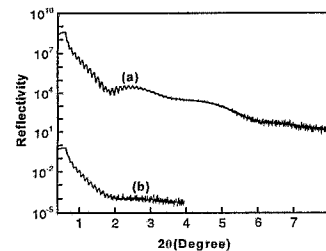


Fig.1: Reflectivity curves of the PTCDA/GaAs system using a) the synchrotron facility b) a laboratory facility.

The use of biologically important organic molecules such as DNA bases for device fabrication are becoming an emerging field of interest [7]. Thin films of these molecules such as Cytosine, Guanine and Thymine are prepared by OMBD under UHV conditions on hydrogen passivated Si(100) substrates. Fig. 2 displays reflectivity curves obtained using $\lambda = 1.54 \text{ \AA}$ at ROBL for Guanine films with various thicknesses. Each curve is recorded in the range of 0.1° – 0.4° . A typical experimental reflectivity curve is calculated with the Parrat's formalism for two interfaces, taking into account the roughness [8]. Fitting of these curves gives information of the film thickness, surface and interface roughness. The simulated dispersion absorption value, δ (7.8×10^{-7}) of Si substrate is found to match well with the expected value, 7.66×10^{-7} . δ values of guanine films are found to be nearly the same for various thicknesses with a value $\sim 3.0 \times 10^{-7}$. However, the surface roughness is observed to increase with thicker films. The surface roughness of a 37 nm film is 0.8 nm and the same for a film of ~ 125 nm is 1.4 nm. This clearly indicates that the surface morphology of the thicker film becomes rougher. Surface morphologies of these films are gathered from AFM measurements. This also supports the increasing surface roughness of guanine films with thickness and measured roughness (average height) are 0.8 nm and 1.6 nm for film thicknesses 37 nm and 125 nm, respectively. However, no clear oscillation due to the interference could be seen for cytosine films in the reflectivity measurements. Interestingly, further AFM investigation on cytosine films revealed that the surface roughness is very high (>3 nm). This suggests why no well defined interference pattern in x-ray reflectivity was observed for these films.

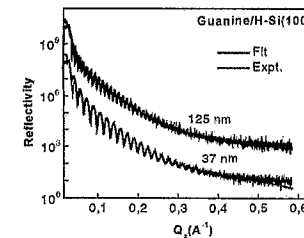
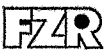



Fig. 2: X-ray reflectivity curves of Guanine films on hydrogen passivated Si(100) substrates.

References:

- S.R. Forrest, *Chem. Rev.* **97** (1997) 1793
- H. Ishii, K. Sugiyama, E. Ito, and K. Seki, *Adv. Mater.* **11** (1999) 605
- K. Glöckler, C. Siedel, A. Soukopp, M. Sokolowski, E. Umbach, M. Böhlinger, R. Berndt and W.D. Schneider, *Surf. Sci.* **405** (1998) 1
- S. Park, T.U. Kampen, D.R.T. Zahn, W. Braun, *Appl. Phys. Lett.* **79** (2001) 4124
- R. Fink, D. Gador, U. Stahl, Y. Zao, and E. Umbach, *Phys. Rev. B* **60** (1999) 2818
- M. Tolan, *X-ray scattering from soft-matter thin films, Springer Tracts in Modern Phys.* **148**
- Rosa Di Felice, Arrigo Calzolari, and Elisa Molinari, *Phys. Rev. B* **65**, 45104
- A. Das, G. Salvan, T.U. Kampen, W. Hoyer and D.R.T. Zahn, *Appl. Surf. Sci.* (in print)

 ROBL-CRG	Experiment title: <i>In-situ x-ray diffraction during reactive magnetron sputter deposition of nanocrystalline metals (nc Au)</i>	Experiment number: 20_02_063 20_02_604
	Beamline: BM 20	Date of experiment: from: 02.10.2002 to: 10.10.2002
Shifts: 25	Local contact(s): Dr. Norbert Schell	<i>Received at ROBL:</i> 02.12.02
Names and affiliations of applicants (* indicates experimentalists): * N. Schell, ROBL-CRG, Germany * J. Böttiger, University of Aarhus, Denmark		

 ROBL-CRG	Experiment title: <i>In-situ x-ray diffraction during reactive magnetron sputter deposition of nanocrystalline metals (nc Au)</i>	Experiment number: 20_02_063 20_02_604
	Beamline: BM 20	Date of experiment: from: 02.10.2002 to: 10.10.2002
Shifts: 25	Local contact(s): Dr. Norbert Schell	<i>Received at ROBL:</i> 02.12.02
Names and affiliations of applicants (* indicates experimentalists): * N. Schell, ROBL-CRG, Germany * J. Böttiger, University of Aarhus, Denmark		

Report:

Nanocrystalline materials with their extremely small grain sizes and correspondingly large volume fraction of atoms located at grain boundaries have unique properties and thus offer a great potential for industrial applications [1]. Magnetron sputtering has turned out to be a versatile technique for their deposition as thin films. In order to tailor the films for specific applications, the dependence of the nanostructure on the deposition parameters and the mechanisms that control its formation and evolution have to be established.

Gold was chosen as a nanocrystalline model material (no oxidation) which we used for the experimental study of the evolution of the nanostructure during growth and after subsequent annealing. In continuation of earlier work (see **Experimental Report 20_02_051 B**) this report describes the experimental studies at ROBL of the *texture evolution of magnetron-sputtered gold films during the non-epitaxial growth and subsequent heat treatments*.

EXPERIMENTAL

The **deposition chamber** is described in detail in Ref. 2. The incident *x-rays* were monochromatized to 13.120 keV / $\lambda = 0.945 \text{ \AA}$, and mainly one scattering geometry was used: **Bragg-Brentano** large-angle scattering (XRD) giving the out-of-plane lattice strain, grain sizes and microstrain (lattice defects). To get the *orientation distribution of the dominating (111) grains* (with (111) planes forming a small angle to the film surface), χ scans were carried out (θ , 2θ fixed for Au(111) and sample tilt measured with tilt axis lying both in the film surface and in the scattering plane). As a quantitative measure of the orientation distribution (the texture), we used the widths (FWHM) of the χ scans.

Further experimental parameters were: base pressure 5×10^{-4} Pa, target material Au, sputter gas Ar (99.9996%) at a pressure of 0.6 Pa. The magnetron (only one at the time) was run at a dc power of 10 W, resulting in a *deposition rate of approximately 1.3 Å/s* on Si(100) with a 180 nm amorphous oxide layer on top. The temperature varied from room temperature (deposition) up to 220°C (annealing), a negative bias voltage of -30 V was applied.

Report:


Nanocrystalline materials with their extremely small grain sizes and correspondingly large volume fraction of atoms located at grain boundaries have unique properties and thus offer a great potential for industrial applications [1]. Magnetron sputtering has turned out to be a versatile technique for their deposition as thin films. In order to tailor the films for specific applications, the dependence of the nanostructure on the deposition parameters and the mechanisms that control its formation and evolution have to be established.

Gold was chosen as a nanocrystalline model material (no oxidation) which we used for the experimental study of the evolution of the nanostructure during growth and after subsequent annealing. In continuation of earlier work (see **Experimental Report 20_02_051 B**) this report describes the experimental studies at ROBL of the *texture evolution of magnetron-sputtered gold films during the non-epitaxial growth and subsequent heat treatments*.

EXPERIMENTAL

The **deposition chamber** is described in detail in Ref. 2. The incident *x-rays* were monochromatized to 13.120 keV / $\lambda = 0.945 \text{ \AA}$, and mainly one scattering geometry was used: **Bragg-Brentano** large-angle scattering (XRD) giving the out-of-plane lattice strain, grain sizes and microstrain (lattice defects). To get the *orientation distribution of the dominating (111) grains* (with (111) planes forming a small angle to the film surface), χ scans were carried out (θ , 2θ fixed for Au(111) and sample tilt measured with tilt axis lying both in the film surface and in the scattering plane). As a quantitative measure of the orientation distribution (the texture), we used the widths (FWHM) of the χ scans.

Further experimental parameters were: base pressure 5×10^{-4} Pa, target material Au, sputter gas Ar (99.9996%) at a pressure of 0.6 Pa. The magnetron (only one at the time) was run at a dc power of 10 W, resulting in a *deposition rate of approximately 1.3 Å/s* on Si(100) with a 180 nm amorphous oxide layer on top. The temperature varied from room temperature (deposition) up to 220°C (annealing), a negative bias voltage of -30 V was applied.

	Experiment title: Structure modifications in materials irradiated by ultra-short pulses of VUV free electron laser	Experiment number: 20_02_064 20_02_605 EU #30
	Beamline: BM 20	Date of experiment: from: 06.11.2002 to: 10.11.2002
Shifts: 12	Local contact(s): Dr. Norbert Schell, Andreas Bauer	<i>Received at ROBL:</i> 02.12.02
Names and affiliations of applicants (* indicates experimentalists): Jerzy B. Pelka^{* a}, Andrzej Andrejczuk^{* a b}, Henryk Reniewicz^{* b} ^a Institute of Physics, Polish Academy of Sciences Al. Lotnikow 32/46, 02-668 Warsaw, Poland ^b Institute fo Experimental Physics, University of Bialystok ul. Lipowa 41, 15-424 Bialystok, Poland		

Report:

The objective of the project was to characterize structural changes induced in samples by irradiation with free electron laser (FEL) working in the VUV region. The samples – Si(001) wafers and deposited on the wafers films composed of Au, Al or graphite 50-200 nm thick – were irradiated at VUV TESLA Test Facility FEL at DESY, Hamburg, with the quantum energy centered around 14 eV, in short pulses of only 50 fs and of peak power up to 1 GW. The FEL beam was focused on the sample surfaces to microspots of size 10-100 μm . The energy density in the spots varied from below the ablation threshold (“annealing mode”) up to far above this threshold (“damage mode”).

The x-ray measurements were recorded at $\lambda = 1.23984 \text{ \AA}$ by mapping the samples with the diffractometer fixed at a particular angular position deflected from exact Bragg reflection of the order of $10^{\pm 5}$. The incident x-ray beam was confined by external slits to the dimensions of about $40 \times 30 \mu\text{m}^2$.

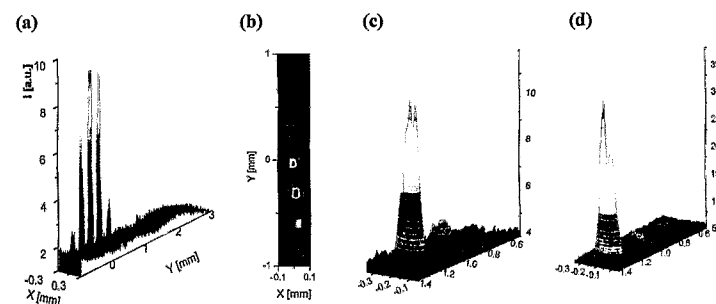



Fig. 1. Recorded Si(400) x-ray diffracted intensity distribution maps around seven spots irradiated by FEL in Si(001) monocrystal (a, b) and around three spots irradiated in thin film of AuAl intermetallic compound deposited on Si(001) wafer (c at $\theta < \theta_B$, d at $\theta > \theta_B$). The distance between the centers of the spots was 300 μm .

In Fig. 1 examples of the x-ray diffracted intensity distribution maps recorded on samples with a mesh grid of 20 μm around chosen spots irradiated by FEL are shown. The maps determine the damage distribution range and intensity around the spots. It was found that, even in the case of the most intense FEL irradiation, the detectable damaged area surrounding the center of irradiation is localized within the radius of 120-170 μm . The intensities observed in the spots are commensurate with the FEL irradiation fluencies applied. In the centers of strongly damaged spots a split in the maximal intensity occurs with a well pronounced minimum, of the intensity 15-30% lower, indicating places with extremely strong damage of the sample material, its amorphization or ablation (see Figs 1c, 1d). The obtained results allowed also for identification of relatively weakly damaged spot areas, which are hardly observable by conventional optical microscopy.

For chosen spots, the mappings were completed at the exact Bragg reflection and at few positions declined from the reflection toward the higher and the lower angles. Comparing maps obtained at both sides of exact Bragg reflections, we found a shift in intensity maxima positions around some damaged centers reaching as much as 100 μm (compare Figs 1c and 1d). The reason of this shift is not clear, though it seems to be connected with oblique beam incidence on the sample surface during FEL irradiation.

	Experiment title: Structure refinement of silicon carbide polytypes 4H and 6H: determination of the refinement parameters from multi-beam-measurements	Experiment number: 20_02_IH5
	Beamline: BM 20	Date of experiment: from: 15.04.01 to: 16.04.01 18.07.01 21.07.01 12.12.01 15.12.01
Shifts: 23	Local contact(s): Andreas Bauer	<i>Received at ROBL:</i> 18.10.02
Names and affiliations of applicants (* indicates experimentalists): Andreas Bauer* ESRF Sector 21-6 ROBL - CRG BP 220 38043 Grenoble Cedex France		

Report:

The atomic structure of the two SiC polytypes, 4H- and 6H-SiC, differs by the stacking sequences of the Si-C bilayers in the [0001] direction. Conforming with the space group symmetry, the atoms are in principle allowed to move freely in [0001]-direction (atomic relaxations) [1]. These small deviations can be determined by x-ray investigations using so called "quasi-forbidden" reflections, which are very sensitive with respect to extremely small variations in the structure.

In our former work [2, 3], absolute values of structure factors of "quasi-forbidden" reflections were obtained from integrated intensities of rocking curves. The relaxation parameters were calculated from the integrated intensities due to a equation system. Nevertheless, it is not possible to obtain unambiguous refinement parameters with this method. This problem was solved by using multi-beam-cases [4]. Contrary to that we obtained in this work the complex structure factor (absolute value and phase) of the "quasi-forbidden" reflections direct from measurements of multi-beam cases.

To acquire the experimental, data rocking curves (ω -scans) of "quasi-forbidden" reflections in the vicinity of multi-beam-cases were measured. The integrated intensities of these rocking curves in dependence of the azimuth angle ψ were compared to calculated multi-beam profiles. To calculate the multi-beam profiles the programs "dreist" and "multi" from E. WECKERT were used. These two programs are able to simulate three- and multi beam profiles according to the dynamical theory, respectively [5].

The determination of the phases of the "quasi-forbidden" reflections becomes possible by superposition of a "quasi-forbidden" reflection **H** with "Umweg" reflections (**L** and **H-L**). When choosing a three beam geometry the two remaining reflections **L** and **H-L** have to be strong reflections, because strong reflections are independent of the atomic relaxations. Following that approach, the phase, and therefore the real and imaginary part of the structure factor of the "quasi-forbidden" reflection **H** can be determined by

$$\phi_H = \phi_L + \phi_{HL} - \phi_{mv}$$

where ϕ_{mv} is the phase invariant of the three-beam-case.

From the structure factor $F(\mathbf{H})$ of the "quasi-forbidden" reflection the relaxation parameters η and ζ (for details see [2-4]) can be calculated. As an example, the structure factor of the 4H-SiC 00.6 reflection is given by:

$$F_{4H}(00.6) = 12 \left[-\pi\sqrt{2}f_C\zeta_{4H} + i(\pi\sqrt{2}f_C\zeta_{4H} + 2\pi f_{Si}\eta_{4H}) \right]$$

where f_{Si}, f_C are the atomic scattering factors of silicon and carbon, respectively. From the real part of $F_{4H}(00.6)$ we obtain ζ_{4H} and subsequently from the imaginary part η_{4H} .

Fig. 1 shows a comparison of simulated and measured data of a three beam case.

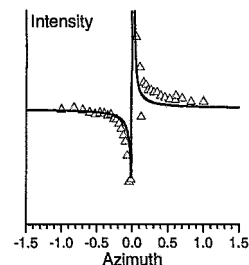


Fig. 1: The triangles represent the measured integrated intensities of the three-beam case: H: 00.6, L: 20.-2 (4H-SiC). The solid line represents the simulation with the program "dreist" of the same reflection.

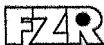
As a result, we obtained following relaxation parameters for the polytype 4H-SiC: $\eta_{4H} = 0.5 \cdot 10^{-4}$, $\zeta_{4H} = 9 \cdot 10^{-4}$. And for 6H-SiC: $\eta_{6H}(1) = 2 \cdot 10^{-4}$, $\zeta_{6H}(1) = 2 \cdot 10^{-4}$, $\eta_{6H}(2) = 0.5 \cdot 10^{-4}$, $\zeta_{6H}(2) = 9 \cdot 10^{-4}$.

Acknowledgement:

The author is grateful to E. Weckert from HASYLAB for the possibility to use his three- and multi-beam simulation programs "dreist" and "multi".

References:

- [1] KÄCKELL *et al.*, *Phys. Rev. B50* (1994) 17037-17046.
- [2] BAUER *et al.*, *Phys. Rev. B57* (1998) 2647-2650.
- [3] BAUER *et al.*, *Materials Science and Engineering B61-62* (1999) 217-220.
- [4] BAUER *et al.*, *Acta Cryst. A57* (2001) 60-67.
- [5] WECKERT & HÜMMER, *Acta Cryst. A53* (1997) 108-143.

 ROBL-CRG	Experiment title: Powder diffraction on uranyl compounds (combined with EXAFS measurements at low temperature)	Experiment number: 20_02_IH6
	Beamline: BM 20	Date of experiment: 11.04.01 + 16.04.01 + 13.06.01 + 26.10.01
Shifts: 11	Local contact(s): Dr. C. Hennig, Dr. N. Schell	<i>Received at ROBL:</i> 24.11.02
Names and affiliations of applicants (* indicates experimentalists): C. Hennig ^{1*} , N. Schell ^{2*} , F. Prokert ^{2*} , G. Reck ³ , W. Kraus ³ ¹ Forschungszentrum Rossendorf, Institut für Radiochemie ² Forschungszentrum Rossendorf, Institut für Ionenstrahlphysik und Materialforschung ³ Bundesanstalt für Materialforschung und -prüfung, Richard-Willstätter Str. 11, D-12489 Berlin		

Report:

In crystal structures with uranium the contribution of heavy atoms dominates the x-ray scattering process, whereas light atoms like oxygen contribute only weakly. Therefore, it is no problem to determine the atomic coordinates of uranium using x-ray powder diffraction but it is difficult to locate the light atoms. On the other hand, a method like EXAFS, sensitive on short range order, gives reliable atomic distances in the surroundings of heavy atoms and allows to characterise the coordination polyhedra. These can reveal the main structure motif. Including the information from EXAFS as restraints in the structure solving procedure, the probability increases to obtain the complete structure. As an example the structure of $\text{UO}_2[\text{H}_2\text{AsO}_4]_2 \cdot \text{H}_2\text{O}$ was solved using x-ray powder diffraction data including the information from EXAFS.

The proposed procedure starts with the determination of cell parameters (a,b,c, β) and space group from XRD powder data. In a second step the absolute values of the structure factor |F| are separated by iterating a decomposition formula starting from |F| values arbitrarily set to be equal. In the third step the coordination polyhedra and their connections are determined using EXAFS. Heavy-atom positions will be found by direct methods using atomic scattering factors. The position of light atoms are determined by including the EXAFS results as help for the interpretation of the first difference Fourier synthesis. Subsequently, the complete coordination polyhedron geometry obtained by EXAFS is used as restraints in the first cycles of structure refinement. The final step is the refinement of all structural parameters by releasing the restraints.

In order to avoid crystallite orientation effects, the sample was prepared in a glass capillary and measured by sample rotation in Debye-Scherrer geometry. The high angle resolution was achieved by x-ray powder diffraction measurements carried out at the materials research end station MRH at ROBL in a 2θ range of 8.0-34.7° using a wavelength of $\lambda = 1.05070 \text{ \AA}$. The diffraction pattern is given in Fig. 1. Details of data collection and cell parameters obtained after a profile refinement are given in Tab. 1. This demonstrates that the

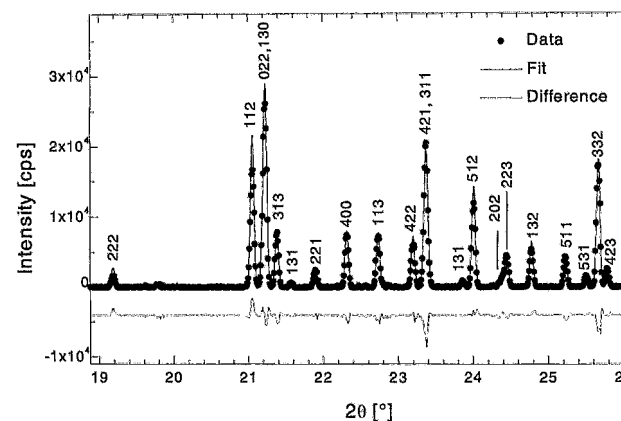



Fig. 1: Detail of the x-ray powder diffraction pattern $\text{UO}_2[\text{H}_2\text{AsO}_4]_2 \cdot \text{H}_2\text{O}$

Tab. 1: Details of data collection and crystallographic data of $\text{UO}_2[\text{H}_2\text{AsO}_4]_2 \cdot \text{H}_2\text{O}$

Diffractometer	6-circle (Huber)
Radiation / λ [Å]	Synchrotron / 1.05070
Scan geometry	Debye-Scherrer
Z	4
Space group	C2/c
a [Å]	13.1650
b [Å]	8.8583
c [Å]	9.0475
β [°]	124.512
2θ range [°]	8.0-34.7
$\Delta 2\theta$ [°]	0.01
No. of reflections	82
Profile function	Gauss
Reflex profile parameter W	0.0043

 ROBL-CRG	Experiment title: CCD camera tests on tourmaline, quartzite and TiNAI	Experiment number: 20_02_IH7
	Beamline: BM 20	Date of experiment: from: 27.11.2002 to: 03.12.2002
Shifts: 18	Local contact(s): Dr. Norbert Schell	<i>Received at ESRF:</i> 03.12.02
Names and affiliations of applicants (* indicates experimentalists): Dr. Kurt Walther ^{*a, b} , Manfred Beckers ^{*b} , Dr. Norbert Schell ^{*b, c} ^a GeoForschungsZentrum Potsdam, Germany ^b Forschungszentrum Rossendorf, Germany ^c ROBL-CRG at ESRF, Germany		

Report:

The aim of the experiments was: 1) to calibrate the DCM sagittal bender for optimum focus at various energies, 2) to compare different CCD x-ray cameras, and 3) to compare texture analysis on minerals with a scanning BEDE scintillator (standard detector) and with a large opening CCD camera (Smart detector).

As *focus examples* for different sagittal bending, Figs 1 and 2 show representative pictures at two different energies taken with the CAMCAD from the ESRF detector pool.

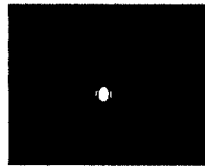


Fig. 1: Direct beam focussed at 15 keV.



Fig. 2: Direct beam focussed at 17.5 keV.

These pictures represent best beam focus conditions at fixed detector distance (appr. 120 cm behind the diffractometer center) obtained for symmetric beam shapes. Fig. 3 shows the calibration of stepper motor steps for best focus against energy of the monochromatic beam. The rtab/ltab stepper values can be fitted by a linear regression.

After focussing the beam at 17.479 keV (MoK_{α}), pictures at the sample position were taken with a Photonics CCD camera. The software package allows direct read-out of the beam dimensions in vertical and horizontal direction as shown in the insets of Fig. 4.

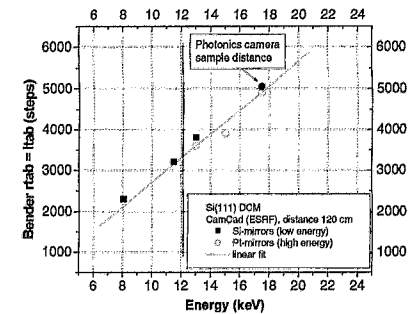


Fig. 3: Stepper motor values of sagittally bending of the 2nd DCM crystal Si(111) for different beam energies.

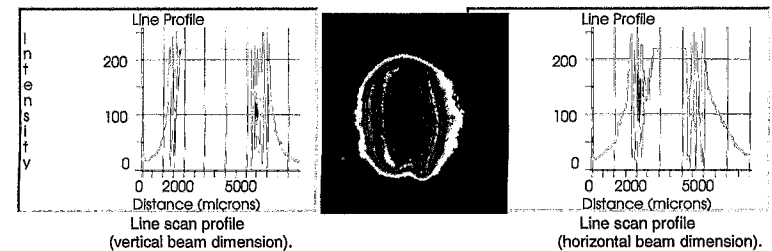


Fig. 4: Focused direct beam on diffractometer calibration needle (Photonics camera).

The geological samples were investigated with the Bruker AXS Smart CCD camera. Fig. 5 (left) shows a representative picture with the typical *Debye-Scherrer circles of the mineral dolomite* taken in horizontal transmission and the detector 6 cm behind the sample. Notice the single grain high intensity superpositions on each Debye-Scherrer circle. In order to compare resolution and sensitivity, *pictures of these single grains* were also taken with the Photonics camera (smaller opening angle) in reflexion mode (for different acquiring times and azimuthal sample tilt angles) Fig. 5 (middle and right).

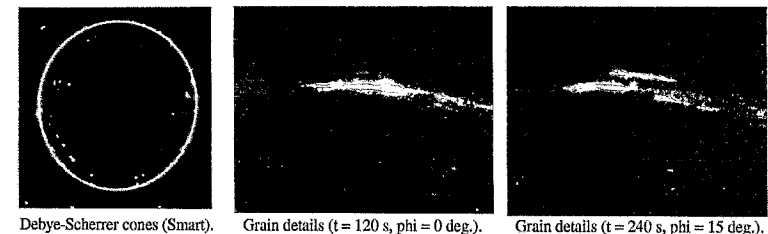


Fig. 5: Debye-Scherrer circles of a dolomite sample taken with Smart (left) and grain details of the same sample taken with the Photonics camera (middle and right).



Experiment title: Sorption of trivalent lanthanides (Ln(III)), onto hydrous ferric oxide (HFO) and evolution of the sorbed species upon HFO aging		Experiment number: ME-240
Beamline: BM20	Date of experiment: from: 7 Feb 2001 to: 11 Feb 2001	Date of report: Received at ESRF:
Shifts: 12	Local contact(s): Andre ROSSBERG	
Names and affiliations of applicants (* indicates experimentalists): Dr. Kathy Dardenne* Dr. Melissa A. Denecke Dr. Jörg Rothe Dr. Patric Lindqvist-Reis*		

Report:
Low temperature XAFS investigation on the lutetium binding changes during the 2Lfh-ferrihydrite alteration process

K. Dardenne, T. Schäfer, P. Lindqvist-Reis, M.A. Denecke, M. Plaschke, J. Rothe, J.I. Kim (submitted)

The time dependent changes of Lu(III) speciation, initially sorbed onto two-line ferrihydrite (2LFh) at pH 5.9, during tempering (70°C) and leading to stable crystalline transformation products is studied at the Lu L3 absorption edge. Lu(III) is used as an analogue for the trivalent actinides. Samples are tempered for 0, 84, 155 and 238 hours. Complementary microscopic studies (AFM, SEM), XRD and FTIR spectroscopy confirm transformation of Lu(III):2LFh (pH 6) to both goethite and hematite, with a predominance of hematite. XRD investigation of a transformation series at pH 8 shows that the cell volume of hematite product increases slightly, suggesting the incorporation of Lu(III) in the structure. The EXAFS results aim at determining the fate of the Lu(III) during transformation.

Fig. 1 shows the experimental and the best fit results and their corresponding FT's. The initial sorption sample (temper time = 0) is fit using two coordination shells, an oxygen and an iron shell. The fit yields (Table 1) seven oxygen atoms (O⁺) at a mean bond distance of 2.31 Å and a Lu-Fe⁺ distance of 3.41 Å. This is in good agreement with previous results¹.

The other samples are fit to structural models including the two possible end products (hematite-like and goethite-like models), with an isotropic expansion of 4% of interatomic distances to simulate Lu(III) incorporation into iron position of the crystal lattice. The coordination numbers are kept constant at expected values during the fits. Results of the best fit are listed in Table 1. The fit to the 238h tempered sample data is only possible using the hematite-like model. It requires inclusion of a Lu-Fe distance near 3.9 Å (Fe4). This

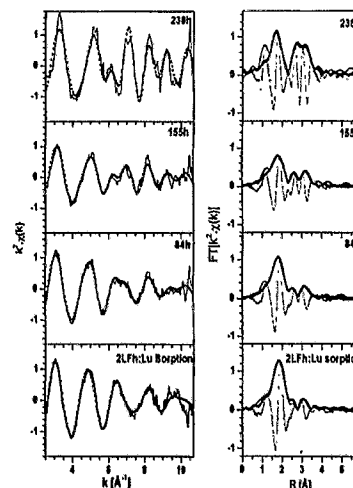


Fig. 1 Left: k^2 -weighted Lu L3 edge EXAFS (lines) and best fit results. (dots). Right: corresponding FT.

distance is absent in the goethite-like cluster. No good fit is possible using solely the goethite-like cluster model. If Lu(III) is incorporated into goethite, its EXAFS contribution is completely masked by Lu(III) in hematite.

Data from the 84 and 155h tempered samples is modeled with a combination of the temper time = 0 and 238h species. The first coordination shell bond lengths and coordination numbers are fixed to the values obtained for samples with temper times 0 and 238h and scaled with a ratio factor, rf. The rf is the proportion of the Lu(III) incorporated into hematite species (temper time = 238h). Results of the fits are also given Table 1. EXAFS for both 84h and 155h tempered samples is very well modeled with this combination of species. This shows that both species, Lu(III) sorbed onto 2LFh and Lu(III) incorporated into hematite crystal structure, coexist in the intermediate temper time samples.

Table 1: Coordination number (N), interatomic distance (R), relative ionization energy shift (ΔE_0), mean-square-displacement (σ^2) and relative amount Lu incorporated into hematite (rf) obtained from fits to the EXAFS shown in Fig. 1.

Sample	Neighbor	N**	R	ΔE_0	σ^2	rf
Temper time (h)			[Å]	[eV]	[10 ⁻³ Å ²]	
0	O ⁺	7.2	2.31	7.64	7.44	0
	Fe ⁺	1*	3.41	4.8	5.10	
84h	O	1.54	2.19	6.79	7.46	0.26
	O ⁺	5.20	2.31	6.79	7.37	
	Fe1 + Fe2	1.02	3.17	0.80	15.03	
	Fe3 + Fe ⁺	1.51	3.42	0.80	5.60	
	Fe4	1.54	3.93	0.80	10.7	
155h	O	3.98	2.19	6.79	14.68	0.66
	O ⁺	2.61	2.31	6.79	5.23	
	Fe1 + Fe2	2.65	3.12	0.01	13.14	
	Fe3 + Fe ⁺	2.32	3.42	0.01	5.60	
	Fe4	3.98	3.89	0.01	17.2	
238h	O	6*	2.19	6.74	7.22	1.00
	Fe1 + Fe2	4*	3.08	0.01	10.17	
	Fe3	3*	3.41	0.01	2.12	
	Fe4	6*	3.88	0.01	12.1	

* fixed at this value **N(O⁺)=(1-rf)*7.2, N(O)=rf*6 and, N(Fe3+Fe⁺)=(1-rf)*1+rf*3

These results corroborate XRD results on a transformation series at pH 8 that Lu(III) sorbed onto 2LFh is incorporated into the transformation product hematite crystal lattice, as opposed to being occluded or remaining a sorbed species on the surface.

¹ Dardenne, K.; Schäfer, T.; Denecke, M.A.; Rothe, J.; Kim, J.I. *Radiochim. Acta* 2001, 89, 469 - 479



Experiment title: EXAFS/XANES studies on speciation of Tc-99 under reducing conditions		Experiment number: CH - 1050
Beamline: BM -20	Date of experiment: from: 28/03/2001 to: 31/03/2001	Date of report: 14/8/2001
Shifts: 9	Local contact(s): André Rossberg	<i>Received at ESRF:</i>
Names and affiliations of applicants (* indicates experimentalists): Kathleen Geraedts*, André Maes*, Christophe Bruggeman* K.U.Leuven, Laboratorium voor Colloïdchemie, Kasteelpark Arenberg 23, B-3001 Heverlee, Belgium Luc Van Loon* Paul Scherrer Institute, Laboratory for Waste Management, OHLB/409a, CH-5232 Villigen PSI, Switzerland		

Report:

The redox-sensitive fission product technetium-99 is of great interest in nuclear waste disposal studies because of its potential of contaminating the geosphere due to its very long half-life and high mobility. Under oxidising conditions, technetium is present as pertechnetate, a highly soluble, anionic species, that does not sorb significantly on minerals or sediments [1]. Under suitable reducing conditions, eg. in the presence of a reducing solid phase which can act as an electron donor, the solubility can be limited by the reduction of pertechnetate followed by the formation of a surface precipitate [2]. However, in presence of soluble (mobile) humic substances, reduced technetium might be soluble due to the formation of Tc-HS complexes [3]. One of the main questions related to the behaviour of Tc-99 under natural reducing conditions and in presence of humic substances is the one concerning the oxidation state of reduced technetium. So far no direct proof of the oxidation state and the speciation of Tc has been given neither in the solution phase nor in solid phases (surface precipitate, sorbed species).

Four series of samples were prepared at K.U.Leuven. Series 1 consisted of reduced forms of Tc adsorbed or precipitated onto 3 different reducing surfaces (FeS, Fe₃O₄ and FeS₂) in absence and presence of humic substances added as real Gorleben water. Series 2 consisted of concentrated reduced forms of Tc in precipitated humic substances. Series 3 were the humic substances containing supernatant solutions of the above mentioned samples of series 1 and series 4 were the supernatant solutions of samples which contained Gorleben sand as the reducing solid phase. For security reasons, it was not allowed to measure series 1 and 2 because of problems with the containment. The remaining 2 series of samples, however contained a Tc concentration too low to be measured by EXAFS, and therefore, only XANES studies were performed.

The 9 allocated shifts were used to measure the XANES spectra of 5 liquid samples (see Table 1) in the fluorescence detection mode and 1 reference sample (pertechnetate) both in transmission and fluorescence mode. The 5 liquid samples (from series 3 and 4) were collected from batch experiments, in which different solids (magnetite, pyrite, ironsulphide and Gorleben sand) were contacted with humic rich pertechnetate solutions in an anoxic atmosphere. The Tc concentrations in samples 2 till 6 were extremely low for X-ray



Experiment title: EXAFS/XANES studies on speciation of Tc-99 under reducing conditions		Experiment number: CH - 1050
Beamline: BM -20	Date of experiment: from: 28/03/2001 to: 31/03/2001	Date of report: 14/8/2001
Shifts: 9	Local contact(s): André Rossberg	<i>Received at ESRF:</i>
Names and affiliations of applicants (* indicates experimentalists): Kathleen Geraedts*, André Maes*, Christophe Bruggeman* K.U.Leuven, Laboratorium voor Colloïdchemie, Kasteelpark Arenberg 23, B-3001 Heverlee, Belgium Luc Van Loon* Paul Scherrer Institute, Laboratory for Waste Management, OHLB/409a, CH-5232 Villigen PSI, Switzerland		

Report:

The redox-sensitive fission product technetium-99 is of great interest in nuclear waste disposal studies because of its potential of contaminating the geosphere due to its very long half-life and high mobility. Under oxidising conditions, technetium is present as pertechnetate, a highly soluble, anionic species, that does not sorb significantly on minerals or sediments [1]. Under suitable reducing conditions, eg. in the presence of a reducing solid phase which can act as an electron donor, the solubility can be limited by the reduction of pertechnetate followed by the formation of a surface precipitate [2]. However, in presence of soluble (mobile) humic substances, reduced technetium might be soluble due to the formation of Tc-HS complexes [3]. One of the main questions related to the behaviour of Tc-99 under natural reducing conditions and in presence of humic substances is the one concerning the oxidation state of reduced technetium. So far no direct proof of the oxidation state and the speciation of Tc has been given neither in the solution phase nor in solid phases (surface precipitate, sorbed species).

Four series of samples were prepared at K.U.Leuven. Series 1 consisted of reduced forms of Tc adsorbed or precipitated onto 3 different reducing surfaces (FeS, Fe₃O₄ and FeS₂) in absence and presence of humic substances added as real Gorleben water. Series 2 consisted of concentrated reduced forms of Tc in precipitated humic substances. Series 3 were the humic substances containing supernatant solutions of the above mentioned samples of series 1 and series 4 were the supernatant solutions of samples which contained Gorleben sand as the reducing solid phase. For security reasons, it was not allowed to measure series 1 and 2 because of problems with the containment. The remaining 2 series of samples, however contained a Tc concentration too low to be measured by EXAFS, and therefore, only XANES studies were performed.

The 9 allocated shifts were used to measure the XANES spectra of 5 liquid samples (see Table 1) in the fluorescence detection mode and 1 reference sample (pertechnetate) both in transmission and fluorescence mode. The 5 liquid samples (from series 3 and 4) were collected from batch experiments, in which different solids (magnetite, pyrite, ironsulphide and Gorleben sand) were contacted with humic rich pertechnetate solutions in an anoxic atmosphere. The Tc concentrations in samples 2 till 6 were extremely low for X-ray



Experiment title: XAS study of uranium and plutonium local environment in (U,Pu)O ₂ solid solution		Experiment number: ME-312
Beamline: BM 20	Date of experiment: from: 09 november 2001 to: 13 November 2001	Date of report: 28/02/2002
Shifts: 12	Local contact(s): Dr. Andreas BAUER	<i>Received at ESRF:</i>
Names and affiliations of applicants (* indicates experimentalists):		
* Dr. MARTIN Philippe Centre de Cadarache DEN/DEC/SESC/LLCC Bat 315 13108 Saint Paul Lez Durance Cedex		
* Dr. RIPERT Michel Centre de Cadarache DEN/DEC/SESC/LLCC Bat 315		
* Dr. CARLOT Gaëlle Centre de Cadarache DEN/DEC/SESC/LLCC Bat 315		
* Dr. GRANDJEAN Stéphane CEA/VALRHO, DEN/DRCP/SCPS/LPCA, Bat 399 BP 17171 30207 Bagnols sur Cèze Cedex, France		
Dr. PETIT Thierry Centre de Cadarache DEC/SESC/LLCC Bat 315		
Dr. BLANC Pierre CEA/VALRHO, DEN/DRCP/SCPS/LPCA Bat 399.		

references Y foil (17.052 keV) and Zr foil (17.998 keV) positioned after the second ionisation chamber. As observed on these XANES spectra, the position of the white line is, at the uranium edge, the one of the UO₂ and at the plutonium edge, the one of PuO₂. Thus, whatever the plutonium content is, the oxidation state of uranium and plutonium remains equal to +IV.

The evolutions of the Fourier Transform are summarised on the figures 1 and 2. The overall shape of the spectra is almost always the same while the global intensity varies a lot with the plutonium content. Thus, an important decrease of oscillations for the 30 and 15% Pu samples is observed. X-ray diffraction leads to the same result showing a greater disorder than for the PuO₂ and 50 % Pu samples.

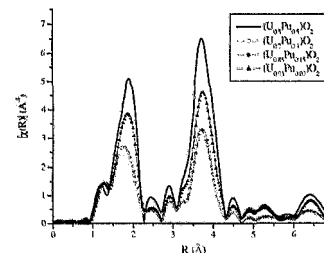


Figure 1 : Fourier Transforms of the uranium L_{III} edge EXAFS (k-range: 2 → 12 Å⁻¹).

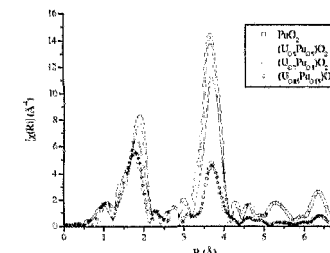


Figure 2 : Fourier Transforms of the plutonium L_{III} edge EXAFS (k-range: 2 → 14 Å⁻¹).

At the uranium L_{III} edge, the best fit of the 50% Pu sample leads to the following distances: R_{U-O}}=2.352 (5) Å, R_{U-U}}=R_{U-Pu}}=3.845 (5) Å and R_{U-O}}=4.51 (1) Å. The oxygen neighbours are the same as in UO₂ (8 and 24 for the first and third coordination shells) and the U/(U+Pu) ratio is 0.51. The uranium local environment is clearly the one of an ideal solid solution. The case of plutonium environment is a little more complicated. Indeed, the fitting of the first peak of the Fourier transform of the plutonium L_{III} edge spectra leads to values unsuitable with the fluorite structure. As seen on the figure 2, the shape of this peak (first coordination shell) is no longer gaussian. To fit it, we had to introduce an additional asymmetry term (third cumulant)[1]. Using this method, we finally obtain a shell of 8 oxygen neighbours at a distance of 2.351 (5) Å, which is consistent with the result obtained at the uranium edge. Considering the plutonium-metal shell, we also find an ideal solid solution structure with Pu-Pu and Pu-U distances equal to 3.845 (5) Å. The Pu/(U+Pu) ratio thus obtained is 47%. The results of the analysis at the two edges clearly show that the chemical procedure used to prepare the (U_{0.5}Pu_{0.5})O₂ sample is validated.

For the intermediate plutonium concentrations of 15 and 30%, the local environment of uranium and plutonium is highly perturbed as seen in figures 1 and 2. On the opposite to the 50% plutonium sample, a third cumulant has to be introduced in the fitting procedure even at the uranium edge. The results obtained for the first coordination shell consist in 8 oxygen atoms at distances equal to the ones given in table 1. The main difference appears to be a doubling of the Debye-Waller (σ^2_{U-O} (30% Pu) = 0.014 Å² instead of σ^2_{U-O} (50% Pu) = 0.0065 Å²). This is the signature of a higher disordered structure.

It is interesting to note that EXAFS appears to be the lone technique outlining this discrepancy in plutonium and uranium local environment. Some steps of the process via the wet route checked in this study are currently modified considering their potential influence on the mechanisms of formation of ideal solid solutions, particularly with plutonium content lower than 50%. By the way, we ask for a prolongation of this proposal to validate these changes.

[1] Stern, E. A. (1988) *X-ray absorption: Principles, Applications, Techniques of EXAFS, SEXAFS and XANES, chapter 9: amorphous and liquid systems*, edited by D. C. Koningsberger & R. Prins, volume 92 of chemical analysis, New York, John Wiley.

The plutonium generated in nuclear power reactors can be re-used at least partially through the exploitation of a Mixed Oxide (U,Pu)O₂ fuel. Industrially, the manufacture of the MOX fuel proceeds in UO₂ and PuO₂ powders co-crushing, pelletizing and sintering. With this method, a fluorite-type solid solution (U,Pu)O₂ is obtained. Currently, rather than a mechanical mixing of pulverulent compounds, a new technique of manufacture for specific needs is under development, based on a co-precipitation of uranium and plutonium (chemical mixture). A better homogeneity of the U and Pu repartition in the solid and at lower temperature is awaited by this wet route. The homogeneity of the final products may represent a significant criterion for an optimized behaviour in power reactors.

During our experiments we analysed samples whose plutonium content was equal to 7, 15, 30 et 50%. The PuO₂ reference compound was synthesised following the same chemical procedure. Those samples were analysed by X-ray diffraction. In each case, a face centred cubic structure was observed and the cell parameter deduced obeys the Vegard's law as seen in the following table.

(% Pu)	a (XRD) (Å)	a (Vegard's law) (Å)	First shell Metal-O (Å)	Second shell Metal-Metal (Å)	Third shell Metal-O (Å)
0	5.47	5.47	2.369	3.868	4.535
7	5.4652	5.4648	2.367	3.864	4.532
15	5.4566	5.4589	2.363	3.858	4.524
30	5.444	5.4478	2.357	3.849	4.514
50	5.434	5.4330	2.353	3.842	4.506
100	5.3976	5.3960	2.337	3.817	4.475

Table 1 : cell parameter a measured by XRD and calculated with Vegard's law, and 3 first coordination shells of metal-o in (U,Pu)O₂ solid solution

For each sample, the transmission and fluorescence signals were collected at the uranium (17.126 keV) and plutonium (18.056 keV) L_{III} edges. Energy calibration of the XANES data was achieved using the

	Experiment title: Short range order investigations in the Fe₇₂Cr₂₈ solid solution by combination of EXAFS and differential anomalous x-ray wide-angle scattering	Experiment number: HS-1626
	Beamline: BM 20	Date of experiment: from: 26.11.2001 to: 01.12.2001
Shifts: 9 + 3	Local contact(s): Dr. Norbert Schell, Dr. Tobias Reich	<i>Received at ESRF:</i> 06.11.02
Names and affiliations of applicants (* indicates experimentalists): Prof. Yu.A. Babanov*, Dr. A.F. Sidorenko, S.A. Kiryanov, Dr. A.V. Ryazhkin, Dr. L.N. Romashev, Dr. A.M. Patselov Institute of Metal Physics, S.Kovalevskaya str. 18, GSP-170, Ekaterinburg 620219, Russia Prof. T. Reich*, Dr. H. Funke*, Institute of Radiochemistry, Forschungszentrum Rossendorf, P.O. Box 510119, 01314 Dresden, Germany Dr. F. Prokert*, Dr. N. Schell*, Institute of Ion Beam Physics and Materials Research, Forschungszentrum Rossendorf, P.O. Box 510119, 01314 Dresden, Germany		

Report:

Atomic structure investigation of Fe/Cr systems is very difficult because of the close position of Fe and Cr in the periodic table of chemical elements. In this case, the solid state solutions of Fe-Cr would be an attractive model system as a first step in the study. It would provide developing techniques of the experimental determination of partial pair correlation functions (pPCFs) close to the Fe/Cr multilayers short range investigations.

The purpose of the present experiments is the determination of the positions of the coordination spheres, the partial coordination numbers for the first shell and the local ordering in Fe_{78.4}Cr_{21.6} solid state solution.

Fig.1 shows the picture of anomalous x-ray scattering recorded at the Fe K-edge (E = 7105 eV). On the last two peaks (Fig. 1) solid state solution stratification on three bcc-phases is clearly seen. The first two peaks cannot give such information due to weak s-space resolution. X-ray scattering data obtained using Cr K_α radiation do not contain any splitting (a = 2.872 Å).

Lattice parameters of the three phases determined on the last two peaks are a₁ = 2.874 Å, a₂ = 2.872 Å, a₃ = 2.871 Å. Using the dependence of the lattice parameters from the Cr concentration for Fe-Cr alloys, the Cr concentration in each phase was obtained: c₁ = 0.383, c₂ = 0.216, c₃ = 0.128. Assuming the phase with Cr concentration c₂ = 0.216 dominates (~90%) and the parts of the other phases are small (~5%). The weighted average lattice parameter a = 2.872 Å and the interatomic distance r = 2.487 Å are determined.

From Fe and Cr EXAFS data separately, the partial interatomic distances were determined by the Tikhonov regularization method [1]. It is known from model calculations that partial pair correlation functions in the case of absolutely disordered solid state solutions is the same and the coordination numbers are defined by the concentrations of the elements. It is clearly seen that the error in the determination of the positions from EXAFS data is greater than from diffraction data (Table 1). The coordination numbers obtained by the special method [2] for the first coordination sphere are shown in Table 2.

According to the Cowley parameter definition $\eta = 1 - N_{ij}^{ex} / N_{ij}^*$ (i ≠ j) we obtained the average value $\eta = 0.05 (\pm 0.01)$. The positive value means that solid state solution stratification.

Conclusion: The results obtained from EXAFS and AWAXS data allow to conclude: Fe_{78.4}Cr_{21.6} solid state solution stratifies on three phases with lattice parameters 2.874 Å, 2.872 Å, 2.871 Å and the corresponding Cr concentrations 0.383, 0.216, 0.128. Besides, it was shown that the Cowley parameter calculated was $\eta > 0$. It is an evidence of stratification in chemical short range order¹.

Table 1: The partial interatomic distances for Fe_{78.4}Cr_{21.6} solid state solution:

Fe-Fe	Fe-Cr	Cr-Fe	Cr-Cr
2.48 ± 0.01, Å	2.49 ± 0.01, Å	2.47 ± 0.01, Å	2.48 ± 0.01 Å

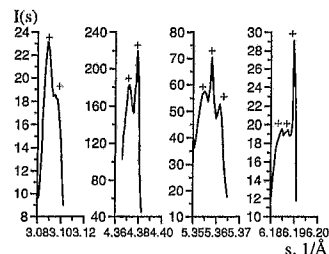


Fig. 1: Anomalous X-ray scattering near the Fe edge (E = 7105 eV) in S-space; peaks: 110, 200, 211, 220, respectively.

Table 2: Partial coordination numbers for the first sphere of Fe_{78.4}Cr_{21.6} solid state solution

Coordination numbers obtained from Fe EXAFS		Cowley parameter η
Fe-Fe	Fe-Cr	
6.491	1.625	0.06
6.272*	1.728*	0
Coordination numbers obtained from Cr EXAFS		Cowley parameter η
Cr-Fe	Cr-Cr	
6.014	2.007	0.04
6.272*	1.728*	0

* - corresponds to the absolutely disordered solid state solution.

- [1] A.N. Tikhonov and V.Ya. Arsenin, Solution of ill posed problems (John Wiley & Sons, 1977).
 [2] Yu.A. Babanov, A.V. Ryazhkin, T. Miyayaga, T. Okazaki, A.F. Sidorenko, N.V. Fadyushina, NIM A 448 (2000) 364.

¹ Accepted paper at Materials Conference SR-2002 (Novosibirsk) to be published at NIM A.

Anomalous X-ray scattering and EXAFS study in the determination of the short range order of the solid state solution Fe_{78.4}Cr_{21.6}

S.A. Kiryanov^{a*}, A.F. Sidorenko^a, Yu.A. Babanov^{a,b}, A.V. Ryazhkin^a, L.N. Romashev^a, A.M. Patselov^a, T. Reich^c, H. Funke^c, F. Prokert^d, N. Schell^d

^a Institute of Metal Physics, S.Kovalevskaya str. 18, GSP-170, Ekaterinburg 620219, Russia

^b Udmurt State University, Izhevsk, Russia

^c Institute of Radiochemistry, Forschungszentrum Rossendorf, PO Box 510119, 01314 Dresden, Germany

^d Institute of Ion Beam Physics and Materials Research, Forschungszentrum Rossendorf, PO Box 510119, 01314 Dresden, Germany

Abstract

The results of studying local atomic structure for the solid state solution Fe_{78.4}Cr_{21.6} by extended X-ray absorption fine structure (EXAFS) and anomalous wide angle X-ray scattering (AWAXS) are presented. From the anomalous X-ray scattering data we find the solid state solution decomposition on three bcc-phases, with different lattice parameters and compositions. From EXAFS data the partial interatomic distances and the partial coordination numbers for the first shell are obtained. We calculate the Cowley parameter and find stratification in chemical short range order.



Experiment title: Uranyl speciation in cement phases using XAS		Experiment number: ME-308
Beamline: BM20	Date of experiment: from: 24-01-2002 to: 31-01-2002	Date of report: 26-08-2002
Shifts: 18	Local contact(s): Christoph HENNIG	<i>Received at ESRF:</i>
Names and affiliations of applicants (* indicates experimentalists): I. Bonhoure*, J. Tits*, R. Daehn*, D. Kunz*, E. Wieland, A. M. Scheidegger. Waste Management Laboratory Paul Scherrer Institute, CH 5232 Villigen, Switzerland		

While the speciation of U(VI) in alkaline solution is relatively well known, the interaction of U(VI) with cement and cement phases remains poorly understood. Some authors have reported inner-sphere complexation between uranyl and hydrothermally altered concrete in the pH range 9-12. However the chemical phase responsible for this process has not been identified. Moreover the identification of the U solubility limiting phase in cementitious systems is subject to debates. To deepen our knowledge on the U(VI)/cement system, a XAS study was initiated and measurements at the U L₃ edge (17.17 keV) carried out. Selected XANES (X-ray Absorption Near Edge Structure) and EXAFS (Extended X-ray Absorption Fine Spectroscopy) spectra are presented in Figure 1. For oversaturated conditions with respect to the precipitation of the U-solubility limiting phase(s), the spectra of HCP-Ov are similar to those of the UO₂-Ca reference (synthesized at pH=13.3 in the presence of Ca(II)). Some complementary experiments are on the way to identify UO₂-Ca solid but it most likely corresponds to becquerelite (Ca[(UO₂)₆O₄(OH)₆].8H₂O). For undersaturated conditions, the spectra of HCP-Und display some marked differences with those of UO₂-Ca but are similar to those of CSH-0.7, which may reveal that CSH phase is the U(VI) uptake-controlling phase in cementitious systems. Data fitting are currently undertaken to identify the U(VI) coordination mode in the CSH and HCP solids.

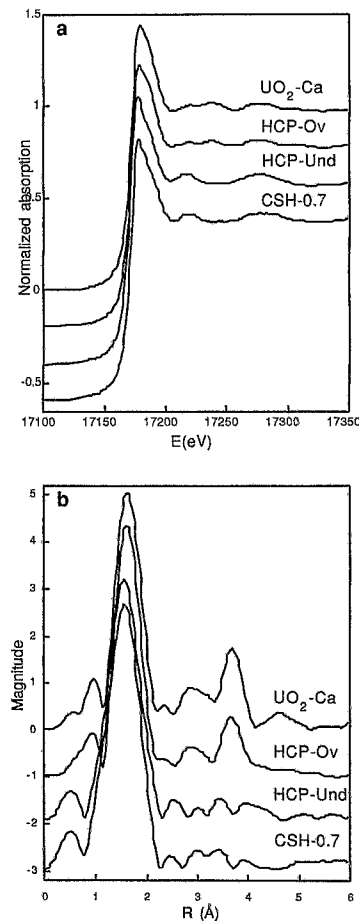



Figure 1: XANES (a) and PRDF (b) spectra of UO₂-Ca (reference compound), U(VI) immobilized on HCP (HCP-Ov: Oversaturated conditions; HCP-Und: Undersaturated conditions) and on CSH (CSH-0.7)

 ROBL-CRG	Experiment title: Uranium complexation by adenosine phosphates	Experiment number: 20_01_38 CH-1264
	Beamline: BM 20	Date of experiment: from: 25.04.01 to: 26.04.01 from: 09.06.01 to: 10.06.01 from: 27.02.02 to: 02.03.02 from: 24.01.02 to: 31.01.02
Shifts: 15 + 9	Local contact(s): Christoph Hennig	<i>Received at</i> ROBL: 28.11.2002
Names and affiliations of applicants (* indicates experimentalists): C. Hennig*, G. Geipel*, T. Reich*, A. Günther, G. Bernhard Forschungszentrum Rossendorf e.V., Institute of Radiochemistry, D-01314 Dresden		

Report:

Uranium(VI) can be bound to phosphoryl groups in microorganisms [1]. The most important phosphoryl containing enzymatic compounds are the adenosine phosphates which are able to transfer the phosphate groups from one to another molecule [2]. Heavy metal ions fixed onto adenosine phosphates can be transported into living cells and then deposited. Possible complex formation between adenosine phosphate and heavy metal ions therefore can be the pathway to understand the mechanisms of transportation. The fluorescence properties of uranium are changed upon complex formation in shifting of the emission bands of about 6 nm and in an increase of the fluorescence lifetime to more than 20 μ s. Additionally the adenosine molecule shows a dynamic quench effect onto the fluorescence. As example, the formation of 1:1 U(VI) adenosine triphosphate complex with a formation constant of $\log K = -3.8$ was determined using laser spectroscopy [3].

The complex compounds were prepared by mixing 1 M uranyl nitrate solution with 1 M adenosine triphosphate and adenosine monophosphate stock solutions at pH 1.8 - 2.5 and room temperature. The precipitate was filtered, washed and dried.

At Fig. 1 are shown the U L_{III}-edge EXAFS spectra of U(VI) adenosine monophosphate (U-AMP) and U(VI) adenosine triphosphate (U-ATP). The first Peak at the Fourier transform (FT) originates from the uranyl oxo group. The second shell of U-ATP comprises nitrogen and/or oxygen atoms at a distance of 2.36Å whereas the equatorial shell of U-AMP shows a splitting of bond distances into 2.36Å and 2.54Å. The phosphoryl groups of U-AMP and U-ATP are coordinated

in a monodentate fashion proofed by the U-P distance of 3.87Å (U-AMP) and 3.61Å (U-ATP).

Tab. 1: EXAFS parameters of U L_{III}-edge measurements.

sample	shell	R [Å]	N	σ^2 [Å ²]	ΔE [eV]
U-AMP	U-O _{ax}	1.791(2)	2.2(1)	0.0021(2)	-9.7
	U-MS	3.58	2.2	0.0042	
	U-N/O _{eq1}	2.356(4)	2	0.0061(5)	
	U-N/O _{eq2}	2.541(8)	3	0.0055(6)	
	U-P	3.871(6)	0.9(4)	0.0024(2)	
U-ATP	U-O _{ax}	1.773(1)	1.9(1)	0.0019(2)	-12.9
	U-MS	3.546	1.9	0.0038	
	U-N/O _{eq}	2.361(4)	4.1(3)	0.0073(6)	
	U-P	3.606(7)	1.0(3)	0.002(1)	

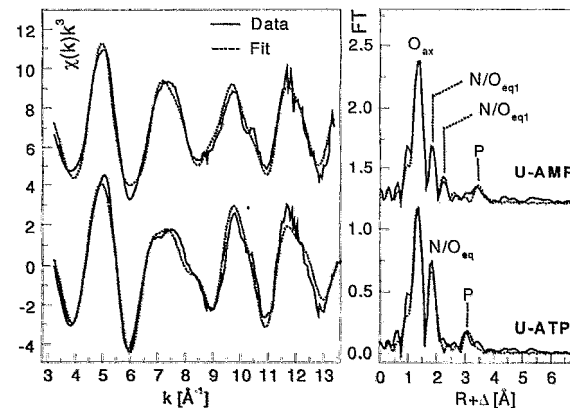


Fig. 1: U L_{III}-edge EXAFS spectra (left) and their Fourier transform (right) of U-AMP and U-ATP.

[1] Hennig, C. et al.: EXAFS investigation of uranium(VI) complexes formed at *Bacillus cereus* and *Bacillus spiaricus* surfaces, *Radiochim. Acta* 89 (2001) 625

[2] Mildvan, A.S. et al.: The role of divalent cations in the mechanism of enzyme catalyzed phosphoryl and nucleotidyl transfer reactions, *Structure and bonding*, 20 (1974) 2

[3] Geipel, G. et al.: Complex formation between uranium(VI) and adenosine triphosphate; NRC5, 5th International Conference on Nuclear and Radiochemistry, Pontresina, Switzerland, Sept. 3-8, 2000, Extended Abstracts, Vol. 2, p.473



Experiment title:		Experiment number:
Solid speciation of uranium in radioactive particles		ME-394
Beamline:	Date of experiment:	Date of report:
BM 20	from: 17.04.2002 to: 21.04.2002	29.11.2002
Shifts:	Local contact(s):	<i>Received at ESRF:</i>
12	Christoph Hennig	29.11.02
Names and affiliations of applicants (* indicates experimentalists):		
Brit Salbu ^{1*} , Ole Christian Lind ^{1*} , Koen Janssens ^{2*} , Tobias Reich ^{3*} , Christoph Hennig ^{4*}		
¹ Agricultural University of Norway, Isotope Laboratory, Norway		
² University of Antwerp, Department of Chemistry, Belgium		
³ Universität Mainz, Institut für Kernchemie, Germany		
⁴ Forschungszentrum Rossendorf, Institut für Radiochemie, Germany		

Report:

A major objective of the project was to identify the possibility to utilise ROBL for the characterisation of small-sized radioactive particles with respect to oxidation states (XANES) and fine structure such as coordination number (EXAFS). As the ROBL beam line is authorised to handle radioactive material, in particular uranium (U) and plutonium (Pu), there should be a significant international interest in the development of these techniques for radioactive particles.

The particles were mounted on a slide holder and marked in order to identify their positions with a magnifying glass. The first XANES spectrum measured with SS1 $0.5 \times 8 \text{ mm}^2$ showed some distortions even after dead-time correction, indicating normalization problems or sample heterogeneities. Therefore, the beam size was reduced with SS1 set to $0.05 \times 0.1 \text{ mm}^2$. This improved the XANES spectrum, but at the expense of strong reduction in photon flux. Also, due to the horizontal beam movement across the slit, the photon intensity varied by 1 order of magnitude during an energy range of 400 eV. Since SS1 is 3 – 4 m away from the sample, a x-gap of 0.1 mm cuts into the sagittally focussed beam. The conclusion for future experiments is to install a slit system close to the sample, i.e., just in front of the IO chamber.

Table 1: XANES images (edge position) of samples included in the experiment.

No.	Sample	Size	Edge position (eV)
29	U metal	grains	17166.8
1	UO ₂	powder	17170.2
2	U ₃ O ₈	powder	17172.3
33	UO ₂ (ac) ₂	powder	17172.0
14	"Dust" particle	≈100 μm	17172.1
40	"West" particle	25 x 40 μm	17169.0
44	"North" particle	on capillary	17172.0

Table 1 summarizes the edge positions of the U L3-edge XANES spectra of the particles measured in fluorescence mode. Several sweeps were averaged, calibrated and dead-time corrected using EXAFSPAK. The edge position is defined as the maximum of the first derivative (PROCESS, standard settings). The spectra were, however, not corrected for self absorption. By comparing the edge positions of the Chernobyl particles with those of the reference samples, one could conclude that metallic uranium was not present and

that all particles were oxidized, as was expected. Furthermore, U in the "Dust particle" (No 14) and the "North particles" (No 44) were present in a higher oxidation state (probably V or VI) than "West particle" (No 40), which is in accordance with earlier observations. From the XANES images, U in No 14 and No 44 was probably present as U(V or VI), while U in particle 40 seems to be more like U(IV).

Figure 1 shows the U L3-edge XANES spectra of the reference samples and the Chernobyl particles. The spectra have not been corrected for self absorption. The vertical bars indicate the white-line (WL) maximum and the position of a resonance in the spectrum of UO₂. The spectrum of particle No 40 shows the same energy positions for the WL and the resonance as in UO₂. The WL of particles No 14 and No 44 are slightly higher than for UO₂ indicating a higher degree of oxidation. This agrees with the conclusions drawn from the edge positions and agrees well with previous experiments, for instance at HASYLAB, Germany.

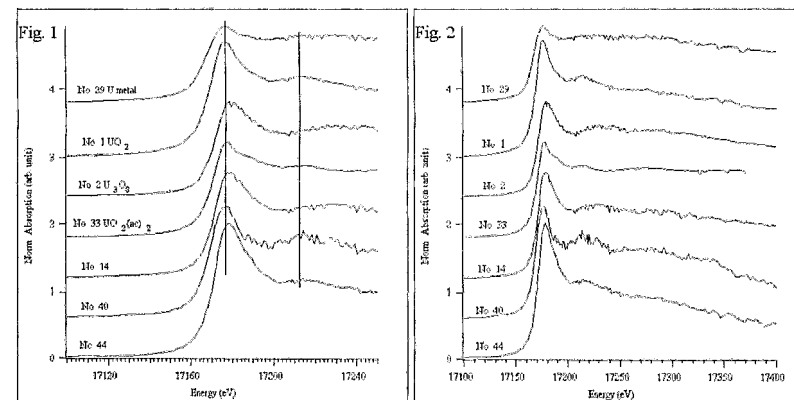


Fig. 1: XANES spectra of U standards and samples.

Fig. 2: XANES spectra of U standards and samples into the EXAFS region

Figure 2 shows the entire U L3-edge spectra to judge the asymptotic behaviour of the absorption spectra and the distortions in the EXAFS region. It seems that the magnitude of distortions in the EXAFS region prevents the determination of metrical parameters. A large degree of distortions occurred for the smallest particle (40 μm), probably due to the large mismatch between beam and particle sizes. However, additional EXAFS analyses based on well-characterised standard particles (e.g. reference sample No. 2 and 33) should be further explored.

Conclusions

In summary, the first U L3-edge XANES experiments on micrometer particles at ROBL were successful. The Si(111) bender was essential for the experiment. The intensity of the fluorescence signal coming off the high-density uranium particles was high and did not limit the signal statistics. Improvements in the future are needed on the slit system and the alignment of the second crystal. In addition, the reference samples should be large particles, i.e. larger than micrometer size. The correction of the XAFS signal from small particles for self-absorption effects has also to be taken into account.

Future experiment with a slit system closer to the sample and a better overlap of particle size and beam dimension should increase the potential of EXAFS for characterisation of small micrometer particles. As the advantage of ROBL is the possibility to handle transuranium elements, a future installation of additional focussing devices like capillary lenses, as in HASYLAB, at ROBL should be considered.



Experiment title: EXAFS/XANES studies on the speciation of reduced technetium-99 in presence of humic substances		Experiment number: SI-790
Beamline: BM -20	Date of experiment: from: 23/07/2002 to: 26/07/2002	Date of report: 22/08/2002
Shifts: 9	Local contact(s): André Rossberg	<i>Received at ESRF:</i>
Names and affiliations of applicants (* indicates experimentalists): Kathleen Geraedts*, André Maes*, Christophe Bruggeman* K.U.Leuven, Laboratorium voor Colloïdchemie, Kasteelpark Arenberg 23, B-3001 Heverlee, Belgium Luc Van Loon Paul Scherrer Institute, Laboratory for Waste Management, OHLB/409a, CH-5232 Villigen PSI, Switzerland		

Report:

Introduction

The redox-sensitive fission product technetium-99 is of great interest in nuclear waste disposal studies because of its potential of contaminating the geosphere due to its very long half-life and high mobility. Under oxidising conditions, technetium is present as pertechnetate, a highly soluble, anionic species, that does not sorb significantly on minerals or sediments [1]. Under suitable reducing conditions, eg. in the presence of a reducing solid phase which can act as an electron donor, the solubility can be limited by the reduction of pertechnetate followed by the formation of a surface precipitate with a low solubility [2]. However, in presence of dissolved humic substances, the solubility may be enhanced due to the formation of Tc-HS complexes [3].

In March 2001, a first series of measurements were performed at ESRF. From these measurements, it was unequivocally demonstrated by XANES spectroscopy of samples with very low Tc content, that Tc(IV) species were formed and were associated with mobile humic substances. In samples containing variable amounts of Tc(VII) and Tc(IV), both fractions could be calculated from the recorded spectra. These results were presented in a paper by Geraedts et al., which will be published in Radiochimica Acta [4]. It was the intention from the EXAFS measurements given in the present report to further elucidate the nature and kind of Tc(IV)-humic substances species (Gorleben and Boom Clay humic substances) and to identify Tc(IV) species formed on solid phases (pyrite and magnetite).

Sample preparation

At KULeuven, different series of samples were prepared in batch experiments: series 1 consisted of Tc species in presence of 2 different iron-containing surfaces (acting as the necessary reducing solid phase): pyrite and magnetite. These solid phases were brought in contact with humic rich (Gorleben groundwater) and humic free solutions. This set-up was used to determine the Tc species in presence of the different solid phases. A next series of samples was made to mimic a more natural environment: 1) a suspension of Gorleben sand in Gorleben groundwater and 2) Boom clay sediment in equilibrium with a synthetic

groundwater, resulting in an equilibrium distribution of humic substances and Tc between the solid and the liquid phase. From these last two samples, Tc-HS species could be obtained via centrifugation of the high weighted molecular humic substances. A final series of samples was made using a methodology developed at KULeuven for collecting (and measuring the concentration of) Tc-humic substances species from solution by induced flocculation of the organic matter with the trivalent cation La^{3+} [5].

The 9 allocated shifts were used to measure the XANES/EXAFS spectra of the abovementioned samples in the fluorescence detection mode. For the iron-containing samples, a special chromium filter was used to suppress the influence of the high X-ray absorption from iron.

Results

- 1) No differences were observed between spectra of samples containing Tc associated with solid humic substances and Tc associated with dissolved humic substances which were precipitated by La^{3+} . This indicates that 1) the Tc(IV) association with both solid and dissolved humic substances is alike and 2) La-precipitation of dissolved humic substances did not alter the Tc-HS association.
- 2) Unexpectedly, there were significant differences between the spectra obtained for samples containing Tc species associated with Boom Clay- and Gorleben humic substances, indicating a different interaction between Tc and the different types of humic substances (Boom Clay humic substances versus Gorleben humic substances). Preliminary calculations did not allow to quickly elucidate the chemical environment of Tc in these samples. Therefore, since no EXAFS literature data are available for these types of Tc species, additional EXAFS measurements on carefully chosen reference Tc-complexes are necessary in order to compare them with the obtained results with Boom Clay and Gorleben humic substances.
- 3) The Tc species formed on solid phases (magnetite and pyrite) both in absence and presence of humic substances were tetravalent Tc species. The exact coordination numbers and bond lengths will be calculated and compared with literature values of TcO_2 and TcS_2 in order to identify the formed Tc solid phase species on the different surfaces.

References

- [1] Lieser K. H., Bauscher Ch., Radiochimica Acta, 42 (1988) 205.
- [2] Cui D, Eriksen T. E., Environ. Sci. Technol., 30 (1996) 2263.
- [3] Sekine T., Watanabe K., Kim, J. I., Radiochimica Acta, 63 (1993) 87.
- [4] Geraedts K., Maes A., Bruggeman C., Van Loon L., Rossberg A., Reich T., Radiochimica Acta (2002), in press
- [5] Geraedts K., Maes A., Vancluyse J., Third technical progress report of the EC-project No.: F14W-CT96-0027 Report FZKA, 6524, Ed. G. Buckau (2000).



Experiment title: Plutonium and neptunium speciation in anaerobic natural groundwater rich in humic substances		Experiment number: CH-1357
Beamline: BM 20	Date of experiment: from: 13.11.2002 to: 16.11.2002	Date of report: 27.11.2002
Shifts: 9	Local contact(s): Dr. André Roßberg	<i>Received at ROBL:</i> 27.11.2002
Names and affiliations of applicants (* indicates experimentalists): M.A. Denecke*, A. Seibert*, K. Dardenne*, P.J. Panak* Forschungszentrum Karlsruhe, Institut für Nukleare Entsorgung		

Report:

Pu and Np L3 XAFS speciation investigations are performed on Pu and Np added to Gorleben groundwater. The groundwater used is from an anaerobic aquifer rich in humic substances (HS). The studies aim at 1) determining the actinide cation oxidation state of Pu/Np-HS complexes, 2) identifying HS functional groups binding Pu/Np cations and 3) characterizing any formation of mixed hydroxo-Pu(IV)/Np(IV)-humate species or Pu(IV)/Np(IV) polynuclear species.

Our own previous investigations suggest that Pu under anaerobic and neutral pH conditions of the same Gorleben groundwater is present in both the Pu(III) and Pu(IV) states, strongly associated with HS. Studies of the interaction of HS with other tetravalent elements (Th(IV), Hf(IV)¹) and other valent cations (Np(V), U(VI)^{2,3}), implicate HS carboxylate groups responsible for metal cation complexation. The formation of mixed hydroxo fulvate Np(IV) complexes⁴, of dimers in Np(V)-humates and of polynuclear hydrolysis Pu(IV) species associated with Pu(IV)-fulvates⁴ have been reported.

Pu solutions with required oxidation states are produced electrolytically and the oxidation state purity verified by absorption spectroscopy. Samples are prepared under Ar/1% CO₂ atmosphere by

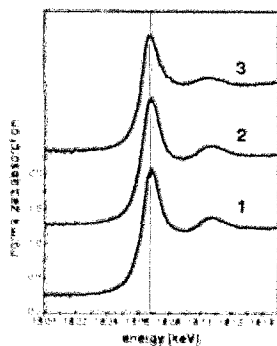


Fig. 1: Pu L3 XANES for Gorleben groundwater samples following addition of Pu(III) (sample 1), Pu(IV) (sample 2) and Pu(VI) (sample 3).

adding an aliquot of Pu(III), Pu(IV), Pu(VI) or Np(V) solutions to Gorleben groundwater (GoHy-532 with ~50 mg/L DOC) and readjusting the pH to neutral where necessary. Pu concentrations are 1*10⁻⁴ mol/L. Pu and Np L3 edge EXAFS spectra are recorded in fluorescence mode.

Although initial capillary electrophoresis results suggest that part of the Pu(IV) is reduced to Pu(III) after being added to the groundwater, the energy of XANES features (Fig. 1) shows that Pu is present mostly as Pu(IV), regardless if Pu(IV) or Pu(III) is added.

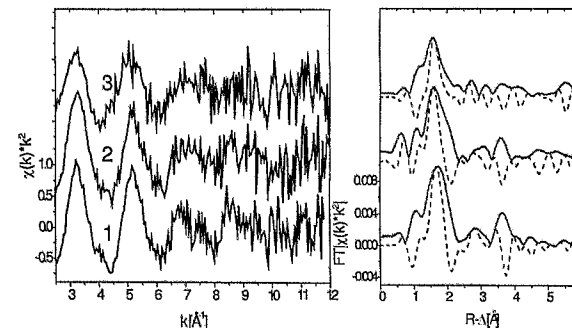


Fig. 2: Pu L3 EXAFS spectra (left) and corresponding Fourier transforms (FT, right) for the same samples as Fig. 1.

Only the groundwater to which Pu(VI) is added shows a XANES energy shift from that of Pu(IV). This is from the presence of plutonyl cations, as confirmed from analysis of the

Fits to filtered first-

shell EXAFS show Pu-O bond distances in all three samples to be much shorter than Pu-O distances in Pu aquo ions of varying Pu valence⁵. This shortening is from the formation of hydroxy complexes and polymeric species. The Pu-Pu interaction, especially evident as a 3.65 Å FT peak in Fig. 2, indicates polymeric species formation.

XANES and EXAFS data (not shown) show that Np(V) is not reduced but remains Np(V) in the groundwater. However, no Np-O-Np dimer complexes, as observed for Np(V) complexed with purified humic acid², are observed.

- 1 M.A. Denecke, D. Bublitz, J.I. Kim, H. Moll, I. Farkes, J. Synchrotron Rad. **6**, 394-96 (1999).
- 2 M.A. Denecke, K. Dardenne, C.M. Marquardt, J. Rothe, M.P. Jensen, Proceedings of the 2nd OECD-NEA Workshop on Speciation, Techniques and Facilities for Radioactive Materials at Synchrotron Light Sources, Grenoble, France, 10.-12. September 2000.
- 3 M.A. Denecke, T. Reich, S. Pompe, M. Bubner, K. H. Heise, H. Nitsche, P.G. Allen, J.J. Bucher, N.M. Edelstein, D.K. Shuh, K.R. Czerwinski, Radiochim. Acta **82**, 103-8 (1998).
- 4 M.A. Denecke, C.M. Marquardt, J. Rothe, K. Dardenne, M.P. Jensen, J. Nuclear Science Technology (*in print*).
- 5 S.D. Conradson, I. Al Mahamid, D.L. Clark, N.J. Hess, E.A. Hudson, M.P. Neu, P.D. Palmer, W.H. Runde, C.D. Tail, Polyhedron **17**, 599-602 (1998).



Experiment title: X-ray investigation of silicon / germanium nanocrystals on silicon carbide		Experiment number: SI 622
Beamline: BM 20	Date of experiment: from: 31.01.2001 to: 04.02.2001	Date of report: 09.01.2002
Shifts: 12	Local contact(s): Dr. Norbert Schell	<i>Received at ESRF:</i> 09.01.02
Names and affiliations of applicants (* indicates experimentalists): Dr. G. Heß *, DP A. Bauer, Dr. N. Schell, DP B. Wunderlich *, Dr. J. Kräußlich * Prof. K. Goetz Friedrich-Schiller-University of Jena Institute of Optics and Quantumelektronics Department of X-ray Physics Max-Wien-Platz 1 07743 Jena / Gemany		

Report:

The aim of the experiment was to investigate the habit, size, arrangement and constitution of Si- and Ge-nanocrystals which were grown by molecular beam epitaxy on SiC(0001)-substrates using the Stranski-Krastanov growth mode. For these purposes, high resolution x-ray diffraction measurements were carried out using the new material research goniometer of the CRG-beamline ROBL. The performed measurements were successful in acquiring significant results which are well suitable to characterize the grown nanocrystals. The results were already published in the journal of:

Thin Solid Films 380 (2000) 86-88

Si/Ge-nanocrystals on SiC(0001)

G. Heß^a, A. Bauer^a, J. Kräußlich^a, A. Fissel^b, B. Schröter^b, W. Richter^b, N. Schell^c, W. Matz^c, K. Goetz^a

^aInstitut für Optik und Quantenelektronik, Friedrich-Schiller-Universität Jena, Max-Wien-Platz 1, 07743 Jena, Germany

^bInstitut für Festkörperphysik, Friedrich-Schiller-Universität Jena, Max-Wien-Platz 1, 07743 Jena, Germany

^cForschungszentrum Rossendorf, Postfach 510119, 01314 Dresden, Germany

Abstract

The growth and structure of Si- and Ge-nanocrystals was investigated using high resolution X-ray diffraction (HRXRD) and atomic force microscopy (AFM). AFM-images were used to determine the lateral and vertical dimensions of the nanocrystals. HRXRD measurements show clearly that Si- and Ge-nanocrystals grow on 6H-SiC(0001) preferentially in two different orientations - <111> and <110> - with respect to the surface normal. The growth of Ge-nanocrystals on Si-rich 6H-SiC(0001) surfaces leads to the formation of Si/Ge-alloy nanocrystals. Both types of nanocrystals grow coherently with respect to the substrate. Hence, due to the respective lattice mismatch, the degree of coherence was found to be much better for Si-nanocrystals.



Experiment title: Strain in Si/Ge-nanocrystals (Ge nanocrystallites grown on SiC)		Experiment number: SI 685
Beamline: BM 20	Date of experiment: from: 27.06.2001 to: 02.07.2001	Date of report: 19.12.2001
Shifts: 15	Local contact(s): Andreas Bauer	<i>Received at ESRF:</i> 15.11.02
Names and affiliations of applicants (* indicates experimentalists): Dr. J. Kräußlich ¹⁾ *, DP B. Wunderlich ¹⁾ *, DP F. Wunderlich ¹⁾ *, Dr. G. Hess ¹⁾ , B. Schröter ²⁾ , Prof. K. Goetz ¹⁾ Friedrich-Schiller-University of Jena ¹⁾ Institute of Optics and Quantumelektronics / Department of X-ray Physics ²⁾ Institute of Solid-State Physics Max-Wien-Platz 1, 07743 Jena / Germany		

Report:

The aim of the experiment has been to characterize Ge-nanocrystals grown on 6H-SiC(0001) substrates by means of high resolution x-ray diffraction methods (HRXRD). Preferred crystallographic orientations in respect to the substrate lattice, the size of the grown nanocrystals as well as the chemical phase are of special interest for both the nanocrystals producers and optoelectronic device developer.

Ge-nanocrystals have been produced on the Si-side of on- and off-axis oriented 6H-SiC(0001) surfaces by means of molecular beam evaporation [1]. Substrate temperatures from 470°C to 550°C and evaporation rates of Ge from 0.1 to 1.5 nm/min have been used. At first, on the Si-terminated ($\sqrt{3}\times\sqrt{3}$)R30° reconstructed 6H-SiC(0001) surface a mono-atomic Ge wetting layer was established with homogeneously distributed 2D-islands of 2-3 nm diameter from which 3D-Ge-nanocrystals grew according to the Stranski-Krastanov's theorem. Finally, these were covered with SiO₂ in order to get a long-term stability. Fig. 1 shows the corresponding AFM image.

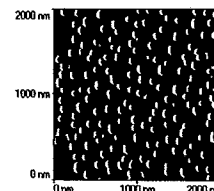


Fig. 1: AFM image of the Ge nanocrystallites grown on 6H-SiC(0001) at 550°C at a rate of 1.5 nm/min.

The scattering volume of the grown nanocrystals is very small, particularly with regard to substrate volume. For this reason, high-intensity synchrotron radiation, which should be well collimated and monochromated, is required to analyse the nanocrystals by x-ray diffraction methods. Furthermore, an x-ray diffractometer set-up equipped with an Eulerian cradle is essential in order to adjust symmetric, asymmetric as well as oblique crystal reflections. These requirements are well accomplished by the new material research diffractometer at the CRG-beamline (ROBL) at the ESRF [2].

The x-ray diffraction pattern (Fig. 2) taken by using the coupled $\omega/2\theta$ -mode proves the crystalline phase of the Ge-nanocrystals which were produced on the 6H-SiC(0001) with the above indicated parameters. Besides the strong directly and 'umweg'-excited substrate peaks, the diffraction pattern shows also peaks which could be explicitly assigned to the Ge-nanocrystals. These peaks are the 111-, 220-, 311- and 400-reflections. They point out to the different orientation of the Ge-nanocrystals in respect to the substrate surface. These 'orientation diversity' suggests a homogenous orientation distribution of the grown Ge-nanocrystals. However, the rocking curves taken with each of the hkl-reflections indicate a distinctive alignment of the corresponding crystallites in respect to the substrate (Fig. 3). The growth of exclusively (111)-oriented Ge-nanocrystals could successfully be realized by using a special sample preparation.

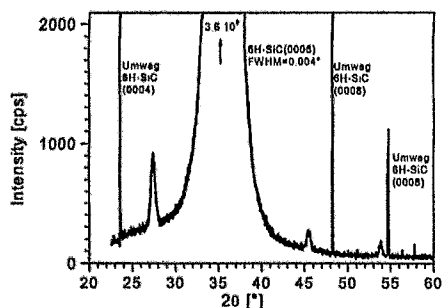


Fig. 2: Large area $\omega/2\theta$ -diffraction pattern of Ge-nanocrystals grown on the 6H-SiC(0001). The little peaks arising from the Ge nanocrystals point out that they are differently oriented in respect to the substrate.

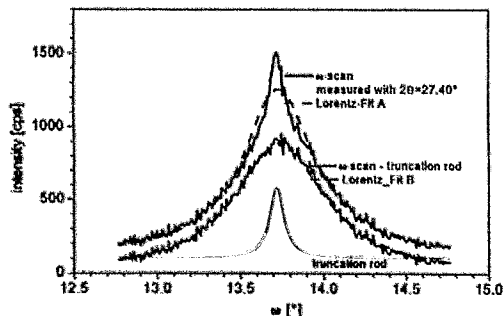


Fig. 3: Rocking curve (ω -scan) recorded with the 111-Ge reflection of Fig. 2. The tail of the strong 0006-SiC substrate reflection (truncation rod) had been eliminated in order to obtain the reflection broadening caused by size of the nanocrystals. $FWHM_{\omega} = 0.65^{\circ} \rightarrow$ lateral size of the Ge-crystallites $D_{lateral} = 25.3$ nm.

The 'fittleness' of the crystallite dimension causes a diffraction peak broadening both in the $\omega/2\theta$ -diffractogram and in the ω -scan diffractogram. From this and neglecting the inherent crystallite strain,

which here is fulfilled for the epitaxially grown crystallites, one can evaluate their size in-plane and normal to the surface, $D_{lateral}$ and D_{normal} , respectively. The modified Scherrer equation can be used:

$$D_{normal} = \frac{0.88 \cdot \lambda}{\cos \Theta \cdot \Delta(2\Theta)_{FWHM}} \quad \text{applicable to the } \omega/2\theta\text{-scan mode}$$

$$D_{lateral} = \frac{0.44 \cdot \lambda}{\sin \Theta \cdot \Delta\omega_{FWHM}} \quad \text{applicable to the } \omega\text{-scan mode}$$

Hence, the complete set of the measured values for the Ge-crystallites with (111), (110) and (311) orientation, respectively, gives the crystallite sizes indicated in Fig. 4. The diagram shows the similarity of the differently oriented crystallites in respect to their average size and aspect ratio.

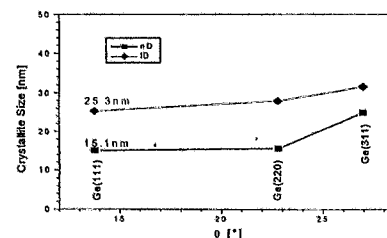


Fig. 4: Average crystallite size of Ge-nanocrystals differently oriented grown on the 6H-SiC(0001): D_{normal} - crystallite size perpendicular to substrate surface, $D_{lateral}$ - crystallite size parallel to substrate surface.

Note, that the results acquired by the x-ray diffraction methods represent integral values averaged over the area at the wafer surface of approximately 1 mm^2 defined by the incident x-ray cross section. They characterize a large ensemble of same type nanocrystals. Therefore, the results due to the x-ray diffraction are useful in supplementation and for comparison to the TEM and AFM investigations which characterize only a single or a few nanocrystals, respectively.

We thank all members of the ROBL beamline team, especially Dr. Schell and A. Bauer, for all the helpful support at the time of execution this experiment.

[1] B. Schröter, K. Komlev, U. Kaiser, G. Heß, G. Klipshtzde, and W. Richter
Germanium on SiC(0001): surface structure and nanocrystals
Materials Science Forum 353-356 (2001) 247-250

[2] W. Matz, N. Schell, G. Bernhard, F. Prokert, T. Reich, J. Claufner, W. Oehme, R. Schlenk, S. Dielen, H. Funke, F. Elchhorn, M. Betzl, D. Pröhl, U. Strauch, G. Hüttig, H. Krug, W. Neumann, V. Brendler, P. Reichel, M.A. Denecke and H. Nitsche
ROBL - a CRG beamline for radiochemistry and materials research at the ESRF
Journal of Synchrotron Radiation 6 (1999) 1076-1085



Experiment title: Reflectometry on FeCo single and multilayer		Experiment number: ME-217
Beamline BM 20	Date of experiment from: 28.02.01 to: 03.03.01	Date of report 30.08.01
Shifts: 9	Local contact(s) Dr. N. Schell, Dr. A. Bauer	<i>Received at ESRF:</i>
Names and affiliations of applicant(s) (# indicates experimentalists): S. Dieter*, A. Pyzalla***, T. Poeste*		
*Hahn – Meitner – Institut, Bereich Strukturforschung, Glienicke Straße 100 D – 14109 Berlin, Germany, Tel. ++49 / (0)30-8062-3095, Fax: ++49 / (0)30-8062-3195 Email: dieter@hmi.de, poeste@hmi.de		
** now: TU Berlin, Institute for Materials Science and Technology, Sekr. BH 18, Ernst-Reuter-Platz 1, D – 10623 Berlin, Germany Email: Anke.Pyzalla@TU-Berlin.de		
Report		
Experiment ME-217 was carried out at beamline BM20 of the ESRF. The focus of this experiment was the determination of layer thicknesses and layer roughness of FeCo/SiO ₂ multilayers. The experiment is part of a strategyfunds project of the Helmholtz Society which aims at an optimization of multilayers for microinductor applications. The multilayers are produced by magnetron sputtering at Forschungszentrum Karlsruhe, Germany.		
In order to link the magnetic properties of the microinductors to their multilayer structure, the dependence of layer thicknesses and layer roughness of the FeCo- and the intermediate SiO ₂ layers had to be determined with respect to their dependence on the deposition parameters such as the sputter power and the argon partial pressure. This could only be done non-destructively by reflectometry experiments using synchrotron radiation. By performing further experiments in the laboratories at the HMI Berlin the crystallographic structure of the layers, their morphology, texture and residual stress state was characterized.		
The reflectometry experiments were performed on the 6-circle-diffractometer at BM20 using a scintillation detector (detector slit width = 12mm, detector slit height 0,22mm). The energy of the monochromatic synchrotron radiation was set to 7,1 keV, near to the absorption edge of the FeCo compound. For the determination of the layer thicknesses, layer roughness and layer densities specular scans were performed in ω -2 θ -geometry in the range of the critical angle of total reflection. For the evaluation of the experimental data simulations were carried out using different models of the multilayer structure. Results of the experiments and the subsequent modeling are given in tab.1.		

Tab. 1: Deposition parameters, residual stresses, magnetic properties, layer thickness and roughness from simulations of the FeCo-SiO₂ multilayer system

	FCS6Z1	FCS6Z4	FCS6Z5	FC6Zn6	FC6Zn7
sputter power FeCo P [W]	100	100	100	300	200
sputter power SiO ₂ P [W]	300	100	300		
argon partial pressure p [mbar]	0,006	0,006	0,006	0,006	0,006
residual stresses [MPa]	-690	-860	-880	230	-70
saturation magnetization [T]	2,31	2,27	2,32		
coercivity [T]	0,01732	0,01606	0,00342		
total layer thickness [Å]	4800	5000	5000	5600	5165
FeCo layer thickness [Å]	5*500	5*500	7*500	5*500	5*500
SiO ₂ layer thickness [Å]	5*500	5*500	7*250	5*500	5*500
FeCo layer thickness [Å], model	493	478	504	468	516
SiO ₂ layer thickness [Å], model	503	546	263	578	579
FeCo roughness [Å], model	51	27	29	45	20
SiO ₂ roughness [Å], model	11	7	10	11	11
oxide layer thickness [Å], model	100	74	74	62	67

The layer thicknesses of the FeCo layers and the SiO₂ layers are in good agreement with the specification of 50nm \pm 10%. But, the reflectometry tests showed that an oxide coating on the sample surface is present, which has not been detected before and which might influence the magnetic properties. This is still under investigation.

The experimental results show further on, that there is a roughness difference between the FeCo and the SiO₂ layers. In order to link this to the morphology of the layers additional transmission electron microscopy tests were performed at HMI (fig. 1, 2).



Fig. 1: FeCo single layer with Ti bond coat on the Si-substrate the columnar grains grew through the whole layer
[N. Wankler, M. Macht HMI Berlin]



Fig. 2: Columnar layer growth of FeCo-SiO₂ multilayer FC6Z2 (A = FeCo-SiO₂ interface, B = SiO₂-FeCo interface)
[N. Wankler, M. Macht HMI Berlin]

The TEM micrographs indicate that the reason for the roughness differences of the layers is that the morphology of the FeCo layers is columnar whereas the SiO₂ layers grow up nondirectionally. The experiments further reveal a significant influence of the sample position in the deposition chamber on the lateral homogeneity of the layer thickness and thus the magnetic performance.



Experiment title: Influence of dopant atoms in cubic boron nitride (c-BN) thin films on lattice parameters and intrinsic stress investigated by X-ray diffraction		Experiment number: ME-311
Beamline: BM20	Date of experiment: from: 31-Oct-2001 to: 5-Nov-2001	Date of report: 05-Feb-2002
Shifts: 15	Local contact(s): N. Schell	<i>Received at ESRF:</i>
Names and affiliations of applicants (* indicates experimentalists): F. Richter, Th. Peifer, V. Linß, S. Peter* TU Chemnitz, Institut fuer Physik -123202- , D-09107 Chemnitz, Germany W. Hoyer, Th. Halm* TU Chemnitz, Institut fuer Physik -123402- , D-09107 Chemnitz, Germany		

Report:

According to our previous experiments, where we investigated thin polycrystalline c-BN films doped with a few at.% aluminium [1], the aim of our last experiment was to investigate the possibility to manipulate the lattice spacing in cubic boron nitride (c-BN) due to the incorporation of the noble gas krypton.

A preliminary study on such c-BN films revealed that the reflex of the (111) lattice planes is well pronounced, therefore, this reflex was chosen to be studied. To obtain a great variety of different orientations of these (111) planes relative to the sample surface, a monochromatic beam of 1.1 Å was used. The angle between the incident beam and the sample surface was fixed at values of 0.3 ° (slightly above the angle of external total reflection).

To access differently oriented planes, the detector was moved either around a horizontal axis (2θ) or a vertical axis (2ω) while the remaining axis was held constant.

The $\sin^2\Psi$ method (where Ψ is the angle between the vector normal to the lattice plane and the vector normal to the sample surface) was applied to analyze the biaxial stress state.

Assuming a reliable value for the c-BN POISSON'S ratio from the literature, the spacing $d_0(111)$ of the unstressed lattice planes was obtained.

We found that, contrary to aluminium incorporation, in the krypton doped films the c-BN (111) unstressed lattice constant $d_0(111)$ does not depend on the krypton concentration. Assuming YOUNG'S modulus of the bulk c-BN, the biaxial compressive stress value of the films varied in the range between -11 and -20 GPa at one and the same krypton content. Additional secondary ion mass spectroscopy measurements show that the krypton concentration in the films is independent of the krypton concentration in the process gas. Furthermore the krypton atoms are probably incorporated at interstitial sites and prior into the hexagonal phase. For a better understanding of the influence of dopant atoms on interstitial sites additional experiments are necessary.

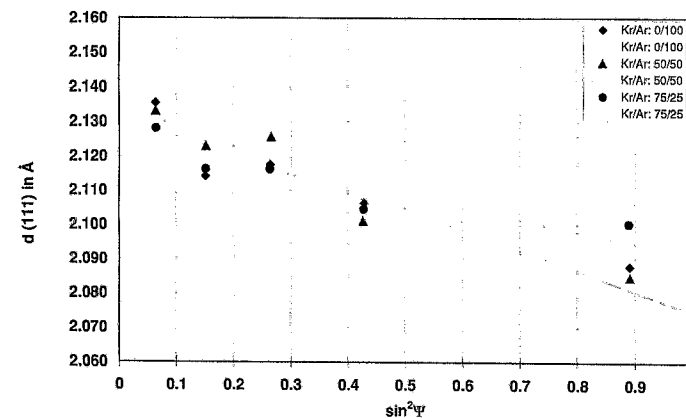



Fig. 1 Lattice spacing of (111) planes having different orientations with respect to the sample surface: cubic BN layer with incorporated Kr for different process gas mixtures Kr/Ar = 0/100, 50/50 and 75/25.

[1] Halm, T., Linß, V., ESRF Experimental Report, Feb. 2001

 ESRF	Experiment title: Short range order investigations in the Fe_{78.4}Cr_{21.6} solid solution by combination of EXAFS and differential anomalous x-ray wide-angle scattering	Experiment number: HS-1626
	Beamline: BM 20	Date of experiment: from: 26.11.2001 to: 01.12.2001
Shifts: 9 + 3	Local contact(s): Dr. Norbert Schell, Dr. Tobias Reich	<i>Received at ESRF:</i> 06.11.02
Names and affiliations of applicants (* indicates experimentalists): Prof. Yu.A. Babanov*, Dr. A.F. Sidorenko, S.A. Kiryanov, Dr. A.V. Ryazhkin, Dr. L.N. Romashev, Dr. A.M. Patselov Institute of Metal Physics, S.Kovalevskaya str. 18, GSP-170, Ekaterinburg 620219, Russia Prof. T. Reich*, Dr. H. Funke*, Institute of Radiochemistry, Forschungszentrum Rossendorf, P.O. Box 510119, 01314 Dresden, Germany Dr. F. Prokert*, Dr. N. Schell*, Institute of Ion Beam Physics and Materials Research, Forschungszentrum Rossendorf, P.O. Box 510119, 01314 Dresden, Germany		

Report:

Atomic structure investigation of Fe/Cr systems is very difficult because of the close position of Fe and Cr in the periodic table of chemical elements. In this case, the solid state solutions of Fe-Cr would be an attractive model system as a first step in the study. It would provide developing techniques of the experimental determination of partial pair correlation functions (pPCFs) close to the Fe/Cr multilayers short range investigations.

The purpose of the present experiments is the determination of the positions of the coordination spheres, the partial coordination numbers for the first shell and the local ordering in Fe_{78.4}Cr_{21.6} solid state solution.

Fig.1 shows the picture of anomalous x-ray scattering recorded at the Fe K-edge (E = 7105 eV). On the last two peaks (Fig. 1) solid state solution stratification on three bcc-phases is clearly seen. The first two peaks cannot give such information due to weak s-space resolution. X-ray scattering data obtained using Cr K_α radiation do not contain any splitting (a = 2.872 Å).

Lattice parameters of the three phases determined on the last two peaks are a₁ = 2.874 Å, a₂ = 2.872 Å, a₃ = 2.871 Å. Using the dependence of the lattice parameters from the Cr concentration for Fe-Cr alloys, the Cr concentration in each phase was obtained: c₁ = 0.383, c₂ = 0.216, c₃ = 0.128. Assuming the phase with Cr concentration c₂ = 0.216 dominates (~90%) and the parts of the other phases are small (~5%). The weighted average lattice parameter a = 2.872 Å and the interatomic distance r = 2.487 Å are determined.

From Fe and Cr EXAFS data separately, the partial interatomic distances were determined by the Tikhonov regularization method [1]. It is known from model calculations that partial pair correlation functions in the case of absolutely disordered solid state solutions is the same and the coordination numbers are defined by the concentrations of the elements. It is clearly seen that the error in the determination of the positions from EXAFS data is greater than from diffraction data (Table 1). The coordination numbers obtained by the special method [2] for the first coordination sphere are shown in Table 2.

According to the Cowley parameter definition $\eta = 1 - N_{ij}^{ex} / N_j^*$ (i ≠ j) we obtained the average value $\eta = 0.05 (\pm 0.01)$. The positive value means that solid state solution stratification.

Conclusion: The results obtained from EXAFS and AWAXS data allow to conclude: Fe_{78.4}Cr_{21.6} solid state solution stratifies on three phases with lattice parameters 2.874 Å, 2.872 Å, 2.871 Å and the corresponding Cr concentrations 0.383, 0.216, 0.128. Besides, it was shown that the Cowley parameter calculated was $\eta > 0$. It is an evidence of stratification in chemical short range order¹.

Table 1: The partial interatomic distances for Fe_{78.4}Cr_{21.6} solid state solution:

Fe-Fe	Fe-Cr	Cr-Fe	Cr-Cr
2.48 ± 0.01, Å	2.49 ± 0.01, Å	2.47 ± 0.01, Å	2.48 ± 0.01 Å

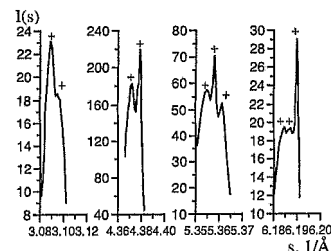


Fig. 1: Anomalous X-ray scattering near the Fe edge (E = 7105 eV) in S-space; peaks: 110, 200, 211, 220, respectively.

Table 2: Partial coordination numbers for the first sphere of Fe_{78.4}Cr_{21.6} solid state solution

Coordination numbers obtained from Fe EXAFS		Cowley parameter η
Fe-Fe	Fe-Cr	
6.491	1.625	0.06
6.272*	1.728*	0
Coordination numbers obtained from Cr EXAFS		Cowley parameter η
Cr-Fe	Cr-Cr	
6.014	2.007	0.04
6.272*	1.728*	0

* - corresponds to the absolutely disordered solid state solution.

- [1] A.N. Tikhonov and V.Ya. Arsenin, Solution of ill posed problems (John Wiley & Sons, 1977).
 [2] Yu.A. Babanov, A.V. Ryazhkin, T. Miyanaga, T. Okazaki, A.F. Sidorenko, N.V. Fadyushina, NIM A 448 (2000) 364.

¹ Accepted paper at Materials Conference SR-2002 (Novosibirsk) to be published at NIM A.

Anomalous X-ray scattering and EXAFS study in the determination of the short range order of the solid state solution Fe_{78.4}Cr_{21.6}

S.A. Kiryanov^{a*}, A.F. Sidorenko^a, Yu.A. Babanov^{a,b}, A.V. Ryazhkin^a, L.N. Romashev^a, A.M. Patselov^a, T. Reich^c, H. Funke^c, F. Prokert^d, N. Schell^d

^a Institute of Metal Physics, S.Kovalevskaya str. 18, GSP-170, Ekaterinburg 620219, Russia

^b Udmurt State University, Izhevsk, Russia

^c Institute of Radiochemistry, Forschungszentrum Rossendorf, PO Box 510119, 01314 Dresden, Germany

^d Institute of Ion Beam Physics and Materials Research, Forschungszentrum Rossendorf, PO Box 510119, 01314 Dresden, Germany

Abstract

The results of studying local atomic structure for the solid state solution Fe_{78.4}Cr_{21.6} by extended X-ray absorption fine structure (EXAFS) and anomalous wide angle X-ray scattering (AWAXS) are presented. From the anomalous X-ray scattering data we find the solid state solution decomposition on three bcc-phases, with different lattice parameters and compositions. From EXAFS data the partial interatomic distances and the partial coordination numbers for the first shell are obtained. We calculate the Cowley parameter and find stratification in chemical short range order.



Experiment title: X-ray investigation of Ge-nanocrystals implanted in SiC		Experiment number: Me 309
Beamline: BM 20	Date of experiment: from: 10.02.2002 to: 14.02.2002	Date of report: 06.11.2002
Shifts: 12	Local contact(s): Andreas Bauer	<i>Received at ESRF:</i> 06.11.02
Names and affiliations of applicants (* indicates experimentalists): Dr. G. Heß, Dr. J. Kraeusslich*, DP B. Wunderlich*, DP F. Wunderlich*, Prof. K. Goetz Friedrich-Schiller-University of Jena Institute of Optics and Quantumelectronics Department of X-Ray Physics Max-Wien-Platz 1 07743 Jena / Germany		

Report:

The aim of the experiment has been to characterize Ge-nanocrystals implanted in 4H-SiC(0001) substrates by means of high resolution x-ray diffraction methods (HRXRD). Special interests for the optoelectronic device developer are: preferred crystallographic orientation of the formed Ge-nanocrystals in respect to the substrate lattice, the size of the grown nanocrystals as well as the chemical phase of the Ge-nanocrystals.

Samples

Ge⁺-ions with an energy of 250 keV were implanted into 4H-SiC(0001) crystal wafers produced and supplied by Cree Research Inc. The implantation temperature was kept at 20°C and 700°C, respectively. The high implantation temperature was chosen to prevent amorphization of the crystals. The ion current density was less than 1 μAcm^{-2} . Samples were tilted about 6°-8° to the ion beam to avoid channeling effects during implantation. The ion fluence of $1 \cdot 10^{16} \text{ cm}^{-2}$ we used causes a Ge-peak concentration of approximately 1 at.% within the projected ion range in the deepness of 105 nm below the surface. Thermal annealing was carried out at temperatures up to 1600°C in Ar-atmosphere (pressure 20 kPa) using a rapid thermal annealing machine working with the samples placed between two electrically heated graphite stripes. To prevent significant decomposition the annealing process was done face-to-face with an unimplanted SiC piece [1]. Fig. 1 shows the corresponding cross section TEM image of a Ge-nanocrystal formed in the SiC matrix.

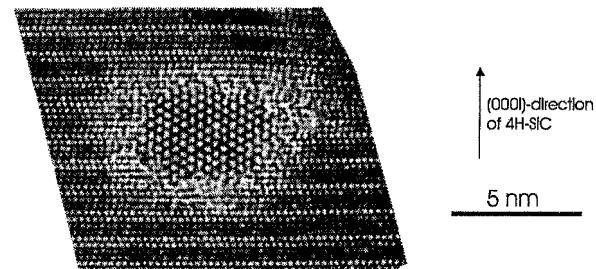


Fig. 1: High resolution TEM image of a Ge-nanocrystal formed after implanting and annealing at 1600°C in the 4H-SiC(0001) wafer.

Characterization

The x-ray diffraction experiments carried out at ROBL can be separated in two parts.

- Firstly, characterization of Ge-nanocrystals formed in SiC samples exposed to different process parameters

Sample	34-0	34-1	34-3	46-2	45-1	45-2	34-2	46-1
Implantation at 700°C	-	X	X	X	X	X	X	X
Annealing temperature	-	-	1400°C	1500°C	1600°C	1600°C	1600°C	1600°C
Annealing time	-	-	30 s	30 s	1s	30 s	120s	360 s

Tab. 1: The list of the measuring samples.

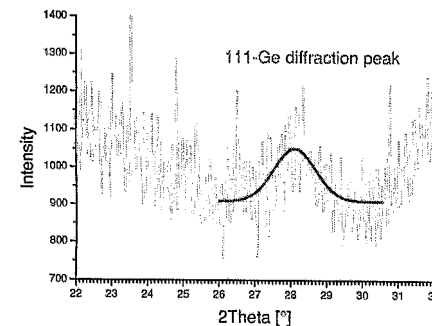


Fig. 2: $\theta/2\theta$ -scan of the symmetric Ge-111-reflection, sample 34-2, $\lambda = 0.154685 \text{ nm}$.

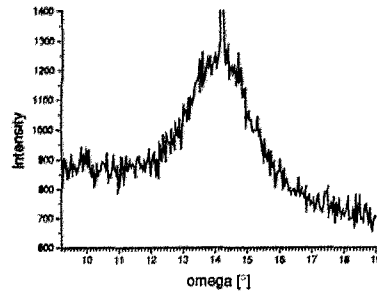


Fig. 3: ω -scan of the symmetric Ge-111-reflection, sample 46-1, $\lambda = 0.154685$ nm.

Only samples which were annealed at 1600°C have shown a 111-Ge diffraction peak. The occurrence of 111-Ge diffraction peaks (Fig. 2) in the XRD pattern of the annealed samples reveals the formation of crystallized Ge inside the SiC samples. The observed reflection broadening is caused by the crystallite size. Using Scherrer's formula the measured full width at half maximum $(FWHM)_{2\theta}$ results in the crystallite size perpendicular to the wafer surface (see table 2). Reflection broadening in the ω -scans (Fig. 3), carried out at the 2θ angle position of the 111-Ge reflection, is caused by the lateral crystallite size. The measured $(FWHM)_{\omega}$ is equivalent to a lateral crystallite size (see table 2). In-plane, the lateral crystallite size is rotation symmetric. We did not find any dependence on the lateral orientation angle ϕ . It is obvious that the maximum of the 111-Ge diffraction peak is located at $2\theta = 28.2^\circ$. Compared to the value for crystalline Ge ($2\theta = 27.3^\circ$) this means a significant shift of the Bragg angle toward the value for crystalline Si ($2\theta = 28.4^\circ$). We can discuss two possible reasons for this behavior. The Ge-nanocrystallites could be added impurities of Si atoms. On the one hand, the XRD measurements cover a sample area of nearly 1 mm² and for that a large volume of implanted SiC. The measurement represents an average of all crystallites in that area, including crystallites with different chemical composition. On the other hand, the shift of the Bragg angle can be caused by strain in the crystallites. The observed shift corresponds to a change of the lattice constant of $\Delta a/a = 3.1 \cdot 10^{-2}$.

Using Hook's formula, the hydrostatic pressure p inside the crystallites can be estimated to be $7.8 \cdot 10^8$ Nm⁻². In comparison with the in-plane strain of $\sigma_1 = \sigma_2 = 2.26 \cdot 10^8$ Nm⁻² in the case of 3C-SiC deposition on 6H-SiC. This seems to be a realistic value.

Sample	45-2	34-2	46-1
Implantation at 700°C and annealing at 1600°C	X	X	X
Annealing time	30 s	120 s	360 s
$(FWHM)_{2\theta}$	1,98°	1,16°	0,30°
crystallite size perpendicular to the wafer surface	4 nm	7 nm	10 nm
$(FWHM)_{\omega}$	2,98°	2,20°	1,84°
lateral crystallite size	5 nm	7 nm	9 nm

Tab. 2: The crystallite sizes lateral and perpendicular to the wafer surface of the Ge-nanocrystals formed after implanting and annealing at 1600°C in the 4H-SiC(0001) wafer.

➤ Secondly, characterization of the SiC substrates in the different stages of the nanocrystals-production-process

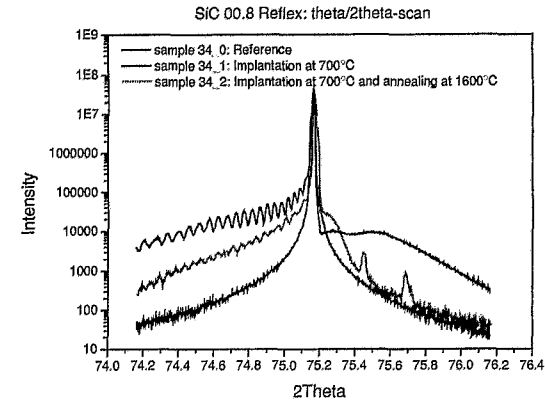


Fig. 4: $\theta/2\theta$ -scan of the symmetric SiC-0008-reflection – three stages of the nanocrystals-production-process:

- (1) a untreated 4H-SiC(0001) bulk single crystal wafer (sample 34-0)
- (2) a sample after the Ge⁺-ions implantation with an energy of 250 keV and a ion fluence of $1 \cdot 10^{16}$ cm⁻² at 700°C (sample 34-1)
- (3) a sample after the Ge⁺-ions implantation and thermal annealing at 1600°C in Ar-atmosphere (pressure 20 kPa) for 120 s (sample 34-2).

The implantation of Ge-atoms generates in the SiC lattice a strong disordered interlayer in a depth of 100 nm and with a thickness of approx. 10 nm. The crystal area above the strongly disordered interlayer is structural nearly undisturbed. The left side wing oscillation of the symmetric SiC-0008-reflection, as shown in Fig. 4, is caused by the interference effects of the diffracted x-ray beam due to the layer thickness above the buried strongly disturbed interlayer. Hence, the depth of the interlayer can be determined using the oscillation period. The interference effect was reduced after the thermal annealing at 1600°C. This is understandable by formation of Ge-nanocrystals (see Fig. 1) and the strong disordered interlayer heals partially up.

The x-ray diffraction experiments have been very useful in characterization of the implanted and annealed Ge:SiC wafer. Additional investigations are required to clear up the observed reflection shift of the Ge-nanocrystals. Is this caused by any impurities or hydrostatic strain of the Ge-nanocrystals.

We thank all members of the ROBL beamline team, especially Dr. N. Schell and A. Bauer for the helpful support at the time of execution on this experiment.

[1] Ch. Schubert, U. Kaiser, A. Hedler, W. Wesch, T. Gorelik, U. Glatzel, J. Kräußlich, B. Wunderlich, G. Heß, and K. Goetz; Journal of Applied Physics 91 (3) (2002) 1520-1524.



Experiment title: Scanning XRD Investigations of strain-induced Martensite Distribution in fatigued austenitic steel 321		Experiment number: ME395
Beamline: BM20	Date of experiment: from: 09.03. to: 13.03.2002	Date of report: 25.10.2002
Shifts: 12	Local contact(s): Dr. N.Schell	<i>Received at ESRF:</i>
Names and affiliations of applicants (* indicates experimentalists): Mirco Grosse*, Markus Niffenegger* Paul Scherrer Institut Villigen, Switzerland		

159

Report:

Cyclic strains lead to material degradation known as fatigue damage. In some meta-stable austenitic steels mechanical load is accompanied by strain-induced martensitic transformation [1]. The ferromagnetic martensite phase can be detected by non-destructive measurements of magnetic and electric properties of the material. The different testing methods like susceptibility measurements or the determination of the eddy current impedance have different penetration depths. In order to discuss the differences in their results the distribution of martensite in the sample has to be known.

In the performed experiments the martensite distribution at cross sections of 16 fatigued samples differ in their chemical composition and in the applied fatigue test conditions, were investigated. With a beam cross section of $0.4 \text{ mm} \times 0.8 \text{ mm}$ and a wave length of 0.1787 nm a gauge cross section of about $0.8 \text{ mm} \times 0.8 \text{ mm}$ was realised. The sample cross section was scanned with 1 mm steps in both directions. The texture is known from former neutron diffraction experiments, therefore the martensite content was estimated from the relation between (111) austenite and (110) martensite peak intensity [2].

The intensity of the (111) austenite peak shows a strong dependency on the lateral sample position. Reason for this dependency is not only a different phase composition but also the bad grain statistics caused relative large austenite grains compared with the gauge cross section. In contrast to the austenite, the grain size of martensite is small enough and the number of martensite needles high enough for a good grain statistic. Therefore the (111) austenite intensity averaged over the whole cross section was used for the estimation of the martensite content.

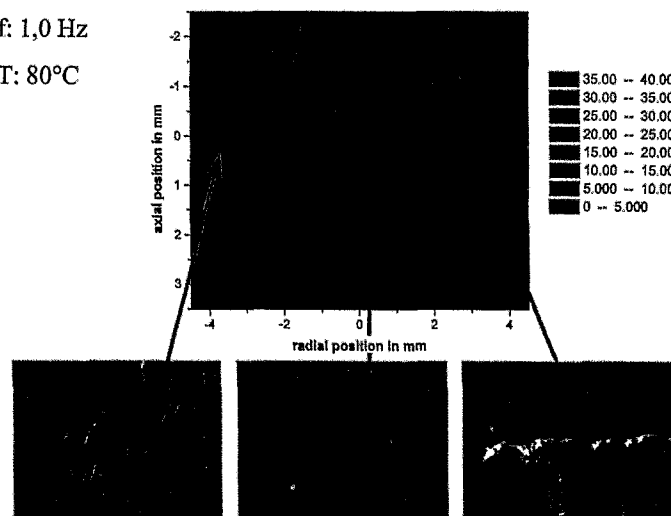
As an example of the results the determined martensite distribution is compared with typical metallographic images of surface, bulk and crack regions of sample FT31 (strain amplitude: 0.4 %, load cycle number: 11570, test frequency: 1.0 Hz, test temperature 80°C). In the metallographic images using polarised light the austenite has a blue colour whereas the martensite is yellow-green.

N: 11570

f: 1,0 Hz

T: 80°C

Content of martensite in % for specimen FT31



The quantitative results of the scanning XRD experiments are in good agreement with the metallographic images. In each sample where strain-induced phase transformation occurred the martensite is concentrated in the bulk (middle of radial direction) wear as the concentration of martensite close to the surface is significantly lower. Also in axial direction the martensite content varies, but, -as expected-, not systematically. At crack positions the highest martensite contents were found. At these positions stress and strain concentrations occurred during the fatigue test which results in a stronger strain-induced phase transformation. Different chemical compositions, strain amplitudes and fatigue test temperatures might influence the total content of martensite but not the general martensite distribution in the sample.

The measured lateral distribution of martensite is essential for a better understanding of the results from different applied non-destructive testing methods. Since susceptibility measurements provide information from the bulk (penetration depth about 10 mm) this method is better suitable to detect the material state than eddy current measurements with typical penetration depths of 0.1 .. 1.0 mm.

References

- [1] M. Grosse, M. Niffenegger, D. Kalkhof: J.Nucl.Mater 296 (2001), 305
- [2] G.Fanninger, U.Hartmann: HTM 27 (1972), 233

Experiment title: Deformation-induced change of grain structure and internal strains in micro-, submicro- and nanocrystalline nickel		Experiment number: HS-1774
Beamline: BM 20	Date of experiment: from: 03.04.2002 to: 08.04.2002	Date of report: 11.11.2002
Shifts: 15	Local contact(s): Dr. Norbert Schell	Received at ESRF: 06.12.02
Names and affiliations of applicants (* indicates experimentalists): Ellen Thiele*, Robert Klemm*, Lutz Hollang* Institute of Physical Metallurgy Technical University Dresden, D – 01062 Dresden, Germany		

Report:

Motivation. The aim of the experiment was to examine the influence of cyclic plastic deformation on the change of grain structure and internal stresses in Ni specimens, which exhibit very different mean grain sizes D and defect structures in their initial stages. Six different types of samples were investigated: on the one side fine- (fc) and micro-crystalline (mc) Ni with $D \approx 35\mu\text{m}$ and $3\mu\text{m}$, respectively, and a nearly stress-free initial stage and, on the other side, samples produced by equichannel angular pressing at room-temperature (RT-ECAP, $D \approx 0.5\mu\text{m}$) and at 250°C (ET-ECAP, $D \approx 0.8\mu\text{m}$), by electrodeposition (PED), and by hot-compaction of ball-milled Ni powder (CBM), all of them showing a certain amount of internal stresses already in the as-produced stage. All these samples had been cyclically deformed at constant plastic strain amplitude ε_{pa} at room temperature.

Experimental. Using a wavelength $\lambda = 0.1534$ nm, BRAGG-diffraction profiles of seven different $\{hkl\}$ -reflections were measured with a position sensitive detector (3380 channels for 8.28° in 2θ) from the $\{111\}$ - to $\{331\}$ -type. In order to ensure that a sufficient number of crystallites is in Bragg-position also in the case of fc and mc Ni, the samples were rotated round the surface normal which was parallel to the diffraction vectors g . The evaluation procedures given by Williamson-Hall (WH) [1], Warren-Averbach (WA) [2] and Krivoglaz-Wilkens (KW) (cf. [3]) were used to analyse the BRAGG-profiles with a negligible instrumental broadening.

Results and discussion. It was found that for the fc, mc and CBM samples the size d of coherently scattering regions decreases due to cyclic deformation whereas for all other samples a maximum value d occurs at $\varepsilon_{pa} \approx 2 \times 10^{-3}$ (cf. Fig. 1a, where d_{WA} was determined by the WA-analysis). In all cases, the size D of grains with high angle grain boundaries is at least ten times higher than d . Results of transmission electron microscopy suggest that d could be correlated with the thickness of regions with high dislocation density forming fatigue-induced dislocation patterns.

Taking the root mean square stress $\langle \sigma^2 \rangle^{1/2}$ calculated by a WH-analysis (cf. Fig. 1b) as a global measure for internal stresses of different range, then for the fc, mc and CBM Ni samples an increase of internal stresses was observed at small deformation amplitudes. In contrast, for the RT-ECAP, ET-ECAP and PED Ni samples the initial internal stresses are decreased at first. It seems, that there should be a common value of $\langle \sigma^2 \rangle^{1/2} \approx 50$ MPa for all types of samples at deformation amplitudes $\varepsilon_{pa} \geq 2 \times 10^{-3}$ independently from the grain size of the samples. This means that at sufficiently large ε_{pa} the cyclic plastic deformation is able to compensate the influence of the different prehistory of these samples on $\langle \sigma^2 \rangle^{1/2}$. A similar behaviour was

observed also for the root mean square strains $\langle \varepsilon^2 \rangle^{1/2}$ determined by the WA-analysis where L is the Fourier-length.

In order to proof the existence and to estimate the density ρ of dislocations, a KW-analysis was performed. For that purpose a function ψ was calculated from the Fourier-coefficients A_n of the diffraction profiles with

$$\psi = -\frac{\ln A_n}{L^2} = \frac{1}{Ld} + B \left(\ln \frac{R_{eff}}{L} \right) \quad \text{with } B = \frac{\pi}{2} (bg)^2 C\rho, \quad \text{where } R_{eff} \text{ is an outer cut-off radius for the stress field}$$

of the dislocation arrangement, b is the burgers vector and C is a mean contrast factor for the dislocations. From a fit of the ψ -function it follows that dislocations exist after cyclic plastic deformation in all kinds of samples, so that dislocations should assumed to be responsible for the elementary deformation processes even in grain structures with $D \approx 0.5\mu\text{m}$. For the RT-ECAP, ET-ECAP and PED Ni samples the high initial dislocation density is reduced by the fatigue, whereas in fc and mc Ni samples the dislocation density increases with increasing ε_{pa} (cf. Fig. 1c).

Considering the shape parameter $IB/FWHM$ of the diffraction profiles ($IB \dots$ integral breadth, $FWHM \dots$ half width) in dependence on ε_{pa} there is a conspicuous agreement of all kinds of samples. Starting from small values in the initial stage a maximum shape parameter can be observed at $\varepsilon_{pa} \approx 2.5 \times 10^{-4}$. For higher deformation amplitudes, $IB/FWHM$ seems to saturate at a value of about 1.35. For comparison, the corresponding values for fatigued single crystals are added [4]. From the agreement of the data it can be supposed that the arrangement of dislocations due to the cyclic plastic deformation is very similar independently from the grain size: at small and medium ε_{pa} there is a large volume fraction of thick regions with a high density of dislocation dipoles. The reduction of the shape parameter could be explained by a decrease of thickness and volume fraction of these regions with increasing ε_{pa} .

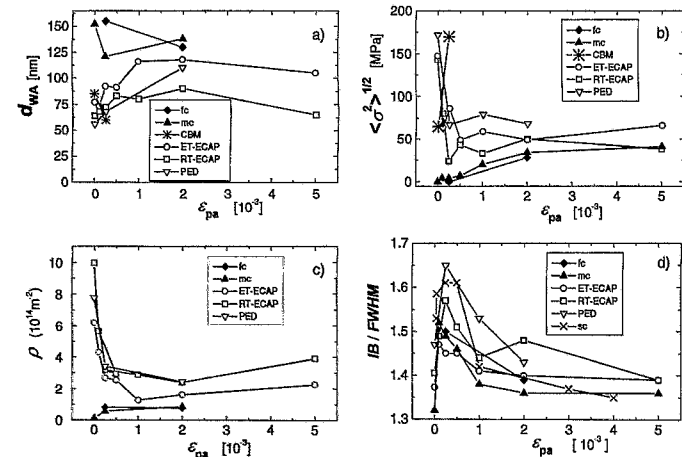


Fig. 1: Dependence of the size d_{WA} of coherently scattering regions (a) of the rms stress $\langle \sigma^2 \rangle^{1/2}$, (b) of the mean dislocation density ρ , (c) of the profile shape parameter $IB/FWHM$, and (d) on the plastic strain amplitude ε_{pa} for the different kinds of samples.

- [1] R. Klemm, E. Thiele, C. Holste, J. Eckert, N. Schell, Scripta Mater. 46 (2002) 685
- [2] B.E. Warren (1990), X-Ray Diffraction, Dover Publications Inc., New York
- [3] D. Breuer, P. Klimanek, U. Mühle, U. Martin, Z. Metallkd. 88 (1997) 680
M. Hecker, E. Thiele, C. Holste, Z. Metallkd. 88 (1997) 321



Experiment title: Characterisation of the oxide layers on bond coats of thermal barrier coatings		Experiment number: ME-393
Beamline: BM 20	Date of experiment: from: 10.07.2002 to: 16.07.2002	Date of report: 29.11.2002
Shifts: 18	Local contact(s): Dr. N. Schell, A. Bauer	<i>Received at ESRF:</i> 29.11.02

Names and affiliations of applicants (* indicates experimentalists):

W. Reimers, A. Pyzalla, B. Camin*, S. Dieter*, H. Freydanck*

TU Berlin
Sek. BH 18
Ernst-Reuter-Platz 1
D - 10587 Berlin
Germany

Tel. ++49 / (0)30-8062-3095, Fax: ++49 / (0)30-8062-3195

Report:

Thermal barrier coatings bonded by an NiCoCrAlY-alloy on a Ni-base-superalloy as well as intermetallics on γ -TiAl-base have met considerable interest as potential materials for high-temperature applications. Because of the good high-temperature-strength and strength-to-weight ratio of γ -TiAl, investigations focus on this new class of lightweight materials. Improving the oxidation resistance, which is the major drawback of TiAl at high temperatures, additions of further elements like Ag were tested that favour the formation of highly protective aluminium surface scales. The characterisation of the oxide scales in the early stages of oxidation by in-situ heating experiments includes analyses of phase and stress development which can be responsible for the initiation of cracks in the protection layer.

In previous experiments it was proven, that phase and residual stress analyses using synchrotron radiation offer numerous advantages compared to conventional X-ray diffraction. Among these advantages is the high intensity of the synchrotron X-ray which permits measurements at short measurement times, that are necessary carrying out in-situ experiments detecting phase changes. Due to the high intensity and parallelism of the synchrotron beam, the resolution of the very closely situated peaks of the Ti-Al-O System is possible which could not be achieved using conventional X-ray radiation.

In-situ experiments were accomplished using a furnace (Fig. 1) with halogen lamps for heating up to 800°C in air. The measurements were carried out in theta-2theta modus with an energy of 6930,3 eV (corresponds to the wavelength of Co K α -radiation) by using a scintillation detector. A range of 2theta between 40° and 53° was chosen, because in that range peaks with a high intensity of all phases of bulk material and oxides were expected.

The typical surface morphology of an oxide scale of a Ti-50Al-2Ag sample after 8h in-situ heating at 800°C is shown in Fig. 2.

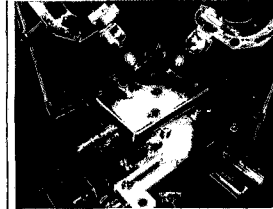


Fig. 1: Furnace for in-situ heating.



Fig. 2: SEM image, surface oxid scale, in-situ 800°C, 8h.

Fig. 3 shows the spectra obtained in an in-situ heating experiment at 800°C of a Ti-50Al-2Ag sample after adjusting the heating temperature as well as after appr. 3h and 8h annealing time. In the initial state there is one peak of very high intensity of 111 γ -TiAl (not all shown) and a smaller one of 002 Ti₃Al. After 3h annealing several peaks of γ -TiAl, Ti₃Al, Al₂O₃, TiO₂ and a cubic Ti₅Al₃O₂ phase (called Z-phase [1]) were found. After 8h annealing there are Ti₃Al, Al₂O₃, TiO₂ and Z-phase only.

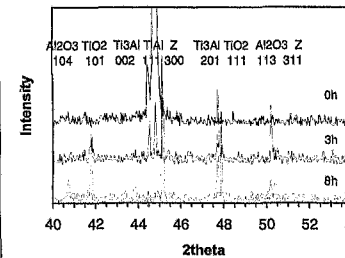


Fig. 3: In-situ spectra of Ti-50Al-2Ag at several times.

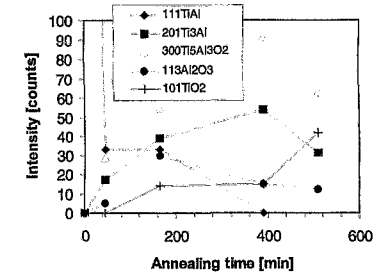


Fig. 4: Development of several peak intensities.

In Fig. 4 the development of the peak intensities in dependence of the annealing time of the same sample is shown. Whereas the peak intensity of the TiAl substrate decreases rapidly after a short oxidation time, oxide peaks appear and increase after further heating. A mixed scale of Al₂O₃ and TiO₂ instead of a dense Al₂O₃ scale as reported by [2] was found. The increasing of the Ti₃Al peak might be related to the formation of a Ti₃Al sublayer because of outward Al diffusion [3] during the oxidation as found in Ti-46.5Al-4(Cr,Nb;Ta,B) [2]. The Z-phase might have formed due to the reaction of Ti₃Al with O and/or Al₂O₃ in following the equation: 2Al₂O₃ + 5Ti₃Al → 3Ti₅Al₃O₂ [3]. This might be the reason for the same distribution of intensity of Ti₃Al and Z-phase (Fig. 4). However, the exact procedure of the formation of the Z-phase by reaction of oxygen with Al and Ti₃Al is unclear at the moment, this reaction plays an important role in the formation of a dense Al₂O₃ layer on the surface of the alloy.

In-situ stress analyses were carried out using the sin² ψ -method and tilting to 4 different ψ angles. For the calculation of the residual stresses from the strain distribution, the knowledge of diffraction elastic constants is essentially. The analysis of the data and the determination of these constants is still in progress.

[1] V. Shemet, et al., Intermetallics 5 (1997) 271-280

[2] L. Niewolak, et al., Structural Intermetallics 2001, TMS (2001) 535-540

[3] M.R. Yang, S.K. Wu, Oxid. Met. 54 (2000) 473-490



Experiment title:		Experiment number:
XRD of modified Ge-nanocrystals		SI 851
Beamline:	Date of experiment:	Date of report:
BM 20	from: 01.09.2002 to: 06.09.2002	06.11.2002
Shifts:	Local contact(s):	<i>Received at ESRF:</i>
12	Andreas Bauer	06.11.02
Names and affiliations of applicants (* indicates experimentalists):		
<u>DP B. Wunderlich*</u> , Dr. J. Kräußlich*, DP F. Wunderlich*, Prof. K. Goetz Friedrich-Schiller-University of Jena Institute of Optics and Quantumelectronics Department of X-Ray Physics Max-Wien-Platz 1 07743 Jena / Germany		

Report:

The aim of the experiment has been to characterize very small Ge-nanocrystals by means of high resolution x-ray diffraction methods (HRXRD). The Ge-nanocrystals forming in 4H-SiC(0001) substrate wafers after implantation and annealing with sizes under 5 nm are of special interest. The current nanocrystals forming process has been advanced by supplementary implantation of Xe ions. For this, the former successful methods of the crystal characterization used, in recent periods of HRXRD measurements [June 2001/ February 2002] at the CRG-beamline ROBL BM 20, shall be applied once more.

Additional investigations are required to clear up the recently observed angle shift of the Ge-reflections. Is this caused by any impurities with Si or by hydrostatic strain inside of the Ge-nanocrystals. Therefore, the stoichiometric composition of Ge-nanocrystals should be determined with measurements at different wavelengths apart and in the vicinity of the Ge-K-absorption-edge. This allows a distinction between Ge respectively Si contribution in the diffractograms in consequence of changing the x-ray atomic scattering factor f of Ge.

Samples

Ge⁺ ions with an energy of 250 keV were implanted into 4H-SiC(0001) crystal wafers produced and supplied by Cree Research Inc. The implantation temperature was kept at 700°C. The ion current density was less than 1 μAcm^{-2} . Samples were tilted about 6°–8° to the ion beam to avoid channeling effects during implantation. The ion fluency of $1 \cdot 10^{16} \text{ cm}^{-2}$ we used causes a Ge peak concentration of approximately 1 at.% in the deepness of 105 nm below the surface. Thermal annealing was carried out at temperatures up to 1600°C in Ar-atmosphere (pressure 20 kPa) using a rapid thermal annealing machine. The samples were placed between two electrically heated graphite stripes. To prevent significant decomposition, the annealing process was done with a sample arrangement face-to-face to an unimplanted SiC piece [1]. Ge-nanocrystals in 4H-SiC with sizes under 5 nm are most interesting for

applications. Up to our knowledge these nanocrystals have not yet been realized. A new procedure of preparation has been applied to our samples.

Xe ions with a very high energy of 390 MeV at 20°C and a dose of $1 \cdot 10^{14} \text{ cm}^{-2}$ have been implanted in the samples after their primarily implantation and annealing process of Ge⁺ ions as described above. This procedure should activate the Ge-nanocrystals formation inside of the crystalline SiC matrix.

Characterization

The x-ray diffraction experiments carried out at ROBL can be separated in two parts:

⇒ Firstly, characterization of Ge-nanocrystals formed in SiC samples after implantation with Xe ions

Samples which were implanted with Ge⁺ ions and annealed at 1600°C have shown a significant 111-Ge diffraction peak. The occurrence of 111-Ge diffraction peaks in the XRD pattern of the annealed samples indicate the formation of Ge crystallized inside the SiC samples. After the added implantation of Xe the 111-Ge diffraction peak was no longer observed.

Obviously, the Ge-nanocrystals disappear in samples which have been implanted with Xe ions after the implantation and annealing process of Ge⁺ ions. Furthermore, the upper layer of the substrate was strongly destroyed because of the implantation of Xe ions with a very high energy of 390 MeV. The reflections of substrate were split up into many peaks. Therefore, a determination of the inherent strain in the crystalline substrate was very difficult.

⇒ Secondly, investigations to clear up the observed angle shift of the Ge-reflections

It is obvious that the measured maximum of the 111-Ge diffraction peak is located at $2\theta = 28.2^\circ$. Compared to the theoretical value for crystalline Ge ($2\theta = 27.3^\circ$) this means a significant shift of the Bragg angle toward the value for crystalline Si ($2\theta = 28.4^\circ$). We can discuss two possible reasons for this behavior. The Ge-nano-crystals could be added impurities of Si atoms. On the one hand, the XRD measurements cover a sample area of nearly 1 mm^2 and for that a large volume of implanted SiC. The measurement represents an average of all crystallites in that area, including crystallites with different chemical composition. On the other hand, the shift of the Bragg angle can be caused by strain in the crystallites. The observed shift corresponds to a change of the lattice constant of $\Delta a/a = 3.1 \cdot 10^{-2}$.

Therefore, the stoichiometric composition of Ge-nanocrystals should be determined with measurements at different wavelengths apart and in the vicinity of the Ge-K-absorption-edge. This allows a distinction between Ge respectively Si contribution in the diffractograms in consequence of changing the x-ray atomic scattering factor f of Ge. Because the size of the nanocrystals are smaller as the extinction distance we therefore can use the kinematical approximation. The reflected intensity I is proportional to $|F_{\text{hkl}}|^2$ in the case of the kinematical approximation. For Ge in the diamond structure we have following terms:

$$\left[F_w \left(\frac{\sin \theta}{\lambda} \right) \right]^2 = 32 [(f_0 + f_1)^2 + (f_2)^2] \quad \text{für } h+k+l=4n \pm 1$$

f_0 – atomic scattering factor of Ge

f_1 – real part of the dispersion correction of the atomic scattering factor of Ge

f_2 – imaginary part of the dispersion correction of the atomic scattering factor of Ge

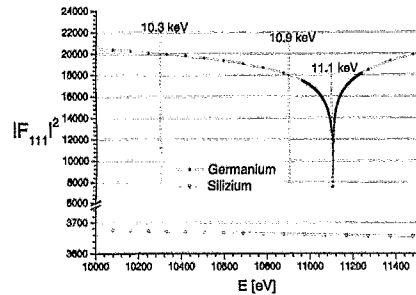


Fig. 1: The absolute value of the quadratic x-ray scattering factor F_{111} for Ge and Si in the vicinity of the Ge-K-absorption-edge ($E = 11.103 \text{ keV}$).

Considering the wavelengths and the anomalous dispersions corrections of the structure factor (Fig. 1), the ratio of the integrated reflectivity between a Ge-reflection at 10.3 keV and a Ge-reflection at 11.1 keV for a pure Ge-crystal (in the case of the kinematical approximation) is 1 to 1.631. The fitted peak areas can be used to calculate the ratio of the integrated reflectivity between the Ge-nanocrystals peak at 10.3 keV and the peak at 11.1 keV.

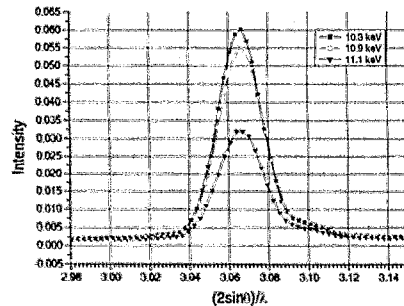


Fig. 2: The measured X-ray diffractograms ($\theta/2\theta$ -scans) of Ge-nanocrystals grown on 6H-SiC(0001) at three different wavelengths in the vicinity of the Ge-K-absorption-edge, represented in terms of the reciprocal lattices vector $(2\sin\theta)/\lambda$. (a) 10.3 keV, $\lambda = 0.12039 \text{ nm}$ (b) 10.9 keV, $\lambda = 0.11374 \text{ nm}$ (c) 11.1 keV, $\lambda = 0.11169 \text{ nm}$ (measured in a recent period of HRXRD measurements [June 2001] at the CRG-beamline ROBL BM 20).

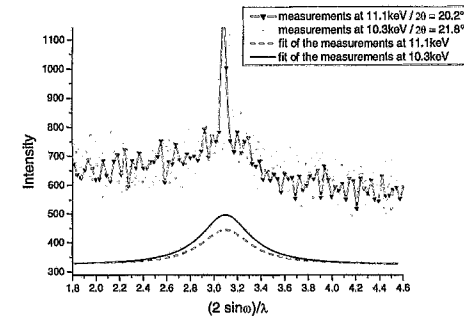


Fig. 3: The X-ray diffractograms (ω -scans) of Ge-nanocrystals having been produced in 4H-SiC by implantation of Ge^+ -ions and subsequent rapid thermal annealing at two different wavelengths apart and in the vicinity of the Ge-K-absorption-edge, represented in terms of the reciprocal lattices vector $(2\sin\theta)/\lambda$. (a) 10.3 keV, $\lambda = 0.12039 \text{ nm}$ (b) 11.1 keV, $\lambda = 0.11169 \text{ nm}$ (measured in the last period of HRXRD measurements [September 2002] at the CRG-beamline ROBL BM 20).

The evaluation of the x-ray diffraction measurements (Fig. 2) obtained by Ge-nanocrystals grown on 6H-SiC(0001) results in a ratio of 1 to 1.594 ± 0.026 . Hence, these Ge-nanocrystals consist in $84\% \pm 10\%$ of germanium.

The assessment of the Ge-nanocrystals produced in 4H-SiC by implantation of Ge^+ -ions and subsequent rapid thermal annealing is more difficult because the reflected intensity of the 111-Ge diffraction peak is very low and thus the ratio of the line – underground is dramatically decreased (see Fig. 3).

This investigation has shown that the stoichiometric composition of Ge-nanocrystals can be determined with measurements at different wavelengths apart and in the vicinity of the Ge-K-absorption-edge. But for the determination of the stoichiometric composition of Ge-nanocrystals having been produced in 4H-SiC by implantation of Ge^+ -ions and subsequent rapid thermal annealing the method has to advance to the limit of the resolution.

We thank all members of the ROBL beamline team, especially Dr. N. Schell and A. Bauer for the helpful support at the time of execution on this experiment.

Notes of the Editor

The Experimental Report 20_01_031C had already been printed in the previous ROBL Bi-Annual Report 1999/2000 due to late printing at that time and also in order to give a complete overview of similar experiments which represented a Ph.D. thesis work done at ROBL. As the experiments for report 20_02_031C had been done in the beginning of 2001, however, for completeness the report is reproduced.

Some reports for long-term experiments had been split into sub-reports A and B, respectively, because they represent different results which will accordingly be published as separate papers (20_02_41A/B and 20_02_051A/B).

Contrary to splitting, some reports have been combined in order to represent work which is connected (20_01_033_062, 20_01_036_053, 20_01_038_CH-1264, 20_01_041_052, and 20_01_055_066). They are listed only once (at the lower number). Twice reproduced is CH-1264 because it was also scheduled as an ESRF experiment. Also HS-1626 is twice reproduced because it combines EXAFS and XRD data, taken at both experimental stations.

The reports for ESRF experiments ME-479 and ME-475 will be published in the next Bi-Annual Report 2003/2004, because they were finished when this report passed its editorial deadline.

Whether the reports for experiments ME-246, 20_01_035, 20_01_047, 20_01_051, 20_01_059, 20_01_063, 20_01_600 and 20_01_610 will (ever) be published is pending for quite diverse reasons: maternity leave of main proposer, dissolution of university group, no sufficient data, or no reply before the editorial deadline.

In order to allow rapid scheduling, i.e. within only a week normally due to late sample preparation, several experiments in the materials end-station had to be declared as *technical shifts* without the usual specific experiment number. If they represented new experiments, they led accordingly to an in-house experimental report (20_02_IH5, 20_02_IH6, and 20_02_IH7).

To the end of the reporting period, the ESRF introduced forcefully an automatic submission system whereby a unique number is attached to every *submitted* proposal at the time of submission, independent and regardless of future rejection or chronological scheduling. The reports concerned start with number 600 and are not complete because of the aforementioned automatism.

The complete Bi-Annual Report 2001/2002 will be published on the net – as the previous two ROBL Reports – under http://www.esrf.fr/exp_facilities/BM20/BM20_Publi_e.html, i.e. the home page of the ESRF with branching into our beamline *bm20/publications and reports*.

For their help in organizing and checking the experiments and data concerning the radiochemistry end-station, I would like to thank Dr. C. Hennig and Dr. A. Roßberg, and also our technician U. Strauch who took some more workload as usual to allow us to sink deeply into the paperwork of writing this bi-annual report.

Special thanks are also and foremost due to all authors who contributed timely the Experimental Reports and especially the more thorough Highlight Reports at a time when everybody is busy finishing an old and starting a new year.